Transition metal dichalcogenide (tmd) nanosheets and fullerenes for beyond lithium-ion storage: a study of composite structure engineering and voltage-cutoff optimization

by

Sonjoy Dey

B.S., Khulna University of Engineering and Technology, 2018

AN ABSTRACT OF A DISSERTATION

submitted in partial fulfillment of the
requirements for the degree

DOCTOR OF PHILOSOPHY

Alan Levin Department of Mechanical and Nuclear Engineering
Carl R. Ice College of Engineering

KANSAS STATE UNIVERSITY
Manhattan, Kansas

2023

Abstract

The insatiable appetite for energy storage technologies has pushed the boundaries of innovation − enabling humans to transition from fossil fuel-based inefficient, environmentally unsustainable equipment to e-mobility devices/vehicles − three decades ago, which was thought to be unattainable. Most of such achievements are due to the proliferation of Li^+ ion-based rechargeable energy storage devices. But today, the depletion of resources (limited supply of Li) leading to cost increase has made it clear that developing alternative technologies and taking proper measures is imperative. With similarities in chemistry and working principles - providing ease in technological development and abundance due to precursors in natural resources like water, sodium, and potassium ion-based storage systems are considered the best alternatives. However, while advancements in LIB technology have reached their acme, developments in Sodium-ion batteries (NIBs) and Potassium-ion batteries (KIBs), specifically different cell components like electrodes and electrolytes, are nowhere near their peak. Therefore, this thesis aims to investigate novel, negative electrode materials for state-of-the-art NIBs and KIBs.

With Novoselov and Geim's discovery of individual Graphene nanosheets, two-dimensional (2D) materials have received uplifted interest for various applications. In this scenario, transition metal dichalcogenides (TMDs) with similar lamellar structure and versatile chemistry present further opportunities with attractive properties − comparatively higher uptake and faster diffusion of Li^+, Na^+, and K^+ ions being some of them. Although 2019 Nobel Prize winner in Chemistry, M. Stanley Whittingham, in the early 70s, started investigating the electrochemical properties of TMDs; the research was inevitably short-lived due to the poor stability of such classes of material. This report, therefore, examines in detail the fascinating properties of distinctive nanostructures of TMDs − where solutions to research challenges are yet to be proposed.

One inherent issue that all TMD-based electrodes face while applied as Li^+-based storage systems is the irreversibility of the conversion reaction. On top of that, when storage of larger ions such as Na^+/K^+ is considered, further complexities arise as volume changes and subsequent pulverization of materials occur. The first two studies involve composite structure formation using different nanostructures of sulfide-based TMDs, specifically WS_2 nanosheets (WS_2NS) and WS_2 nanotubes (WS_2NTs), to rectify the abovementioned intricacies. The composite structure was fabricated utilizing a chemically robust molecular polymer-derived ceramic matrix of silicon-oxycarbide (SiOC). As various studies have assessed the efficacy of high volume-to-strength ratio fiber-containing nanofillers, herein, we first investigated the fiber production feasibility using WS_2NS and WS_2NTs embedded within ceramic SiOC fibers utilizing electrospinning followed by pyrolysis at elevated temperatures. The pyrolyzed fibers containing WS_2NS and WS_2NTs, when tested beyond Li^+-based storage systems, demonstrated synergistic effects − rendering 2-3 times the capacity of the neat material. Furthermore, the typical capacity fading behavior of the neat TMDs was also absent in the composite electrodes − providing the basis for the initial hypothesis that SiOC fibers protect the nanofillers from degradation.

The third study investigated a different nanostructure of sulfide-based TMDs, namely WS_2 inorganic fullerenes (WS_2IFs), beyond Li^+ ion storage applications. Such closed cage fullerene-like structures have been previously studied in light-matter interaction − that extensively encompasses application fields of frequency conversion, optical imaging, and information processing. Additionally, their usage as lubricants or protective films for high load-bearing applications has been explored in depth. Being motivated by the numerous attractive properties and layered structure of WS_2IFs, they were applied to Na^+ and K^+ ion storage applications. Like the typical TMD nanosheets, such WS_2IFs also suffer from irreversible conversion reactions for which inefficiency in cycling behavior was observed − leading to capacity fading when larger ions than Li^+ are stored. Therefore, we utilized upper and lower voltage cut-off techniques to suspend conversion reactions at various stages. The kinetics of Na^+ and K^+ ion storage within WS_2IFs were further explored by employing different electrochemical analysis techniques − rendering the faradaic and non-faradaic processes

taking place. With higher capacity achievement in the case of Na^+ ion storage and higher coulombic efficiency realization in $Li^+/Na^+/K^+$ ion storage, this study lays the ground for future studies concerning efficient storage within cage-bound like fullerene structures.

Fine-tuning the physical properties of TMD nanosheets by continuous modulation of elemental composition has resulted in further band structure optimization − therefore, substituting metal or chalcogen atoms has rendered a new class of material such as TMD alloys, which expands the versatility of TMD nanosheets. In the fourth work, a cation-substituted TMD alloy, namely $MoWSe_2$¬ in its nanosheet form, was utilized in its nanosheet form to explore the Na^+ and K^+ ion storage properties. This investigation also used the upper voltage cut-off experiment to curb the increased conversion reaction from two transition metals. Three-dimensional (3D) surface plots of differential capacity analysis up to prolonged cycles revealed the convenience of voltage suspension as a viable method for structural preservation. Moreover, the cells with higher potential cut-off values conveyed improved cycling stability, higher and stable coulombic efficiency for Na^+ and K^+ ion half-cells, and increased capacity retention for Na^+ ion half-cells, respectively, with half-cells cycled at higher voltage ranges. Selenide-based TMDs ($MoSe_2$) were fabricated with SiOC matrix employing electrospinning technique further to test the viability of composite formation with TMD nanosheets. Finally, mechanical testing of the composite fibers was implemented to investigate the practicability of such fibermats in next-generation bendable, stretchable, free-standing devices.

Transition metal dichalcogenide (tmd) nanosheets and fullerenes for beyond lithium-ion storage: a study of composite structure engineering and voltage-cutoff optimization

by

Sonjoy Dey

B.S., Khulna University of Engineering and Technology, 2018

A DISSERTATION

submitted in partial fulfillment of the
requirements for the degree

DOCTOR OF PHILOSOPHY

Alan Levin Department of Mechanical and Nuclear Engineering
Carl R. Ice College of Engineering

KANSAS STATE UNIVERSITY
Manhattan, Kansas

2023

Approved by:

Major Professor
Dr. Gurpreet Singh

Copyright

© Sonjoy Dey 2023

Abstract

The insatiable appetite for energy storage technologies has pushed the boundaries of innovation − enabling humans to transition from fossil fuel-based inefficient, environmentally unsustainable equipment to e-mobility devices/vehicles − three decades ago, which was thought to be unattainable. Most of such achievements are due to the proliferation of Li^+ ion-based rechargeable energy storage devices. But today, the depletion of resources (limited supply of Li) leading to cost increase has made it clear that developing alternative technologies and taking proper measures is imperative. With similarities in chemistry and working principles - providing ease in technological development and abundance due to precursors in natural resources like water, sodium, and potassium ion-based storage systems are considered the best alternatives. However, while advancements in LIB technology have reached their acme, developments in Sodium-ion batteries (NIBs) and Potassium-ion batteries (KIBs), specifically different cell components like electrodes and electrolytes, are nowhere near their peak. Therefore, this thesis aims to investigate novel, negative electrode materials for state-of-the-art NIBs and KIBs.

With Novoselov and Geim's discovery of individual Graphene nanosheets, two-dimensional (2D) materials have received uplifted interest for various applications. In this scenario, transition metal dichalcogenides (TMDs) with similar lamellar structure and versatile chemistry present further opportunities with attractive properties − comparatively higher uptake and faster diffusion of Li^+, Na^+, and K^+ ions being some of them. Although 2019 Nobel Prize winner in Chemistry, M. Stanley Whittingham, in the early 70s, started investigating the electrochemical properties of TMDs; the research was inevitably short-lived due to the poor stability of such classes of material. This report, therefore, examines in detail the fascinating properties of distinctive nanostructures of TMDs − where solutions to research challenges are yet to be proposed.

One inherent issue that all TMD-based electrodes face while applied as Li^+-based storage systems is the irreversibility of the conversion reaction. On top of that, when storage of larger ions such as Na^+/K^+ is considered, further complexities arise as volume changes and subsequent pulverization of materials occur. The first two studies involve composite structure formation using different nanostructures of sulfide-based TMDs, specifically WS_2 nanosheets (WS_2NS) and WS_2 nanotubes (WS_2NTs), to rectify the abovementioned intricacies. The composite structure was fabricated utilizing a chemically robust molecular polymer-derived ceramic matrix of silicon-oxycarbide (SiOC). As various studies have assessed the efficacy of high volume-to-strength ratio fiber-containing nanofillers, herein, we first investigated the fiber production feasibility using WS_2NS and WS_2NTs embedded within ceramic SiOC fibers utilizing electrospinning followed by pyrolysis at elevated temperatures. The pyrolyzed fibers containing WS_2NS and WS_2NTs, when tested beyond Li^+-based storage systems, demonstrated synergistic effects − rendering 2-3 times the capacity of the neat material. Furthermore, the typical capacity fading behavior of the neat TMDs was also absent in the composite electrodes − providing the basis for the initial hypothesis that SiOC fibers protect the nanofillers from degradation.

The third study investigated a different nanostructure of sulfide-based TMDs, namely WS_2 inorganic fullerenes (WS_2IFs), beyond Li^+ ion storage applications. Such closed cage fullerene-like structures have been previously studied in light-matter interaction − that extensively encompasses application fields of frequency conversion, optical imaging, and information processing. Additionally, their usage as lubricants or protective films for high load-bearing applications has been explored in depth. Being motivated by the numerous attractive properties and layered structure of WS_2IFs, they were applied to Na^+ and K^+ ion storage applications. Like the typical TMD nanosheets, such WS_2IFs also suffer from irreversible conversion reactions for which inefficiency in cycling behavior was observed − leading to capacity fading when larger ions than Li^+ are stored. Therefore, we utilized upper and lower voltage cut-off techniques to suspend conversion reactions at various stages. The kinetics of Na^+ and K^+ ion storage within WS_2IFs were further explored by employing different electrochemical analysis techniques − rendering the faradaic and non-faradaic processes

taking place. With higher capacity achievement in the case of Na^+ ion storage and higher coulombic efficiency realization in $Li^+/Na^+/K^+$ ion storage, this study lays the ground for future studies concerning efficient storage within cage-bound like fullerene structures.

Fine-tuning the physical properties of TMD nanosheets by continuous modulation of elemental composition has resulted in further band structure optimization − therefore, substituting metal or chalcogen atoms has rendered a new class of material such as TMD alloys, which expands the versatility of TMD nanosheets. In the fourth work, a cation-substituted TMD alloy, namely $MoWSe_2$¬ in its nanosheet form, was utilized in its nanosheet form to explore the Na^+ and K^+ ion storage properties. This investigation also used the upper voltage cut-off experiment to curb the increased conversion reaction from two transition metals. Three-dimensional (3D) surface plots of differential capacity analysis up to prolonged cycles revealed the convenience of voltage suspension as a viable method for structural preservation. Moreover, the cells with higher potential cut-off values conveyed improved cycling stability, higher and stable coulombic efficiency for Na^+ and K^+ ion half-cells, and increased capacity retention for Na^+ ion half-cells, respectively, with half-cells cycled at higher voltage ranges. Selenide-based TMDs ($MoSe_2$) were fabricated with SiOC matrix employing electrospinning technique further to test the viability of composite formation with TMD nanosheets. Finally, mechanical testing of the composite fibers was implemented to investigate the practicability of such fibermats in next-generation bendable, stretchable, free-standing devices.

Table of Contents

List of Figures xv

List of Tables xxiii

Acknowledgements xxiv

Dedication xxvi

1 Introduction 1

1.1 Motivation 1

1.2 Researh Questions 6

1.3 Thesis Objectives 6

2 Background and Literature Review 8

2.1 Electrochemical Energy Storage Devices 8

2.1.1 Historical Background 8

2.1.2 Components of Electrochemical Energy Storage Devices 9

2.1.3 Batteries 10

2.2 Energy Storage in Lithium-ion Batteries 12

2.2.1 Historical Background 12

2.2.2 Method of Charging and Discharging in LIBs 13

2.2.3 Electrode Materials for LIB 15

2.3 Development and Research Progress of Na^+-ion Batteries 20

2.3.1 Historical Background 20

2.3.2 NIB Negative Electrode Materials 21

2.4 Development and Research Progress of Potassium ion Batteries 24
2.4.1 Historical Background 24
2.4.2 Traditional Anode Materials for KIBs and their Shortcomings 25
2.5 Transition Metal Dichalcogenides 27
2.5.1 Composition and Structure of TMDs 27
2.5.2 Synthesis techniques of TMDs 28
2.5.3 Distinctively Nanostructured TMDs 31
2.5.4 TMD Alloys and their Origin 32
2.5.5 Energy Storage Mechanism of TMDs 33
2.6 Polymer Derived Ceramics 35
2.6.1 General structure of pre-ceramic polymers and their varieties 35
2.6.2 Processing Technique of PDCs 36
2.6.3 Microstructure of PDCs 38
2.6.4 Electrochemical Properties of PDCs 40

3 Experimental Methods and Instrumentations 44
3.1 Experimental Methods 44
3.1.1 Electrospinning 44
3.1.2 Preparation of Fibermats 47
3.2 Characterization Techniques 48
3.2.1 Microscopic Techniques 48
3.2.2 Spectroscopic Techniques 50
3.2.3 Electrochemical Analysis Techniques 53

4 WS_2 Nanosheet rooted SiOC Fibermat for beyond Li^+- ion Storage 57
4.1 Preface 57
4.2 Introduction 58
4.3 Materials and Methods 60

4.3.1 Electrospinning Solution Preparation . . . 60
4.3.2 Electrospinning Conditions and Fibermat Fabrication . . . 61
4.3.3 Characterization Techniques . . . 62
4.3.4 Electrochemical Techniques . . . 62
4.4 Results and Discussions . . . 63
4.4.1 Microscopic Analysis . . . 63
4.4.2 Spectroscopic Analysis . . . 66
4.4.3 Electrochemical Analysis . . . 70
4.5 Conclusion . . . 78

5 Sodium and Pottasium ion Storage inside WS_2 Nanotube Embedded SiOC Composite Fibers . . . 84
5.1 Preface . . . 84
5.2 Introduction . . . 85
5.3 Materials, Methods and Characterization . . . 87
5.3.1 Fibermat Synthesis Process . . . 87
5.3.2 Characterization Techniques . . . 88
5.3.3 Electrochemical Measurements . . . 89
5.4 Results and Discussion . . . 90
5.4.1 Microscopic Analysis . . . 90
5.4.2 Spectroscopic Analysis . . . 94
5.4.3 Electrochemical Analysis . . . 101
5.5 Conclusion . . . 106

6 Addressing Irreversibility and Structural Distortion in Quantum-Confined WS_2IF nanoparticles: Effects of Voltage Cut-off Experiments in Beyond Li^+-ion storage Applications . . . 112
6.1 Preface . . . 112

6.2 Introduction . . . 113
6.3 Materials and Methods . . . 115
6.3.1 Morphologic and spectroscopic characterization . . . 115
6.3.2 Electrochemical Measurements . . . 115
6.4 Results and Discussions . . . 116
6.4.1 Spectroscopic and Microscopic Analysis . . . 116
6.4.2 Electrochemical Analysis . . . 118
6.5 Post-Cycling Analysis . . . 128
6.6 Conclusion . . . 130

7 Sodium and Potassium ion storage in Cation Substituted 2D $MoWSe_2$: Insights into the Effects of Upper Voltage Cut-off3 . . . 143
7.1 Preface . . . 143
7.2 Introduction . . . 144
7.3 Materials, Methods, and Characterization . . . 146
7.3.1 Morphologic and Spectroscopic Characterization . . . 146
7.3.2 Electrochemical Characterization . . . 147
7.4 Results and Discussions . . . 147
7.4.1 Microscopic and Spectroscopic Analysis . . . 147
7.4.2 Electrochemistry . . . 151
7.5 Post-Cycling Analysis . . . 160
7.6 Conclusion . . . 163

8 Enhanced Li-Ion Rate Capability and Stable Efficiency Enabled by $MoSe_2$ Nanosheets in Polymer-Derived Silicon Oxycarbide Fiber Electrodes . . . 172
8.1 Preface . . . 172
8.2 Introduction . . . 173
8.3 Materials and Methods . . . 175

8.3.1 Materials 175
8.3.2 Methods 177
8.4 Results and Discussions 180
8.4.1 Morphological Characterization 180
8.5 Summary and Conclusion 193
8.6 Mechanical Testing of Fibermats 194

9 Conclusion and Future Direction 197
9.1 Dissertation Summary 198
9.2 Direction of Future Work 201

Bibliography 204

List of Figures

1.1 a. plot describing energy production scenario as a function of different classes of energies and correlated number of published articles; b. interruptions in solar power output (percentage of rated capacity) from a solar plant situated in Arizona, USA; c. fluctuations in wind power generation from five different sites in USA. 2

1.2 a. A map of the Li reserves and soda ash reserves (sodium reserves) in the world reported in 2020[118], Copyright 2020 WILEY-VCH Verlag GmbH & Co. KGaA, Weinheim; b. Elemental composition of brine from the Salar de Atacama in Chile[311], Copyright 2018, Macmillan Publishers Limited. 4

1.3 Experimental overview of five different investigations conducted for reaching goals of the thesis. 7

2.1 Different types of commercial lithium-ion rechargeable batteries: a. cylindrical cells; b. prismatic cells; c. pouch cells[54]. Copyright 2016, Macmillan Publishers Limited. 12

2.2 Schematic illustration of the working principle of lithium-ion batteries[167], Copyright The Royal Society of Chemistry 2014. 14

2.3 Schematic energy diagram of a lithium cell at open circuit[177], Copyright 2018 WILEY-VCH Verlag GmbH & Co. KGaA, Weinheim. 16

2.4 Schematic representation of graphite, soft carbon, and hard carbon used for anodes in Li-ion batteries[224], Copyright © 2001 John Wiley & Sons, Inc. and The Japan Chemical Journal Forum. 17

2.5 An overview of challenges in the materials and process technologies for future flexible lithium-ion battery research[121;181]. Copyright 2019, The Royal Society of Chemistry. 19

2.6 a. Shared history of NIB and LIBs[38], Copyrights 2020 The Authors. Published by Wiley-VCH GmbH; b, and c. Rise in publication and research activity related to NIBs[105], Copyright 2020 Wiley-VCH GmbH. 22

2.7 Illustration of various negative electrode materials available for NIB systems[128], Copyright The Royal Society of Chemistry 2017. 24

2.8 a. Summary of challenges for KIB anode materials[384], Copyright 2019 Science Advances; b. Potassiation/Depotassiation of Sn_4P_3/C electrode[385], Copyright 2017 American Chemical Society; c. Capacity vs. voltage and cycle number plots of various anode materials of KIBs[384], Copyright 2019 Science Advances. 26

2.9 (a) schematic illustration of lithium intercalation based exfoliation[371], Copyright 2011 WILEY-VCH Verlag GmbH & Co. KGaA, Weinheim; (b) schematic illustration of anion intercalation based exfliation[194], Copyright 2014 American Chemical Society. 29

2.10 Effects of strong sonication of MoS_2 flakes dispersed in isopropyl alcohol: a. Breaking between Basal Planes and b. great fragmentation of the lamellae[219], Copyright 2015 American Chemical Society. 30

2.11 Charge storage mechanisms for TMDs in different alkali metal ion batteries[39], Copyright 2020, Royal Society of Chemistry. 34

2.12 Simplistic formula of polymer derived ceramics and different pre-ceramic organosilicon polymers[58], Copyright 2010 The American Ceramic Society. 37

2.13 Various shaping techniques for the production of PDC components[335], Copyright 2010 The American Ceramic Society. 38

2.14 The processes involved in forming PDCs at different temperatures[58], Copyright 2010 The American Ceramic Society. 39

2.15 a. Proposed model of nanodomains in polymer derived SiOC based ceramics[335], Copyright 2016, American Association for the Advancement of Science, b. Schematic representation of lithium-ion storage mechanism in SiOC based ceramics[285;335], Copyright 2018 The American Ceramic Society. 41

2.16 a, b. Na^+-ion cycling performance of SiOC ceramics derived from silicone oil[33], Copyright 2018 Elsevier B.V. All rights reserved; c. Alkali-metal ion insertion into SiOC ceramics and consecutive phase formation[35], Copyright 2021 Elsevier B.V. All rights reserved. 43

3.1 Fiber formation by electrospinning method[114], Copyright © 2011, Springer Science Business Media, LLC. 45

3.2 Schematic illustration of solution preparation process for electrospinning. . . 48

3.3 Schematic illustration of basic XPS equation[289], Rights managed by AIP Publishing. 50

3.4 Schematic of Stokes and Anti Stokes Scattering[239], Copyright 2003 WILEY-VCH Verlag GmbH & Co. KGaA, Weinheim. 52

4.1 SEM and TEM micrographs, EDS color maps and spectra of WS_2/SiOC fibermat 65

4.2 Raman and FTIR spectra of WS_2/SiOC fibermat 67

4.3 XPS survey and high-resolution spectra of pyrolyzed WS_2/SiOC fibermat . . 68

4.4 GCD profiles of WS_2/SiOC composite electrode in Na-ion and K-ion half-cells. 74

4.5 Post-cycling SEM micrographs of disassembled WS_2/SiOC electrodes of Na and K-ion half-cells. 77

4.6 Digital camera images of the WS_2/SiOC composite fibermats in (a) as-spun; (b) cross-linked; (c) pyrolyzed forms with corresponding weight retention and linear shrinkage values. 79

4.7 GCD profiles of neat WS_2 and SiOC electrodes in Na-ion half-cells. 82

4.8 GCD profiles of neat WS_2 and SiOC electrodes in Na-ion half-cells. 83

5.1 Schematic of the synthesis process of WS_2NT/SiOC fibermat from electrospinning to cross-linking to pyrolysis steps through controlled annealing. . . 90

5.2 SEM micrograph, EDS mapping, and EDS spectra of WS_2NT/SiOC fibermats. 92

5.3 TEM micrographs and SAED patterns of neat WS_2NTs and WS_2NT/SiOC fibers. 94

5.4 Raman and FTIR spectra of WS_2NT/SiOC fibermats. 96

5.5 XPS survey scan, high-resolution spectra and XRD reflections of WS_2NT/SiOC fibermats. 100

5.6 GCD profiles and rate capability tests ofWS_2NT/SiOC composite electrode when tested in a Na-ion half-cell setup. 102

5.7 SEM micrographs of recovered electrodes after cycling in Na-ion systems. . . 106

5.8 Fiber diameter distribution plot of (a) As-spun; (b) Cross-linked; and (c) Pyrolyzed fibermats. 107

5.9 SEM micrograph of SiOC pyrolyzed fibers at (a) lower magnification and (b) higher magnification exhibiting some irregularities (bead-like formation) in the fiber geometry. 109

5.10 GCD profiles of neat WS_2NT and SiOC electrode in Na-ion half-cell. 110

5.11 Fiber diameter distribution plot of the cycled electrode. 111

6.1 SEM, TEM, Raman Spectra, XRD Reflection, XPS Survey Scan of WS_2IF powders. 117

6.2 GCD profiles and 3D dq/dV curves of WS_2IF electrodes for NIB and KIB cells cycled at different voltage ranges. 120

6.3 Cycling stability and consequtive coulombic efficiency of: a. NIB 0.01-2.5 V and NIB 0.01-1.5 V cells, b. KIB 0.01-2.5 V and KIB 0.01-1.5 V cells. 125

6.4 CV curves and storage contributions of NIB and KIB cells cycled within different potential ranges for WS_2IF electrodes. 128
6.5 Post cycling microscopic and spectroscopic characterizations of NIB and KIB cells cycled within different potential ranges. 130
6.6 Optional: GCD curves of a1. LIB 0.01-2.5 V, a2. LIB 0.01-1.5 V; differential capacity curves of b1. LIB 0.01-2.5 V, b2. LIB 0.01-1.5 V; differential capacity curves plotted as a function of cycle index for c1. LIB 0.01-2.5 V, c2. LIB 0.01-1.5 V half-cell. 132
6.7 Surface plots derived from the 3D differential capacity curves for LIB half-cells during a1. 0.01-2.5 V delithiation stage, a2. 0.01-1.5 V lithiation stage, b1. 0.01-1.5 V delithiation stage, b2. 0.01-1.5 V lithiation stage. 133
6.8 Surface plots derived from the 3D differential capacity curves for NIB half-cells during a1. 0.01-2.5 V desodiation stage, a2. 0.01-1.5 V sodiation stage, b1. 0.01-1.5 V desodiation stage, b2. 0.01-1.5 V sodiation stage. 134
6.9 Surface plots derived from the 3D differential capacity curves for KIB half-cells during a1. 0.01-2.5 V depotassiation stage, a2. 0.01-1.5 V potassiation stage, b1. 0.01-1.5 V depotassiation stage, b2. 0.01-1.5 V potassiation stage. 135
6.10 Cycling stability test of LIB half-cells cycled at 0.01-1.5 V and 0.01-2.5 V range. 136
6.11 GCD curves of: a1. NIB 0.25-1.5 V, a2. NIB 0.5-1.5 V, a3. KIB 0.25-2.5 V, a4. KIB 0.5-1.5 V half-cells; differential capacity curves of: b1. NIB 0.25-1.5 V, b2. NIB 0.5-1.5 V, b3. KIB 0.25-2.5 V, b4. KIB 0.5-1.5 V half-cells. . . . 137
6.12 Cycling stability test of a. NIB half-cells cycled at 0.25-1.5 V and 0.5-2.5 V range; b. KIB half-cells cycled at 0.25-1.5 V and 0.5-2.5 V range. 138
6.13 CV curves of a1. LIB 0.01-1.5 V, a2. LIB 0.01-2.5 V half cells; capacitive and diffusion-controlled contribution ratios for different scan rates of b1. LIB 0.01-1.5 V, b2. LIB 0.01-2.5 V half-cells. 139

6.14 Fitting of anodic and cathodic voltammetric sweep data of a1. LIB 0.01-1.5 V, a2. NIB 0.01-1.5 V, a3. KIB 0.01-1.5 V, b1. LIB 0.01-2.5 V, b2. NIB 0.01-2.5 V, b3. KIB 0.01-2.5 V half-cells. 140
6.15 XRF spectrum and elemental composition (determined by XRF) of the neat electrode (before cycling). 141
6.16 Raman spectrum of the neat electrode (before cycling). 142

7.1 a) Low-resolution TEM images of the $MoWSe_2$ flakes; b, c) high-resolution TEM images of $MoWSe_2$ nanosheets; d) six-fold symmetrical SAED spot pattern generated from the $MoWSe_2$ bulk flake shown in the index; e) Raman spectrum of bulk $MoWSe_2$ alloy depicting different vibrational modes. 148
7.2 a) XPS survey scan depicting the presence of different materials within $MoWSe_2$; high-resolution b) Mo3d; c) W4f; d) Se3d XPS spectra of the $MoWSe_2$ material illustrating the chemical bonding states. 150
7.3 GCD profiles and 3D dQ/dV curves of $MoWSe_2$ electrodes in NIB half-cells. 153
7.4 Rate capability and consecutive cycling stability tests of $MoWSe_2$ electrodes in NIB half-cells. 155
7.5 GCD profiles and 3D dQ/dV curves of $MoWSe_2$ electrodes in KIB half-cells. 158
7.6 Rate capability and consecutive cycling stability tests for investigating K^+ ion storage behavior of half-cells cycled within different potential ranges. 159
7.7 Post cycling analysis of $MoWSe_2$ electrodes after cycling in NIB and KIB systems. 162
7.8 Fringe distance determination from TEM image of Figure 1c. a) FT image, b) Inverse FT image, and c) Fringe profile plot from the inverse FT image derived from Figure 7.1c. 165
7.9 Raman spectra of bulk a) $MoSe_2$ and b) WSe_2 powders for clear comparison with bulk $MoWSe_2$ powder; c) schematic of vibrational modes typically obtained from TMDs. 166

7.10 Differential capacity curves of Na^+ ion half-cells of $MoWSe_2$ electrode cycled within potential ranges: a) 0.01-2.5 V; b) 0.01-2.0 V; c) 0.01-1.5 V. 167
7.11 Cycling stability test of $MoWSe_2$ electrodes cycled within the potential range of 0.01-1.5 V, 0.01-2.0 V, 0.01-2.5 V in Na^+ ion half-cells. 168
7.12 Differential capacity curves of K^+ ion half-cells of $MoWSe_2$ electrode cycled within potential ranges: a) 0.01-2.5 V; b) 0.01-2.0 V; c) 0.01-1.5 V. 169
7.13 Digital camera photographs of disassembled electrodes from a) $MoWSe_2$ 0.01-2.5 V Na^+ ion half-cell, b) $MoWSe_2$ 0.01-2.5 V K^+ ion half-cell; c) $MoWSe_2$ 0.01-1.5 V Na^+ ion half-cell, d) $MoWSe_2$ 0.01-1.5 V K^+ ion half-cell. 170
7.14 XRF plots and corresponding elemental composition of a) neat $MoWSe_2$ electrode, b) 0.01-1.5 V $MoWSe_2$ Na^+ ion half-cell, and c) 0.01-1.5 V $MoWSe_2$ K^+ ion half-cell. 171

8.1 Solution preparation process for (a) PVP/SiOC/$MoSe_2$ fiber mat; (b) schematic showing electrospinning process for the fabrication of the PVP/SiOC/$MoSe_2$ composite fiber mats. 176
8.2 SEM images of (a) PVP fiber mat carbonized at 800 °C, (b) PVP/SiOC fiber mat pyrolyzed at 800 °C, (c) PVP/SiOC/$MoSe_2$ fiber mat pyrolyzed at 8000 °C, and (d–f) corresponding high-magnification images of these fiber mats (inset shows diameter distribution of the fibers). 179
8.3 TEM images of (a) PVP fibers carbonized at 800 °C, (b) PVP/SiOC fibers pyrolyzed at 800 °C, (c) PVP/SiOC/$MoSe_2$ fibers pyrolyzed at 800 °C, and corresponding HRTEM (d–f) and diffraction pattern (g–i) images of these fibers. Diffraction pattern of pyrolyzed PVP/SiOC/$MoSe_2$ indicates the presence of $MoSe_2$ particles in the pyrolyzed fiber mat. 181

8.4 Raman spectra of carbonized PVP fiber mat with integrated peaks; (b) Raman spectra of pyrolyzed PVP/SiOC fiber mat with integrated peaks; (c) Raman spectra of bulk $MoSe_2$ powder and the region of 200–300 cm^{-1} from the pyrolyzed SiOC/$MoSe_2$ fiber mat; (d) Raman Spectra of pyrolyzed PVP/SiOC/$MoSe_2$ fiber mat with integrated peaks in the region of 800–2000 cm^{-1}. 184

8.5 XPS survey scan of pyrolyzed PVP, PVP/SiOC, and PVP/SiOC/$MoSe_2$ fiber mats. 185

8.6 High-resolution XPS spectra of three pyrolyzed fiber mats: (a–c) PVP fiber mat; (d–f) PVP/SiOC fiber mat; (g–k) PVP/SiOC/$MoSe_2$ fiber mat. 187

8.7 FTIR spectra of (a) as-spun, (b) cross-linked, and (c) pyrolyzed fiber mats. Each figure consists of the FTIR spectra shown for PVP, PVP/SiOC and PVP/SiOC/$MoSe_2$ fiber mats from bottom to top. 188

8.8 Charge–discharge profile of (a) PVP fiber mat electrode; (b) PVP/SiOC fiber mat electrode; (c) $MoSe_2$ drop coated fiber mat electrode; (d) PVP/SiOC/$MoSe_2$ electrode and differential capacity curves of (e) PVP fiber mat electrode; (f) PVP/SiOC fiber mat electrode; (g) $MoSe_2$ drop coated fiber mat electrode; (h) PVP/SiOC/$MoSe_2$ electrode; (i) cycle performance comparison for PVP, PVP/SiOC, PVP/SiOC/$MoSe_2$ electrode at different current densities. . . . 190

8.9 Solidworks 3D model of the grip designed for tensile testing of x-linked fibermats with digital camera images. 194

8.10 Stress-strain plots of a. best performing fibermats from all samples; b. PVP; c. SiOC; d. $MoSe_2$/SiOC; e.WS2NT/SiOC; f. WS2NS/SiOC fibermats. . . . 195

List of Tables

4.1 Elemental Composition of the fibermats by XPS 79

4.2 Summary and comparison of electrochemical performance for Na^+ storage of other nanomaterial-based structures with this work. 80

4.3 Summary and comparison of electrochemical performance for K^+ storage of other nanomaterial-based structures with this work. 81

5.1 Elemental Composition of the fibermats by XPS 108

5.2 Elemental Composition of the spent electrode by XPS 108

5.3 Summary and comparison of electrochemical performance for Na^+ storage of other nanomaterial-based structures with this work. 108

6.1 Elemental composition of the electrodes determined by XRF 132

6.2 Elemental composition determined by XPS 135

6.3 Comparative electrochemical properties of different WS_2 quantum-confined structures. 136

8.1 Tensile properties of fibermats with or without reinforcement. 196

Acknowledgments

I want to start with a few lines from "Invictus" by William Ernest Henley, the poem that inspired me during challenges:

"Out of the night that covers me,

Black as the pit from pole to pole,

I thank whatever gods may be

For my unconquerable soul."

"It matters not how strait the gate,

How charged with punishments the scroll,

I am the master of my fate:

I am the captain of my soul."

I want to express my sincere gratitude and appreciation to the individuals who have contributed to the completion of this thesis.

First and foremost, I extend my heartfelt thanks to my thesis supervisor, Dr. Gurpreet Singh, whose guidance, expertise, and unwavering support were instrumental throughout this research journey. Your mentorship and invaluable insights have significantly shaped the outcome of this work, and I am grateful for your dedication to my academic and personal growth.

I am deeply indebted to my lab colleagues at the Nanoscience and Engineering lab – Dr. Shakir Bin Mujib, Dr. Davi Marcelo Soares, and Arijit Roy, who created a stimulating research environment filled with camaraderie and collaboration. Your diverse perspectives and willingness to share knowledge have enriched my understanding of the subject matter and made this research experience truly rewarding. I would also like to thank Dr. Scott Fan for introducing me to Lithography, Dr. Andrei Sokolov for training me on clean room practices and instruments, and Dr. Dan Boyle for his training on TEM.

To my parents (Priya Lal Dey, and Shipra Dey) and Sister (Priyanka Dey), your unwavering love, encouragement, and sacrifices have been the foundation of my educational pursuits. Your belief in my abilities has always motivated me, and I am profoundly grateful for your boundless support and sacrifices—additionally, a person whose unwavering belief in my abilities made everything possible: Manash Ranjan Bhadra.

I would also like to acknowledge the invaluable assistance and guidance provided by Dr. Reshef Tenne, and Dr. Alla Zak, who generously shared their expertise and resources.

Financial support from National Science Foundation grants 1743701, 1454151, and 2025298 is gratefully acknowledged. The research was performed in part in the Nebraska Nanoscale Facility: National Nanotechnology Coordinated Infrastructure and the Nebraska Center for Materials and Nanoscience (and/or NERCF), which are supported by the National Science Foundation under Award ECCS: 2025298, and the Nebraska Research Initiative.

Lastly, I extend my heartfelt thanks to my cousins and well-wishers (Abu Sayed Maroof, and Partha Pratim Chakraborti in particular), who have been a source of encouragement and motivation. This thesis would not have been possible without these individuals' collective support and encouragement. Thank you for being part of this academic journey.

Dedication

For those who exist in my thoughts and offer a comforting perspective with their enduring presence:

"When you awaken in the morning's hush

I am the swift uplifting rush

Of quiet birds in circled flight.

I am the soft stars that shine at night.

Do not stand at my grave and cry,

I am not there; I did not die."

- Mary Elizabeth Frye

This thesis is dedicated to the cherished memory of my beloved grandfather, Bijoy Chandra Dey, who graced this beautiful world for a remarkable 102 years and played a pivotal role in educating a nation. I also dedicate this work to my dear uncle, Chandan Dey, both of whom left us during the initial two years of my Ph.D. journey.

Chapter 1

Introduction

1.1 Motivation

The impact of fossil fuels on the well-being and way of life of humanity on Earth is undeniable and can best be gauged through the progress of human society and population growth. Nevertheless, such a supreme gift has also brought numerous detrimental consequences – air pollution due to the emission of greenhouse gases resulting in global warming and related health issues are most prominent. On top of that, depleting resources due to the ever-growing population poses a severe threat, forcing humans to search for alternative technologies. Combating the obstacles stated above is no easy task, for which the search for simple, sustainable resources providing long-term constant energy outcomes with minimal adverse consequences, otherwise known as renewable energy sources, took place. Prominent renewable energy sources are pump hydro, wind, and solar-based energy generation technologies, which can be expanded to geothermal, ocean, and biomass-derived sources. Figure 1.1a shows the energy production scenario in GWh on different renewable energy classes and the number of published and funded research articles: where significant participants are the United States and China[7]. However, there is no way to overlook the intermittent nature of such renewable energy sources. For example, Figures 1.1b, and c show the fluctuations in solar power output varying as a result of moving clouds from a 4.6 MW solar array in

Springerville, Arizona, and uneven wind power output (percentage of rated capacity) at five different sites (Amarillo, Corpus Christi, Presidio AEI, Sweetwater, and North Washburn in Texas USA) respectively[291]. Such an imbalance in power output puts the reliability of grids in question; the solution lies in using energy reservation technologies using battery systems.

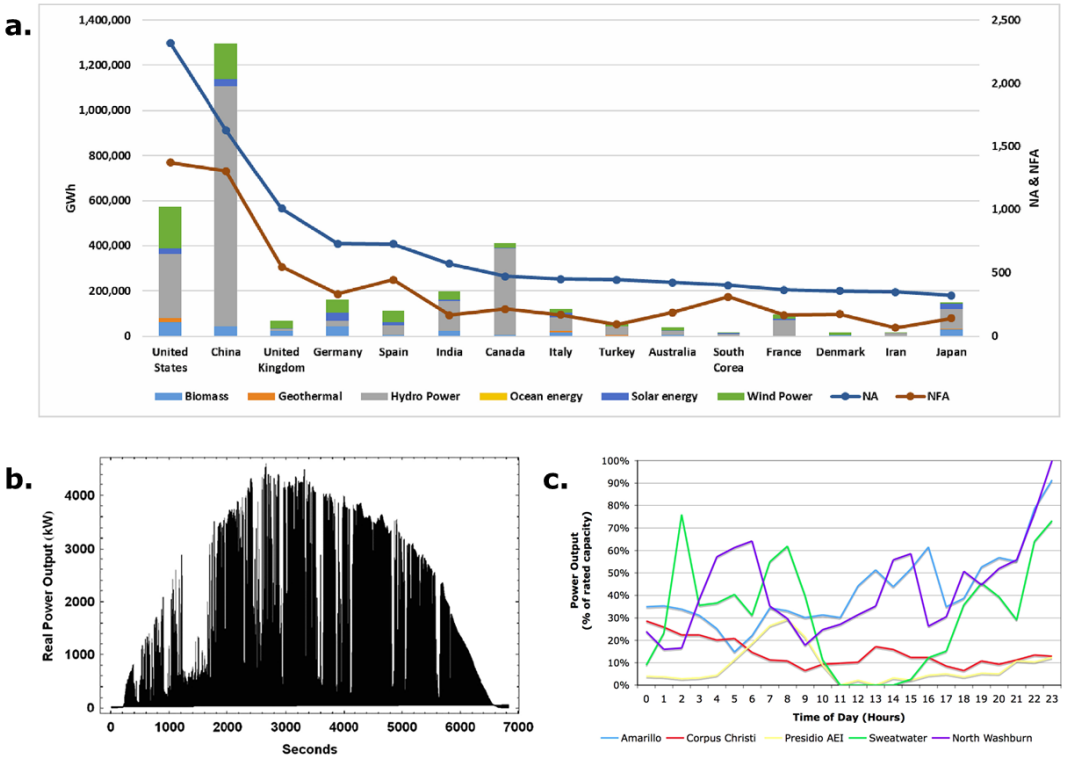


Figure 1.1: *a. plot describing energy production scenario as a function of different classes of energies and correlated number of published articles; b. interruptions in solar power output (percentage of rated capacity) from a solar plant situated in Arizona, USA; c. fluctuations in wind power generation from five different sites in USA.*

2019 was the year when a long overdue recognition was handed out to John Goodenough, M. Stanley Whittingham and Akira Yoshino in the form of the Nobel Prize in Chemistry, for their part in clarifying the chemistry behind versatile energy storage devices, otherwise known as LIBs. Commercialized in 1991 by SONY corporation, LIBs immediately experienced immense growth, after three decades of which such technology is powering portable consumer electronic devices to battery electric vehicles[38]. However, recent years have witnessed a price hike in LIB raw materials due to increased demand for manifold applications. For instance, since 2010, the price hike in LIB raw material - Li_2CO_3, was 151% (from \$5180 to \$13,000

per metric ton)[42]. The problem has been exacerbated due to geopolitical reasons: at present, lithium mining is concentrated in particular regions around the globe, with Chile (8.6 million tons) and Australia (2.8 million tons) playing significant roles, where Argentina and China follow[118].

Nevertheless, mining itself is never a sustainable process, and Li mining does not defer from life-threatening incidents. An excellent example is the reporting of toxic leakage into groundwater near at least one Li mine in South America, China, and Australia. As a result of the leakage in China and Australia, activities in the mining process were temporarily halted or blocked from extension[227]. Furthermore, Li brine processing requires evaporation techniques that consume hefty amounts of water, leading to the depletion of groundwater levels in arid areas[309]. On top of all these, the COVID-19 pandemic provided a wake-up call for the world as lockdowns in China resulted in supply disruption of half of the world's battery raw materials. Pressingly, now is the time to look for complementary battery technologies, more than ever, to be better prepared for the growing demand, the unforeseen supply chain disruption event, or to achieve cleaner, reliable alternative energy production technology[5].

When complementary battery technologies are considered – NIBs stand out for various reasons, the most convincing of them is the global availability of raw materials, which include Na_2CO_3, Na_2SO_4, and NaCl, which are all cheap and highly obtainable from minerals and brine (Figure 1.2a). The search for raw material of Li often results in the production of other abundant metals. For example, the brine deposit in Salar de Atacame, Chile (Figure 1.2b), from where the highest amount of Lithium is produced, contains Sodium (9.1 wt.%), Potassium (2.36 wt.%), Magnesium (0.97 wt.%), Lithium (0.16 wt.%), and Boron (0.04 wt.%), Li being the least concentrated among them[228]. Another important motivating factor for utilizing NIBs derives from the cost-effectiveness on a cell level realized from using an Aluminium (Al) current collector in the negative electrode side. Al (2.7%) provides a cheaper alternative at a cell level than traditional Cu (11.6%) current collectors, reducing 55% mass, and improving power density. The reason behind the replacement stems from the binary alloy formation of Al with Li at a lower potential. Although NIB research efforts started with applying $Na/NaCoO_2$ cells in the early 70s, the commercialization of LIB

systems halted such activities. Investigations regarding high-temperature NIBs and Na-S batteries were still taking place[38]. Still, the rejuvenation and consequent unprecedented progress came three decades later – realizing the same equipment for LIB production can be used for NIB production and the importance of possessing various battery technologies to attenuate supply risks and increase the application diversity[309]. The recent series of pandemic-related incidents has added clarity to the rationale above.

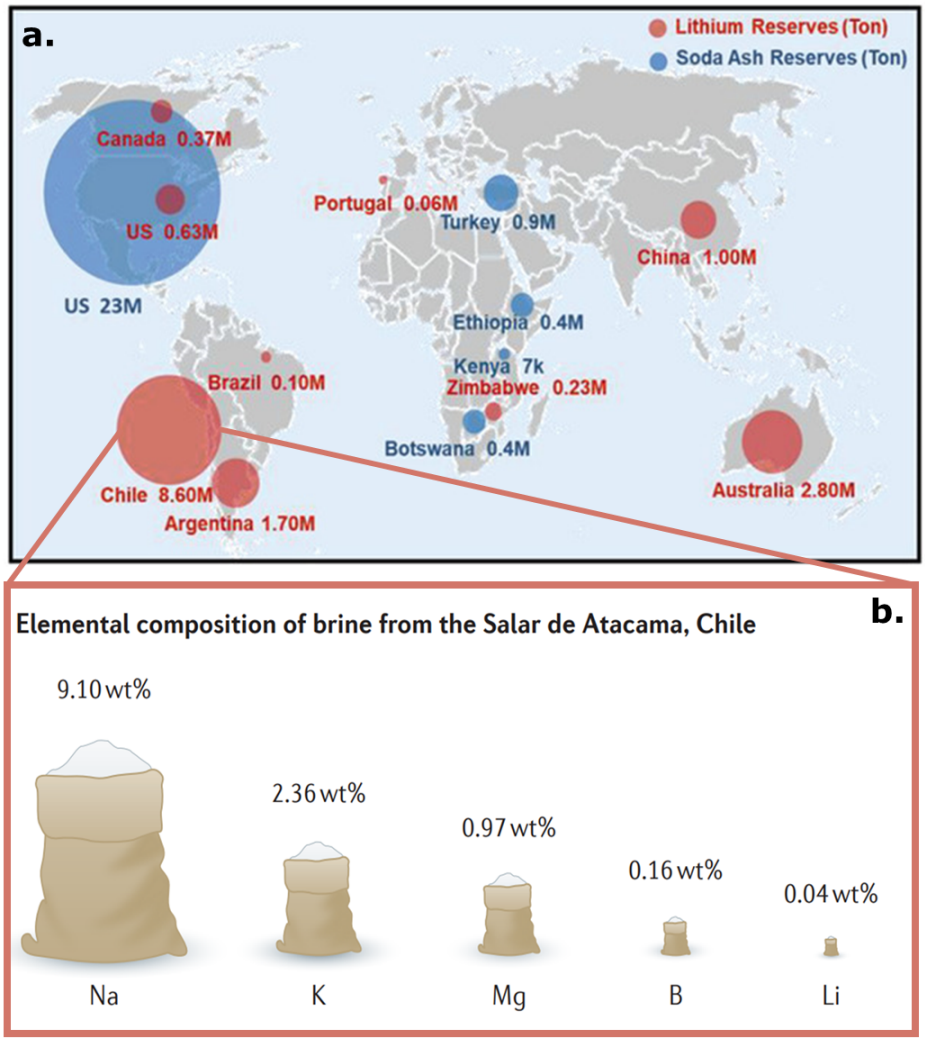


Figure 1.2: *a. A map of the Li reserves and soda ash reserves (sodium reserves) in the world reported in 2020*[118]*, Copyright 2020 WILEY-VCH Verlag GmbH & Co. KGaA, Weinheim; b. Elemental composition of brine from the Salar de Atacama in Chile*[311]*, Copyright 2018, Macmillan Publishers Limited.*

When related complementary battery technologies are considered, KIBs come to our mind next, with potassium being the next alkali metal residing in Group 1 and Period 4 of the periodic table. Relative low reduction potential (-2.936 V vs. SHE) and being the seventh most abundant metal on earth's crust makes potassium (K) further lucrative for application in battery technologies[375]. Industrial-grade potassium metal (13024.6 USD/ton) is much cheaper than Lithium (125180.9 USD/ton)[375]. The advantage of low reduction potential can also be realized from higher energy density achievement. Notably, the much weaker Lewis acidity of K^+ ions results in smaller solvated ions when compared with Li^+ and Na^+ - as a consequence, ionic conductivity in the electrolyte increases, and solvated K^+ ions are much smaller[248]. Given the numerous benefits and concentrated efforts in searching for complementary battery technologies, KIBs are now considered potential candidates in advanced energy storage, surpassing traditional LIBs.

Being aware of the myriad advantages that NIB and KIB technologies present to us, this thesis further looks into the opportunity to utilize different nanostructured materials as electrodes. Traditional LIB, NIB, or KIBs electrode materials comprise micrometer scale ($\geq$ 1 µm) particles. Development in nanotechnology has enabled researchers to substitute micron-sized particles with nanomaterials with sizes ranging 1-100 nm. When applied as electrodes, such nanoparticles exhibit different kinetic, thermodynamic, and mechanical properties than traditional electrodes. Firstly, switching to nanoparticles decreases the time required for alkali metal ion diffusion - enabling fast charging capability essential for the electrification of automobiles.

Additionally, nanostructured electrodes reduce the miscibility gap for which solid solubility of alkali metal ions increases, allowing higher reversible capacity delivery. Nanomaterials further present a mechanical advantage over traditional materials mainly due to their reduced size, as strain mismatch between particles is overcome as the particle size is equal to or below the typical crack size during charge storage[133]. Therefore, this thesis investigates the application of nanostructured TMDs (sulfide and selenide-based nanosheets, nanotubes, and fullerene-like nanoparticles) in beyond Li^+ ion storage. After analyzing the deficiencies of such materials in alkali metal-ion storage applications, we employ composite structure

formation and voltage cut-off techniques and further explore ways to apply them to next-generation mechanically deformable devices.

1.2 Researh Questions

Variability in dimensions and structure of the TMD nanosheets and fullerene-like structures, poses several questions:

1. How does quantum confinement in TMD structures influence alkali metal ion storage?
2. How do the storage properties of different alkali metals with similar chemistry vary in other TMD nanostructures?
3. What are the traditional drawbacks of TMD nanosheets during alkali metal ion storage?
4. Do the traditional drawbacks of TMD nanosheets during alkali-metal ion storage also hold true for fullerene-like structures?
5. If certain drawbacks exist in quantum-confined structures of TMDs, what nanoscale engineering techniques can be suggested to curb such disadvantages?

Answers to such critical inquiries provide feedback to design investigations for utilizing such materials for next-generation earth-abundant alkali metal ion batteries. Answers to such fundamental questions also drive us to look for better analysis techniques to investigate the structural changes during alkali-metal ion storage and optimize the experimental design for producing better complementary battery technologies.

1.3 Thesis Objectives

This research aims to investigate the impact of quantum confinement structures in TMDs on the reversible storage of alkali-metal ions beyond Li+. To fulfill the goals, five different studies are highlighted in the upcoming sections, which aim to clarify the following specific objectives:

1. Investigate how reversible storage of earth-abundant larger alkali metal ions, much alike Li^+, influences the structure of TMDs with different dimensionalities.

2. Develop and suggest engineering techniques and methodologies leading to efficient storage of Na^+ and K^+ ions inside quantum confinement structures of TMDs.

3. Identify and utilize analysis and engineering techniques to fabricate electrodes utilizable in next-generation devices.

Figure 1.3 illustrates an overview of the different investigations carried out to fulfill the overall goal of this thesis.

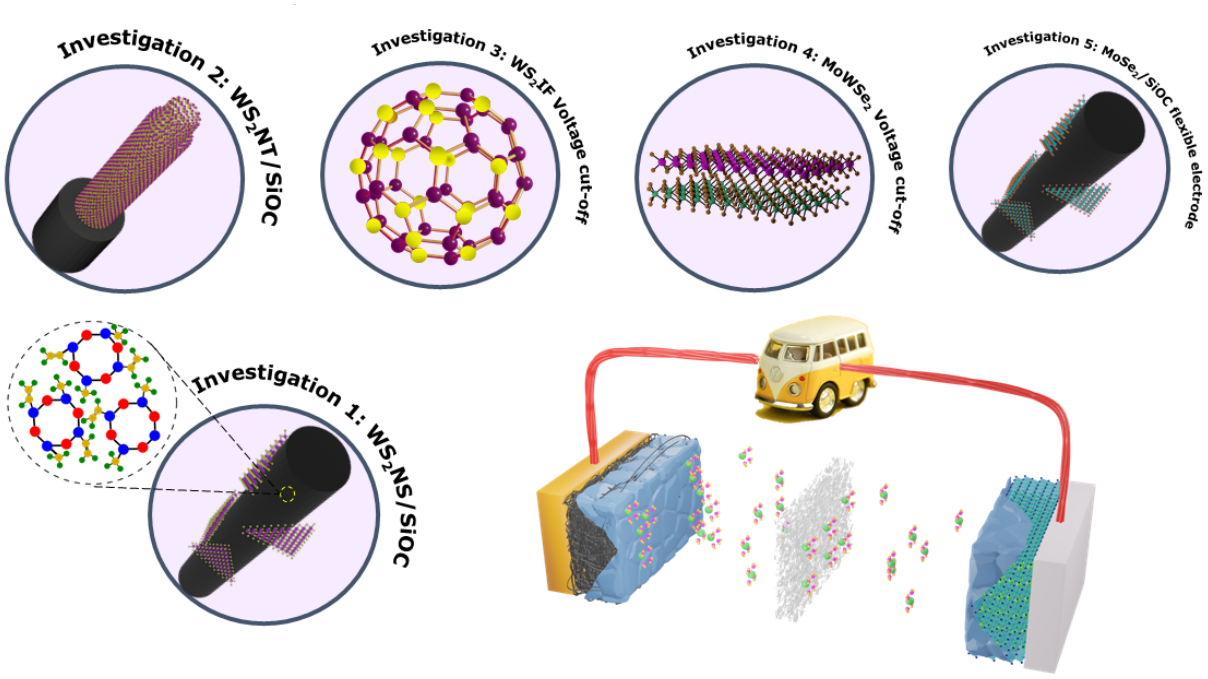


Figure 1.3: *Experimental overview of five different investigations conducted for reaching goals of the thesis.*

Chapter 2

Background and Literature Review

2.1 Electrochemical Energy Storage Devices

2.1.1 Historical Background

The battery stands out as by far the most common energy storage device, the invention of which can be dated back more than 2000 years ago by ancient Persians[251]. Another interesting addition to this history was the 'Parthian Battery, which dates back to the Parthian empire (247 B.C.-224 A.D.) but was found in 1936 at an archaeological excavation near Baghdad[226]. The first modern battery was Volta's cell, which consisted of alternating discs of zinc and copper separated by cardboard, and brine was used as the electrolyte solution. The following sets of evolutions in the battery were the innovation of the Daniel cell (1836), the Leclanche cell (1866), and then the present dry cell with the use of zinc anode and manganese oxide cathode (1949). The next breakthrough came as rechargeable batteries, also known as secondary cells, were discovered, which developed over time from lead-acid (1859) through nickel-cadmium (1899) and nickel-metal hybrid (the mid-1980s) to Lithium-ion (1972)[336].

On the other hand, in 1745, the unexplained phenomena of rubbing amber with a cloth and small particles being attracted to it were used to innovate the very first known capacitor: the Leyden Jar[147]. The "valve metals" such as aluminum and tantalum allow the conduction

of electricity in one direction but hinder the current flow in the opposite direction by creating oxide dielectric. Owing to this property, the first electrolytic capacitor was patented in 1896, which was derived from a high-purity etched aluminum foil with aluminum oxide as a dielectric[25]. The following noteworthy inventions in the field of capacitors were the mica dielectric capacitor, developed in 1909, the polyethylene terephthalate capacitor, developed in 1941; and the plastic dielectric capacitors, developed beginning in 1959. General Electric in 1957 first patented and described the concept of electric double-layer charge storage utilizing porous carbon and coating it on a metallic current collector in a sulfuric acid solution[119]. The development and use of electrochemical capacitors in commercial devices started when Nippon Electric Corporation launched the first double-layer capacitor (1.0 F, 5.5 V)[278]. NEC, Inc. (Tokyo, Japan) devised the term "Supercapacitor" for the first successful EDLC, and Pinnacle Research Institute (USA) termed the device "Ultracapacitor"[226]. However, Trasatti and Buzzanca first announced the idea of pseudocapacitance in 1971, which helped scientists improve the specific capacitance of different systems[308]. After the first report of micro-supercapacitors in 2003 with polypyrrole electrodes came the addition of ingenious strategies such as lithographic microfabrication, inkjet printing, layer-by-layer assembly, laser scribing, and screen printing. Although these techniques paved the way for advanced lithium-ion batteries and capacitive energy storage devices, the industry demand still is not fulfilled. Thus, afterward, high-tech energy storage devices with more complex functionalities and enhanced properties, such as flexible, bendable, stretchable, foldable, and wearable[226].

2.1.2 Components of Electrochemical Energy Storage Devices

In an electrochemical power source, chemical energy is converted into electrical energy. The energy of an electrochemical reaction is mainly available as electric current at a defined voltage and time[191]. There are three categories of electrochemical energy storage systems: (1) Batteries (primary and secondary batteries), (2) Supercapacitors, (3) Hybrid systems. Electrochemical cells/devices comprise a positive electrode, a negative electrode, an electrolyte, a separator, and a current collector. Electrodes are active components in an energy

storage system, permitting electrons to pass from one half-cell through an external circuit to another. The electrolyte in a cell/device is a chemically stable liquid, gel, or solid material that allows the conduction of ions. Between the positive and negative terminals of the cell/ device stands a permeable membrane named separator, which permits the transportation of ionic conductors that are essentially necessary for closing the circuit. The separator prevents instant self-discharge and an electrical short circuit between two electrodes. For the systematic transfer of electrons from the electrodes to the battery's terminals, current collectors are used. Nevertheless, well-interconnected carbon nanotubes, graphene, carbon fibers, or 2D metal carbides with metallic conductivity can be an alternative to current collectors[199]. Mechanical support, protection of the electrolyte from evaporation, and the averting negative influence from outside are done by the casing[226].

2.1.3 Batteries

Classification of Batteries

Batteries can be classified into two basic categories: (1) primary cells, known as non-rechargeable batteries, and (2) secondary cells (Figures 2.1:a-c), known as referred to as rechargeable batteries24. Other groups can be created within the above-mentioned category based on specific structures and designs.

Stationary vs. Flow Batteries

Electrodes remain motionless in the stationary type of batteries, wherein Flow Batteries the redox moieties are in the solution phase. In flow batteries, the redox species flow and undergo their charge transfer reactions through stationary electrodes. Examples of Flow Batteries are Zn-Br_2, and $V_2^+/V_3^+ - V_4^+/V_5^+$ batteries[359].

Dissolution/deposition-vs. intercalation/de-intercalation-based batteries

The energy of dissolution/deposition-based batteries is stored because of chemical reactions occurring inside the cell. The Intercalation/de-intercalation-based batteries work on the principle that charged ions (e.g., Li^+, Na^+) are commuted between positive and negative electrodes during charging and discharging cycles[226].

Closed vs. Open Batteries

When the active material within a cell makes up a sealed battery, forming a closed system, it is called a sealed battery. On the contrary, in an open battery, the active material, such as oxygen, is provided from the atmosphere. Thus, it's not a part of the electrodes. Based on the nature of electrolytes and their physical state batteries are categorized as:

Aqueous vs. non-aqueous batteries

Lead-acid, nickel-cadmium, and nickel-metal hydride batteries are the most customarily used aqueous batteries where the water-salt solution is used as an electrolyte. On the other hand, the polar-aprotic electrolyte is used because of reactivity considerations in non-aqueous batteries[191].

Solid electrolyte vs. Liquid electrolyte Batteries

Most batteries use a liquid as an electrolyte between two electrodes to regulate current flow. But there are some instances where, in Li-ion batteries, the liquid electrolyte led to safety issues. Therefore, all-solid-state lithium-ion batteries (SSLIBs) present a real solution employing a solid-state electrolyte (SSE). SSEs possess higher electrochemical windows above 5V and suppress Li dendrite formation[88;157;247]. SSEs can be further divided into two classes: inorganic solid electrolytes, including sulfides and oxides, and solid polymer electrolytes, such as PEO, PVDF, PMMA, and PAN-based electrolytes. Although SSE-based rechargeable batteries show prospects by mitigating the challenges of high safety and high energy density, their feasibility is restricted by other roadblocks such as poor interfacial contact, high manufacturing cost, and relatively low ionic conductivity at room temperature[46].

Acidic vs. Alkaline Batteries

There are three common groups such as: acidic batteries (lead acid battery), near neutral batteries (zinc-air battery), and alkaline batteries (nickel-cadmium and zinc-manganese dioxide batteries)[226].

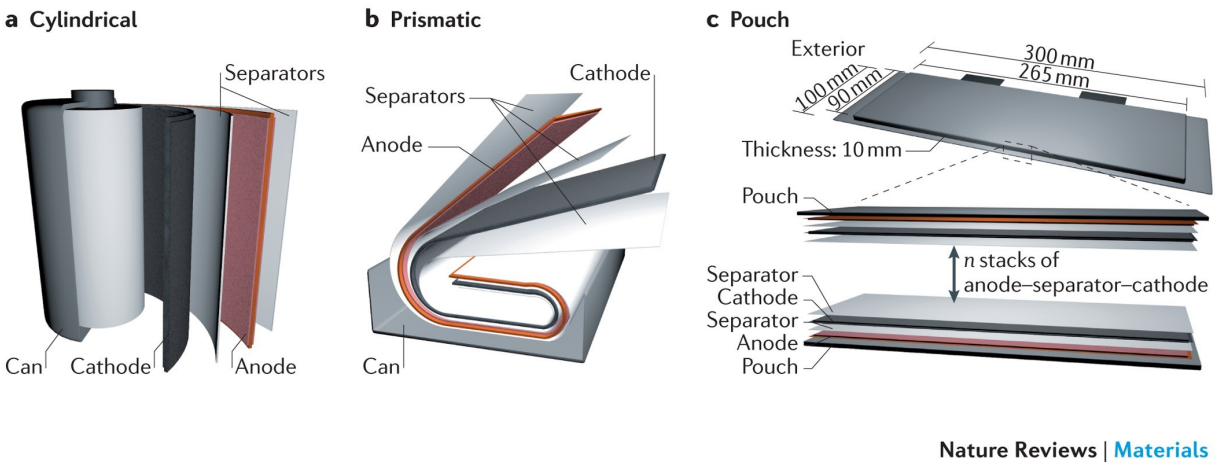


Figure 2.1: *Different types of commercial lithium-ion rechargeable batteries: a. cylindrical cells; b. prismatic cells; c. pouch cells*[54]. *Copyright 2016, Macmillan Publishers Limited.*

2.2 Energy Storage in Lithium-ion Batteries

2.2.1 Historical Background

Lithium shows exciting properties such as high operating voltage, low weight, and high energy-storage density. In addition, it is the most reducing element and the lightest material in the periodic table. These fascinating features have shed light upon lithium used in primary and secondary batteries since the 1950s[27;127]. The earliest lithium rechargeable battery was based on molten lithium, and molten sulfur as electrodes and molten salt as electrolyte and operated around 450 °C[339].

Electrochemical intercalation of guest molecules into layered hosts, which was previously known as a synthesis technique, was thought to be used for energy storage and energy release in battery electrodes by Whittingham and others in 1970. In 1970, Whittingham, while working at Exxon, developed the first intercalation-based cathode TiS_2[337;338]. This $LiTiS_2$ battery was commercialized in 1977 but flawed by the nucleation of dendrites at the lithium metal anode upon repeated cycling, which lost mechanical or electrochemical contact with the anode or grew across the electrolyte to the cathode, short-circuiting the battery and resulting in fire hazard[341]. $LiMoS_2$, LiV_3O_8, and $LiMnO_2$ batteries were discontinued after being brought into the market due to safety hazards and longer charging time[26;64;211;258].

These four failed Li-metal anode batteries mark the challenge of commercializing batteries with Li-metal anode. Metallic lithium anodes indicate compelling material but are certainly unusable due to safety concerns and have become the 'holy grail' of Li-battery research. The trick for avoiding such safety issues called for alternative approaches, such as modifying the negative electrode or the electrolyte. The method of rocking-chair batteries was used in the 1980s, and early 1990s, which solved the problem of dendrite formation as lithium was present in its ionic state rather than the metallic state[164]. However, as the potential of the negative electrode increased, the necessity for high-potential insertion compounds was there for the positive electrode. Goodenough recognized that $LiCoO_2$ had a lamellar structure and lithium can be removed electrochemically[164]. In 1991, a carbon host structure containing $LiCoO_2$ at the anode instead of lithium metal was manufactured and brought into the market by Sony, having potential exceeding 3.6V(thrice the density of the alkaline systems) and gravimetric energy densities as high as 120-150 W h kg^{-1} (three times those of Ni-Cd batteries)[306]. Since their introduction in 1991, the energy density of cells has almost doubled, and new batteries with better anodes have been developed.

2.2.2 Method of Charging and Discharging in LIBs

When the positive and negative terminal of a direct current power source are connected to the anode and cathode side, respectively, the phenomenon of charging happens. Potential arises because of the connection mentioned above. The extraction of Li^+ from the interstitial space between the atomic layers within the active material of the cathode happens, driving it to the interstitial space between the atomic layers of the active material of the anode through the electrolyte. In this way, the ceLi+ ion gets inserted into the anode, and the process is generally known as 'lithiation' or 'insertion'. On the other hand, in the cathode, the opposite process happens, known as 'delithiation' or 'extraction'. Again, as the influx of electrons reduces the anode, it becomes the negative electrode, while simultaneously, the cathode becomes the positive electrode.

On the other hand, in discharging the LIB, the anode and cathode experience polarity

reversal. Thus, the Li^+ ion gets extracted from the anode and moves to the cathode. At that time, an equivalent number of electrons move from the anode to the cathode through the externally connected device.

For instance, the positive-electrode material is commonly a metal-oxide having a layered structure such as lithium cobalt oxide ($LiCoO_2$) or a material possessing a tunneled frame like lithium manganese oxide ($LiMn_2O_4$) situated on a current aluminum collector. On the other hand, the negative electrode material in the current technologies used is generally carbon-based material like graphite located on a current copper collector. The electrochemical process described above is shown as a schematic in Figure 2.2. Two half-cell reactions of both cathode and anode are defined in Eq (2.1) and (2.2). The overall response in this cell is also presented in Equation 2.3[306].

$$Cathode : LiMO_2 + C \longleftrightarrow LixC + Li_{(1-x)}MO_2 \tag{2.1}$$

$$Anode : C + xLi^+ + xe^- \longleftrightarrow Li_xC \tag{2.2}$$

$$Overall : LiMO_2 \longleftrightarrow Li_{(1-x)}MO_2 + xLi^+ + xe^- \tag{2.3}$$

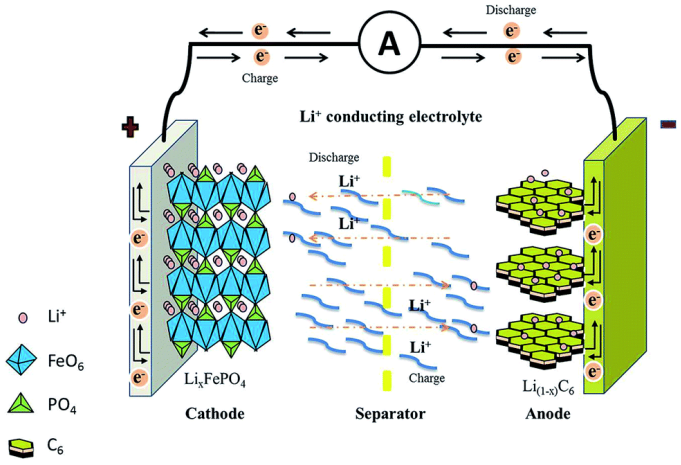


Figure 2.2: *Schematic illustration of the working principle of lithium-ion batteries*[167]*, Copyright The Royal Society of Chemistry 2014.*

2.2.3 Electrode Materials for LIB

The open circuit voltage Voc of a lithium cell is defined by the difference in the lithium chemical potential between the cathode and the anode. The equation can be written as equation 2.4

$$V_{oc} = \frac{\mu_{Li(c)} - \mu_{Li(a)}}{F} \tag{2.4}$$

Here, F is the faraday constant. The cell voltage depends on the energies involved in both the electron transfer and the Li^+ transfer. The energy involved in electron transfer is related to the work function of the cathode and anode. The energy involved in Li^+ transfer is associated with the site's crystal structure and coordination geometry into or from which Li^+ ions are inserted or extracted. Additionally, the redox energies of the cathode (Ec) and the anode (Ea) need to lie within the bandgap (Eg) of the electrolyte according to the thermodynamic stability considerations because of unwanted reduction or oxidation of the electrolyte occurring during the charge and discharge process. So, a limitation on the cell voltage is imposed for the electrochemical stability requirement, which can be described from the equation 2.5.

$$eV_{oc} = \mu_{Li(c)} - \mu_{Li(a)} < E_g \tag{2.5}$$

Figure (2-3) shows a schematic energy diagram of a cell at an open circuit. The lowest unoccupied molecular orbital (LUMO) and the highest occupied molecular orbital (HOMO) regulate its electrochemical stability window. The electrolyte is a chemically inert medium that permits efficient ionic transport between the two electrodes to maintain the charge balance. The rechargeable batteries work within this window of LUMO and HOMO. In summary, the lithium insertion compound should satisfy the criteria below for being a successful electrode material:

- The insertion compound LixMyXz (X = anion) should possess a high lithium chemical potential (μLi(c)) to maximize the cell voltage.
- The insertion compound LixMyXz should allow the insertion or extraction of a large amount of lithium, x, to maximize the cell capacity. Combining high capacity and

cell voltage can maximize the energy density, which is a product of the capacity and voltage.

- The lithium insertion or extraction should be reversible with minimal changes in the host structure over the entire range x of lithium insertion or extraction to provide a good cycle life for the cell. This implies that the compound should have good structural stability without breaking M-X bonds.

- The insertion compound should support mixed conduction. In general, it should have good electronic conductivity σ_e and lithium-ion conductivity σ Li for minimizing the polarization losses during the charge or discharge process, thus supporting high current density and power density.

- The insertion compound should not react with the electrolyte over the entire range, x, of lithium insertion or extraction and be chemically stable.

- From a commercial point of view, the insertion compound should be inexpensive, environmentally benign, and lightweight[3;177].

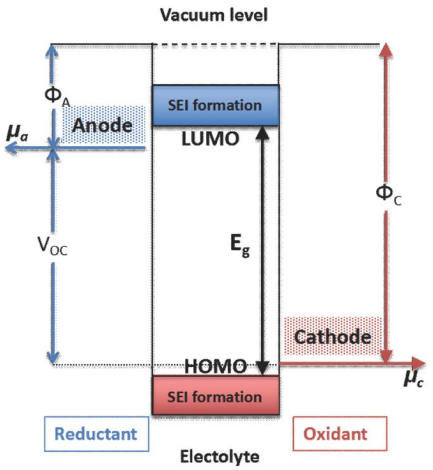


Figure 2.3: *Schematic energy diagram of a lithium cell at open circuit*[177]*, Copyright 2018 WILEY-VCH Verlag GmbH & Co. KGaA, Weinheim.*

Materials for Negative Electrodes

Finding a suitable anode material to replace the perfect anode material - Lithium metal was the last major obstacle for developing a Li-ion battery, which was motivated by dendrite formation. Thus, intercalation anodes were introduced where Li^+ intercalated alternately into the anode and cathode, storing and releasing energy as the battery 'rocks' back and forth between its two states[50;186]. As a result, carbon materials became an appealing alternative for intercalation anodes as they could accept lithium ions by insertion or intercalation going through little volume change at an electrochemical potential near that of Lithium metal. Because of the simplest and highly ordered carbon material, graphite became a good choice but faced several challenges because of its interaction with electrolytes in harmful ways, such as co-intercalation of solvents and Li^+ exfoliation of graphite and carbon being decomposed at lower potentials in the discharge cycle[89].

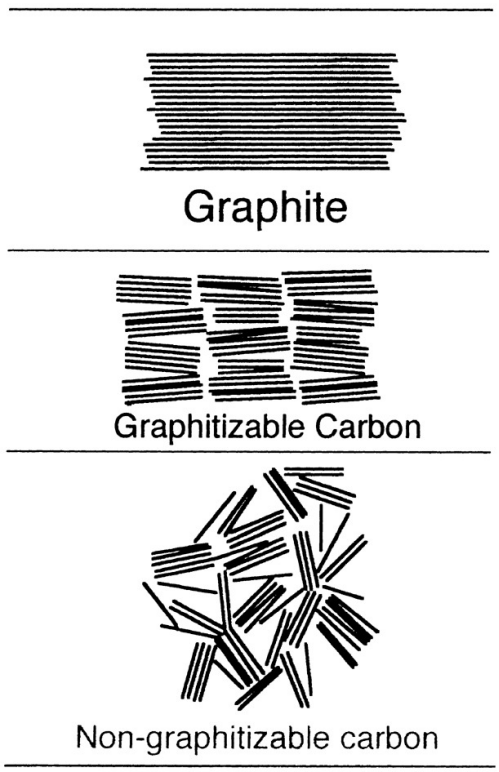


Figure 2.4: *Schematic representation of graphite, soft carbon, and hard carbon used for anodes in Li-ion batteries*[224]*, Copyright © 2001 John Wiley & Sons, Inc. and The Japan Chemical Journal Forum.*

A credible solution to the problem discussed above arises with the inauguration of "soft carbon" (moderately disordered carbon and converted to graphite by heat treatment around 23000C), and "hard" carbon (highly disordered and not easily converted to graphite by heat treatment) shown in Figure 2.4. Sony used soft carbon as the anode in the first Li-ion battery with propylene carbonate as the electrolyte with no adverse side reactions, achieving an energy density of 80 kWh kg^{-1}. In its second generation of lithium-ion batteries, the soft carbon was replaced by hard carbon by Sony for its higher voltage and capacity for lithium insertion, increasing the energy density to 120 kWh kg^{-1} [224;232]. In its third generation of batteries, Sony introduced graphite with a flatter discharge voltage profile and higher capacity above 3.0 V. It was more of a market decision rather than a technological decision which led to the use of graphite as many cell phones require a minimum of 3.0 V to operate [238].

The most recent advancement in energy storage and conversion systems was the instigation of flexible or bendable systems, which were fabricated to be portable, lightweight, and wearable, being mechanically flexible and having high energy density [8]. However, the preparation methods, assembly process, and selection of proper electrolytes to transform traditional energy storage devices are challenging. The conventional LIBs usually consist of a carbon-based anode, a transition metal oxide-based cathode, a polymer separator, and an organic liquid electrolyte. In such devices, heavy metal foils are always used as conductive substrates and structural supports with a slurry of active materials, binders, and conductive additives on their surface. As the metal foil possesses a smooth surface, the active materials can easily get detached from the current collector.

Additionally, there's an increase in internal impedance and passivation of active materials due to relatively poor chemical stability. Moreover, conductive additives such as carbon black, carbon nanotubes, and graphite account for 10-20 wt% of the whole slurry and have no or little contribution to the capacity of the electrodes. The polymer binders such as polyvinylidene fluoride (PVDF) are electrochemically inactive or even insulating, making their presence a hindrance to the transportation of lithium-ion and electrons. The flexible electrodes replace the traditional metal-foil-based heavy current collectors and standard binders with light substrates or in-bedded current collectors. The approach is to make a

combination of active materials and flexible substrates by taking advantage of the conductive and flexible matrix as embedded in the current collector, or substrates with functional materials firmly entrapped on them through novel methods like coating, spraying, or depositing[121;324;333] shown in Figure 2.5.

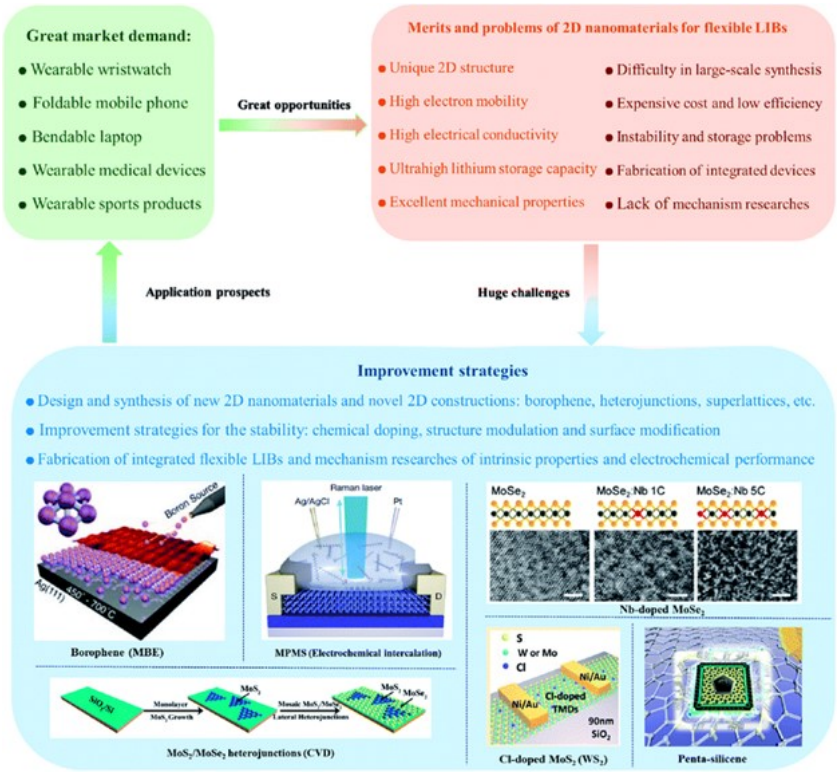


Figure 2.5: *An overview of challenges in the materials and process technologies for future flexible lithium-ion battery research[121;181]. Copyright 2019, The Royal Society of Chemistry.*

Although the use of CNT and graphene as both active materials and current collectors has been widely studied, other forms of carbon materials and some novel metal-based current collectors are now more highlighted. An effective chemical oxidation and reduction method to increase the surface area of carbon materials using a carbon cloth-based solid-state supercapacitor was prepared by Wang et-al.[317]. A novel bamboo-like structure was reported in 2005, which showed excellent mechanical flexibility, foldability, and electrochemical performance. Polyacrylonitrile and tetraethyl orthosilicate in dimethylformamide were used to make the nanofibers via electrospinning[298]. In this study, a similar approach was taken using Polyvinylpyrrolidone (PVP) as a precursor to producing the basic carbon nanofibers and

other suitable materials for better-performing LIBs.

2.3 Development and Research Progress of Na^+-ion Batteries

2.3.1 Historical Background

The almost equal capability of Na^+-ions intercalating into compounds (specifically, TiS_2) as much as Li^+-ions was first reported by Whittingham in 1976[338]. Following the research, along with the discoveries of the layered metal-oxide family of compounds in 1980, came the initiative of research into $NaMeO_2$ (Me = Co, Ni, Cr, Mn or Fe) compounds by Delmas and co-workers[68]. As the deep delve into the development of Li^+ ion intercalation system conducted by Goodenough and co-workers were continuing at that time, the research efforts of Na^+-ion intercalation compounds halted - concerning cell-voltage, $LiCoO_2$ showed double the open-circuit voltage compared to that of TiS_2. Furthermore, electrochemical properties of Li^+ ion-based compounds were found to be superior to those of Na^+ -ion-based compounds.

Following the commercialization of Li^+-ion batteries by SONY, the 1990-2000 period witnessed a sharp decline in NIB research (Figure 2.6b). Nevertheless, developments in high-temperature sodium batteries were still being investigated, which did not go unnoticed. Such development programs include a joint consortium between Ford Motor Company and Japanese TEPCO and NGK concerning their study of NaS batteries[231]. ZEBRA cells, developed by Zeolite Battery Research Africa, working in a slightly lower temperature range of 250-300 °C is another instance of a high-temperature NaS system under development at that time. Such techniques were widely applied in grid-scale energy storage, e-mobility, and space missions.

The renewed research thrust in room temperature NIBs started in early 2000, after the discovery of hard carbon negative electrodes by Dahn and co-workers[288]. Although this research proved to be a turning point in the advancement of room temperature NIBs, a spark

in the number of research papers still was not visible until 2012 (Figure 2-5b). Therefore, the reason behind the unprecedented heightened research activity was actually the supply risk of LIB resources. Hard carbon is still the most prominent negative electrode material for NIBs, although a decade has passed after Dahn's discovery – the merits and disadvantages of which will be explained in the next section. A historical development of LIB and NIB technology can be seen in Figure 2.6a.

Current advancements in NIB technology have pushed them into applications towards heavier and larger stationary applications. Heavier and larger batteries are suitable for power tools or starters that do not require continuous operation. Batteries for stationary storage require as little space as possible with less regard for weight. In this application mentioned above, the current technology of NIBs fits the best, especially for grid storage applications where suitable energy density, relatively low cost, and potential to offer improved safety are required[118]. Commercial applications of such NIBs have been represented by five companies mainly. Faradion's (UK) 140-160 kWh kg^{-1} in a 32 A.h pouch cell at 4.2-1 V with a good cycling life is suitable for e-scooters and e-bikes. HiNa Battery Technology Co. Ltd. (China) 2019 established the world's first 30 kW/100 kW h NIB energy storage system. Aquion Energy (Pennsylvania, USA) has claimed to have produced non-flammable, non-explosive, abundant, and nontoxic materials, including the Aspen series, suitable for residential, commercial, or industrial-scale energy storage systems. Initially founded by John B. Goodenough's group, Novasis Energies has demonstrated 3.2 V individual cells with normal energy in the range of 100-130 Wh $^{kg-1}$. Natron Energy (California, USA) is developing NIB technology for energy storage applications like backup power systems, transportation, material handling, etc[391]. A small overview of such companies and their product is viewed in the extension of Figure 2.6c.

2.3.2 NIB Negative Electrode Materials

In this section, the main focus will be on the latest progress in the negative electrodes of NIBs, building upon the thorough investigation of nanostructured materials of negative

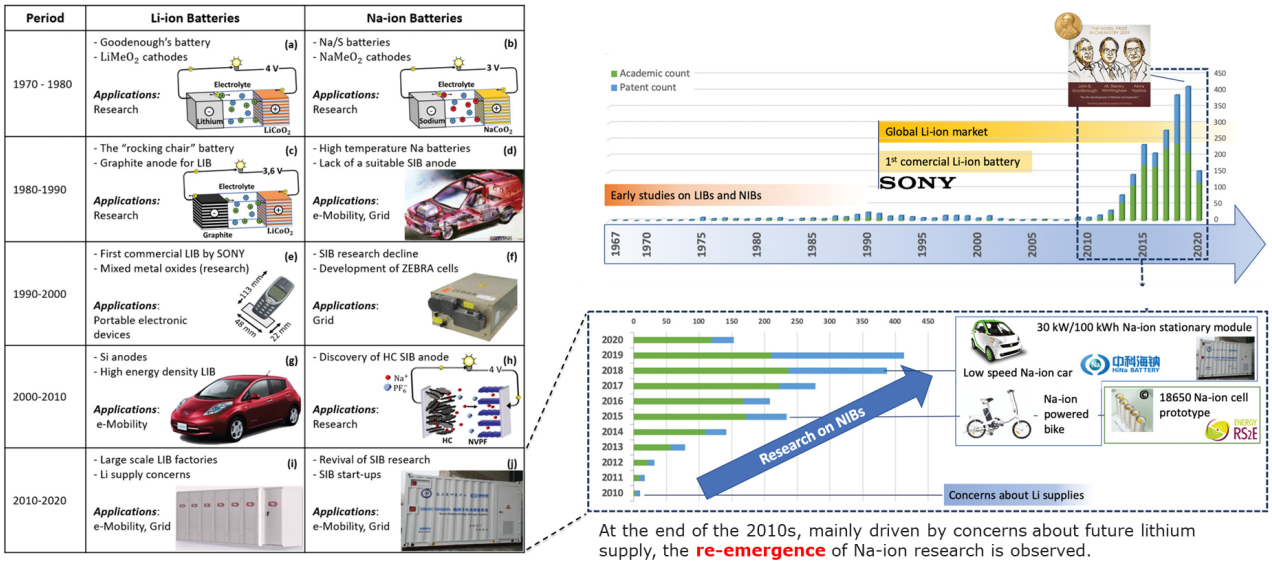


Figure 2.6: *a. Shared history of NIB and LIBs*[38]*, Copyrights 2020 The Authors. Published by Wiley-VCH GmbH; b, and c. Rise in publication and research activity related to NIBs*[105]*, Copyright 2020 Wiley-VCH GmbH.*

electrode materials presented in this thesis. Graphite – universally known as the robust electrode material for LIBs due to it's low price, ease of fabrication, and excellence of cycling stability, cannot be applied as a negative electrode material for NIBs. It was found that Na metal electroplating on the surface of carbon is energetically more favorable than Na+ ions being inserted into the layers of graphite[60].

Conversion and alloying materials such as Sn, Sb, or P transition metal oxides, nitrides, and phosphides were deemed as suitable electrodes for their high specific capacity. Nevertheless, significant volume change during reversible electrochemical processes and pulverization of active materials. One major disadvantage of utilizing conversion-based cathodes in Na-ion batteries is the relatively large potential gap between the charge and discharge process, otherwise termed hysteresis. First principles studies revealed the cause of this behavior due to a significant mismatch in ionic mobilities between an alkali metal. They displaced ionic species (mostly transition metals), an insufficient thermodynamic driving force that could not redistribute the displaced ions upon the charging process- possibly taking place due to different reaction paths in the conversion reaction. The potential gap in the conversion type anode material Co_3O_4 is shown in Figure 2.7. Overpotential or hysteresis leads to energy

loss and can be understood from a detailed analysis of equation 2.6. The round-trip energy efficiency can be quantified by the final derived form given in equation 2.8.

$$V_{dis} = V_{oc} - \eta(q, I_{dis}) \tag{2.6}$$

$$V_{ch} = V_{oc} - \eta(q, I_{ch}) \tag{2.7}$$

Where η denotes different overpotential at different currents. The overpotential decreases the discharge voltage and increases the charge voltage from the open-circuit voltage. As a result, the power density decreases, as a decrease in efficiency is seen according to the equation 2.8

$$Efficiency = 100\% \times \frac{v_{dis}(q)dq}{v_{ch}(q)dq} \tag{2.8}$$

A possible approach to overcome such hurdles is to combine properties with conductive additives such as Graphene[198] and composite formation with bimetal sulfides such as Ni@$NiCO_2S_4$ – revealing a new path to attain enhanced performance metrics[376].

Hard carbons are the up-to-date negative electrode material for rechargeable NIBs. Hard carbons, including graphitized hard carbons and porous hard carbons, show a specific capacity of 200-500 mAh g^{-1}, and initial coulombic efficiency (ICE) in the range of 30-80% - even when cycled at high rates. Typically, sodium storage in such materials happens in three mechanisms: adsorption on the edges, defects and functional groups, insertion in the graphitic interlayers, and filling in the pores. In the charge curve, highly graphitized hard carbons show a low potential plateau (0.01-0.10 V) and a high-potential slope (0.10-1.00 V). The reversible capacity is obtained primarily because of the plateau region. But when the battery is operated at high current rates, the plateau region gets affected by polarization or hysteresis discussed beforehand[346]. Thus, it is imperative to search for an alternative for the negative electrode material as an alternative to hard carbons, which possess a high specific capacity and will enhance the energy density of the full cell.

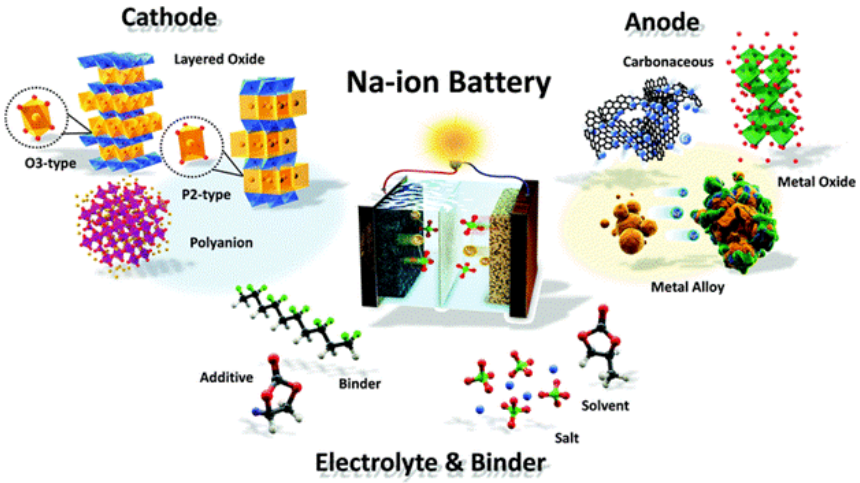


Figure 2.7: *Illustration of various negative electrode materials available for NIB systems*[128], *Copyright The Royal Society of Chemistry 2017.*

2.4 Development and Research Progress of Potassium ion Batteries

2.4.1 Historical Background

Research efforts in KIB systems only began two decades ago with efforts from Ali Eftekhari, who illustrated the KIB prototype with Prussian blue cathode in 2004[81]. With a robust cycling performance of 500 cycles and amazing capacity retention of 88%, this material was more than satisfactory in front of the community. Continuing on this effort came the patent application of KPF_6 as the viable electrolyte for KIB applications[315]. Only two years later, the first commercialized product – a portable media player was brought to the market by Starsway Electronics, operated by a KIB system[248]. The surge in research and publications regarding KIB systems came a decade later, in 2015. With KIB's immense potential, novel and innovative electrode materials are being investigated carefully.

2.4.2 Traditional Anode Materials for KIBs and their Shortcomings

A summary of drawbacks faced by KIB anodes is illustrated in Figure 2.8a. Although Graphite is not utilizable in NIB systems, it is far more suitable for KIBs, as KC8 forms during intercalation, and the achievable theoretical specific capacity is around 279 mAh g^{-1}. However, intercalation of K^+ ions into Graphite leads to a substantial increase in interlayer distance (volume change observed up to 61%), and related strain causes such material's practical application ineffective[310]. Other than Graphite, non-graphitic soft carbon, carbon nanofibers, and reduced graphene oxide also show considerable K^+ ion storage properties. However, the notable capacity achievement of approx. 350 mAh g^{-1} is witnessed from functionalized carbon materials such as N-doped graphene[274]. The major challenge behind such material's practical utilization lies in the origin of slope-like voltage characteristics, which might lead to potassium plating-related safety risks. All the issues related to current KIB anodes are illustrated in Figure 2.8a and described in this section.

Alloying and conversion reaction-based materials were thought to be promising for KIB applications, but the development of research activities was hindered due to the origination of intermediate states, which again alters the typical shape of the charge-discharge curve – rendering them to be sloping in shape. For example, the potassiation of Sn_4P_3 leads to the formation of Sn particles and K(3-x)P matrix (Figure 2.8b). Subsequently, in the latter stages K_4Sn_{23} forms, leading to the final product of K-Sn alloys. A high theoretical capacity is achieved from this formation process, however, the reverse process creates electrically dead areas within the electrode. Additionally, notable volume change within the material also occurs (approx. 681% for Sn_4P_3)[385].

Conversion-type materials were also deemed suitable candidates as anode materials for KIBs due to comparatively high initial capacity compared to Graphite. Examples of such materials include Co_3O_4-Fe_2O_3 composite anode with 750 mAh g^{-1} initial specific discharge capacity. However, the capacity loss was significant starting from the second cycle[294]. Such degrading behavior of the electrode material is attributed to structural re-alignment of mate-

rial during potassiation/depotassiation when adjusting the chemical transformation, energy dissipation as a result of voltage hysteresis during repeated charging/discharging, and severe side reactions leading to consumption of electrolytes[386].

Literature also suggests several intercalation compounds suitable as negative electrode material. Examples include $K_2Ti_4O_9$ with large interlayer spacing (8.5 $\AA$), presenting very low volume change during cycling. However, the capacity achievement from such materials is significantly low – 80 mAh g^{-1} at 100 mA g^{-1} current density[156], which questions the applicability of such materials. Other than the above-mentioned drawbacks, KIB anodes also need more energy and power density due to the large atomic mass of K and sluggish reaction kinetics during insertion and extraction. Dendrite growth remains a challenge when K metal is used as an anode. A summary of recent electrode materials and their capacity as a function of cycle number and voltage is shown in Figure 2.8c.

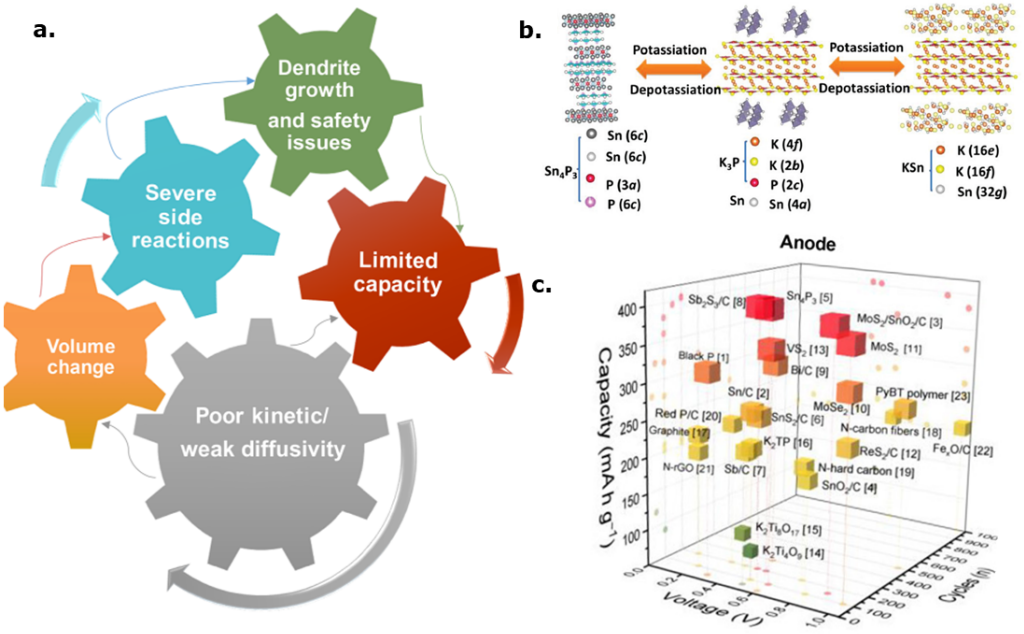


Figure 2.8: *a. Summary of challenges for KIB anode materials*[384]*, Copyright 2019 Science Advances; b. Potassiation/Depotassiation of Sn_4P_3/C electrode*[385]*, Copyright 2017 American Chemical Society; c. Capacity vs. voltage and cycle number plots of various anode materials of KIBs*[384]*, Copyright 2019 Science Advances.*

2.5 Transition Metal Dichalcogenides

It has been seen in recent research that along with the composition and arrangement of atoms in materials, dimensionality also plays a crucial role in determining the essential properties. Graphene being produced from bulk graphite has been one of the most studied materials over time because of such qualities mentioned beforehand, specifically showing condensed matter phenomena absent in the bulk graphite form[99]. As the research in graphene made swift progress, other 2D materials, specifically transition metal dichalcogenides (TMDs), having layered structures much like graphene, achieved notable recognition because some were semiconductors and naturally abundant[207;284].

2.5.1 Composition and Structure of TMDs

TMDs are a class of layered material with a generalized formula MX_2, where M stands for transition metal (from groups 4 to 10 in the periodic table) and X corresponds to chalcogen species, i.e., sulfur (S), selenium (Se), or tellurium (Te). With this general formula, there exist more than 60 TMDs, among which at least two-thirds possess a lamellar structure, thus presenting the opportunity of versatile chemistry with varying mechanical and electronic properties along with polymorphism[281;345].

TMDs consist of a hexagonally packed layer of metal atoms sandwiched between two chalcogen atoms, where each layer has a thickness of 6 to 7 $\mathring{A}$. The weak van der Waals forces coupled the sandwich layers, permitting the crystal to cleave along the layer surface readily. On the contrary, the intralayer M-X bonds are primarily covalent[18]. As the oxidation states of the metal atoms and the chalcogen atoms are +4 and -2, respectively, the metal atoms provide four electrons to fill the bonding states of TMDs. The layer surfaces get discontinued because of the lone-pair electrons of the chalcogen atoms, and the layers stabilize against environmental species as there are no present dangling bonds. The metal coordination of multilayer TMDs can be either trigonal prismatic or octahedral (usually distorted and often referred to as trigonal anti-prismatic). Because each discrete MX_2 monolayer comprises three atomic layers (X-M-X), they can be in either of the two phases; bulk TMDs

display a broad range of stacking polytypes and polymorphs. 1T,2H, and 3R are the most frequent polymorphs, with the letters standing for trigonal, hexagonal, and rhombohedral, respectively. In a unit cell, the amount of X-M-X units is indicated by the integers[51].

The works in this study are concerned with a specific TMD, which is $MoSe_2$. $MoSe_2$ can have multiple phase structures, much like MoS2. However, while the 2H trigonal prismatic symmetry is semiconducting, the 1T octahedral symmetry is metallic. Still, it deliberately converts into the former phase because of thermodynamic instability, rendering it not desirable for application[82].

2.5.2 Synthesis techniques of TMDs

The anisotropy in the characteristics of TMDs, notably in their electronic and crystallographic structure, renders them one of the essential two-dimensional materials with a wide range of applications. As a result, the focus is on synthesis methods through which researchers try to alter the interlayer gap and microstructural morphology to tailor these features to the application's demands. Moreover, the center of attention is on synthesis approaches that provide a maximum material yield while being scalable, energy-efficient, and cost-effective.

The first obstacle to carrying out fundamental research or making industry-based applications is the suitable material synthesis techniques. Generally, when producing two-dimensional TMDs, two routes are to be followed- the top-down or the bottom-up approach. As the names of these routes speak for themselves, in the top-down approach, one starts with bulk precursor material and reaches the final goal of desirable material with a particular morphology. In contrast, in the bottom-up approach, atomic layers are deposited in step by step fashion.

In 2004, Novoselov et al. used the mechanical exfoliation method to produce single layers of two-dimensional crystals from bulk materials, such as graphite, MoS_2, BN, $NbSe_2$[166]. Although the single-layer TMD crystals fabricated using this method guarantee good quality, unlike their graphene counterpart, the main drawback stems from meager material yield. It

offers a small production volume. However, the materials produced by this method are used for examining their fundamental properties at lab scale by microscopic techniques such as scanning tunneling microscopy (STM), atomic force microscopy (AFM), transmission electron microscopy (TEM), and so on[205].

The intercalation-based exfoliation or natural exfoliation in solvents ensures the significant production rate of TMDs in the form of a single or few layers. Previous studies indicate that intercalation-based exfoliation has been carried out in two routes, namely, lithium intercalation-based exfoliation and anion intercalation exfoliation. In lithium intercalation-based exfoliation, the force required for separating the TMD layers is produced by the H_2 gas bubbles formed. SO_2 or O_2 gas bubbles exert the required force[194;360], as illustrated in Figure 2.9a-b.

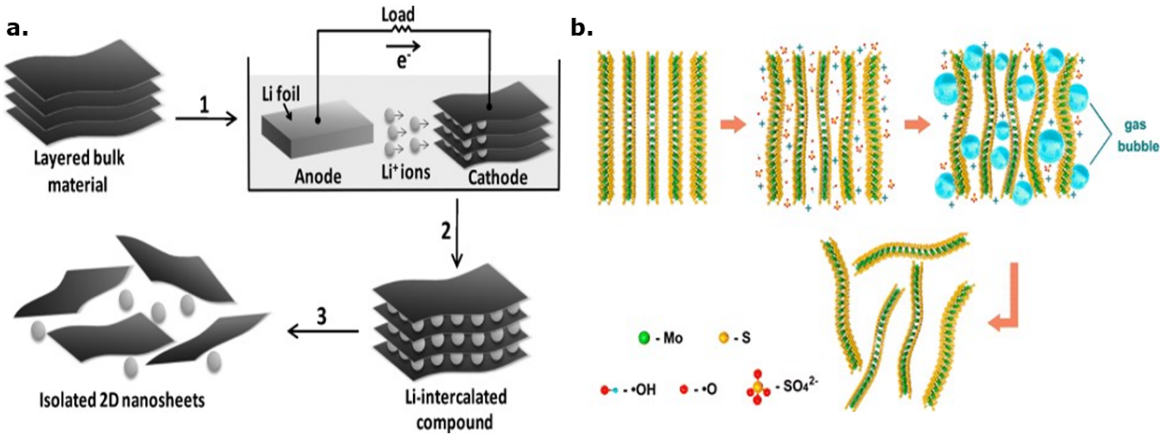


Figure 2.9: *(a) schematic illustration of lithium intercalation based exfoliation[371], Copyright 2011 WILEY-VCH Verlag GmbH & Co. KGaA, Weinheim; (b) schematic illustration of anion intercalation based exfliation[194], Copyright 2014 American Chemical Society.*

The liquid phase exfoliation process consists of three steps: a) immersing the bulk TMDs in a solvent, b) sonicating the bulk TMDs using ultrasound, c) separating nanosheets from dispersion (the first two steps are illustrated in Figure 2.10(a, b). There are various param-

eters for selecting a solvent Hildebrand solubility parameter, Hansen parameter, and surface energy. Coleman et al. primarily sonicated as received commercial TMD bulk materials in several solvents with varying surface tensions. They found that the solvents that minimized the power of sonication were the better-performing ones. For instance, N-methyl pyrrolidone (NMP) and isopropanol (IPA) show more promising performance than the other ones[57]. In the sonication process, the physical effect of very high energetic transient acoustic cavitation comes into play. The ultrasound produced in this process gives rise to cavitation containing enough high kinetic energy, which collapses afterward. These collapsed bubbles convert the high surface energy into chemical energy. The result of this process is the separation of platelets from the bulk material (figure 2.10). Sonication also changes the temperature of the medium, and the increase in temperature is linear to time. So, the temperature must be kept at the optimum for best results[381]. In addition, sonication time affects not only the shape of the nanosheets but also the characteristics. However, with the increase in sonication time, smaller nanosheets possess a larger area and improved edge sites, features desirable for many applications.

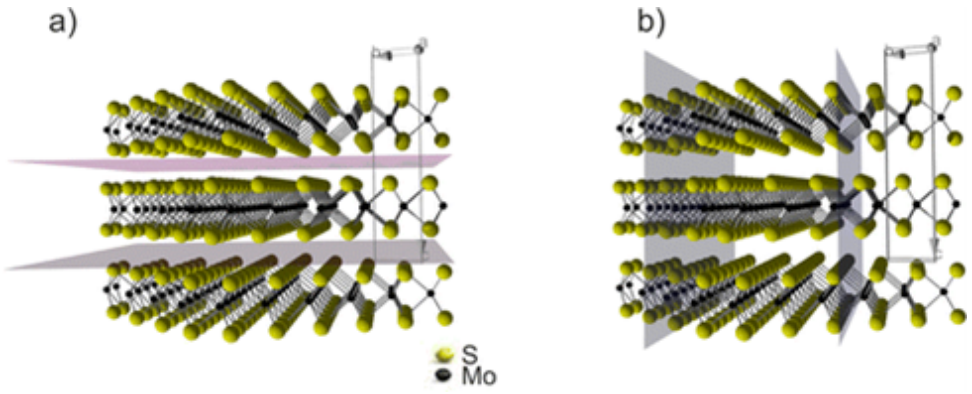


Figure 2.10: *Effects of strong sonication of MoS_2 flakes dispersed in isopropyl alcohol: a. Breaking between Basal Planes and b. great fragmentation of the lamellae*[219]*, Copyright 2015 American Chemical Society.*

The chemical vapor deposition method is widely used to fabricate nanosheet material for achieving large-area growth. For example, Zhan et al. studied the synthesis of MoS_2 film by annealing in an atmosphere made out of sulfur with deposition of a Mo thin film on SiO_2/Si surface[373]. Substrates such as quartz, glassy carbon, and oxidized silicon have been

used to grow uniform TMD films. However, the uncontrollable sulfur/selenium diffusion and anisotropy of TMD layers have made the growth process arduous. However, Wang et al. reported a facile process by synthesizing MoO_2 nanoplates by thermally evaporating MoO_3 powder in a sulfur environment and further sulfurizing at higher temperatures to yield MoS_2 flakes with higher crystallinity[329]. This bottom-up approach of growing thin films of TMD materials has found its wide application in electronic devices, optoelectronic devices, and gas sensing devices. But for using TMDs in energy storage devices, most studies regarding fabrication in the literature consist of the top-down approach.

2.5.3 Distinctively Nanostructured TMDs

A heightened application of carbon-based nanostructures like nanotubes, graphene, and nanoparticles has brought a revolution in different fields. Inspired by such activities, the driving force behind research in nanostructures of TMDs came along and gained interest in the fields of material science, chemistry, and condensed matter physics in recent years. Previously research thrust was in TMD nanosheets – rigorous investigations leading to the discovery of exciting electronic and optical properties as a function of layer number.

The discovery of inorganic nanotubes (NTs) and fullerene-like nanoparticles (IFs) can be dated back to more than three decades. Practically at first, the synthesis of inorganic NTs and IFs proved to be exceedingly tricky. However, with the development in synthesis techniques, catalyst-free, scalable growth of TMD-based 0D and 1D was rendered possible by Zak et. Al, primarily led by Reshef Tenne et. Al.[52]. This work utilized WS_2-based NTs and IFs for their energy storage applications synthesized by Zak et. Al.

Interesting features of such nanoparticles, render them quite different from their bulk counterparts. For example, zone folding and strain-induced for the tubular structure enable such materials to change electronic properties as a function of diameter. Moreover, with smaller mechanical strength and larger specific weight than their carbon counterpart, these materials still apply in high-strength nanocomposites, primarily because of high compression strength. Importantly, their application as solid lubricants because of their superior tribolog-

ical behavior cannot be called into question[302]. Moreover, IF-like TMD nanocages have also found manifold applications in medical device fabrication, which will be highlighted later in specific chapters.

2.5.4 TMD Alloys and their Origin

Bilayer formation with several 2D materials is already evident in the literature and has wide applications due to a combination of individual properties. Being inspired by such structures, engineering of 2D TMDs provides us with more exciting opportunities as TMDs themselves are versatile and widely applicable to nanoscale devices. Among many interesting properties that 2D materials present, fine-tuning the valence band (VB) and conduction band (CB) positions is very important to engineering properties at the nanoscale. With TMDs presenting us with band gaps ranging from zero to UV region, the scientific community has pushed the utility of such materials further – this is possible by skillful substitution of transition metal cations or chalcogen anions in different proportions according to the needs. Usually, anion substitution of TMDs is carried out because of lesser lattice mismatch, and the process is easier, examples include Mo/W-X_2 where X is S/Se/Te. However, conversely, substituting cations with different transition metals is quite challenging due to larger lattice mismatch. However, there exists plenty of examples of cation-substituted TMD alloys: $Mo_{1-x}W_xS_2$, $TaS_{2(1-x)}Se_{2x}$, $ReS_{2(1-x)}Se_{2x}$ and so on.

Applications of TMD alloys are plenty, starting from Field Effect Transistors (FETs) due to carrier scattering and electron mobility, optoelectronic devices due to superlinear photocurrent generation with an increase in illumination power, and hydrogen evolution catalysis for offering H_2 affinity fine-tuning ability[348]. Although, with an asymmetry, more cations or anions providing higher storage sites and lattice mismatch resulting in increased interlayer spacing in certain TMD alloys, there is a possibility of superior electrochemical behavior, these particles nevertheless have been less explored. Therefore, in this investigation, we curiously investigate how Na^+ and K^+ ion storage is affected when a cation in TMDs is substituted with another cation. Specific details of the literature study and motivation

behind electrochemical characterization are highlighted later in the chapter.

2.5.5 Energy Storage Mechanism of TMDs

To accommodate different kinds of guest species, especially in energy storage applications (Li^+ ions in LIB systems), TMDs possess the necessary interlayer spacing. Furthermore, as lithiation of bulk TMD materials results in structural instability, the exfoliated counterparts became the points of interest because, in exfoliated form, the nanosheets stay loosely attached and can withstand structural deformities. For instance, TMDs such as MoS_2 (0.615 nm), MoSe2 (0.646 nm), WS_2 (0.618 nm), WSe_2 (0.651 nm), TiS_2 (0.569 nm), VS_2 (0.573 nm), TaS_2 (0.601 nm) have higher interlayer spacing than graphite (0.335 nm)[352]. Additionally, with the help of various chemical and physical methods, this interlayer spacing can be tuned. Moreover, as different reaction mechanisms such as intercalation, conversion, and alloying are observed building upon the applied potential change, TMDs become more attractive. For example, in 2012, Fang et al. and his group confirmed that MoS_2, one of the most investigated TMD materials, shows reversible reactions when the cutoff voltage is 0.8 V[86]. Zhang et al., using XRD and in situ, XAS, demonstrated that 2H to 1T phase transition occurs in intercalation reaction at a voltage window of 0.8-3.0 V[377]. However, the low theoretical storage capacity restricts the use of TMDs in various sectors, although the intercalation mechanism ensures good cycling performance. As the conversion reaction happens in low discharging voltage with the ability to transfer up to 6 electrons, reducing the cutoff voltage (0.01 V) is feasible to obtain a significant increase in capacity. The alloying reaction, which occurs at a shallow potential, needs to be covered in this thesis.

To summarize, as the alkali metal ions, have similar physical properties, they exhibit identical charge storage mechanisms, which are presented in the figure 2.11. In figure 2.11, M' indicates V, Mo, W, Re, and M" indicates Ti, Nb (the transition metals), X marks the chalcogen atoms (S, Se, Te), and A denotes the alkali metal ions (Li, Na, K)[39].

This study concerns $MoSe_2$ as the TMD material with a similar sandwich structure to the most studied TMD material, MoS_2. However, electrodes based on $MoSe_2$ suffer from

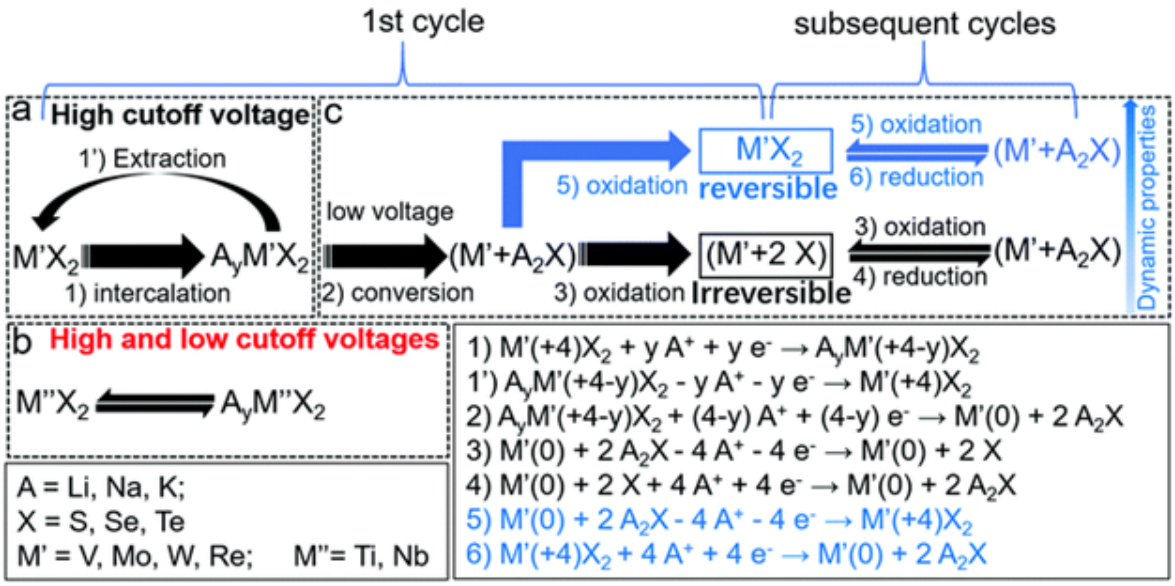


Figure 2.11: *Charge storage mechanisms for TMDs in different alkali metal ion batteries*[39], *Copyright 2020, Royal Society of Chemistry.*

low cycling stability and unsatisfactory rate capability, possessing a narrower bandgap and lower electronic conductivity. The subsequent efforts have been implemented to understand better such hurdles: preparing material mixing with selenides, mixing with chalcogenides, and preparing composite electrodes with carbonaceous material. In such an event, Beatriz et al. fabricated $MoSe_2$ nanoplatelets/SWCNTs electrode via spray-deposition method without conductive additives, which showed improved cycling stability and rate capability from the $MoSe_2$ nanoplatelet electrode[210]. In a similar study, Furong et al. prepared a composite electrode with mesoporous $MoSe_2$/C via a nano-casting method and tested that in the LIB system. As a result, it displayed 618 mAh g^{-1} at the current density of 200 mA g^{-1}, the reason for which can be ascribed to mesoporous structure providing enough space for the volumetric expansion and product of charging and delivering a short diffusion pathway[246]. However, for the relevance of this study, the details are limited to composite electrodes with carbon-related material.

2.6 Polymer Derived Ceramics

The conventional process of fabricating ceramic materials calls for powder technology, which is a burdensome technique involving the existence of sintering additives. On the contrary, ceramics produced via the PDC route involve pre-ceramic polymers as the base material, using which layers of fabric, ceramic fibers, or composite material can be fabricated, which was impossible using powder technology. Specifically, the polymeric precursors are flexible to be used in run-of-the-mill forming techniques, and once they are formed, they can be converted into ceramics by applying heat. Furthermore, by controlling this heating environment, one can modify the final ceramic product as the organization of their nanostructure depends on the inorganic/organometallic polymeric precursors. Enhanced thermo-mechanical properties at elevated temperatures make these materials desirable for various applications, including high-temperature withstanding applications in energy materials, automotive and aerospace sectors, or the field of micro/nanoelectronics acting as a functional material[17].

2.6.1 General structure of pre-ceramic polymers and their varieties

As discussed in the previous paragraph, the pre-ceramic polymer influences the ceramic produced by the composition and the number of phases and phase distributions. The strong bonding between the silicon and carbon makes the carbon stable in the polymer compound, stopping the carbon from desiccating away during pyrolysis in small molecular hydrocarbon form[256]. Briefly, for the PDC route, the pre-ceramic polymers should hold the following properties:

- Having adequate high molecular weight for circumventing volatilization of the small molecular compounds.
- For the shaping processes, these polymers must own specific rheometry, such as explicit solubility and viscoelasticity.

- Having no properties of gelation such that aging of polymers does not happen without control.
- For specific curing properties, functional groups should be present.

An organosilicon polymer can be illustrated simply by the figure. The pre-ceramic polymer can be tailored and modified in the following ways:

- Changing the group X in the backbone of this structure yields various groups of the silicon-based polymer. For example X=Si, CH2, O, NH, N=C=N yields polyorganosilanes, polyorganocarbosilanes, polyorganosiloxanes, polyorganosilazanes and ployorganosilylcarbodiimides, respectively.
- Changing the R1 and R2 functional groups can tune the final ceramic product's electronic, rheological and optical properties depending on the pyrolysis temperature.

These R groups mentioned above are also responsible for the free carbon, which appears after the pyrolysis when hydrogen atoms are removed. G.T. Burns et al. first studied the effects of R groups on the final SiCN and SiOC-based ceramics. They found that the yield of free carbon content on the final ceramic was lower for the saturated R groups such as methyl, ethyl, propyl, and isobutyl. In contrast, for the saturated R groups such as allyl, vinyl, and phenyl, the result of free carbon content on the final ceramic was higher[31]. Different pre-ceramic polymers and derived PDCs are illustrated in Figure 2.12.

2.6.2 Processing Technique of PDCs

From one end to the other of the PDC route consists of three main steps, namely pre-ceramic polymer synthesis from monomers, creation of organic/inorganic network via cross-linking of polymers, and converting the cross-linked polymers to inorganic amorphous material via pyrolysis at an upraised temperature level (which is still lower than the traditional ceramic formation technique). As this study does not concern the synthesis technique of pre-ceramic polymers, the shaping techniques, cross-linking, and polymer-to-ceramic transformation will be highlighted in the following sections.

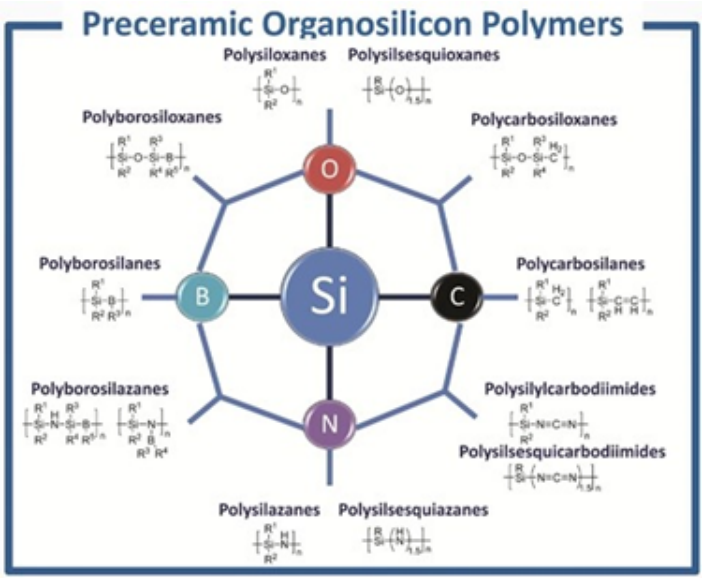


Figure 2.12: *Simplistic formula of polymer derived ceramics and different pre-ceramic organosilicon polymers*[58]*, Copyright 2010 The American Ceramic Society.*

The solubility, fusibility, and viscosity of the pre-ceramic polymers are the most attractive properties, making them appealing for copious shaping techniques according to various applications. Example of such processing techniques expands from a dip or spin coating, fiber drawing, freeze casting, and polymer infiltration to lithography. The most recent advancement in shaping methods has been the introduction of additive manufacturing techniques for producing PDCs. Moreover, the stereotypical drawbacks of ceramic materials, such as tool wear and brittle fracture, can be outmaneuvered by shaping and machining techniques before ceramization[80]. Various shaping techniques utilized for PDCs are illustrated in Figure 2.13.

Cross-linking is a step of great significance where the polymeric precursors are changed into organic/inorganic materials at low temperatures (100-400 °C). Due to this step, the final ceramic yield turns out to be high as the loss of low molecular weight compounds is thwarted. Besides, due to this step, the duroplasts (infusible materials) are formed, maintaining their shape during the pyrolysis step. Hydrosilylation, polymerization, transamination, and dehydrogenation are the chemical reactions in charge of this thermal process. Hydrosilylation usually occurs in the lower temperature(100-120 °C) region and leads to the formation of Si-C-Si and Si-C-C-Si. Dehydrogenation reaction results in Si-N and Si-Si bonds and starts in

the Si-H/N-H or Si-H/Si-H groups at an elevated temperature of 300 °C. Vinyl polymerization, which can be identified as polyaddition, also occurs at a higher temperature. Finally, a Transammination reaction occurs in the case of oligosilazanes by heating thermally at the temperature region of 200-400 °C[80]. As this research concerns polysiloxanes, the reactions responsible for the cross-linking of such material are of concern: hydrosilylation, and hydrolysis.

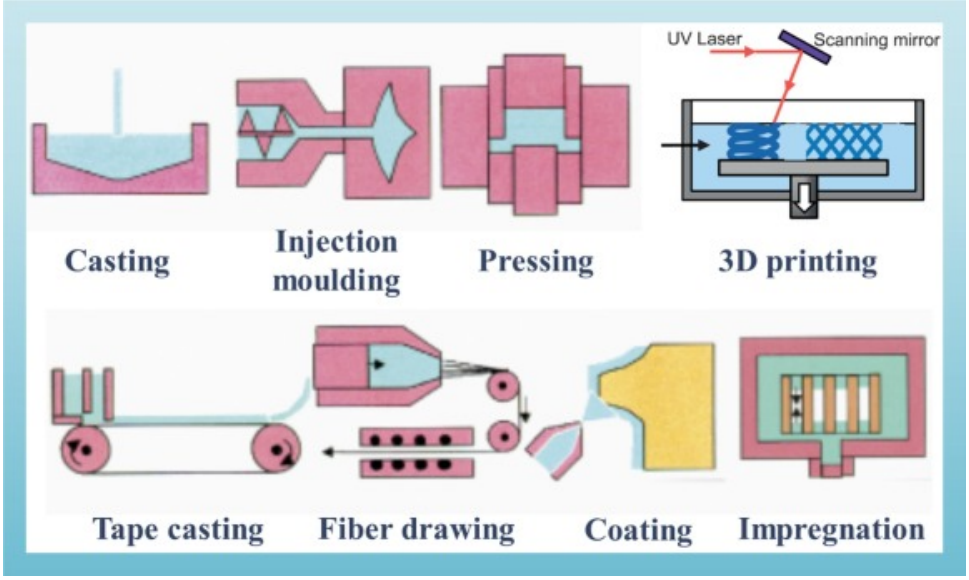


Figure 2.13: *Various shaping techniques for the production of PDC components[335], Copyright 2010 The American Ceramic Society.*

At a higher temperature region of 600-1000 °C, the pre-ceramic materials from the cross-linked stage go through different intermediate stages and turn into amorphous covalent ceramics. Thermolysis and volatilization of the organic groups are the processes that come into play. The shrinkage of the final ceramic product happens, and the product becomes porous because of the pyrolysis process. Figure 2.14 shows the entire process and the formation of PDCs at different temperatures.

2.6.3 Microstructure of PDCs

For boosting the performance according to the different fields of application, the preservation of the final amorphous ceramic product obtained via the PDC route is of paramount

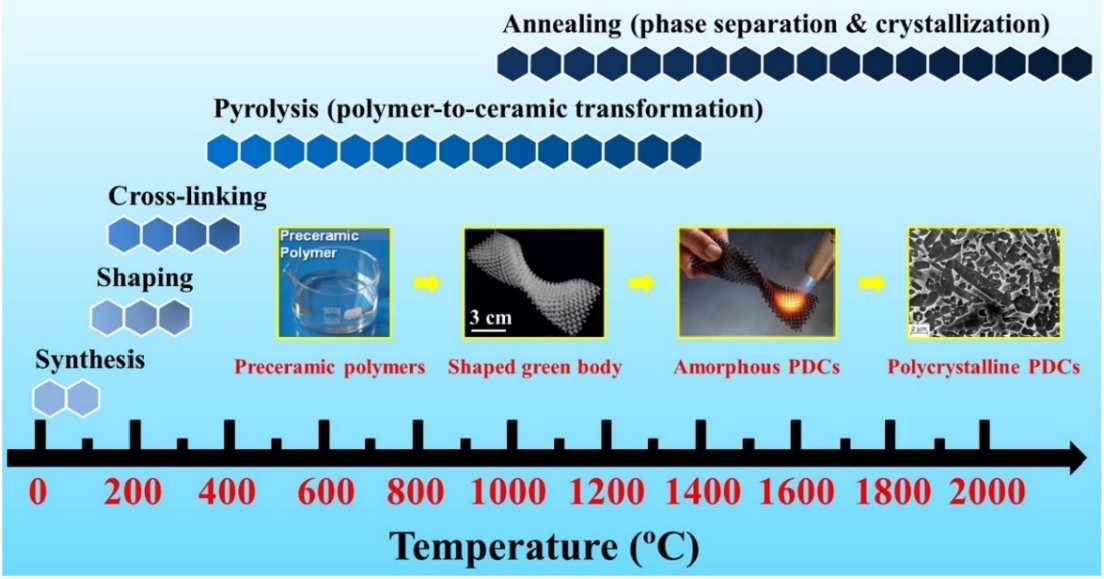


Figure 2.14: *The processes involved in forming PDCs at different temperatures*[58]*, Copyright 2010 The American Ceramic Society.*

interest. Specifically, the chemical bonds get reallocated, phase separation occurs, and the nanocrystals transform into coarse form. Therefore, it is crucial to study the nanostructure evolution in successive thermal treatment stages of the entire route. One exciting aspect is the graphitization process, which plays a significant role in the microstructural evolution of the PDCs. This process takes place in the free carbon phase, happening after the phase separation phase.

As this study involves polymer-derived SiOC-based ceramic, the details of its structure are highlighted. The SiOC-based ceramic is amorphous with silicon atoms tetrahedrally coordinated by oxygen and carbon atoms[212;240]. Therefore, the SiOC ceramic product derived consists of the tetrahedral units of SiC_4, SiC_3O, SiC_2O_2, and SiO_4[212]. Two types of hybridization are seen in the carbon atoms. The sp3 hybridization occurs in the C-Si bonds, and the sp2 hybridization is observed in the C-C bonds in the free carbon phase. Saha et al., in 2005 (Figure 2.15a), proposed the model presented in the figure where the components of the SiOC-based ceramics are as follows:

- The silica tetrahedra build the heart of the nanodomain structure.
- The nanodomains encaged by the graphene-like carbon network.

- The graphene network and silica clusters connected by the single layer of $SiC_xO_(4-x)$ $(0 \leq x \leq 4)$ mixed bonds[261].

2.6.4 Electrochemical Properties of PDCs

Li^+ ion storage inside PDCs

In recent years, the application of PDC materials in electrochemical devices has been widely studied. Due to desirable properties such as high stability during cyclic loading and preserving the structure during very high C-rates has become a material of increasing interest[4;265;314]. In addition, being chemically inert concerning other battery components, being lightweight but boasting superb mechanical properties, and most interestingly, providing a conducting network with the free-carbon phase PDCs are admired all over the industry. Moreover, where there stands a possibility of the carbon being exfoliated during high charging and discharging rates, the silicon matrix plays its role in guarding the carbon and, thus, enhancing the stability and is more desirable than other free-standing carbon materials[11;93;146].

For the ceramics stemming from SiOC-based polymers, in several investigations, it was found that the free carbon phase does not significantly impact the first cycle charge and discharging capacities in lithium-ion batteries[107;265]. However, several experimental studies indicate that PDCs with higher carbon content perform better by showing cycling stability about hundreds of cycles[93–95;106;242]. Furthermore, several studies also indicate that better anodes can be fabricated by preserving the free carbon in an amorphous or highly disordered state by controlling the temperature of thermolysis[106].

To summarize, the free carbon content in SiOC-based ceramics improves lithiation capacity by escalating the electrical conductivity successfully. This phenomenon happens as the transportation of electrons through the electrode materials speeds up due to the increase in the storage sites of lithium ions. Three zones can be observed where lithium ions get reversibly stored: the edges of the graphene layers, the defect sites, and the interstitial spaces. This process is quite similar to the lithium-ion storage mechanism in the amorphous carbons. Therefore, the augmented high capacity and cycling stability can be traced to the current

free carbon phase. Figure 2.15b illustrates the schematic model of the reversible (marked in yellow) and irreversible (marked in green) lithium-ion storage in SiOC ceramics[335].

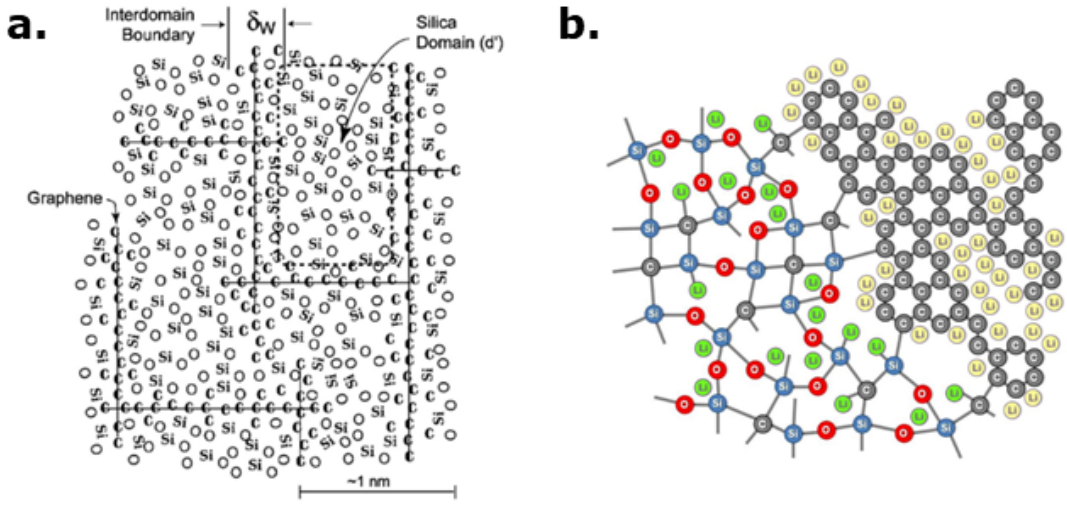


Figure 2.15: *a. Proposed model of nanodomains in polymer derived SiOC based ceramics[335], Copyright 2016, American Association for the Advancement of Science, b. Schematic representation of lithium-ion storage mechanism in SiOC based ceramics[285;335], Copyright 2018 The American Ceramic Society.*

Na^+ ion storage mechanism inside PDCs

Na^+ ion storage inside SiOC amorphous ceramic is a complicated process. Previous investigations have highlighted possible ion storage sites within the ceramics via spectroscopic and theoretical investigations. Four possible sites have been identified as micropores, C-rich SiOC, O-rich SiOC, and some Na^+ ions getting bonded with Si. Density functional theory (DFT) calculations have shown that O-rich SiOC materials firstly prefer the microvoids within the material, which does not significantly cause strain of material. Further, Na^+ ion insertion induces a change in the microstructure – a gradual weakening in the Si-O bonds was observed as Na-O bond attraction increased. Further, Na^+ ion insertion causes cleavage of Si-C bonds and Si-O bonds, respectively. For the time being, the O-rich SiOC material prefers Na-Si bond formation as the bond length in between decreases compared to Si-O and Si-C bonds. On the other hand, C-rich SiOC structure can uptake more Na^+ ions, due

to structural stability, but causes far more volume expansion. Furthermore, it was found that the existence of SiC phases increases the long-term stability of the electrode material[34]. Park and co-workers utilizing Silicone oil AP 150 as precursors found the practical capacity of SiOC material as 50-60 mAh g^{-1} [236]. Using a co-polymer of poly(dimethylsiloxane) and poly(methylphenylsiloxane) Chandra and co-workers observed a capacity of 134 mAh g^{-1} from the synthesized SiOC ceramic[33].

K^+ ion storage mechanism inside PDCs

There exist only a few investigations regarding K^+ ion intake of SiOC material. The storage mechanism is similar to Li^+ and Na^+ ions. Chandra and co-workers evaluated the K^+ ion uptake of the O-rich and C-rich SiOC structure via DFT calculations. They found that as compared to lithiation (2.5%) and sodiation (18.8%), potassiation (36.7%) causes massive volume expansion. After an optimal amount of K^+ insertion, further insertion of ions leads to repulsive interaction – resulting in an abrupt increase of ion insertion voltage. In the same work, the authors demonstrated a comparatively low capacity achievement from practical experiments[35]. Figures 2.16(a-c) illustrate Na^+ and K^+ ion storage mechanisms as depicted in the above-mentioned sections.

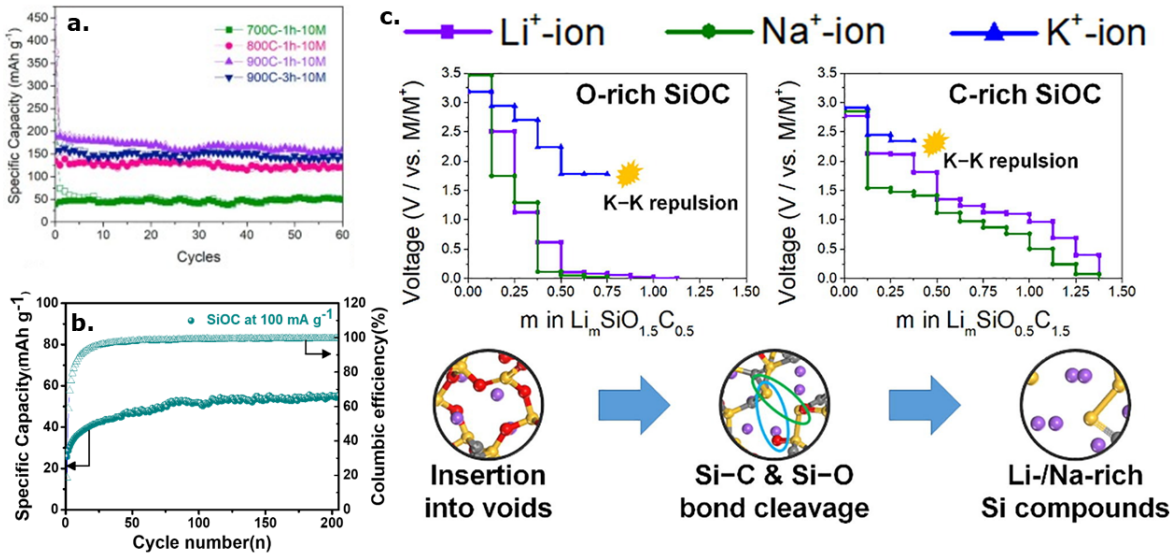


Figure 2.16: *a, b. Na^+-ion cycling performance of SiOC ceramics derived from silicone oil*[33]*, Copyright 2018 Elsevier B.V. All rights reserved; c. Alkali-metal ion insertion into SiOC ceramics and consecutive phase formation*[35]*, Copyright 2021 Elsevier B.V. All rights reserved.*

Chapter 3

Experimental Methods and Instrumentations

3.1 Experimental Methods

3.1.1 Electrospinning

Fibers are universal, having a continuous filament-like shape or appearing as an elongated object. Spiders have existed on Earth for over 140 million years, having the ability to hunt with fiber webs. In addition, silkworms also construct their cocoons with silk filaments. Such natural creatures have been a source of inspiration for humans to produce fibers artificially with a modified diameter[117;313]. With the flow of events, humankind has been producing fibers with polymeric raw materials for numerous applications by wet, dry, melt, and gel spinning methods. On the other hand, making long fibers and continuos in shape with the flexibility of production at the nanometer-scale, electrospinning has recently been explored. Around the turn of the century, electrospinning drew more and more attention as the capability of producing fibers got enhanced with the advent of new materials for manufacturing ceramic and composite nanofibers[162;174]. Additionally, the ability to draw fibers quickly by electrospinning enabled the researchers to use them in various applications such as energy

harvesting, conversion, and storage.

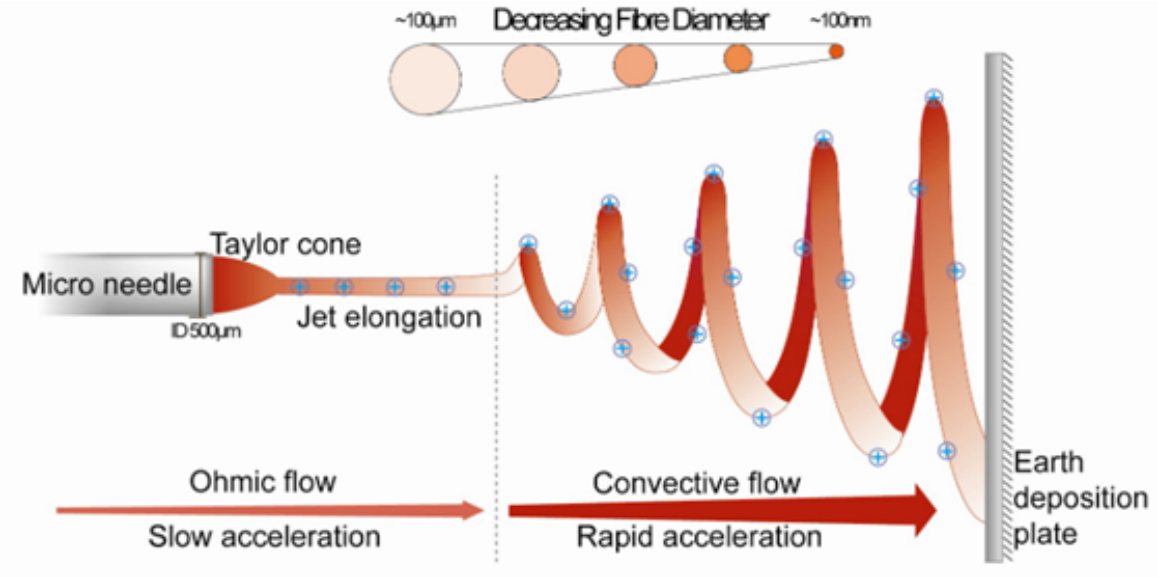


Figure 3.1: *Fiber formation by electrospinning method*[114]*, Copyright © 2011, Springer Science Business Media, LLC.*

The electrohydrodynamic process of electrospinning involves the electrification of liquid droplets, converting them to jets. This jet gets stretched and elongated further and turns into fibers. A basic electrospinning setup illustrated in figure 3.1 can be made in a laboratory setup for producing fibers according to application needs. The setup described in the figure contains a spinneret as a needle connected to a power supply with sufficiently high voltage (5-30 kV), and a plate for collecting the fiber, which should be grounded in a syringe for feeding the solution. The polymer solvent in the syringe is fed at a specific rate to confirm the formation of droplets. The applied voltage on the needle tip is responsible for the stretching of the liquid droplet, and Taylor cone formation occurs. If the cohesion of the molecules in the material is excessive, the stream does not break up. The result of such phenomena is the electrospraying of droplets in a charged jet. The jet derived from the droplet flows toward the applied electric field to the collector. The jet extending in the axis continues such behavior until bending instability occurs due to the electrical field. The current flow changes its mode from ohmic to convective, and the charge inside the jet gets transferred to the surface of the fibers. The jet thus gets bent through 900, forming recurring loops that go

through abrupt acceleration. The process occurring can be named the 'whipping process,' which allows the elongation of fibers to a nanometre scale and thus gets deposited into the collector. The solvent inside the liquid gets evaporated, thus leaving behind the polymer, which gets solidified to form a fiber[63;173]. Figure 3.1 illustrates the fiber formation process during electrospinning.

The fabrication of polymer-derived ceramic fiber involves numerous steps, which begin with spinning the fiber generated from the preceramic polymeric precursor in sol-gel form. However, the raw material required for producing the fibers necessitates specific physical properties. One of such properties is the flowability or viscoelasticity of the raw material. Moreover, properties such as being fundamentally liquid and solubility in certain solvents, thus creating an undistinguishable solution, are desirable for spinning and producing fibers. Monomers and oligomers having infrequent repeating units tend to be present in liquid form in ambient temperatures. For this sole purpose, as the preceramic silicon polymer possessed low molecular weight ($\leq$ 500 g mol^{-1}), which appeared water-like liquid, the inauguration of linear polymers based on carbon materials with high molecular weight was necessary. Introducing a high molecular weight compound ensured the sol-gel obtained would be viscous enough ($\geq$10 poise) for electrospinning. Various parameters affect the final fibers obtained via the electrospinning method. Among them, the following seemed to affect the fiber qualities:

- A stepper motor controls the speed of the polymer-solvent feed rate through the syringe. When the syringe capacity was fixed, the feed rate was directly affected by the rotating speed of the stepper motor. Thus, the high feed rate pushed the distance of the needle tip to the collector to be larger or the voltage to be higher as the polymer solution needed to be converted to fibers. Conversely, after continuous testing, a slower feeding rate ensured the production of good-quality fibers with lower applied voltage.

- The optimization of the applied voltage between the needle tip and collector ensured the formation of the fibers from the solution. However, a higher voltage than the optimized one resulted in the deposition of fibers in other places rather than the collector.

- Needle tip and collector distance be adjusted depending on the feed rate of the polymer solution and applied voltage. The space was preferred to be between 15 and 20 cm for the proper Taylor cone formation and fibers with the best quality without beads.
- Air bubbles in the polymer solvents resulted in inconsistent feed rate through the syringe. So, any air bubbles formed must be removed to ensure the continuous feeding of the solution.

Based on the above engineering parameters, the best conditions for the formation of fibers were found on a trial basis and implemented to produce fiber mats.

3.1.2 Preparation of Fibermats

In this study, different amounts of bulk TMD powders were sonicated for varied amounts of time in isopropanol (IPA) to form a dispersion. Then, 800 mg of Polyvinylpyrrolidone (PVP) powder was added, and the ratio of PVP: IPA was varied for different fibermat fabrication. The solution was stirred via a magnetic stirrer at 200 rpm for an hour. 1, 3, 5, 7- tetramethyl, 1, 3, 5, 7- tetravinyl cyclotetrasiloxane (4-TTCS) was primarily mixed with 1% Dicumyl peroxide (DCP), which was a cross-linking initiator and added to the previous dispersion. The resultant solution was stirred again using a magnetic stirrer for 1 hour and 30 minutes. The final solution was loaded in a 10 mL syringe with a flat metallic needle for electrospinning. The feed rate for the process was 5mL h^{-1}. An alligator pin was connected to the metallic needle and was subjected to a high voltage of 15 kV depending on the viscosity of the solution, and the ground was connected to a cylindrical-shaped roller collector. The distance between the needle tip and the roller was 15 cm. Thus, as-spun fiber mats of dimension 20 $\times$ 20 cm2 were fabricated. After drying the as-spun fiber mat in the open air, the fiber mat was put into a low-temperature oven and cross-linked at 160 °C for 6-24 hours. The cross-linked fiber mats were cut into small pieces, fitted into small ceramic boats, and put into a tube furnace in the argon gas for pyrolysis. Two-step annealing was carried out at 400 °C for 1 hour and 800 °C for 30 mins. The heating rate was 2 °C per minute. Thus, SiOC-functionalized TMD fiber mats were produced. This section gives a general

idea about the fibermat preparation process. Specific details regarding individual fibermat production methods are described separately in each chapter. Figure ?? demonstrates the solution preparation process described above.

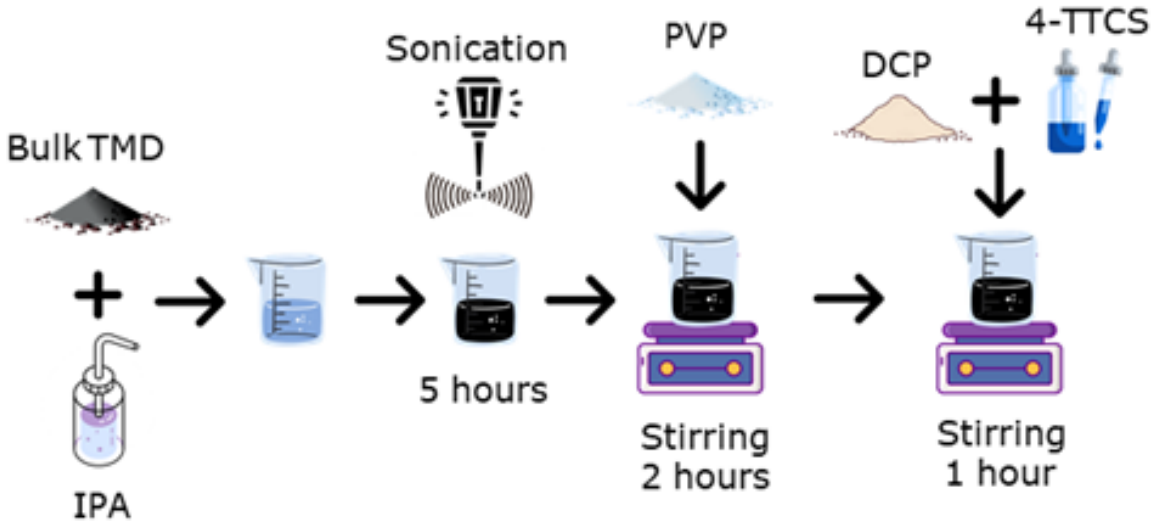


Figure 3.2: *Schematic illustration of solution preparation process for electrospinning.*

3.2 Characterization Techniques

3.2.1 Microscopic Techniques

Scanning Electron Microscopy

For revealing important morphological properties of the materials on the nanoscale, engineers and scientists have been using electron microscopy for many years. Light microscopes, inexpensive, non-destructive, and robust, have also been used for many years. But their inability to tell apart objects less than micrometer-scale has opened up the world of electron microscopes. In scanning electron microscopy (SEM) electron beam is used to bombard the sample and focus on a specific spot. The beam then consecutively scans the whole sample at each location where the gun points at elastic and inelastic interactions. Due to the interactions between backscattered electrons, primary and secondary electrons, and characteristic

X-rays, auger electrons emerge from the sample. Specifically, primary electrons can be differentiated from secondary electrons as the former impacts the specimen. The latter arises from the specimen produced by the interaction of electrons and matter. In SEM, these secondary electrons being detected by the detector are used to reveal the topographic contrast of the sample, i.e., the surface and texture of the sample. Moreover, the average chemical composition of the material can also be studied by investigating the generated X-rays. Thus, EDX spectroscopy in SEM has also been used as a beneficial method for exploring the chemical analysis of various samples.

Transmission Electron Microscopy

While the working principle of transmission electron microscopes (TEM) is quite similar to the SEM, the TEM is primarily used to inspect the intrinsic microstructure of the sample, materials that are on the nanometer scale (such as particles and fibers), and the imaging of the arrangement of atoms within the sample. The electron guns used in a TEM setup generally accelerate the high-voltage electrons (commonly 80-300 keV and samples with very light elements such as carbon with le 100 keV). Compared to SEM, a TEM setup consists of many sets of electromagnetic lenses for adjusting the focus of the specimen to examine the diffraction pattern and magnification of this pattern to the system for detection. To extract the maximum amount of information from the samples, various imaging modes are also available in TEM. For example, the bright field imaging technique reveals internal properties of the samples, such as changed mass, thickness, grain boundaries, and dislocations, with the help of elastic and inelastically scattered electrons. Furthermore, the crystallographic information of the samples can also be identified by the diffraction pattern of the samples. In TEM, the diffraction pattern is developed using elastically scattered electron interference (both constructive and destructive).

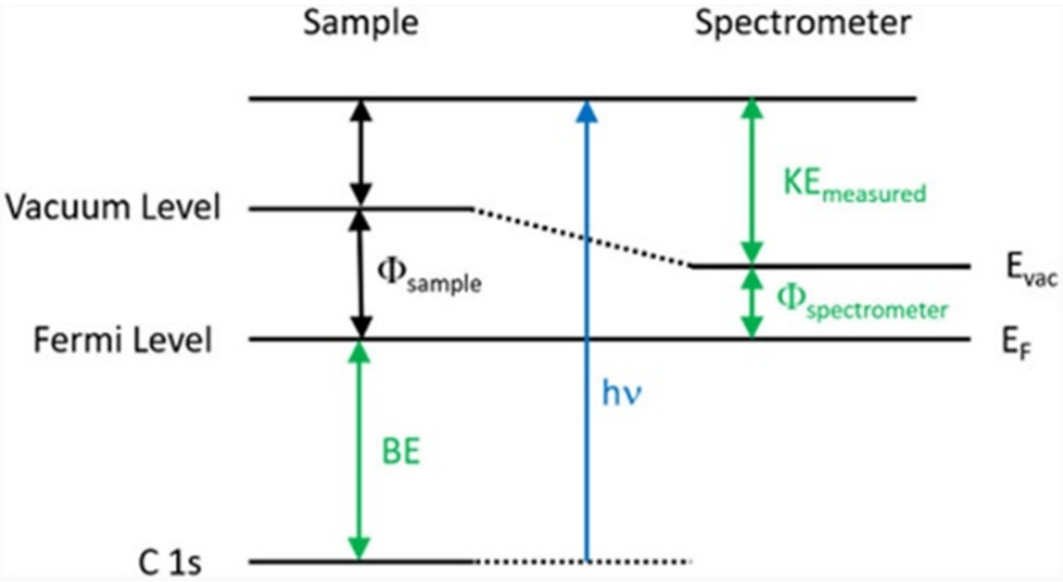


Figure 3.3: *Schematic illustration of basic XPS equation[289], Rights managed by AIP Publishing.*

3.2.2 Spectroscopic Techniques

X-Ray Photoelectron Spectroscopy

Heinrich Hertz first discovered in 1887 discovered the photoelectric effect, based on which the X-ray Photoelectron Spectroscopy (XPS) technique works. In 1905, Albert Einstein more formally described the method of emission of electrons from surfaces by the irradiation of light and was awarded the Nobel Prize in physics in 1921. In this revolutionary technique, the sample is bombarded with X-rays with energies lower than 6 keV. The emitted electrons from the sample's surface have a certain kinetic energy, which is detected and analyzed. The photoelectron emitted from the surface results from the energy transfer from an X-ray to an electron in the atom's core. The kinetic energy of the electron can be calculated from the equation 3.1

$$KE_{measured} = h\nu - BE - \phi_{spectrometer} \tag{3.1}$$

Where the kinetic energy is denoted by KE, the energy of the X-ray is indicated by hν, the spectrometer work function is represented by $\phi_{spectrometer}$ (a constant value), and the binding energy (how tightly the electron is bound to the orbital). The equation is illustrated

schematically in the following figure. The Fermi energy level is known as the zero binding energy. The difference of energy between the Fermi energy level and any energy level below denotes the energy of the ion remaining after the emission of an electron, otherwise named Binding Energy. The photoelectron peaks obtained from the experiment are expressed by the element and the orbital emitted by the electron. For instance, C1s in this picture denotes the electron from the 1s orbital of the Carbon atom[130]. Figure 3.3 illustrates the XPS working principle.

Raman Spectroscopy

Raman spectroscopy works based on the principle of Raman Scattering. Specifically, Raman scattering is based on the principle that there is a difference in the frequency of scattered radiation and incident radiation that is monochromatic. In this method, the sample is irradiated with a monochrome laser of a specific frequency. This monochromatic light interacts with the sample molecules and scatters in different directions. The frequency of this scattered radiation is often the same as the incident radiation and is described as the Rayleigh Scattering. However, only a small amount of scattered radiation contains a frequency different from the frequency of the incident light, which builds up the Raman scattering phenomena (known as Inelastic Scattering). The scattered radiation mentioned above is measured at 900 to the incident light and picked up by a detector after being separated from the Rayleigh scattering (Elastic Scattering). In the figure, the energy transfer process due to the coupling of the incident light and the quantized state of the scattering system is shown. This coupling decides whether the incident photon will lose energy (Stokes scattering) or gain energy (Anti-stokes scattering) on the level of molecular vibration-rotation. Figure **??** illustrates the stokes and anti-stokes scattering processes. Raman Spectra is presented as an intensity vs. Raman shift plot. Using this data, the detection of molecules in the sample is carried out, and the structural transformation during different chemical reactions can be highlighted.

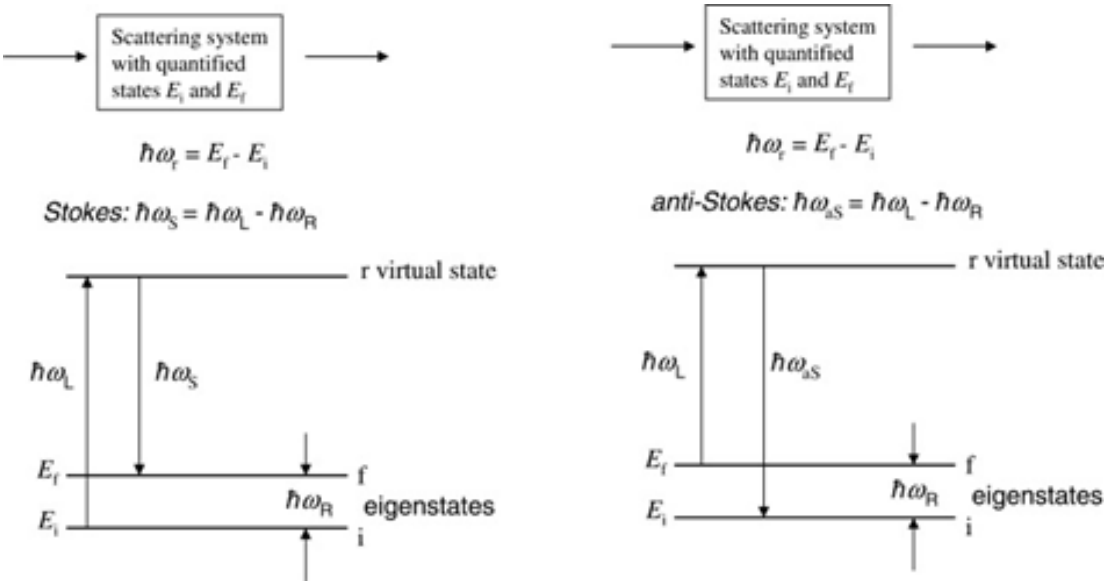


Figure 3.4: *Schematic of Stokes and Anti Stokes Scattering*[239]*, Copyright 2003 WILEY-VCH Verlag GmbH & Co. KGaA, Weinheim.*

Fourier Transform Infrared Spectroscopy

When the molecules absorb electromagnetic radiation, the transition between the rotational energy level and vibrational energy level of the lowest electronic state occurs in the mid-infrared region. However, infrared spectroscopy mainly deals with the vibrational modes of the molecules. Therefore, an FTIR instrument primarily consists of a source that continuously provides infrared radiation, a part that translates this infrared radiation to component wavelengths, and a detector. Thus, the whole procedure can be expressed by the equation 3.2.

$$T(\nu) = \frac{I(\nu)}{I_o(\nu)} \tag{3.2}$$

Where T is denoted as transmittance, I is the intensity of the infrared radiation when the sample is placed between the source and detector, and I_o states the infrared radiation when the sample is not present. The wavenumber is represented by ν, and at equal wavenumber intervals, the transmittance is recorded. The compounds with molecular structures producing increments in dipole antisymmetric vibration are considered infrared active. Thus, the available functional groups and the evolution of structural bonds in such materials are

investigated with this instrument[131].

3.2.3 Electrochemical Analysis Techniques

A range of electrochemical analysis techniques were utilized in this thesis, the working principle of which are briefly discussed below. Specific experimental conditions are discussed in the material and methods section of each chapter.

Galvanostatic Charge Discharge

Galvanostatic charge-discharge (GCD) is one of the most utilized electrochemical analysis techniques for electrode performance evaluation. A constant current is applied to the electrode while charging and discharging the electrode within a specific potential range, and the change in voltage as a function of time is measured. Different energy storage devices – capacitors, pseudocapacitors, and batteries yield distinct GCD profiles due to the unique reactions. The reason behind such behavior falls outside the depth of this research, however, a small description will definitely be provided. The current density affects the diffusive or capacitive controlled behavior and contributions of the total system. At sufficiently low current density, ions access the active sites of the electrode material, and all the reactions get captured in the profile. The opposite happens at higher current density as sufficient time for diffusion of ions is not available at higher scan rates. In practice, the specific capacity of the electrode material is determined from the equation 3.3

$$C_{practical} = \frac{it_{cutoff}}{3.6 \times m} = \frac{i \int V\, dt}{3.6 \times m \times V} (mAhg^{-1}) \tag{3.3}$$

Where V denotes the potential, t is the time for which the experiment was performed, and m denotes the specific weight of the active material within the electrode.

Coulombic efficiency is another important parameter obtainable from the GCD experiment – defined as the ratio of charge drawn out from the cell during discharge and the stored charge during the charging process. As this study utilizes half-cells, an inverse of

this ratio will be considered as the coulombic efficiency (C.E.). GCD also presents different derivative techniques to evaluate the performance of the cell overall. Rate capability is one technique where the device's capability is measured as a function of increasing current density. An electrode possessing fast kinetic properties performs well at higher current densities with a decrease in diffusion pathway and an increase in fast electron/ion transport. Another method of cell-level electrochemical property measurement is predominantly known as cycling stability, where capacity is measured at constant charging/discharging conditions[226].

Cyclic Voltammetry

Highlighting on cyclic voltammetry (CV) drives us back to linear sweep voltammetry (LSV), where current is measured while the potential is linearly swept as a function of time. The voltage change over time can be represented as a slope, otherwise known as scan rate (mV s). Various factors affect the curve obtained from LSV: the rate of electron transfer as the electrochemical reaction takes place, the reactivity of the electrode active material, and the scan rate at which the curve is obtained. The data obtained from the LSV experiment denote either the anodic or cathodic peak. The difference between LSV and CV is that the CV experiment is not particularly limited to a single scan but a loop of multiple scans, and for this very cyclic nature, the technique gained its particular name. The nature of electrochemical processes within the material can be qualitatively identified as reversible, quasi-reversible, or irreversible and can be demonstrated by astute observation of the shape of the CV curve or the correlation between current, scan rate, and potential. The currents within the system always follow the power law as equation 3.4.

$$i = a\nu^b \tag{3.4}$$

Where i is the current in A, v is the scan rate (mV s), and a and b are dependent values.

The b-value from the above-mentioned equation is a sum of the diffusion-controlled and capacitive currents. According to the Randles-Sevcik equation, diffusion-controlled currents yield a proportional change with the scan rate, $v^{1/2}$. On the contrary, capacitive currents

follow a linear relationship with scan rate. Taking the log of the above equation yields,

$$logi = loga + blog\nu \tag{3.5}$$

From where b can be rewritten as:

$$b = \frac{logi - loga}{log\nu} \tag{3.6}$$

This b term in the equation takes a value between 0.5 and 1.0, depending on the type of reaction. Notably, the total current i is a sum of both diffusion-controlled and capacity reactions, which can be expressed as follows:

$$i = k_1\nu + k_2\nu^{\frac{1}{2}} \tag{3.7}$$

Where $k_1 v$ represents the capacitive reaction and $k_2\nu^{\frac{1}{2}}$ represents diffusion controlled reactions. A linear fit of $i/v^{1/2}$ vs. $\nu^{1/2}$ results in specific values of k_1 and k_2 – therefore, k_1 denoting the slope and k_2 denoting the y-intercept value yields a fraction of currents[154;233].

3D differential capacity curves

Differential capacity (dQ/dV) curves are similar to CV experiments with the major difference in the analysis technique from which it is derived. The dQ/dV curves are derived from the experimental data obtained from GCD experiments[154]. In general, the similarity lies in the fact that the CV curve, where current (i) is plotted in the x-axis, can be transformed into dQ/dV, by following the equations stated below:

$$V = \nu t \tag{3.8}$$

$$dt = \frac{dV}{\nu} \tag{3.9}$$

$$I = \frac{dQ}{dt} \tag{3.10}$$

$$\frac{I}{\nu} = \frac{dQ}{dt} \tag{3.11}$$

In this thesis, differential capacity curves were reinvented as an in-situ technique through which changes in electrochemical reactions were measured as a function of the cycle index. While different in-situ techniques (in-situ Raman, FTIR, or XRD) for measuring the material properties of electrodes are expensive, require intricate experimental conditions, and depend on the expertise of the personnel, 3D dQ/dV can be an excellent complementary technique.

Chapter 4

WS_2 Nanosheet rooted SiOC Fibermat for beyond Li^+- ion Storage[1]

4.1 Preface

Transition metal dichalcogenides (TMDs) such as the WS_2 have been widely studied as potential electrode materials for lithium-ion batteries (LIB) owing to TMDs' layered morphology and reversible conversion reaction with the alkali metals between 0 to 2 V (v/s Li/Li^+) potentials. However, works involving TMD materials as electrodes for sodium- (NIBs) and potassium-ion batteries (KIBs) are relatively few, mainly due to poor electrode performance arising from significant volume changes and pulverization by the larger size alkali-metal ions. Here, we show that Na^+ and K^+ cyclability in WS_2 TMD is improved by introducing WS_2 nanosheets in a chemically and mechanically robust matrix comprising precursor-derived ceramic (PDC) silicon oxycarbide (SiOC) material. The WS_2/SiOC composite in fibermat morphology was achieved via electrospinning followed by thermolysis of a polymer solution consisting of a polysiloxane (precursor to SiOC) dispersed with exfoliated WS_2 nanosheets. The composite electrode was successfully tested in Na-ion and K-ion half-cells as a working electrode, which rendered the first cycle charge capacity of 474.88 mAh g^{-1} and 218.91 mAh

[1]Reprinted from Dey, Sonjoy, and Gurpreet Singh. "WS_2 Nanosheet Loaded Silicon-Oxycarbide Electrode for Sodium and Potassium Batteries." Nanomaterials 12.23 (2022): 4185.

g^{-1}, respectively. The synergistic effect of the composite electrode leads to higher capacity and improved coulombic efficiency compared to the neat WS_2 and neat SiOC materials in these cells.

4.2 Introduction

With innumerable advantages such as high round trip efficiency, long cycle life, and minimal maintenance of electrochemical energy storage, rechargeable batteries have opened the door to innovative technologies such as mobile electronics and electrified transportation[135]. Furthermore, the widespread application of electronic devices in the healthcare, fitness, sensing, sports, and textile industries has shifted consumer focus to flexible and stretchable electronics[104]. Consequently, rechargeable batteries, specifically LIB technology, have drastically developed in the last two decades. Although LIBs are superior in the electrochemical energy storage systems (EESS) due to their high energy density and lightweight characteristics, their questionable sustainability, low theoretical capacity (theoretical specific capacity of 372 mAh g^{-1}) of anode material in advanced LIBs (does not match the energy density requirement), and high cost of lithium metal and other battery components have shifted the research attention to other options. Thus, high-capacity batteries based on lighter alkali metals, such as sodium (Na) and potassium (K), are becoming valid contenders due to their abundance and minimal expense[395]. However, Na and K ions have larger ionic radiuses (1.02 Å for Na^+; 1.38 Å for K^+), rendering graphite-based anodes with an interlayer spacing of 3.35 Å useless. Also, high volume expansion (61% for K^+ ions) causes structural disintegration and subsequent capacity fading in graphite during charge and discharge cycles[172;344].

When graphene was first exfoliated from graphite using the mechanical cleavage technique, the scientific community's elevated interest was focused on developing similar two-dimensional (2D) materials. 2D TMDs contain a sheet-like graphene morphology with hexagonally packed layers of transition metal atoms sandwiched between two chalcogen atoms. Although the intralayer metal chalcogen bonds in TMDs are covalent, the sandwich layers are coupled by van der Waals bonds which are typically weak, rendering them useful for ap-

plication in vast fundamental and technological disciplines such as catalysis, energy storage, sensing, and electronic devices[51]. Among the various 2D TMDs, WS_2 contains a lamellar structure with an interlayer spacing of 0.62 nm between (002) lattice planes, thus offering suitable space for the reversible insertion of large-sized Na and K ions[6]. Moreover, because WS_2 has a superior volumetric energy density of 3248 mAh cm^{-3} as a LIB electrode due to the high density (>7 g cm^{-3}), WS_2 is an auspicious choice for anode material[350]. Although significant research has investigated WS_2 as a potential lithium-ion storage application, the application of WS_2 in NIBs and KIBs is somewhat limited. Unique, distinctively tailored nanostructures of WS_2, such as nanoflakes, nanosheets, nanowires, and nanoflowers, have also been studied to determine if they enhance the performances of NIBs[280;316;363;380;382;392]. Still, these require extensive conditions to fabricate such structures. On the other hand, when commercial WS_2 powder was investigated for K-ion storage behavior, the capacity was only 103 mAh g^{-1} in a potential window of 0.01–3.0 V at 100 mA g^{-1} [392]. Furthermore, few investigations have found that when alkali metal ions are inserted and extracted within the layers, the failure of the electrode structure occurs as it goes through significant volume change induced by mechanical stress. As a result, the delamination between the active material and the current collector results in poor stability over a more extended period[70;134;356]. Moreover, the widely studied TMD materials prefer to undergo irreversible conversion reactions rather than reversible intercalation reactions when interacting with alkali metal ions forming an inert layer and causing first-cycle losses[16]. The layer formation is associated with the dissolution of polysulfides in the electrolyte used in the device. With the issues mentioned above, further investigation is needed to determine a simple and cost-effective fabrication process to enhance electrode capacity in NIBs and KIBs.

To overcome the difficulties discussed above, when the TMD materials as battery electrodes, are amalgamated with carbon materials, metal sulfides, oxides, and conducting polymers which impart electronic conductivity within the composite material and boosts the electrochemical properties[286]. With unique physical and chemical properties, PDC materials are also eying candidacy for their use in electrochemical energy storage devices. When the microstructure of PDC is revealed, a network of sp2-bonded carbon atoms can be located at

the tetrahedral silica boundary. In addition, the Si-C bonds are formed in PDCs, and these bonds, along with the free carbon network resembling graphene, prevent the diffusion of chemicals and degradation. For example, Davi et al. have shown that this amorphous structure of PDCs helps protect MoS_2 from degradation and prevents the loss of sulfur species in PDC/MoS_2 composite, thereby improving capacity retention in NIB electrodes[134]. However, the use of PDCs as KIB electrodes is yet to be thoroughly studied, which prompted the current investigation.

The present study sought to chemically functionalize WS_2 nanosheets with PDCs by fabricating a fiber structure via electrospinning, thus obtaining electrodes with lucrative electrochemical properties. The fibermat electrode was achieved by preparing a spinnable solution with liquid phase preceramic oligomer and exfoliated WS_2 nanosheets, followed by pyrolysis. The obtained non-woven fibermat structure contained an arid amount of WS_2 nanosheet embedded into the SiOC structure that helped buffer the volume change induced by the TMD material when used as Na^+ ion and K^+ ion half-cells. The microscopic and spectroscopic analysis confirmed the presence of WS_2 nanosheets and the SiOC structure, exhibiting improved rate capability compared to the neat materials in NIBs and KIBs. This is potentially the first investigation to feature WS_2 nanosheet and PDC in fibermat form for use beyond LIB chemistry.

4.3 Materials and Methods

4.3.1 Electrospinning Solution Preparation

The neat WS_2 powder utilized in this study was purchased from Alfa Aesar (Haverhill, MA, USA). The preceramic silicon oligomer 1, 3, 5, 7-tetramethyl, 1, 3, 5, 7-tetravinyl cyclotetrasiloxane (4-TTCS) was purchased from Gelest (Morrisville, PA, USA) and used without further modification. The solution preparation process for the electrospinning process included sonicating the obtained WS_2 powder with isopropyl alcohol purchased from Fisher Chemical (Lenexa, KS, USA) for 1 h in a probe sonicator. The result was a black dispersion.

This 4-TTCS and Polyvinylpyrrolidone (PVP) with an average molecular mass of 1,300,000 g mol^{-1} purchased from Sigma Aldrich (Missouri, MA, USA) were mixed with the previous solution via stirring until a homogenous mixture was obtained. The weight ratio of the 4TTCS: IPA was kept at 1:9, and the weight ratio of the WS_2 powder: 4TTCS was 1:5. PVP was mixed at a weight ratio of 1:3 with 4TTCS to induce viscosity to the overall solution as the preceramic oligomer possessed low molecular weight (¡500 g mol^{-1}). A small amount of Dicumyl peroxide (1 wt. % of 4TTCS) purchased from Sigma Aldrich was also mixed with this solution which worked as a cross-linking agent.

4.3.2 Electrospinning Conditions and Fibermat Fabrication

Preparation of fibermat containing WS_2 nanosheets is a multistep process in which the first step is to produce a flowable and viscous solution (¿10 poise) favorable for spinning conditions and as described in the previous section. The as-prepared solution was loaded into a syringe with a metallic needle connected with a high-power voltage source grounded with a roller collector. Aside from the prepared solution, the spinnability of fibers depends on various other parameters. Examples include the feed rate of the solution (kept at 5 mL h^{-1}), optimization of the applied electric field between the needle and the roller collector (19 kV was utilized in this study), and the distance between the needle tip and the roller collector (constantly kept at 12 cm). Such conditions enabled us to fabricate the as-spun fibermat about 20 × 20 cm^2 in area and dark greyish in appearance. The as-spun fibermat was kept in a low-temperature oven for 6 h at a temperature of 160 °C to cross-link under ambient conditions. A small portion of this fibermat (30 × 25 mm^2) was taken into a ceramic boat and pyrolyzed at higher temperatures in a tube furnace. The heat treatment was carried out in a two-step process at 400 °C for 1 h and 800 °C for 30 min under an inert atmosphere (Argon gas). The heating rate was kept constant at 2 °C per minute. Thus, the final pyrolyzed WS_2/SiOC fibermat was obtained.

4.3.3 Characterization Techniques

The morphology of the fibermat was investigated with two SEM microscopes, namely Carl Zeiss EVO MA10 and FEI Nova NanoSEM450, with a 5–30 kV impinging voltage. Transmission electron microscopic images were obtained using Phillips CM100 TEM (Nashville, TN, USA) under an accelerating voltage of 100 kV. The chemical analysis of the samples was done by X-ray photoelectron spectroscopy (XPS), obtained using PHI Quantera SXM using monochromatic Al-Kα with an energy of 1486.6 eV. The Raman imaging system of Horiba Jobin Yvon LabRam Aramis was utilized using a He-Ne laser (wavelength of 633 nm and power of 17 mW) to collect the Raman spectra of the pyrolyzed samples. The FTIR spectra of the fibermats were collected utilizing the Spectrum 400 FT-IR spectrometer from PerkinElmer (Waltham, MA, USA).

4.3.4 Electrochemical Techniques

The electrodes studied in this work were prepared in the following composition: 70 wt.% of active material (WS_2/SiOC pyrolyzed fibermats), 15 wt. % of carbon black as the conducting agent (Alfa Aesar, Haverhill, MA, USA), and 15 wt. % of polyvinylidene fluoride as the binder (Alfa Aesar). A homogenous slurry was obtained upon mixing the materials mentioned above by adding 1-Methyl-2-pyrrolidinone (Sigma Aldrich, Missouri, MA, USA) in a dropwise manner. This slurry was then coated on a 9 µm thick copper substrate and then dried at 80 °C for 18 h to remove solvents. The thickness of the then-obtained film was found to be 125 µm. Circular sections were obtained with a 14.29 mm diameter circular punch to be used as a working electrode in the 2032 type coin cell. The active material (WS_2/SiOC) mass loading for the NIB and KIB cells was 0.63 mg each. The negative electrode in the case of NIBs was sodium metal with 1.0 M $NaClO_4$ (Alfa Aesar) in (1:1 v/v) EC: DMC (anhydrous, 99%, Sigma Aldrich) as electrolyte. On the other hand, the negative electrode in the case of KIBs was potassium metal with 1.0 M KPF_6 (Alfa Aesar) in (1:1 v/v) EC: DMC (anhydrous, 99%, Sigma Aldrich) as electrolyte. In both cases, the two electrodes were separated by a monolayer membrane (Celgard), and the glass separator was

soaked with electrolytes. All the cells were assembled in a high-precision argon atmosphere with O_2 and H_2O contents below 0.1 ppm.

4.4 Results and Discussions

4.4.1 Microscopic Analysis

As the fibermats were first electrospun and then cross-linked and pyrolyzed at elevated temperatures, it was essential to investigate the surface of the fibers as the effect of temperature could be diverse. Thus, SEM micrographs were obtained for the as-spun (figure 4.1a), cross-linked (figure 4.1b), and pyrolyzed fibermats (figure 4.1c). The inset of each figure shows distribution plots obtained from ImageJ software to study fiber diameters. The average diameter for the as-spun fibers was 6–7 µm, while the average diameters for the cross-linked fibers were 3–4 µm, and the diameter range of the pyrolyzed fibers was 1.6–2.0 µm. Magnified SEM micrographs (figure 4.1d,e) of the final pyrolyzed fibermat showed regular fibers with no anomalies such as beads or defects. The WS_2 nanosheets were sporadically scattered as islands in the fiber geometry. The fiber diameter decreased as a function of the temperature and was further investigated via spectroscopic methods. The change in fiber diameter in different conditions was comparable to the weight-loss phenomenon recorded in various annealing stages, as shown in Figure 4.6(a–c). A digital camera image showed a gray WS_2/SiOC as-spun fibermat, which correlated to the color of the near WS_2 fibers but differed from the neat SiOC fibermat. The cross-linked fibermat, however, had a light gray appearance with a weight retention of 56.04% and a linear shrinkage of 4.9%. The final pyrolyzed fibermat was black, with a weight retention of 52.27% of the cross-linked fibermat. Linear shrinkage was observed at 51.43%. The weight loss and linear shrinkage records were then corroborated by the fiber diameter from the SEM images. The elemental distribution map obtained from the Energy Dispersive Spectroscopy (EDS) showed an even distribution of the materials in the fibermats. The W-Lα-1 and S-Kα-1 maps in Figure 1f,g show the nanosheet-like distribution for these elements in the fibermat, implying that the

WS_2 nanosheets are well bonded with the SiOC fiber matrix. Si-Kα-1, C-Kα-1,2, and O-Kα-1 maps in figure 4.1h–j show that these elements were distributed in a fiber-like fashion. A qualitative analysis of the elements in the fibermats was also carried out via the EDS, shown in figure 4.1k. Characteristic W-Lα at (8.6 keV) and S-Kα (at 2.52 keV) spectral lines were observed in the fibermat, confirming the presence of WS_2 nanosheet material. In addition to the peaks, spectral lines for Si-Kα (at 1.97 keV), O-Kα (at 0.73 keV), and C-Kα (at 0.48 keV) were also observed, denoting the presence of Si-O-C matrix after pyrolysis. Notably, calibration caused the entire spectra to shift by 0.2 keV.

TEM was conducted to gain further insights into fiber morphologies. Bulk WS_2 powders were first studied (figure 4.1l) to confirm the layered morphology of the crystal. figure 4.1l shows layered WS_2 sheets with edge angles of 120°. The crystalline nature of this sheet was revealed by the selected area electron diffraction (SAED) pattern, denoting the 100 and 110 crystal planes[6;91] (shown in figure 4.1m). The magnified TEM image of the WS_2 nanosheet containing SiOC fibers is illustrated in figure 4.1n, which shows the numerous pores through which the electron beam could pass. These pores are likely being generated due to gas evolution during polymer-to-ceramic transformation at elevated temperatures. Liwen et al. have demonstrated that these pores are beneficial for electrochemical storage applications as the porosity induces the charge transfer at the electrode-electrolyte interface and attenuates the volume change providing a feasible container space[330]. The SAED pattern taken from the WS_2 nanosheet within the fiber shows the same hexagonal spotted pattern observed from figure 4.1o with 100 and 110 crystal planes indicating that the WS_2 nanosheet retains its crystalline nature even after pyrolysis. The micrographs show that the WS_2 nanosheets maintain their crystalline structure even after functionalizing with SiOC material in fiber form. This formation might lessen the polysulfide dissolution when cycled in alkali metal-ion batteries. As the fibermats were first electrospun and then cross-linked and pyrolyzed at elevated temperatures, it was essential to investigate the surface of the fibers as the effect of temperature could be diverse.

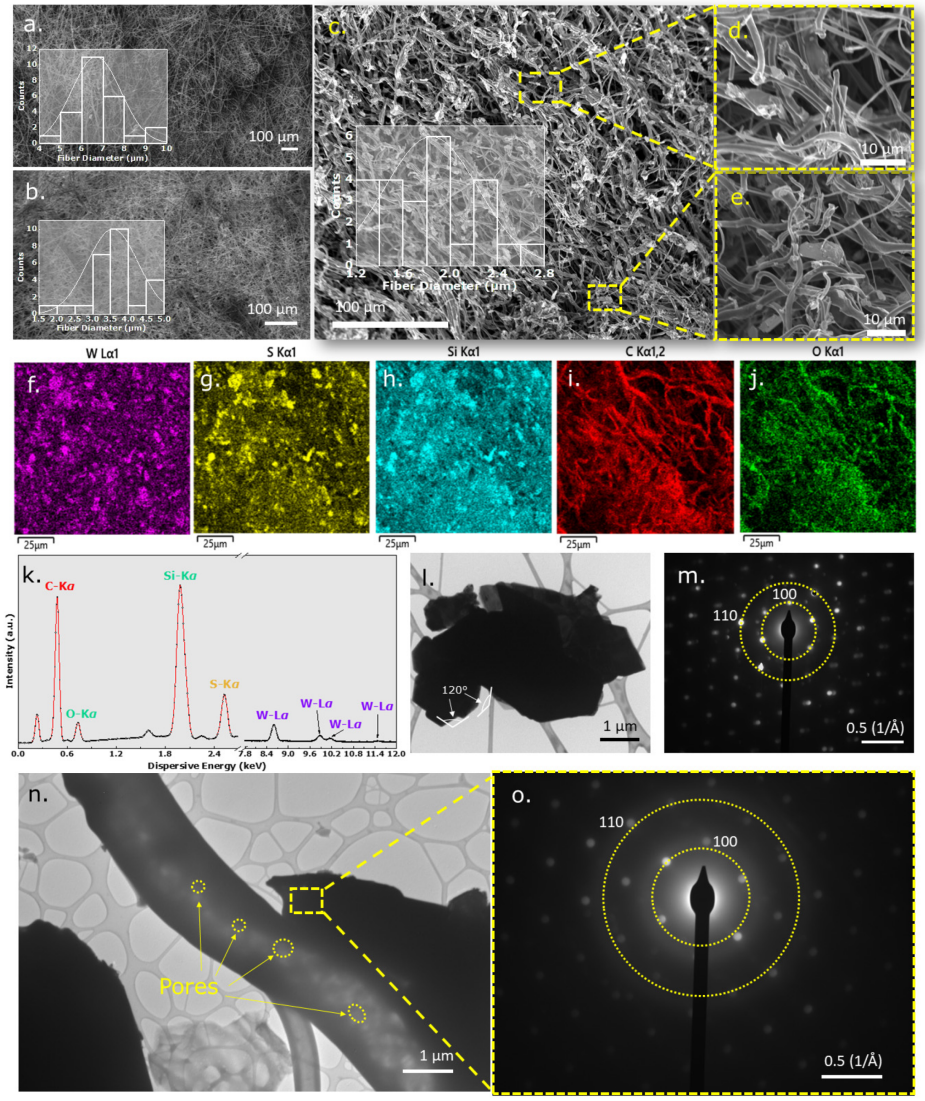


Figure 4.1: *SEM micrograph of (a) as-spun WS_2/SiOC fibermat; (b) cross-linked WS_2/SiOC fibermat; (c) pyrolyzed WS_2/SiOC fibermat; the inset showing the distribution curve of the fiber diameter; (d) magnified SEM micrograph of the pyrolyzed fibermat elucidating the individual fibers; (e) magnified SEM micrograph of the pyrolyzed fibermat showing WS_2 nanosheet dispersed in the SiOC matrix; (f) W-Lα-1; (g) S-Kα-1; (h) Si-Kα-1; (i) C-Kα-1,2; (j) O-Kα-1 EDS color map of the pyrolyzed fibermat; (k) EDS Spectra of the WS_2/SiOC fibermat confirming the presence of the materials within; (l) TEM image of the bulk WS_2 nanosheet; (m) SAED pattern obtained from a part of the WS_2 nanosheet of Figure l; (n) TEM image of the WS_2/SiOC fibermat; (o) SAED pattern of the crystalline WS_2 nanosheet obtained from a specific portion of the WS_2/SiOC fibermat.*

4.4.2 Spectroscopic Analysis

Raman Spectroscopy, an all-embracing technique, was used to decipher the microstructure of the fibermat and designate the free carbon phase and the presence of the WS_2 nanosheet materials. Figure 4.2a illustrates the Raman spectra of the bulk WS_2 powder that can be compared with the WS_2 nanosheet within the fibermat geometry. The figure also shows many major and minor peaks in the spectrum. Minor peaks with low intensity in the spectrum include A_{1g}(M)-LA(M) at 230 cm^{-1}, 2LA(M)-3$E^2{}_{2g}$(M) at 264 cm^{-1}, 2LA(M)-2$E^2{}_{2g}$(M) at 297 cm^{-1}, and 2LA(M) at 350 cm^{-1}. In addition, the spectrum shows two major high-intensity peaks: first-order optical modes $E^1{}_{2g}$ at 354 cm^{-1} and A_{1g} at 418 cm^{-1}. Notably, the 2LA(M) mode overlapped with the $E^1{}_{2g}$ mode. While in backscattering geometry, the first-order modes $E^1{}_{2g}$ and A_{1g} were prominent, with the Brillouin zone edge mode primarily being activated by disorder-induced within the sample, thereby identifying the longitudinal acoustic mode at the M point, namely LA(M). Specifically, the LA(M) mode results from the in-plane collective movement of atoms within the lattice, identical to sound waves. The atoms periodically compress and expand to create such waves along the propagation direction. Additional peaks in the spectra were the result of multi-phonon combinations of the above mode[24;29;203;283;368]. Although the LA(M) mode at 176 cm^{-1} was shallow in this investigation, the 2LA(M) mode combined with the $E^1{}_{2g}$ to render a high-intensity peak. All the first-order and second-order peaks occurred in the WS_2 bulk material and WS_2 nanosheets in the fibermat. For the WS_2/SiOC fibermat sample (shown in Figure 4.2b), the high-intensity peaks were $E^1{}_{2g}$ and A_{1g} bands at 350 cm^{-1} and 417 cm^{-1}, respectively.

Another experimental feature from the WS_2/SiOC sample's Raman spectra was the filler material's layer thickness. Because the exfoliated WS_2 nanosheets were used to prepare the electrospinning solution, some features of the few layers of thick nanosheets were identified as expected. In summary, the A_{1g} peaks underwent a slight red shift. In contrast, the $E^1{}_{2g}$ peak experienced a subtle blue shift, as indicated by the few-layer nature of the nanosheets, potentially due to the sonication of the WS_2 nanosheet material during solution preparation

for the as-spun fibermat[115]. Moreover, the intensity ratio of the E^1_{2g} to A_{1g} peak of the WS_2 nanosheets in the fibermat was 0.83, indicating a few layered natures of the nanosheets within the fibermat. However, the intensity ratio of the two major peaks of the bulk material was in the range of 0.48, which accurately reflects previous studies by Zeng et Al. and Berkdemir et Al.[283].

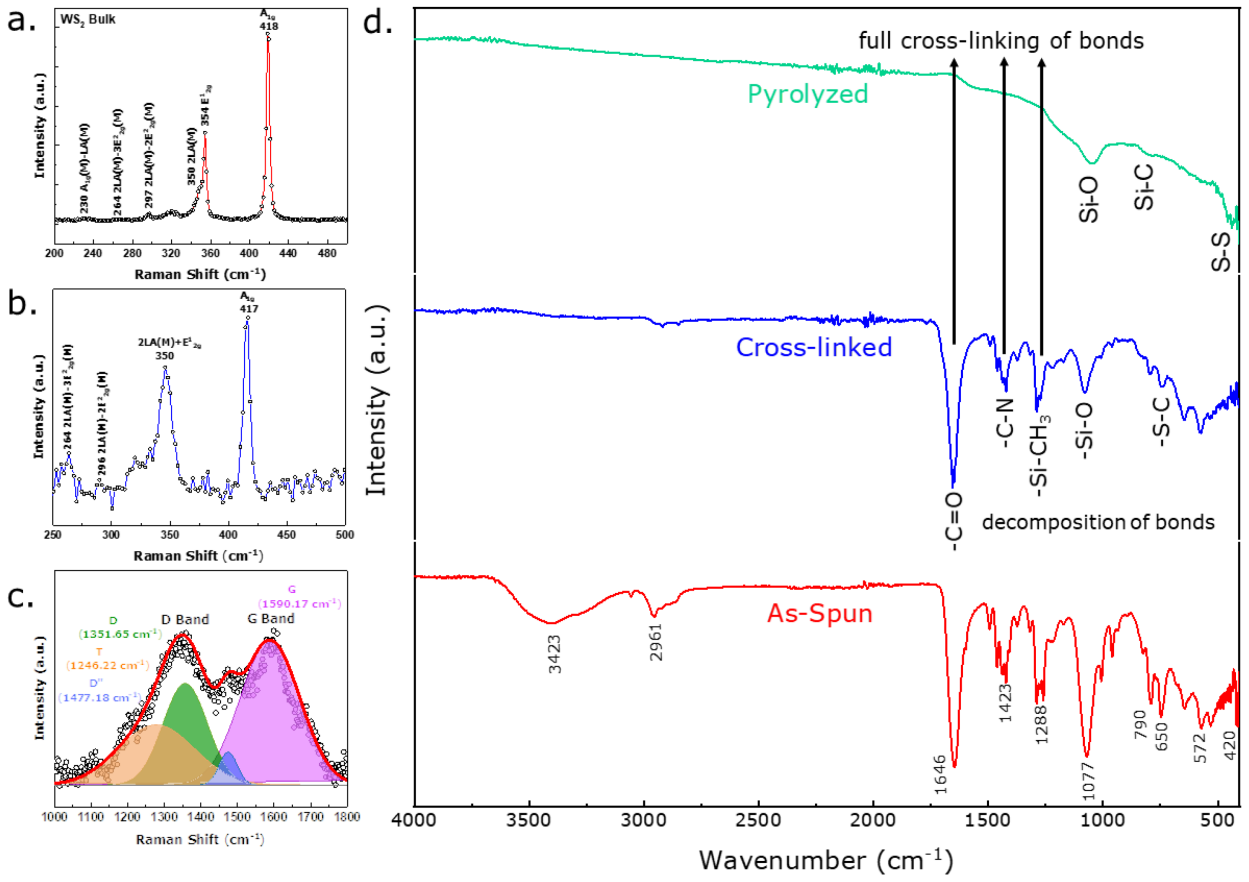


Figure 4.2: *Raman Spectra of (a) Bulk WS_2 powder showing the typical position of the peaks obtained from the neat material; (b) WS_2/SiOC fibermat in the lower wavenumber region confirming the presence of the WS_2 nanosheet material within the fibermat showing the same peaks as the bulk material with subtle differences; (c) WS_2/SiOC fibermat in the higher wavenumber region confirming the free carbon species (integrated spectra using a gaussian function); (d) FTIR spectra of As-spun, cross-linked, and pyrolyzed fibermats. The spectra from top to bottom illustrate data obtained from individual pyrolyzed, cross-linked, and as-spun fibermats.*

Peak-fitted Raman spectra from Figure 4.2c showed the free-carbon phase of the WS_2/SiOC fibermat. The prominent D and G peaks occurred at 1351.65 cm^{-1} and 1590.17 cm^{-1}, re-

spectively. While the D peak was due to disordered carbon in the sample, the G band (E2g symmetry) caused in-plane stretching of the sp2 carbon bonds[29;112]. The deconvoluted Raman spectra revealed T and D" peaks in the shoulder of D and G bands at 1246.22 cm^{-1} and 1481.68 cm^{-1}, respectively. The T band signified the sp2–sp3 carbon-carbon double and triple bonds. The D" band signified the amorphous nature of carbon in the sample, which was verified in TEM diffraction pattern studies[212]. The high degree of disorder present in the fibermats could also be verified from the intensity ratio of the D and G bands. For instance, I_D/I_G ratio for the WS_2/SiOC sample was 0.71.

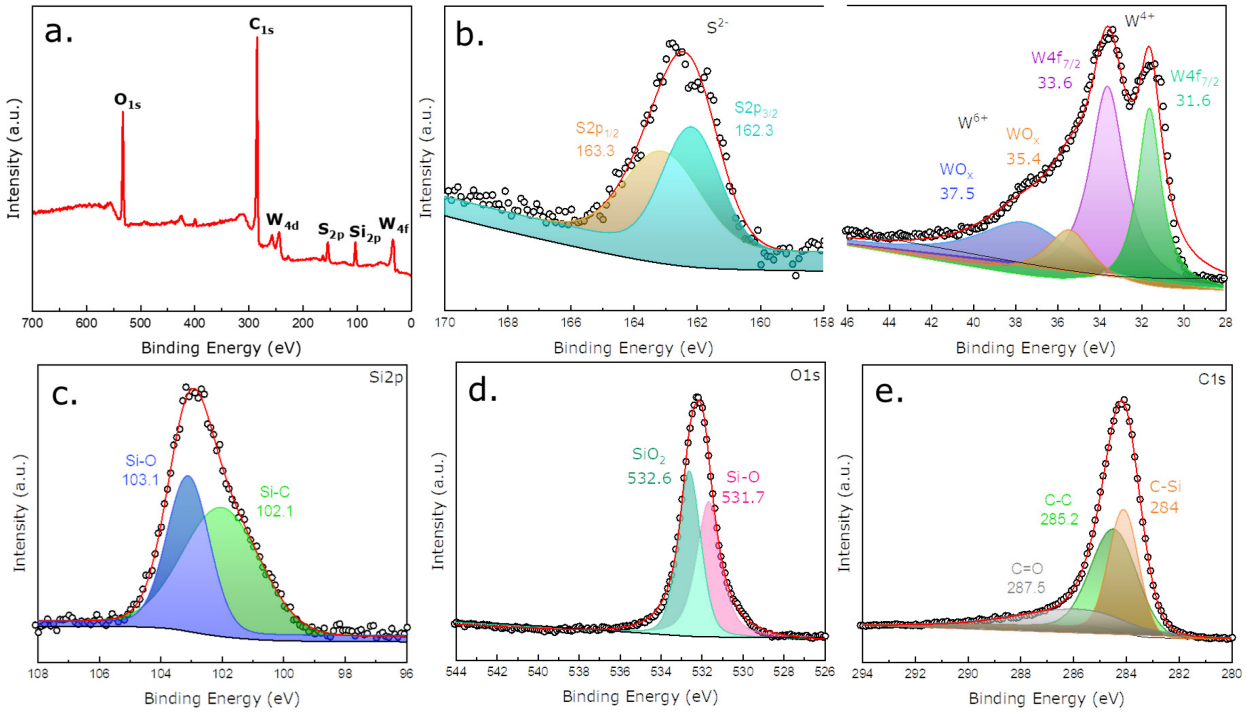


Figure 4.3: *(a) XPS survey scan of WS_2 containing SiOC fibermats representing the presence of individual elements after pyrolysis of the fibermat at high temperature; (b) High-resolution S2p (L) and W4f (R) XPS spectra of the WS_2/SiOC fibermat recording the bonding states due to s.o.s. of W and S; High-resolution: (c) Si2p XPS spectra; (d) O1s XPS spectra; (e) C1s XPS spectra obtained from the WS_2/SiOC fibermat confirming the bonding states of the Si, O and, C, respectively in SiOC matrix.*

Fourier transform infrared spectroscopy (FTIR) was used to identify the polymerization within the fiber geometry during the decomposition stages. Figure 4.2d shows FTIR spectra of the as-spun WS_2/SiOC fibermat. In general, peaks observed in the region of 1265–1285

cm^{-1} were responsible for the -C-N bond originating from the PVP molecule. In addition, peaks in the 1650–1660 cm^{-1} region caused the carbonyl group in the molecule. The two peaks mentioned above in the functional group and fingerprint regions are primary indicators of the presence of the PVP molecule in the as-spun fibermat[15]. FTIR spectra also verified the facile integration of WS_2 nanosheets with carbon-based groups. In addition, the peaks at 650 cm^{-1} and 1080 cm^{-1} were responsible for the W-S and S-S bonds, respectively[108;125]. Multiple peaks at 650 cm^{-1} to 800 cm^{-1} refer to the samples' C-S bonds. For example, the peak at 790 cm^{-1} is characteristic of C-S-S-C, H-C-S, and C-S bonds[269;374]. Furthermore, the strong absorption from 1000 cm^{-1} to 1070 cm^{-1} indicates the Si-O bonds. The presence of the -CH_3 deformation and asymmetric stretching in Si-CH_3 bonds is visible in the range 1261 cm^{-1} and 2961 cm^{-1} region, respectively. The absorption peak at 800 cm^{-1} indicates the Si-C stretching vibration[171]. These peaks confirm the presence of preceramic polymer in the fiber morphology by previous investigations[215;397]. For the cross-linked fibermats (Figure 4.2d; spectra in the middle), peak intensity decreased for both fibermat samples, indicating the occurrence of vinyl polymerization. Finally, the pyrolyzed fibermats (Figure 4.2d; spectra at the top) show Si-O and Si-C bonds.

In this study, XPS, an important technique used in the chemical analysis field for analyzing surface characteristics, was utilized to provide details regarding elements that compose the material and the chemical and electronic state. Figure 4.3a represents the XPS survey scan of the WS_2/SiOC fibermats. The presence of W, S, Si, O, and C can be verified from the survey scan of the fibermats with no contamination with other materials within the instrument sensitivity. Table 4.1 in the Supplementary Information presents the atomic percentage of the elements in the fibermat. WS_2 in the form of nanosheet is found at 1.5% for W and 1.19% for S in the fibermat. Moreover, the high amount of carbon in the fibermat (73.42% found from the survey scan) also confirms the free carbon phase after the pyrolysis cycle, which was previously proven by the Raman spectroscopic analysis. Figure 4.3b. illustrates the high-resolution W4f and S2p spectra of the fibermats, confirming the bonding states of W present in the fibermat. Tougard function was used to subtract the background, and the spectra were fitted using the Voigt function. Spin-orbit splitting (s.o.s.) produced two core

level peaks for each W4f and S2p, namely 4f7/2, 4f5/2, 2p3/2, and 2p1/2, respectively. For example, the binding energy of W4f showed that the W^{4+} state presented 4f7/2 and 4f5/2 bands in 33.6 eV and 31.6 eV, respectively. The XPS spectra efficiently captured the effect of sonication of the bulk WS_2 powder when preparing the electrospinning solution. The sonication caused the formation of 2H and 1T/1T' form, as shown by the abundant W4f7/2 component in the sample due to high peak intensity. Slight oxidation of the layered WS_2 nanosheets was also observed with characteristic peaks of WO_x at 35.4 eV and 37.5 eV. The presence of the WO_x component may result from oxygen functionalities originating from the preceramic polymer.

The high-resolution S2p spectra can also be deconvoluted into two components: 2p1/2 and 2p3/2 at 163.1 and 161.8 eV, respectively. These intermediate doublets were due to sulfur S^{2-} ions in WS_2, as noted in previous investigations of WS_2 nanosheets and nanoflakes[145;290;397]. The high-resolution spectra of the Si2p, O1s, and C1s were also obtained for the fibermat and shown in Figure 4.3c–e, respectively. The deconvoluted Si2p spectra represented the Si-O and Si-C bonds present in the fibermat. From the C1s spectra, the C-Si, C-C, and C=O bonds were identified. From the O1s spectra of the fibermat, the Si-O and, SiO_2 bond states were observed with a dominance of the SiO_2 over the other. From all this information, it is apparent that a good amount of carbon in the sample is also bonded with Si, and individual SiO_2 regions were observable, which validates the SiOC microstructure of the pyrolyzed fibermat even after pyrolysis while including WS_2 in the nanosheet form[69;100].

4.4.3 Electrochemical Analysis

An investigation of Na^+ ion and K^+ ion electrochemical reactions at various potentials was carried out using a galvanostatic charge–discharge (GCD) profile. The differential capacity curves obtained from the GCD profile provide a clearer view of the plateaus available in the GCD profile, converting them into individual peaks. Supplementary Figure 4.6a depicts the GCD profile and corresponding differential capacity curve of the bulk WS_2 nanosheet

material when used as an anode in the Na-ion half-cell. From the differential capacity curve of the Na-ion half-cell (shown in Supplementary Figure 4.6b), it is apparent that the Na-ion insertion process in the bulk material is multistep, with several peaks appearing in the charge and discharge cycles. In the first sodiation process, two major peaks at 0.29 and 0.6 V (vs. Na/Na^+) can be attributed to the irreversible conversion reaction of WS_2 with sodium ions into metallic nanoparticles embedded into the Na2S matrix and the formation of solid electrolyte interphase (SEI) layer on the surface of the electrode[266]. Again, during the 1st desodiation cycle, oxidation of W to WS_2 is located at the curve in regions 1.89 and 2.3 V (vs. Na/Na^+)[24;144]. In the second and third cycles, the peaks at 0.29 and 0.60 V diminish, indicating that the reaction is irreversible. The reversible reaction between Na^+ ions and WS_2 can be traced to the peak at 1.36 V (vs. Na/Na^+), which is apparent only from the second cycle onwards[24]. For the desodiation process in the 2nd and 3rd cycles, the before-mentioned peaks seem to have weakened and broadened. From the GCD curve denoted by Supplementary Figure 4.6b, the first cycle charge capacity of the WS_2 neat electrode is found to be 380.42 mAh g^{-1} with a coulombic efficiency of 67.2% at a current density value of 100 mA g^{-1}. This initial irreversible capacity loss is thought to originate from the conversion reaction and SEI layer formation during the first stages of cycling, which is a typical case for layered compounds. Achieving stability in this layer formation takes some time for a neat WS_2 electrode, so the high capacity drop in the first five cycles is observed. The charge capacity achieved stability after the first five cycles. In a rate capability test (where current density was increased orderly), the material retained its stable coulombic efficiency only after the 10th cycle, reaching nearly 100% and maintaining a similar value till the 45th cycle. In the rate capability test (shown in Figure 4.4c), the capacity retention during the 26th, 31st, 36th, and 41st when the current density was brought back to the initial rate (600, 400, 200, 100 mA g^{-1}, respectively) was found out to be 98.7%, 92.4%, 81.78%, 59.54%, respectively.

Although silicon-based materials are thought to be almost inactive in NIBs, recent investigations report that free-carbon domains existing in such materials are well suited to store Na^+ ions. Therefore, it is logical to expect Na^+ ion storage property originating from the existence of free carbon domains, which is evident in the spectroscopic analysis of the

SiOC material used in this study. Neat SiOC fibermats were studied in GCD experiments at the same condition described before (shown in Supplementary Figure 4.7c). The differential capacity curve obtained from the GCD curves (shown in Figure 4.7d) offers a pair of peaks during the sodiation/desodiation process at 0.01 and 0.09 V, which can be ascribed to the free carbon sites. On the other hand, the peak at 0.57 V region can be assigned to the trapping of Na^+ ions into the highly active defective graphene sites, which is irreversible in the following cycles and the formation of the SEI layer. It is thought that this peak contributes to the fluctuations in the coulombic efficiency of the SiOC electrode seen in Figure 4.4c. Such observations are comparable to the ones made in previous studies conducted regarding using SiOC-based materials in NIB setup[33;170].

In the case of the composite electrode fabricated with WS_2 and SiOC material, the Na^+ ion storage performance was also evaluated via GCD experimentation (Figure 4.4a). The differential capacity curve obtained (shown in Figure 4.4b) from the GCD plots showed a combination of peaks from the neat WS_2 and SiOC materials. For instance, in Figure 4.4b, where the differential capacity curve of the WS_2/SiOC electrode is illustrated, we observe the pair of peaks at 0.01 V and 0.08 V, which is reversible in subsequent cycles originating from the free carbon phase of the SiOC material. Three irreversible 1st cycle peaks exist at 0.3 V, 0.44 V, and 0.63 V region. While the 0.3 V and 0.63 V peaks can be assigned to the conversion reaction of the WS_2 nanosheets and the formation of the SEI layer, the peaks seemed less intense than the neat WS_2 material. Again, the peak residing at the 0.44 V region can be assigned to the Na^+ ions being trapped into the defective graphene edges emerging from the SiOC material. This peak was also less intense than the neat SiOC fibermat electrodes. In addition, reversible peaks were detected at 1.36 V, 2.01 V (in sodiation steps), 2.25 V, and 1.8 V (in desodiation steps). All the peaks, as mentioned earlier, originate from the WS_2 nanosheets within the fiber structure. The WS_2/SiOC electrode was cycled at a gradually increasing current density of 100, 200, 400, 600, and 800 mA g^{-1} and again brought back to the initial rates in the subsequent cycles (shown in Figure 4.4c). The first cycle charge capacity obtained from the composite electrode was 474.88 mAh g^{-1} which is higher than the neat WS_2 electrode (380.42 mAh g^{-1}) and neat SiOC fiber electrode (141.59 mAh g^{-1}).

At varying current densities of 100, 200, 400, 600, and 800 mA g^{-1}, the capacity of the composite electrode stood around 399.68, 313.3, 288.71, 268.1 mAh g^{-1}, respectively, which is also higher than both the neat materials as well. It is observable that after harsh cycling conditions, the capacity retention at the 26th, 31st, 36th, and 41st cycles (when current densities were brought back to the original value) were 95.89%, 96.54%, 79.85%, and 68.2%, respectively which is comparable to the neat electrode. The first cycle coulombic efficiency of the WS_2/SiOC composite electrode stood at 63.95%, similar to the neat WS_2 powder electrode (67.21%) and higher than the neat SiOC electrode (42.33%). Interestingly, while the coulombic efficiency of the composite electrode reached nearly 100% in the 4th cycle, the coulombic efficiency of the WS_2 powder electrode reached a similar value in the 17th cycle. For the neat SiOC electrode, it took 22 cycles.

The K^+ ion storage mechanism of the neat WS_2 powder electrode is evaluated in the GCD curve of Supplementary Figure 4.8a. The differential capacity curve derived from the GCD curve (shown in Supplementary Figure 4.8b) illustrates the 1st potassiation cycle peaks at 0.01, 0.35, 0.51, 0.76, and 1.25 V (vs. K/K^+). The peak at 0.76 V (vs. K/K^+) can be associated with the intercalation of K^+ ions into the WS_2 lattice to form $KxWS_2$[392]. This peak shifts to the 0.83 V region in the subsequent cycles. The peaks below 0.75 V region can be ascribed to the conversion reaction from $KxWS_2$ to K2S and metallic W and construction of the SEI film or other irreversible reactions, as these peaks do not appear in the subsequent cycles[297;316]. During the depotassiation process broad peak at 1.34 V (vs. K/K^+) is observed in all the cycles signifying the deintercalation behavior of WS_2[301]. From the GCD curve in Supplementary Figure 4.7d, it is apparent that the 1st cycle charge capacity was 79.59 mAh g^{-1} with a very low coulombic efficiency of 24.49% at a current density value of 100 mA g^{-1}. This low coulombic efficiency in the 1st cycle is thought to be happening due to the irreversible reactions taking place and also due to the ion size of the K^+ ions, which is comparatively larger than Na^+ ions, which should undergo much more resistance than the Na^+ ions during the cycling process.

For this reason, the cell's capacity is also lower than the NIB half-cell. The coulombic efficiency of the electrode reached nearly 100% after ten cycles of charge-discharge. In the

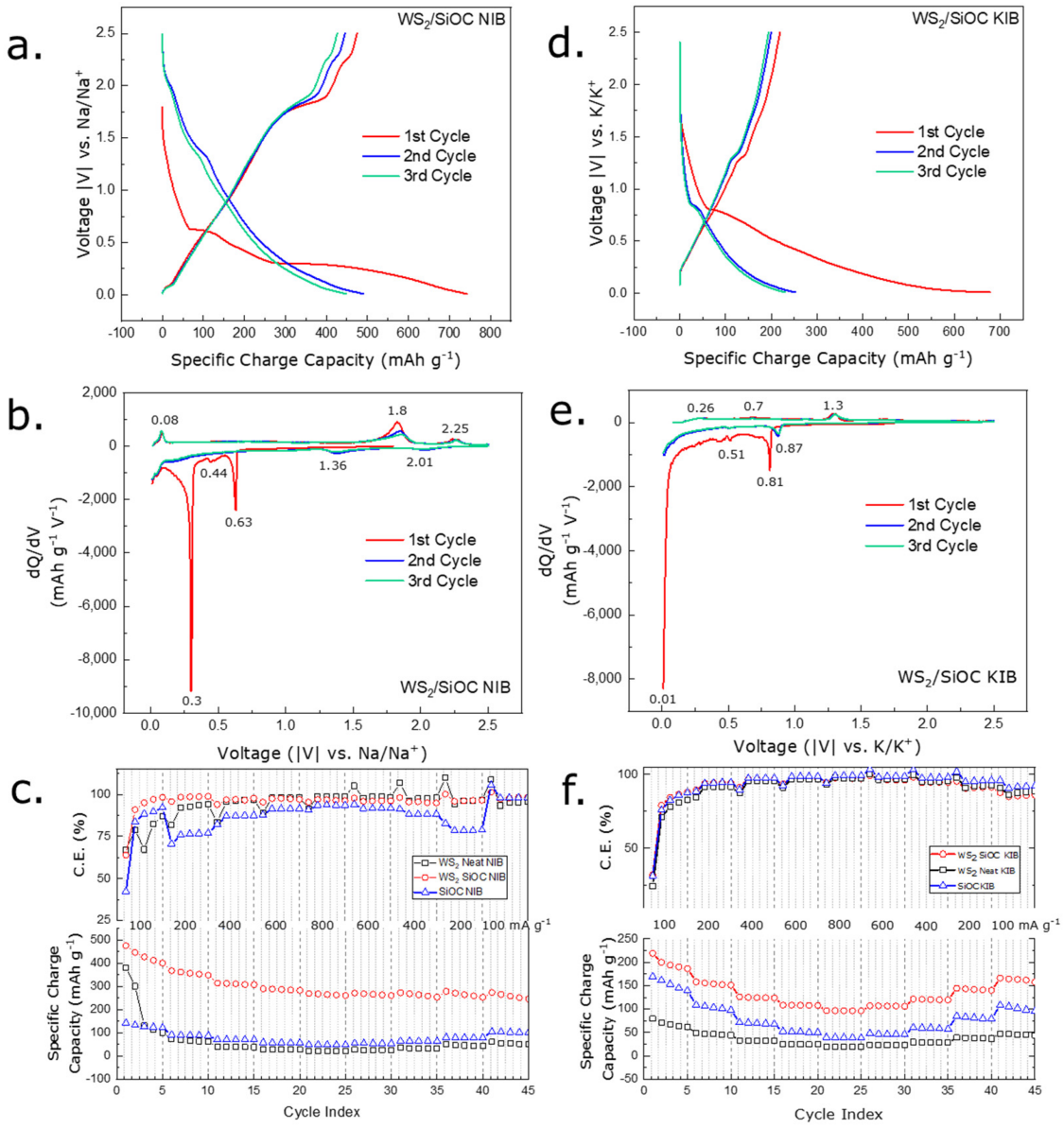


Figure 4.4: *(a) GCD profile of the WS_2/SiOC composite electrode when tested in a Na-ion half-cell setup; (b) differential capacity curve of the WS_2/SiOC composite electrode in Na-ion half-cell setup derived from the GCD profile; (c) Rate capability test performed for the WS_2/SiOC electrode when tested in a Na-ion half-cell setup at increasing current densities and bringing back to initial conditions after five cycles after each step; (d) GCD profile of the WS_2/SiOC composite electrode when tested in a K-ion half-cell setup; (e) differential capacity curve of the WS_2/SiOC composite electrode in K-ion half-cell setup derived from the GCD profile; (f) Rate capability test performed for the WS_2/SiOC electrode when tested in a K^+ ion half-cell setup at increasing current densities and bringing back to initial conditions after five cycles after each step.*

rate capability test (shown in Figure 4.4f), the capacity retention during the 26th, 31st, 36th, and 41st cycles when the current density was brought back to the initial rate (600, 400, 200, 100 mA g^{-1}, respectively) was found out to be 97.5, 92.9, 88.1 and 77.26%, respectively. The K^+ ion storage behavior via the differential capacity curve of the SiOC material (shown in Supplementary Figure 4.7d) offered a pair of peaks at 0.01 V and 0.37 V during the potassiation/depotassiation stages. These peaks are reversible and can be attributed to the reversible K^+ ion insertion and extraction in the free carbon domains within. A few peaks around the 0.14 V and 0.28 V region indicate the SEI layer formation, and this reaction was invisible in the following cycles[190;344].

The WS_2/SiOC composite electrode was tested in the KIB setup (shown in Figure 4.4d) in the same condition as the NIB setup. The differential capacity curve obtained from the GCD experiment of the composite electrode is shown in Figure 4.4e. which disclosed a combination of the phenomenon of the WS_2 neat electrode and SiOC electrode shown in Supplementary Figure 4.8c. From the differential capacity curve of the composite electrode (shown in Figure 4.4e), a pair of reversible peaks at 0.01 V and 0.26 V was observed, comparable to the peaks originating from the neat SiOC material during the potassiation/depotassiation stages. These peaks result from the insertion/extraction of K^+ ions in the free carbon domain of the SiOC material validated by the spectroscopic experiments beforehand. Notably, the SEI formation due to the WS_2 nanosheets contained within the fiber geometry can be identified by the peak at 0.51 V, which was also visible for the neat WS_2 powder electrode that went through a slight decrease in intensity. The peak at 0.81 V, also observed in the WS_2 neat electrode, is the result of the K^+ ions intercalating into the layers of WS_2 nanosheets. This peak similarly shifted in the region of 0.87 V in subsequent potassiation cycles and is indeed reversible. These peaks are observed in 1.31 V and 0.7 V regions during the depotassitation cycle, signifying the deintercalation of the K^+ ions and is also reversible. The first cycle charge capacity obtained from the composite electrode was 218.91 mAh g^{-1} which is higher than the neat WS_2 electrode (79.59 mAh g^{-1}) and neat SiOC fiber electrode (169.66 mAh g^{-1}). At varying current densities of 200, 400, 600, and 800 mA g^{-1}, the capacity of the composite electrode was 158.16, 125.92, 108.41, and 96.45 mAh g^{-1}, respectively,

which is also higher than both the neat materials. It is observable that after harsh cycling conditions, the capacity retention at the 26th, 31st, 36th, and 41st cycles (when current densities were brought back to the original value) were 99.6%, 98.01%, 95.39%, and 89.23%, respectively which is comparable to the neat electrode. The 1st cycle coulombic efficiency of the WS_2/SiOC composite electrode for the KIB cell stood at 32.31%, which is higher than the neat WS_2 powder electrode (24.49%) and the neat SiOC electrode (31.49%). This low coulombic efficiency for all the electrodes can be ascribed to the SEI layer formation of the electrode in the initial cycles. Interestingly, while the coulombic efficiency of the composite electrode was higher than the neat materials from the 2nd cycle onwards and reached near 100% at the 7th cycle, the coulombic efficiency of the WS_2 powder electrode reached a similar value at the 12th cycle. For the neat SiOC electrode, it took 22 cycles.

After 50 electrochemical cycles, the NIB and KIB cells containing the WS_2/SiOC electrodes were disassembled. The spent and desodiated/depotassiated electrodes were recovered for further structural and morphological characterization. Figure 4.5a,b denote the SEM micrographs of the desodiated WS_2/SiOC electrodes. Signs of microcracks in the electrodes are visible and marked with yellow dashed lines. Such microcracks are more visible at a magnified scale when presented in Figure 4.5b, and such phenomena can be correlated with the volume expansion of the WS_2 nanosheets and conversion reaction. However, other significant signs of volume expansion, such as coating delamination and discoloration, were not visible in the electrodes, which signifies the structural integrity of the electrodes. On the other hand, the depotassiated WS_2/SiOC electrodes illustrated by Figure 4.5c,d show very few microcracks, even on a magnified scale. Although there were no visible signs of delamination of particles and discoloration, cubicle-shaped particles were apparent from the magnified SEM micrographs (Figure 4.5d). These particles are considered WS_2 nanosheets, undergoing repeated cycling processes, thus expanding their volume and forming such shapes. One can hypothesize that such cubicle-shaped particles do not appear in the sodiated electrodes because the radius of potassium ions is much larger than that of the sodium ions.

To summarize the overall performance, the composite electrode outperformed the neat WS_2 nanosheet and SiOC electrodes in terms of capacity during harsh cycling conditions,

capacity retention, and coulombic efficiency when individually used as Na^+ ion and K^+ ion half-cells. The composite electrode's synergistic effect originates from the amorphous characteristics of the SiOC matrix not being chemically bonded to the WS_2 nanosheets (evidenced by the spectroscopic investigations of both Raman and XPS). The SiOC material also delivers an addition of graphene-like sp2-bonded carbon atoms situated in the boundary of the silica tetrahedral nanodomains. This carbon also helps improve the composite electrode's conductivity as a whole. Furthermore, the fiber geometry of this SiOC matrix adds the feature of shortening of diffusion length of ions. Additionally, the porous nature of the nanofiber configuration also provides a matrix for the WS_2 nanosheets, suppressing the volume expansion issues experienced by the general TMD materials. This phenomenon can be coordinated with the post-cycling SEM characterization, where only a few microcracks in the cycled electrodes were visible, and no delamination and discoloration of the electrode were visible.

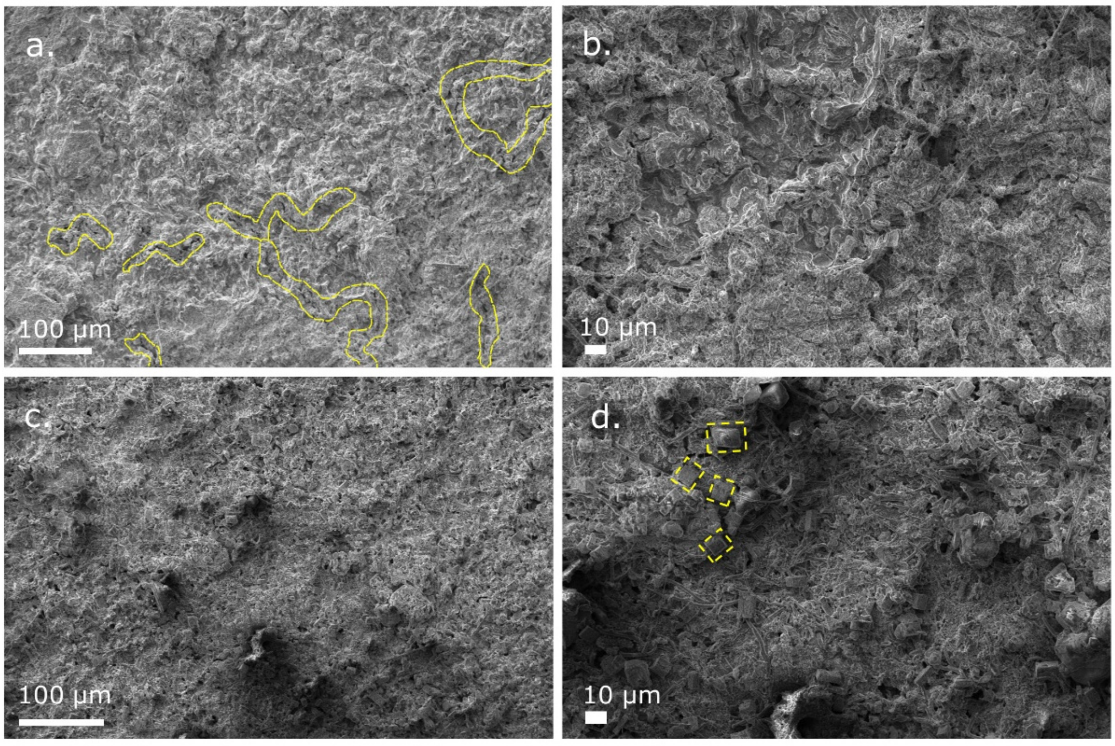


Figure 4.5: *SEM micrographs of disassembled WS_2/SiOC electrodes from (a) NIB half-cell; (b) NIB half-cell with a magnified view; (c) KIB half-cell; (d) KIB half-cell with a magnified view after 50 electrochemical cycles.*

Furthermore, the topological defects of the free carbon phase contained within the SiOC materials and the nanovoids presented by the SiOC material provide additional sites for the alkali metal ion storage[180;387]. The lower capacity obtained from the K^+ ion half-cell compared to the Na^+ ion half-cell is thought to stem from the larger size of the K^+ ions, which, when inserted in the SiOC matrix, causes repulsive interaction between the nearby K^+ ions. Thus, in the case of the SiOC material, a much lower theoretical capacity is estimated by the previous studies (186 mAh g^{-1})[35]. However, a combination of 2D WS_2 nanosheets helps to overcome this hurdle and raises the initial capacity to 218.91 mAh g^{-1} experimentally. Therefore, the successful combination of the two materials discussed above provided a harmonious effect that enabled the composite electrode to dominate over the neat materials when used in advanced next-generation alkali-metal ion half-cells.

4.5 Conclusion

Fabrication of SiOC/WS_2 nanosheet composite fibermat is demonstrated via electrospinning of a preceramic polymer solution dispersed with exfoliated nanosheets followed by high-temperature pyrolysis. The composite was then investigated as a potential electrode for beyond lithium-ion electrochemical energy storage devices, i.e., Na^+ and K^+ batteries. Electron microscopy confirmed the dispersion of the WS_2 nanosheets in the SiOC fiber matrix and the retention of the crystalline structure of the nanosheets even after pyrolysis at high temperatures. Spectroscopic studies further confirmed that the WS_2 nanosheets were well protected during the fibermat pyrolysis stages. Finally, chemical functionalization of WS_2 nanosheets in PDC fibermats in adequate amounts ensured better performance of the composite electrode when used in alkali metal ion half-cell at gradually increasing currents or harsher cycling conditions. The SiOC material provided additional sites for alkali metal ion storage and acted as a container space for volume changes induced by WS_2. SiOC matrix may have reduced the polysulfide dissolution phenomenon in WS_2 as the composite electrode capacity did not abruptly drop or collapse at higher cycling current densities and showed improved recovery at lower cycling currents. The capacity of the composite electrode in the

KIB half-cell is lower than the NIB half-cell. The is attributed to the larger size of the K^+ ion compared to the Na^+ ion. Furthermore, the composite electrode in the NIB and KIB half-cells proved better capacity retention than those with neat WS_2 and neat SiOC materials. Future investigations should be concerned with TMD materials with large interlayer spacing to accommodate K^+ ions to improve cyclability.

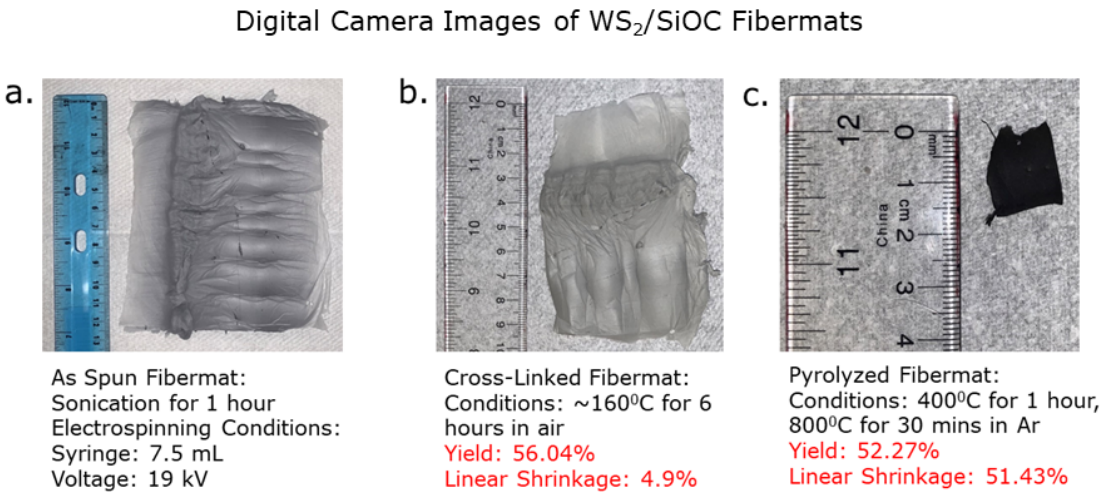


Figure 4.6: *Digital camera images of the WS_2/SiOC composite fibermats in (a) as-spun; (b) cross-linked; (c) pyrolyzed forms with corresponding weight retention and linear shrinkage values.*

Table 4.1: *Elemental Composition of the fibermats by XPS*

Fibermat	Elements (Atomic %)				
	W4f	S2p	Si2p	C1s	O1s
WS_2/SiOC	1.50367	1.19286	9.56574	72.4238	15.3139

Table 4.2: *Summary and comparison of electrochemical performance for Na^+ storage of other nanomaterial-based structures with this work.*

Anode Materials	Rate Capability	Reference
WS2/SiOC	474.88 mAh g^- @100 mA g^-	This work
	399.68 mAh g^- @200 mA g^-	
	313.33 mAh g^- @400 mA g^-	
W0.9Mo0.1S2	262 mAh g^- @1000 mA g^-	[372]
WS2/NC	320 mAh g^- @200 mA g^-	[331]
MoS2/RGO	253.1 mAh g^- @100 mA g^-	[353]
WS2-S/N-C	319 mAh g^- @100 mA g^-	[296]
MoS2-N-RGO	250 mAh g^- @1000 mA g^-	[201]
WS2/3DCD	392.1 mAh g^- @200 mA g^-	[249]
DODA-WS2	318 mAh g^- @1000 mA g^-	[66]
1T-MoS2	324 mAh g^- @1000 mA g^-	[326]
2H-WS2	353.2 mAh g^- @200 mA g^-	[195]
WS2@MoS2@C/rGO	411.8 mAh g^- @500 mA g^-	[176]
WS2/CNT-rGO ordered 3D aerogel	311.4 mAh g^- @100 mA g^-	[24]
	302.8 mAh g^- @200 mA g^-	
	289 mAh g^- @500 mA g^-	
MoS2/graphene paper	240 mAh g^- @25 mA g^-	[183]
	214 mAh g^- @100 mA g^-	
	173 mAh g^- @200 mA g^-	
MXene@Co9S8/CoMO2S4	325 mAh g^- @100 mA g^-	[136]
	309 mAh g^- @200 mA g^-	
	284 mAh g^- @100 mA g^-	

Table 4.3: *Summary and comparison of electrochemical performance for K^+ storage of other nanomaterial-based structures with this work.*

Anode Materials	Rate Capability	Reference
WS2/SiOC	218.91 mAh g^- @100 mA g^-	This work
	158.16 mAh g^- @200 mA g^-	
	125.92 mAh g^- @400 mA g^-	
D-TiS2	124 mAh g^- @50 mA g^-	[293]
	100 mAh g^- @100 mA g^-	
TiSe2	89 mAh g^- @50 mA g^-	[200]
	67 mAh g^- @100 mA g^-	
Commercial WS2	109 mAh g^- @50 mA g^-	[316]
	74 mAh g^- @100 mA g^-	
Hexagonal 2H-WS2	67 mAh g^- @5 mA g^-	[392]
	40 mAh g^- @200 mA g^-	
HeTiO2eC Micro-tubes	197.5 mAh g^- @100 mA g^-	[185]
Graphite	197 mAh g^- @C/2	[344]
Soft Carbon	160 mAh g^- @2C	[344]
Hard Carbon Microspheres	216 mAh g^- @C/10	[184]
Tin Based Composite	110 mAh g^- @25 mA g^-	[312]
Reduced graphene oxide	90 mAh g^- @50 mA g^-	[304]
	50 mAh g^- @100 mA g^-	
Tire -derived Carbon	155 mAh g^- @140 mA g^-	[87]

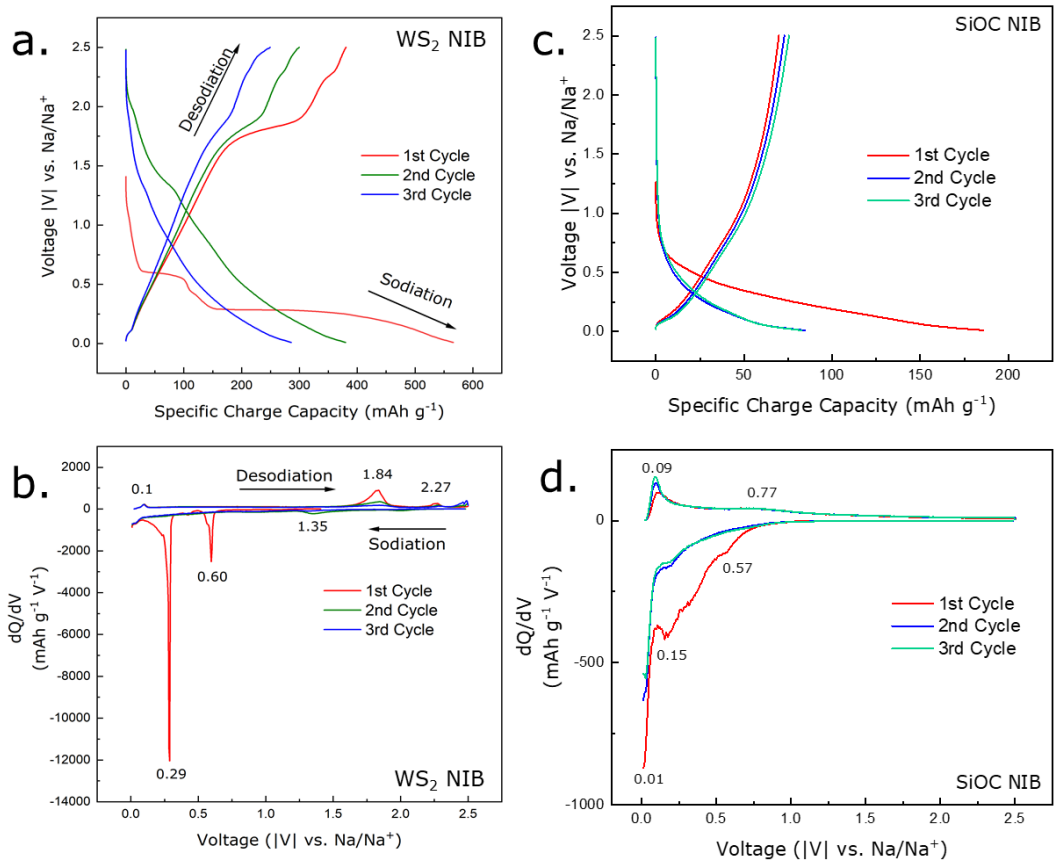


Figure 4.7: *(a) GCD profile of the WS_2 neat electrode when tested in a Na^+ ion half-cell setup; (b) differential capacity curve of the WS_2 neat electrode in Na^+ ion half-cell setup derived from the GCD profile providing information regarding reactions taking place at different voltages; (c) GCD profile of the SiOC fibermat electrode when tested in a Na^+ ion half-cell setup; (d) differential capacity curve of the SiOC fibermat electrode in Na+ ion half-cell setup derived from the GCD profile providing information regarding reactions taking place at different voltages.*

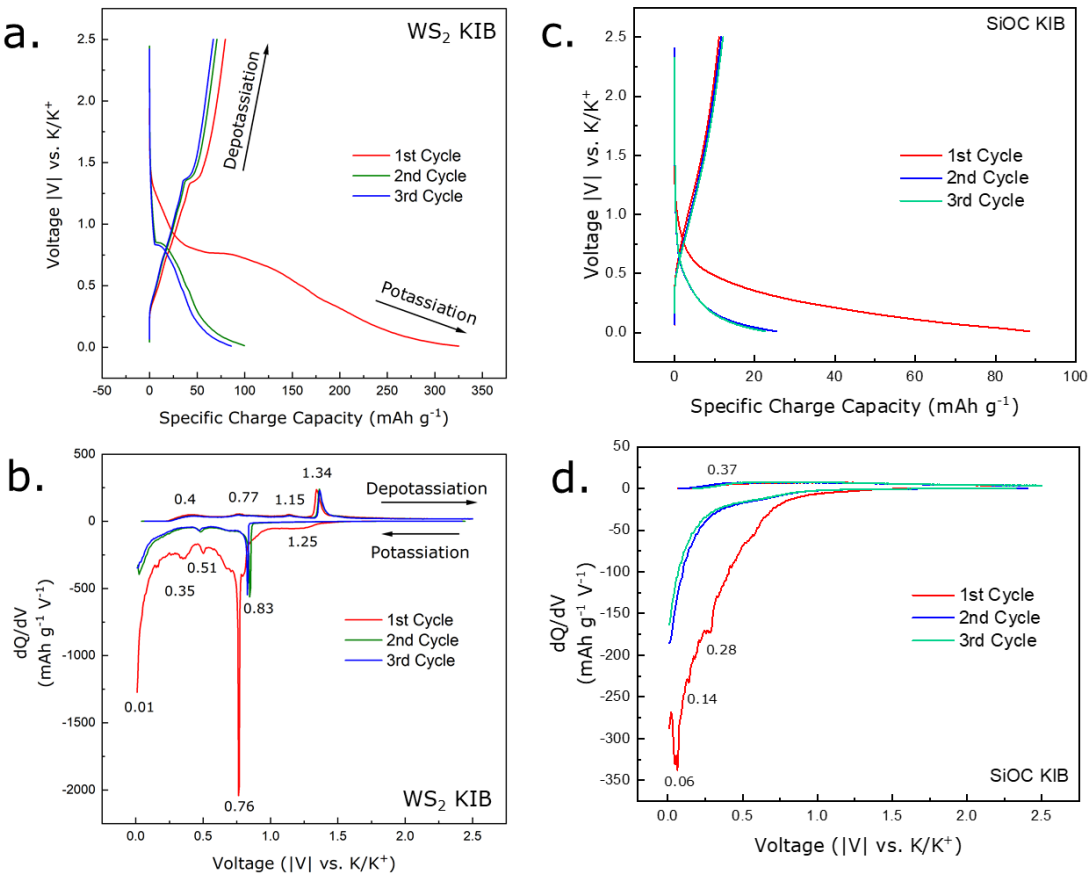


Figure 4.8: *(a) GCD profile of the WS_2 neat electrode when tested in a K^+ ion half-cell setup; (b) differential capacity curve of the WS_2 neat electrode in K^+ ion half-cell setup derived from the GCD profile providing information regarding reactions taking place at different voltages; (c) GCD profile of the SiOC fibermat electrode when tested in a K^+ ion half-cell setup; (d) differential capacity curve of the SiOC fibermat electrode in K+ ion half-cell setup derived from the GCD profile providing information regarding reactions taking place at different voltages.*

Chapter 5

Sodium and Pottasium ion Storage inside WS_2 Nanotube Embedded SiOC Composite Fibers[1]

5.1 Preface

Layered transition metal dichalcogenides (TMDs) such as tungsten disulfide (WS_2) are promising materials for a wide range of applications, including charge storage in batteries and supercapacitors. Nevertheless, TMD-based electrodes suffer from bottlenecks such as capacity fading at high current densities, voltage hysteresis during the conversion reaction, and polysulfide dissolution. To tame such adverse phenomena, we fabricate composite with WS_2 nanotubes. Herein we report on the superior electrochemical performance of ceramic composite fibers comprising WS_2NTs embedded in a chemically robust molecular polymer-derived ceramic matrix of silicon-oxycarbide (SiOC). Such heterogeneous fiber structure was obtained via electrospinning of WS_2NT/preceramic polymer solution followed by pyrolysis at elevated temperatures. The capacity fading in WS_2NT was curbed by the synergistic

[1]Reprinted from Dey, S., Manjunath, K., Zak, A., and Singh, G. (2023). WS_2 Nanotube-Embedded SiOC Fibermat Electrodes for Sodium-Ion Batteries. ACS omega, 8(11), 10126-10138.

effect of the composite WS_2NT/SiOC electrode-high initial capacity of 454 mAh g^{-1}, and capacity retention of the composite electrode is 2-4 times higher compared to neat WS_2NT electrode.

5.2 Introduction

The introduction of heterostructure into the field of energy storage is well appreciated due to various advantageous synergic effects. Unique and composite heterostructures alleviate the bottlenecks of each building block, furnishing the overall property by fine-tuning energy band structures, facilitating ion diffusion kinetics, and perpetuating structural stability[282]. Although two-dimensional (2D) layered materials are efficacious for energy storage applications, new strategies such as wrapping the 2D materials and instigating one-dimensional (1D) nanotubes could bring new initiatives for the scientific community to delve into kind of materials for energy storage devices[179;196]. Similarly, 2D transition metal dichalcogenides (TMDs) possess a sheet-like graphene morphology that consists of covalently bonded chalcogen-metal-chalcogen layers, and individual layers are kept together by weak van der Waals (vdW) forces. This unique structure renders them useful for application in fundamental and technological disciplines such as catalysis, energy storage, sensing, and electronic devices[51]. Among the various 2D TMDs, WS_2 has a lamellar structure with an interlayer spacing of 0.62 nm between (002) lattice planes, thus offering suitable space for reversible insertion of large-sized ions like sodium, for example,[6].

Distinctively tailored nanostructured configuration has recently been proposed with WS_2 materials, and their application has been widely explored for electrochemical energy storage devices. Examples include nanoflakes[321], nanosheets[145], nanohoneycomb[253], nanotubes[280], and nanoflowers[361] of WS_2 to enhance the performances of energy storage devices, specifically LIBs. Unique structures of WS_2 have rarely been studied for cost-effective, abundant alternative alkali metal ion batteries (AMIBs), such as sodium-ion batteries (NIBs)[41;332]. Although their counterparts, namely MoS_2 nanotubes, have been extensively studied for electrochemical energy storage, electrochemical hydrogen storage, and use as field effect tran-

sistors, up-to-date WS_2 nanotubes (WS_2NTs) have only been studied in lithium-ion batteries (LIBs) and NIBs in lesser extent even though they establish stable cycling over a wide voltage range[84;101;197;241;280;334;342]. Theoretical calculations indicated that single-wall WS_2NTs are an exclusive type of semiconductor with an explicit bandgap ranging from 0.1 to 1.9 eV, depending on their diameter[102;109;216;364]. They become both direct (in the case of zigzag) and indirect (in the case of an armchair) bandgap semiconductors controlled by chirality, making them useful for various technological applications such as next-generation electronic and optoelectronic devices and high-quality factor nanoelectromechanical systems[73;111]. However, the electronic properties of multiwall WS_2NT, which are currently produced in large amounts, are not that different from the bulk material, i.e., having an indirect bandgap of 1.9 eV[74]. Such properties make them suitable for the next generation of electrochemical energy storage devices.

In spite of its advantageous properties, WS_2 suffers from low electronic conductivity, restacking nanosheets, dissolution of chalcogen species, and significant volume change during repeated charge and discharge cycles[281]. Therefore, hybrid structures that amalgamate conductive carbon networks with the TMDs in which the TMDs provide numerous active sites and channels for alkali metal-ion intercalation have been widely investigated[101]. Specifically, in rechargeable battery applications, an optimal electrode structure using TMDs should exhibit high electrical conductivity as well as a morphology with sufficient pores and channels to induce the volume change of TMDs, thereby minimizing secondary reactions originating due to the large surface area TMDs[255]. For alleviating the aforementioned deleterious properties, heterostructures of WS_2NT and carbon have been utilized in a recent study where an improvement in the electrochemical properties of WS_2NT material is observed. The investigation led by Zednek and co-workers showed that the composite electrode sustained a capacity of 152 mAh g^{-1} after 60 cycles when tested at a current density of 80 mA g^{-1} in a sodium ion half-cell[325]. However, such a capacity is insufficient to fulfill the need for application in modern technological devices. An alternative hybridization method to minimize the harmful properties of TMD-based 1D structures is to functionalize them with polymer-derived ceramic materials (PDCs). The rationale behind the functionalization of

WS_2NTs with PDCs is that nanotubes possess high mechanical strength, a microstructure with sp2-bonded carbon atoms, and chemical and thermodynamic stability in a degrading environment. While the carbon network in PDCs can provide a conductive pathway and shorten the ion diffusion route[134;260;303].

The primary objectives of this investigation were to exploit the chemical functionalization of 1D WS_2NTs with PDCs and to fabricate a heterogeneous structure with WS_2NTs wrapped with SiOC fibers. This structure was achieved via a single-step electrospinning process where WS_2NTs and a liquid-phase organosilicon precursor were utilized during solution preparation. The as-fabricated non-woven fibermat was then annealed in a high-temperature pyrolysis environment to obtain the final form that was then characterized via microscopic and spectroscopic techniques to confirm the chemical bonding of the materials. After morphological characterization, the fibers were tested as a sodium-ion half-cell at a gradually increasing current rate. The first-cycle charge capacity of the fabricated composite electrode was 454.05 mAh g^{-1} with a columbic efficiency exceeding 50%. The composite electrode showed enhanced capacity retention compared with the neat WS_2NT and SiOC electrodes (2−4 times higher capacity retention in subsequent cycles). This is the first known investigation to report a combination of 1D WS_2NTs within SiOC fibers to create a heterogeneous structure for NIB application.

5.3 Materials, Methods and Characterization

5.3.1 Fibermat Synthesis Process

The solution preparation is the first step in the electrospinning process. Isopropyl alcohol (IPA) purchased from Fisher Chemical (Lenexa, KS, USA), preceramic silicon oligomer, 1, 3, 5, 7-tetramethyl, 1, 3, 5, 7-tetravinyl cyclotetrasiloxane (4-TTCS) purchased from Gelest (Morrisville, PA, USA) and Polyvinylpyrrolidone (PVP) with an average molecular mass of 1,300,000 g mol^{-1} purchased from Sigma Aldrich (Missouri, MA, USA) was mixed with sonicated WS_2NTs (for 10 minutes) until a black homogenous solution was obtained. The

WS_2NTs utilized in this study was prepared by the method described by Pallellappa[52]. A small amount (1 wt. % of 4TTCS) of Dicumyl peroxide purchased from Sigma Aldrich was also mixed with this solution which worked as a cross-linking agent. The weight ratio of the 4TTCS: IPA was kept at 1:9, and the weight ratio of the WS_2NTs: 4TTCS was 1:5. PVP was mixed at a weight ratio of 1:3 with 4TTCS and an 8.5 mL homogeneous black solution was obtained. As the liquid preceramic silicon oligomer, 4TTCS possessed a low molecular weight (¡500 g mol^{-1}), linear organic polymer–PVP was introduced to ensure that the obtained sol-gel after the solution preparation process qualified for electrospinning viscosity demands (viscosity should be ¿ 10 poise). The flowable and viscous solution was loaded into a syringe with a metallic needle and connected to a high-power voltage source. The other end of the voltage source was connected to a roller collector. With a slow feed rate of 5 mL $hour^{-1}$ and the distance between the needle and the roller collector kept at 12 cm, the electrospinning process was initiated with an optimized voltage of 14 kV. As a result, the as-spun fibermat of about 20 × 20 cm^2 was produced, followed by cross-linking the fibermat at 160°C for 6 hours. The final pyrolysis step was carried out in two stages; first, the fibermat was pyrolyzed at 400°C for 1 hour and then at 800°C for 6 hours under an inert Argon gas environment. Thus, the black WS_2NT/SiOC fibermat was obtained. The whole fibermat synthesis process is illustrated in Figure 5.1, showing the electrospinning to cross-linking to the pyrolysis process for obtaining the final fibermat. The predicted structure of SiOC fibers is also illustrated along with the structure of the WS_2NTs on the same schematic.

5.3.2 Characterization Techniques

Carl Zeiss EVO MA10 scanning electron microscope (SEM) was used to obtain SEM micrographs of the fibermats at different stages with 5-30kV impinging voltage. Phillips CM100 transmission electron microscope under an accelerating voltage of 100 kV was used to obtain further insights of fibrous structure. Horiba Jobin Yvon LabRam Aramis with a He-Ne laser of wavelength 633 nm and 17mW power was used to obtain the Raman spectra of the pyrolyzed fibermat. 400 FT-IR spectrometer from PerkinElmer was employed to obtain

the Fourier transform infrared (FTIR) spectra of the samples. PHI Quantera SXM using monochromatic Al-Ka with an energy of 1486.6 eV was utilized to gather information on the chemical bonding states of the fibermat for X-ray photoelectron spectroscopy (XPS). X-ray diffraction (XRD) data were collected using PANalytical Empyrean with 45 kV, 40 mA power setting, and a step size of 0.02°C.

5.3.3 Electrochemical Measurements

The working electrodes for Na-ion half-cells were prepared with the following composition: 70 wt. % of the active material (WS_2NT/SiOC fibermat), 15 wt. % of carbon black as the conducting agent (Alfa Aesar, Haverhill, MA, USA), and 15 wt. % of polyvinylidene fluoride as a binder (Alfa Aesar, Haverhill, MA, USA). A homogeneous slurry was prepared using the materials mentioned above using 1-Methyl-2-pyrrolidinone (Sigma Aldrich, Missouri, MA, USA) as a solvent in a dropwise manner. A 9 µm thick copper substrate was coated with this slurry and dried at 80°C for 18 hours for solvent removal. The obtained film thickness was found to be 125 µm. Circular sections were obtained from this coating to be used as a working electrode for the 2032-type coin cell. The reference and counter electrode, in this case, was sodium metal. 1.0 M $NaClO_4$ (Alfa Aesar) in (1:1 v/v) EC: DMC (anhydrous, 99%, Sigma Aldrich) was used as the electrolyte in the cells, and the two electrodes were separated by glass separator being soaked with electrolytes. All the tested cells were assembled in a high-precision inert (ultra-high purity Argon) atmosphere with O_2 and H_2O contents below 0.1 ppm. The cycled electrodes (after 50 cycles) were de-crimped in the inert atmosphere and washed with DMC solvent to dispose of the separators attached to the electrodes for post-cycling SEM and XPS analysis.

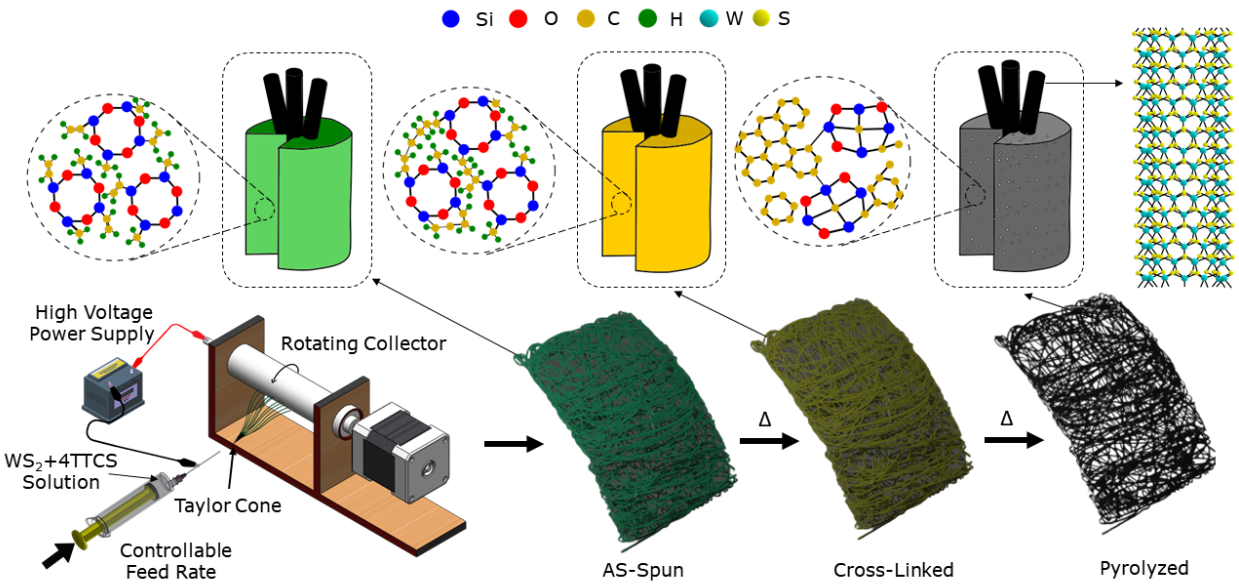


Figure 5.1: *Schematic of the synthesis process of WS_2NT/SiOC fibermat from electrospinning to cross-linking to pyrolysis steps through controlled annealing. The schematic on top shows the predicted structure of 4TTCS, cross-linked 4TTCS, and pyrolyzed SiOC structure, along with the WS_2NT structure embedded within.*

5.4 Results and Discussion

5.4.1 Microscopic Analysis

This study utilized SEM to test the geometry of the as-produced fibermats. Morphology changes of the fibers during as spun, cross-linked, and pyrolyzed states were also investigated using SEM and compared to specimen weight loss during the annealing process. Figure 5.2a shows the fibermat immediately after electrospinning. The inset on the bottom right of the figure shows the digital camera image of the as-spun fibermat. The dark greyish color of the as-spun fibermat indicates primarily the existence of the WS_2NTs in the fibermat structure. Although occasional clumping of the fibers was observed in the fibermat (Figure 5.2a), most of the fibers were uniform in shape, as shown in the magnified view of the fibermat in Figure 5.2b, with only minimal irregularity. No beads were observed in the fibers from the as spun fibermats. Figure 5.2(c-d) shows the SEM micrographs of the cross-linked fibermat.

The digital camera image of the fibermat in the inset of Figure 5.2d denoted a slight change in the color of the fibermat, indicating the vinyl polymerization state with a mass loss of 40% and fibermat (linear) shrinkage of approximately 15%. The magnified SEM figure of the cross-linked fibermat (Figure 5.2c) also shows minimal fiber irregularity during the cross-linking stage. In the final pyrolyzed stage, shown in Figure 5.2e, occasional clumps of fibers were observed. The clumps of fibers are readily visible from the magnified Figure 5.2f. The individual fibers in the pyrolyzed fibermat were regular in shape without beads (Figure 5.2g). The visual appearance of this pyrolyzed fibermat was fully black, as shown in the inset of Figure 5.2e. The weight loss of the final pyrolyzed WS_2NT/SiOC fibermat from the cross-linking stage was approximately 61%, with a linear shrinkage of 50%. The fiber diameter at as-spun, cross-linked, and post-pyrolysis stages was measured by taking an average of 25 measurements-denoted in Figure 5.8(a-c), respectively. A decrease in the average fiber diameter as a function of pyrolysis temperature was observed from the measurements (600-800 nm for as-spun fibers, 500-700 nm for cross-linked fibers, and 400-500 nm for pyrolyzed fibers). SEM micrographs of the pyrolyzed SiOC fibers are included in Figure 5.9 from which the difference between the SiOC fibers containing the WS_2NTs and the neat SiOC fibers can be well understood. The SiOC fibers were electrospun under the same electrospinning condition, nevertheless contained irregularities in the fiber geometry with beads (shown in magnified Figure 5.9b). The gradual decrease in fiber diameter and weight retention of the total fibermat observed during various stages of decomposition is further investigated in spectroscopic methods. Fiber diameters in the final stage of this study correlated well with similar previous studies[165;245;328]. Figure 5.2h provides a qualitative chemical analysis of the fibermats using the energy dispersive spectroscopy (EDS) technique. The characteristic W-Lα at (8.6 keV) and S-Kα (at 2.52 keV) spectral lines were observed in the fibermat, confirming the presence of the WS_2 nanotube material. In addition, spectral lines for Si-Kα (at 1.97 keV), O-Kα (at 0.73 keV), and C-Kα (at 0.48 keV) were also observed, denoting the presence of the set of materials (W, S, Si, O, C) that was as per expectation. Notably, the entire spectra shifted by 0.2 keV due to calibration. Furthermore, the EDS technique resulted in an elemental distribution map of the fibermat, revealing an even distribution of

the desired elements and the efficiency of the electrospinning technique as a robust fabrication method.

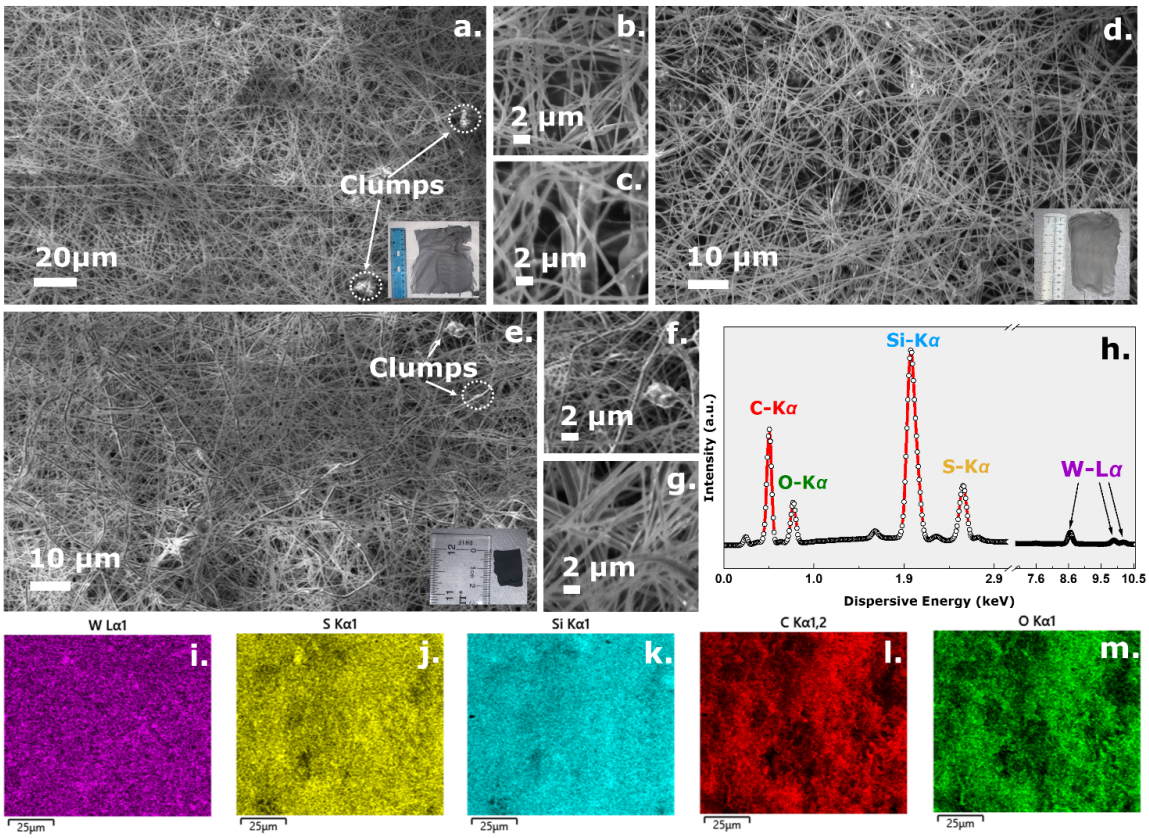


Figure 5.2: *SEM micrograph of (a) as-spun WS_2NT/SiOC fibermat confirming the fibrous structure of the fibermat; the inset showing as-spun fibermat digital camera image; (b) magnified portion of figure (a); (c) magnified portion of the cross-linked fibermat from figure (d); (d) cross-linked WS_2NT/SiOC fibermat confirming the fibrous structure of the fibermat; the inset indicating digital camera image of cross-linked fibermat; (e), (f) magnified portions of pyrolyzed fibermat showing the agglomeration of some fibers; (g) pyrolyzed WS_2NT/SiOC fibermat confirming the fibrous structure of the fibermat; the inset showing digital camera image of the pyrolyzed fibermat; (h) EDS Spectra of the WS_2NT/SiOC fibermat confirming the presence of the materials within; and the corresponding EDS color map for: (i) W-Lα-1 ;(j) S-Kα-1 ;(k) Si-Kα-1 ;(l) C-Kα-1,2 ;(m) O-Kα-1.*

The SEM micrograph in Figure 5.3a shows a dense web of WS_2NTs. Figure 5.3b shows a zoomed-in view (10 nm scale) of a single multilayered nanotube with the core and the multiwall structure highlighted. The average length of the nanotubes was 1.2−2.8 µm, as determined from the resulting distribution plot included on the inset of Figure 5.3c. Notably,

the reduction of nanotube length was initially reported to be 2-20 µm[52;287]- likely due to the solution preparation process for electrospinning. A selected area electron diffraction (SAED) pattern obtained from one of the nanotubes of Figure 5.3c (marked area in the figure) denotes the three-dimensional (3D) curvature of the crystals due to the polycrystalline-like electron diffraction pattern. The six-fold symmetrical spot pattern reflection indicates the in-plane hexagonal arrangement of atoms when WS_2 layers are perpendicular to the electron beam (on the top of the tube roll). At the same time, the 002 plane denotes the vdW gap between the layers when they are parallel to the electron beam. The presence of both orientations was due to the closed nanotube structure yielding parallel and perpendicular to electron beam regions of the vdW planes. The red arrow in the image represents the axis of the nanotube, and multiple spots in the SAED pattern signify that the multiwall tubular structure was comprised of multi-chiral walls that co-exist in the experimental condition. These values and conditions matched well with previous WS_2NTs studies[259;275;328].

Figure 5.3f shows the TEM image of the WS_2NT/SiOC fibermat. The figure also confirms the state when the WS_2NTs can be confined inside the fibers. The enlarged view of this image (Figure 5.3g) reveals that some neat nanotubes and stacked nanotubes were confined inside the SiOC fibers, resulting in a complex structure. The enlarged view of the images (Figures 5-3g-i) also revealed the presence of some pores in the fibers. Heterostructures have been identified as a feasible solution to overcome large volume change and subsequent poor electrical connection in TMD materials. In the heterogeneous fiber structure, the Li+ ions can move freely along the nanotube material, and the shell of the SiOC fiber can act as a reservoir to accommodate the ions via intercalation. The SiOC fiber may also buffer the volume change induced by the intercalated WS_2NTs, thereby preventing structural disintegration and maintaining a stable capacity during high-rate cycling conditions. Inevitable pores in the fibers (Figures 5-3g and 5-2i) can be useful for maintaining the anodic performance caused by enhanced of movement of the ions 248. The SAED pattern of WS_2 nanotubes with fibers (Figure 5.3e) contained the same (hexagonal) spots as the neat nanotubes and the amorphous rings, proving the amorphous shape of carbons characteristic of SiOC-phase-controlling structures.

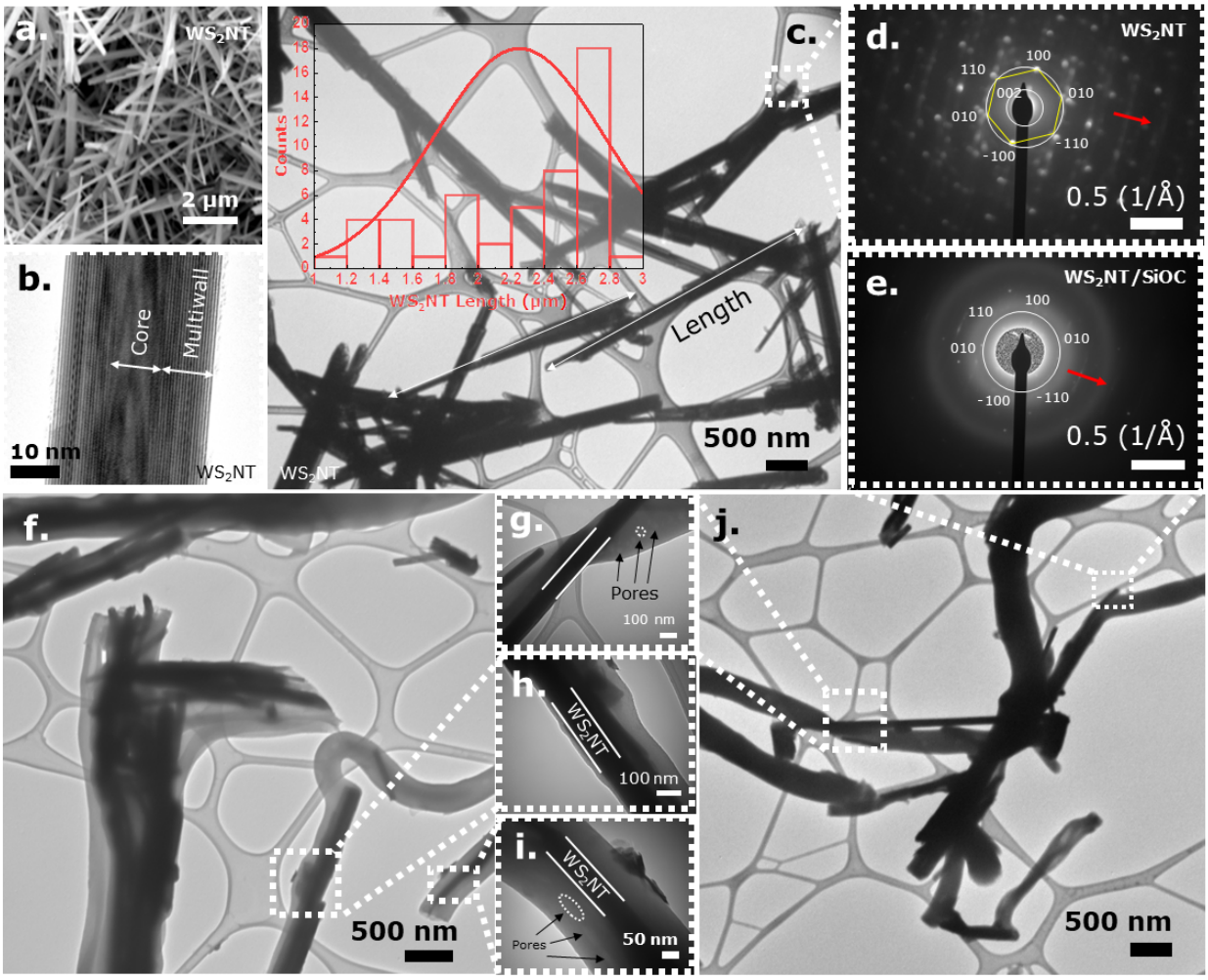


Figure 5.3: *(a) SEM micrograph of dense web of WS_2NTs; TEM micrograph of (b) single WS_2NT elucidating the nanotube inner and outer wall; (c) WS_2NTs elucidating the length of individual nanotubes, the insets show the distribution plot for identifying the length of individual WS_2NTs; SAED pattern of the (d) WS_2NTs showing the tube axis and crystalline nature of the nanotubes with crystal planes denoted; (e) WS_2NT/SiOC fibers where the simi-lar hexagonal pattern of WS_2NTs was spotted along with amorphous ring in the back; (f) TEM micrograph of the WS_2NT/SiOC fibers where the confinement of nanotubes inside the fibers could be identified; (g), (h), (i) magnified view of individual WS_2NT/SiOC fibers where the alignment of the nanotubes inside the fibers could be well specified along with porous feature of the fibers; (j) TEM micrograph of the WS_2NT/SiOC fibers from a magnified view (Figure 5.3g.) and SAED pattern (Figure 5.3e.) was obtained.*

5.4.2 Spectroscopic Analysis

This study also used Raman spectroscopy to decipher the fibermat microstructure and designate the free-carbon phase from the SiOC fibers and the WS_2NT materials. Figure 5.4a

shows the Raman spectra of the neat WS_2NT material. The two intense peaks at 351 cm^{-1} and 416 cm^{-1} (Figure 5.4a) were assigned to in-plane mode $E^1{}_{2g}$ and out-of-plane mode A_{1g}, respectively. The intensity ratio of the $E^1{}_{2g}$ peak to the A_{1g} peak for the WS_2NT bulk material was approximately 0.91, signifying the multi-walled feature of the nanotubes (more than three layers). Additionally, the frequency difference between the two modes was approximately 65 cm^{-1}, revealing multilayer nanotubes. These values correspond well with previous studies[283]. The presence of WS_2 nanotubes in the WS_2/SiOC fibermat was verified by Raman spectra of 300−480 cm^{-1} with prominent $E^1{}_{2g}$ (350.161 cm^{-1}) and A_{1g} (416.58 cm^{-1}) peaks, shown in Figure 5.4c. The frequency difference between the two phonon modes was 66.43 cm^{-1}, which is close to the bulk material. Again, the intensity ratio of these two modes of WS_2NT in the fibermat sample was approximately 0.91, which perfectly matched the bulk material. These two values signify that the use of 1D material in the SiOC fibermat (using this study's technique) advantageously rendered the active material in its raw state. Again, the longitudinal acoustic phonon mode 2LA(M) mode was close to the shoulder of the $E^1{}_{2g}$ mode in the nanotube material[179;222;257]. As shown in Figure 5.4b, the free-carbon phase of the WS_2NT/SiOC fibermat was revealed by the peak-fitted Raman spectra, with prominent D and G peaks at 1331.72 cm^{-1} and 1590.92 cm^{-1}, respectively. Although the D peak was due to a disorder induced in the sample, the G band (E_{2g} symmetry) was responsible for the in-plane stretching of the sp2 carbon bonds.[112;270]. Deconvoluted Raman spectra revealed T and D" peaks in the shoulder of D and G bands at 1197.91 cm^{-1} and 1481.68 cm^{-1}, respectively, in which the T band signified the sp2-sp3 carbon-carbon double and triple bonds and the D" band signified the amorphous nature of the carbon in the sample as verified in TEM diffraction pattern studies[212]. The intensity ratio of the D and G bands of the fibermat was 1.1, revealing the high disorder of carbon induced in the sample.

This study also utilized FTIR to investigate the bonding complexity and interaction of the various molecules within the fiber geometry and the polymeric structure of the as-spun, cross-linked, and pyrolyzed fibermats. The bottom of Figure 5.4d shows the FTIR spectra of the as-spun fibermat. In general, the peaks at 1265−1285 cm^{-1} caused the -C-N bond from the PVP molecule, and the peaks in the 1650−1660 cm^{-1} region were responsible for the

carbonyl group in the molecule. For the as-spun fibermat sample, strong peaks in the areas noted were visible, indicating the presence of the PVP molecule in the as-spun fibermat[15].

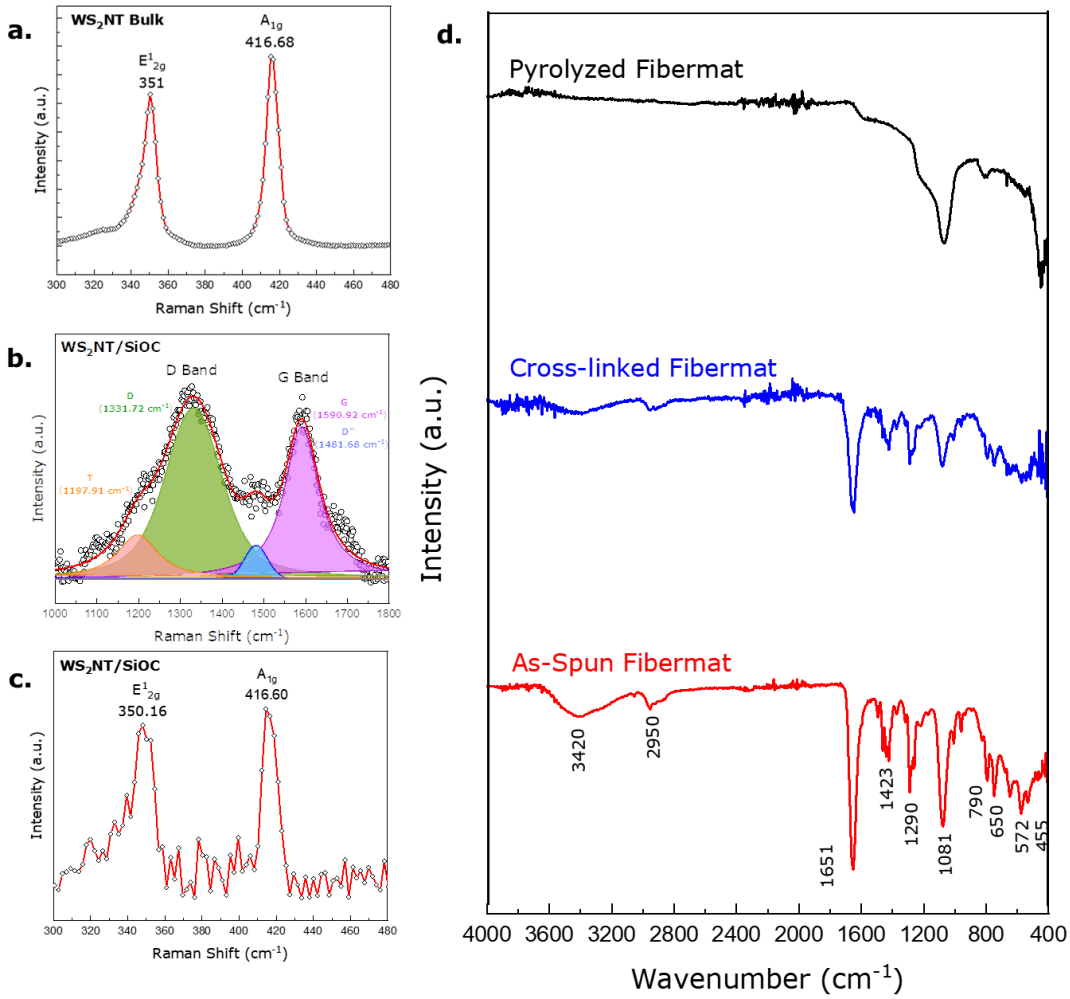


Figure 5.4: *Raman Spectra of a) Neat WS_2NT powder showing the typical position of the peaks obtained from the neat material; b) WS_2NT/SiOC fibermat in the higher wavenumber region confirming the free carbon species (integrated spectra using a gaussian function); c) WS_2NT/SiOC fibermat in the lower wavenumber region confirming the presence of the WS_2 nanotube material within the fibermat showing the same peaks as the neat material with subtle differences; d) FTIR spectra of As-spun, cross-linked, and pyrolyzed fibermats. The spectra from top to bottom illustrate data obtained from individual pyrolyzed, cross-linked, and as-spun fibermats. The spectra analysis signifies the presence of the precursor polymer, TMD material, and PVP material in the fabricated fibermat during the cross-linking stage and after the pyrolysis step.*

The FTIR spectra also verified the facile integration of WS_2NTs with the carbon-based groups. For example, for the as-spun fibermat denoted by Figure 5.4d, the peaks at 650 cm^{-1}

and 1080 cm^{-1} were responsible for the W-S and S-S bonds, respectively[125]. Multiple peaks from 650 cm^{-1} to 800 cm^{-1} highlighted the samples' C-S bonds. For example, the peak at 790 cm^{-1} was characteristic of C-S-S-C, H-C-S, and C-S bonds[269;272;374]. These bonds act as proof of good adhesion between the WS_2NT and polymeric matrix, which enhances mechanical properties[341] and may be very important for providing electrical contact between the WS_2NT and fibers, accelerating the charge transfer. The strong absorption from 1000 cm^{-1} to 1070 cm^{-1} indicates Si-O bonds. The presence of -CH_3 deformation and asymmetric stretching in Si-CH_3 bonds occurred in the $1261-2961$ cm^{-1} region, respectively, and the absorption peak at 800 cm^{-1} indicates the Si-C stretching vibration[171]. All the analysis mentioned above confirms the presence of preceramic polymer in the as-spun fiber morphology, which is in accordance with previous investigations[43;215] For the cross-linked fibermats (the curve in the middle of Figure 5.4d), the peak intensity decreased for both fibermat samples, indicating a polymerization reaction. Finally, Figure 5.4d shows the spectra of the pyrolyzed fibermats (top of the figure) with Si-O and Si-C bonds and a strong peak at 450 cm^{-1} that indicates elemental S-S bonds, ensuring the presence of S from the WS_2 molecule, even after pyrolysis.

This study also utilized XPS to analyze the surface characteristics, determine the material's elements, and the chemical and electronic state of the pyrolyzed sample. Figure 5.5a shows the XPS survey scan of the WS_2NT/SiOC fibermat, revealing the presence of W, S, Si, O, and C in the pyrolyzed fibermats with no material contamination within the instrument sensitivity. Supplementary Table 4-1 presents the atomic percentage of the elements in the pyrolyzed fibermat. The wt.% amount of W (3.1%) and S (3.4%) in the WS_2NT/SiOC fibermat showed that the WS_2 nanotube could sustain the high annealing temperature when pyrolyzed with preceramic polymer material. Moreover, the high amount of carbon in the fibermat also confirmed the free-carbon phase after the pyrolysis cycle, which was previously proven by the Raman spectroscopic analysis. Figure 5.5b shows high-resolution W4f and S2p spectra of the WS_2NT/SiOC fibermat. The Tougard function was used to subtract the background, and the spectra was fitted using the Voigt function. Spin-orbit splitting (s.o.s.) produced two core level peaks for each W4f and S2p, namely 4f7/2, 4f5/2, 2p3/2, and 2p1/2, respectively. For example, the binding energy of the W4f spectra (Figure 5.5b on the left)

showed that the W^{4+} state represented the 4f7/2 and 4f5/2 bands in 32.3 eV and 34.3 eV, respectively. The W spectrum also showed two peaks at binding energies of 35.8 eV and 37.9 eV, signifying the W^{6+} 4f state and indicating a slight amount of WO_x species in the WS_2NTs inside the SiOC fibers. Notably, this WO_x species is highly conductive and can increase the overall conductivity of the fibermat with a free-carbon state. Furthermore, two well-defined peaks in the S2p high-resolution spectra (Figure 5.5b on the left) were attributed to s.o.s. at 162.6 eV and 163.7 eV, representing 2p3/2 and 2p1/2 core levels, respectively, corresponding to S_{2-} orbitals. One more peak was observed in the S2p high-resolution spectra in the binding energy of 169.5 eV, indicating sulfur bonded with carbon from the preceramic polymer. All these peaks agree well with previous WS_2NTs studies[73;92;206;279;365;366]. High-resolution spectra of the Si2p, O1s, and C1s were also obtained for the pyrolyzed fibermat, as shown in Figures 5-5c−e, respectively. Deconvoluted Si2p spectra (Figure 5.5c) showed Si-O and Si-C bonds in both fibermats, and the C1s spectra in Figure 5e reveal the C-Si, C-C, and C=O bonds. The O1s spectra (Figure 5.5d) of both fibermats showed the Si-O, Si=O, and C=O bond states, with dominant SiO_2. The results showed that a good amount of carbon in the sample also bonded with Si, and individual SiO_2 regions were observable, thereby validating the SiOC microstructure of the pyrolyzed fibermat even after pyrolysis with WS_2 nanotubes.

XRD was utilized in this investigation for phase identification of the neat WS_2NTs and WS_2NTs within the WS_2NT/SiOC fibermat. From XRD diffractograms depicted by Figure 5.5f, it was apparent that the reflections from WS_2NT and WS_2NT/SiOC were identical. Both XRD patterns are identical because the SiOC matrix is X-ray amorphous and shows no reflections. The most prominent peak for both XRD patterns originated from the (002) crystalline plane. For the neat nanotube, the peak is located at 14.28°C, which indicates a shift from the bulk WS_2 (14.32°C). This shift may have originated due to the built-in strain in the nanotube lattice − further indicating that the interlayer spacing increased by a small amount[399]. A group of peaks was identified around (002) plane for the WS_2NT/SiOC fibermat sample, which is attributed to $W_{18}O_{49}$ phase - the intermediate precursor residuals, created (from WO_3 -the initial precursor) during the reduction sulfurization reaction for nanotubes' synthesis in their core[149]. Thereby, the peaks at 23.23°C, 24.38°C, and 27.15°C can

be attributed to (002), (200), and (022) planes of crystalline monoclinic WO_x[367]. Among the peaks mentioned above, only the (200) WO_x peak was identified for the neat WS_2NT sample, which could be introduced during the sample preparation. For the WS_2NT/SiOC fibermat, an increase in the intensity of the peaks mentioned above was also observed. The peaks of (100), (101), and (103) planes seem to be broadened and this feature corresponds to three-dimensional (3D) atomic positions within the WS_2NTs-originating from the network rotation along the tube axis, much alike the carbon nanotubes. Peaks occurring at higher 2θ angles, such as (006), (110), (112), (114), and (116) present broad features and are indicative of the elongated periodic layered structure of the WS_2NTs. Again, the broadening of the peaks can also be correlated with the submicron size of the WS_2NTs. In summary, the identical spectra of the WS_2NTs and WS_2NT/SiOC point to the fact that SiOC functionalization of WS_2NTs does not change the crystallinity of the WS_2NTs and no new crystalline phases are generated during the pyrolysis process. The above-mentioned analysis corresponds well with the previous literature regarding XRD analysis of the WS_2NTs[22;132;218].

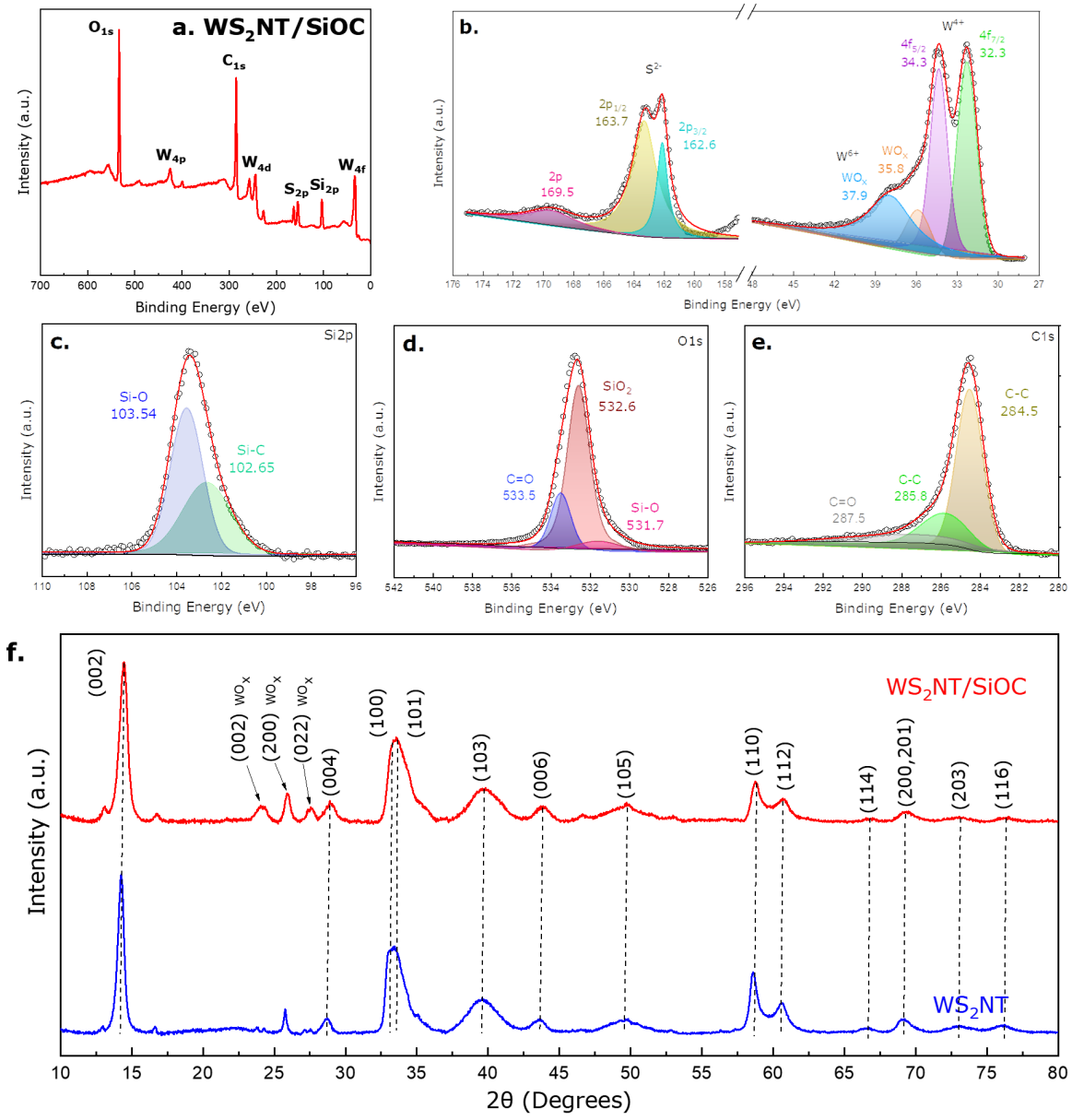


Figure 5.5: *a) XPS survey scan of WS_2NT/SiOC fibermats representing the presence of individual elements after pyrolysis of the fibermat at high temperature; b) High-resolution W4f and S2p XPS spectra of the WS_2NT/SiOC fibermat recording the bonding states due to s.o.s. of W and S, W being bonded with small amounts of O elevating the conductivity of the fibermat; High-resolution; High-resolution: c) Si2p XPS spectra; d) O1s XPS spectra; e) C1s XPS spectra obtained from the WS_2NT/SiOC fibermat confirming the bonding states of the Si, C and, O in SiOC matrix; f) Comparative XRD analysis of WS_2NT (bottom pattern) and WS_2NT/SiOC (top pattern) identifying the crystalline phases of the materials within.*

5.4.3 Electrochemical Analysis

Galvanostatic charge-discharge curves (GCD) and differential capacity curves derived from the GCD curves offered insight regarding reactions at various stages during charging and discharging cycles. Figures 5-6a illustrate the GCD profile and Figure 5.6b illustrates the associated differential capacity curves of the WS_2NT/SiOC composite electrode. The cycling of neat WS_2NT, neat SiOC and, WS_2NT/SiOC composite electrodes at different current densities is represented by Figure 5.5c. Figure S3a depicts the GCD profile of the WS_2NT material from which the differential capacity curve was obtained, and Figure 5.10b shows when cycled in a sodium-ion half-cell. The first sodiation step revealed only one weak peak at approximately 1.2 V due to the reversible sodium intercalation into the layers of WS_2NTs. This phenomenon can be described by the reaction 5-1.

Four more peaks were observed in the first cycle sodiation stage at 0.28V, 0.34V, 0.52V, and 0.64V due to the irreversible conversion reaction at medium (0.52V) voltages and the formation of the solid electrolyte interface (SEI) layer, as described by the following reaction 5-2.

$$xNa^+ + WS_2 + xe^- \longrightarrow Na_xWS_2 \tag{5.1}$$

$$4Na^+ + WS_2 + 4e^- \longrightarrow W + 2Na_2S \tag{5.2}$$

The following sodiation steps revealed new peaks at 1.0V, 1.36V, and 2.02V, which decreased in intensity in subsequent cycles. The peaks at 0.5V and 1.0V indicated the occurrence of a reaction in the opposite direction as described by equation 5-2, while the other two peaks at 1.36V and 2.02 V were due to the multi-step extraction of sodium ions from the NaxWS_2 matrix, as proven by previous studies of WS_2 nanowires and nanoflowers[41;361]. This electrode in this investigation was also tested in a rate capability test at an increasing current density that created a harsh cycling condition for the sodium-ion half-cell. Specifically, the increasing current density was 100, 200, 400, 600, and 800 mA g^{-1}, and the cells underwent five cycles at those current densities and then returned to initial conditions in the subsequent cycles. The first-cycle charge capacity of the electrode was capacity was recorded

when the cell was returned to the initial cycling condition after high current density values, indicating low performance of the electrode at high current rates. The capacity retention of the WS_2NT electrode at the 26th, 31st, 36th, and 41st cycles were 55.95%, 23.36%, 21.42%, and 26.6%, respectively. The low-capacity retention of the electrode was due to irreversible reactions at the electrode surface (intensification of excessive conversion reaction). This behavior correlated to the coulombic efficiency of the WS_2NT electrode not being constantly near 100% through the harsh cycling conditions, potentially indicating a structural change of the material.

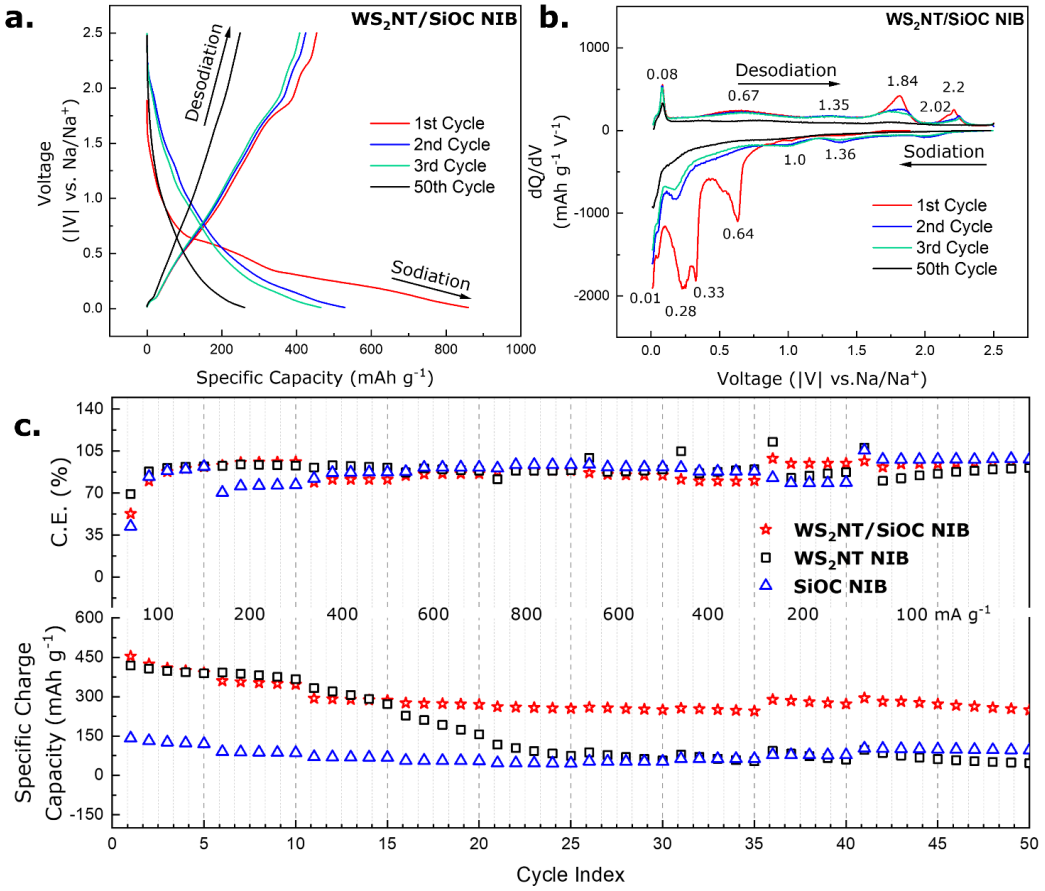


Figure 5.6: *a) GCD profile of the WS_2NT/SiOC composite electrode when tested in a Na-ion half-cell setup; b) differential capacity curve of the WS_2NT/SiOC composite electrode in Na-ion half-cell setup derived from the GCD profile providing information regarding reactions taking place at different voltages; c) Rate capability test performed for the WS_2NT/SiOC electrode when tested in a Na-ion half-cell setup at increasing current densities and bringing back to initial conditions after 5 cycles after each step.*

Although silicon-based materials are nearly inactive in NIBs, recent investigations have found that free-carbon domains in SiOC can efficiently store Na^+ ions. Therefore, the capacity contribution of the SiOC fiber electrode potentially originates from the free-carbon domains and nanovoids. Therefore, this study investigated neat SiOC fibermats in GCD experiments at the same conditions described in supplementary Figure 5.11a. The differential capacity curve obtained from the GCD curves (Supplementary Figure 5.11b) showed a pair of peaks during the sodiation/desodiation process at 0.01 and 0.09 V due to the intercalation of sodium ions in the free-carbon sites. Conversely, the peak at 0.57 V was due to the trapping of Na^+ ions into the highly active defective graphene sites, which is irreversible in the following cycles and the formation of the SEI layer, and the reversible peak at 0.67V in the desodiation step was due to sodium intercalation into the micropores, similar to results of previous studies regarding the use of SiOC-based materials in NIB setup[144;209]. The first-cycle charge capacity of the SiOC electrode was 141.59 mA g^{-1} with a coulombic efficiency of 42.33%. The capacity retention of the SiOC fibermat electrode was higher than the WS_2NT electrode, with capacity retention of 96.95%, 92.98%, 91.30%, and 85.80% in the 26th, 31st, 36th, and 41st cycles, respectively. The coulombic efficiency of the SiOC fibermat electrode was also more stable than the WS_2NT electrode, with a slight deviation of near 100% efficiency in high current densities.

The composite WS_2NT/SiOC electrode was tested under the same conditions in a sodium-ion half-cell setup. Figure 5.6a is the GCD profile, while Figure 5.6b is the corresponding differential capacity curve. As observed in Figure 5.6b, in the first sodiation/desodiation step, a pair of peaks at 0.01V and 0.08 V are ascribed to sodium insertion in the disordered carbon phase and micropores present in the SiOC phase (note that these peaks were prominent in the neat SiOC electrode also) and to a lesser extent the carbon black conducting agent present in the electrode. In addition, similar to the neat WS_2NT electrode, the electrolyte decomposition and formation of the SEI layer were attributed to the peaks at 0.28V, 0.33V, and 0.64V on the first sodiation step. A small peak at 0.52V also was observed on the shoulder of the 0.64V peak due to the conversion reaction of the WS_2NT material, indicated by equation 2. The first desodiation step resulted in peaks at 1.35V, 1.84V, and 2.2V due

to multi-step deintercalation in the interlayer region and into the hollow tube core of the WS_2NT material[358]. One broad peak at 0.67V was attributed to the sodium ion's intercalation into the SiOC matrix's micropores. These peaks were reversible and decreased gradually in intensity during subsequent cycles. The first-cycle charge capacity of the composite electrode occurred at 454.05 mAh g^{-1} with a coulombic efficiency of 52.85%. Under the same rate capability conditions at the 26th, 31st, 36th, and 41st cycles, the capacity retention of the electrode was 96.1%, 94% 83.39%, and 75.9%, respectively, which was higher than the electrodes assembled with the neat WS_2NT material.

The disassembled electrodes were further morphologically analyzed using SEM. The recovered WS_2NT/SiOC electrodes exhibit excellent retention of the fibrous network. No visible microcracks in the electrodes were found − proving evidence of the structural integrity and minimal stress development within the cycled electrodes even after cycling at harsh conditions/incrementally increasing current densities (Figures 5-7 a, b). The digital camera image of the recovered electrode (shown on the inset of Figure 5.7a) showed no visible color change or physical imperfections of the spent electrode. Some white fibers from the separators of the cycled cell were visible in the digital camera image and the SEM micrographs. Figure 5.7c shows an enlarged view of the SEM micrographs illustrating individual fibers from which a distribution curve extrapolated fiber diameter. The obtained average fiber diameter of the cycled electrode was between 600-700 nm − suggesting approximately a 40% size increase compared with the uncycled pyrolyzed fibermat (shown in Supplementary Figure 5.11). The 40% increase in fiber diameter might have minimal effect on the volume change of the whole electrode due to inter-fiber void spaces. Figure 7d shows the XPS survey scan of the recovered electrode. Along with the base materials (W, S, Si, O, and C), Cl and Na (high percentage, 20.47 wt.%) were present, indicating the formation of the solid electrolyte interface (SEI) layer. Table 5-2 in the supplementary section shows the elemental composition of the spent electrode obtained from the XPS spectra. The preservation in the wt.% ratio of W and S element (W = 4.17 wt.%, S= 4.69 wt%) compared to the WS_2/SiOC pyrolyzed fibermat suggests the safeguarding effect of SiOC fibers towards the WS_2NTs. Figures 5-7e and 5-7f show the high-resolution XPS spectra of the W4f and S2p

plots, respectively. W4f spectra were deconvoluted into four individual peaks − WCl_6 (36.9 eV), $Na_{0.1}WO_3$ (35.6 eV), S/W (31.1 eV), and W-S (33.2 eV)[55;159;161;277], stipulating the undergoing reaction and formation of SEI layer. On the other hand, only S-Na (160.6 eV) bond was present in the S2p spectra − most likely arising from a conversion-type reaction with Na ions[183].

The synergistic effect of the composite electrode was evident from the differential capacity curve in which the peaks associated with SEI layer formation and conversion reaction of the WS_2NT electrode decreased in intensity for the composite electrode. Since all the cells were synthesized, assembled, and tested under identical conditions, the assumption was that SiOC prevented such conversion reactions and provided additional storage sites for the material. In addition, because SiOC is amorphous and does not chemically bond with WS_2NTs, as shown via spectroscopic and microscopic analysis, the structure of the neat material (WS_2NTs) did not change. The SiOC material also potentially prevented the agglomeration of TMDs and the dissolution of polysulfides into the electrolyte, as evidenced by the increased capacity retention at high current densities. When the current density returned to the initial values of 600 mA g^{-1}, 400 mA g^{-1}, 200 mA g^{-1}, and 100 mA g^{-1}, the recovered. capacity was 259.38 mAh g^{-1}, 256.04 mAh g^{-1}, 289.07 mAh g^{-1}, and 294.94 mAh g^{-1}, respectively. The capacity values of the composite WS_2NT/SiOC electrode in the cycles mentioned above were 2.96, 4.02, 3.68, and 2.85 times higher, respectively than the capacities of the half-cell assembled with the WS_2NT electrode in the same cycles. The superior performance of the WS_2NT/SiOC electrode (due to the SiOC matrix, which induces stable cycling of Na^+ ions) compared to similar TMD-based composite electrodes is illustrated in Table 5-3. Therefore, the composite electrode's symbiotic behavior reinforces the claim that the SiOC functionalization of the active sulfur-based TMDs in appropriate proportions may prevent polysulfide dissolution in an electrochemical cell.

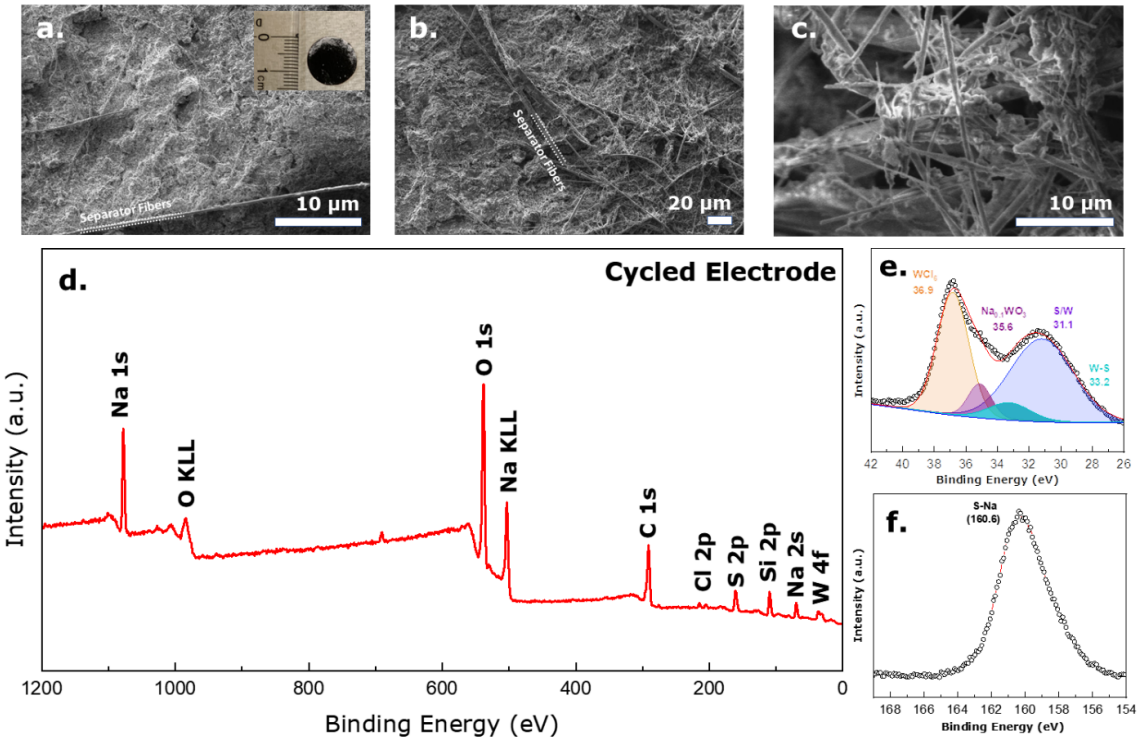


Figure 5.7: *SEM micrograph of a) recovered electrode after cycling showing structural integrity, inset showing the digital camera image; b) cycled electrode (enlarged view); c) cycled electrode showing individual fiber geometry still intact; d) XPS survey scan of the cycled electrode showing individual elements present within; High-resolution XPS spectra of e) W 4f and f) S 2p showing the chemical bonding of W and S elements.*

5.5 Conclusion

This is the first work to study WS_2NTs confined within SiOC fibers to form a heterogeneous structure that provides stable cycling performance in high current densities in an NIB half-cell configuration. The heterostructure was achieved via single-step electrospinning followed by pyrolysis at elevated temperatures. Microscopic (SEM and TEM) and spectroscopic techniques (Raman, FTIR, and XPS) were utilized to identify materials within the heterostructure, the materials' chemical bonding states, the evolution of the fibrous structure during various annealing stages, and the existence of the free-carbon domain within the SiOC fibers. The crystallinity of the WS_2NTs was well preserved within the heterostructure

(proved by XRD and SAED analysis), confirming the facile chemical functionalization of the nanotubes. When tested as a sodium-ion half-cell, the composite electrode increased stability at high current densities and robust capacity retention (2−4 times higher than the capacity of the neat WS_2NTs) at subsequent cycles. The improved electrochemical performance of the heterostructure with the post-cycle analysis of the electrode solidifies the authors' hypothesis that the SiOC fibers might protect the WS_2NTs from negative occurrences to an extent, such as capacity degradation, volume expansion, irreversible conversion reaction, and polysulfide dissolution, and contribute to the fabrication of better-performing electrodes for thriving room temperature NIBs. The superior performance of WS_2NT/SiOC electrode vs. similar TMD-based composite electrodes reported in the literature was attributed to the SiOC matrix which induces stable cycling of Na^+ ions.

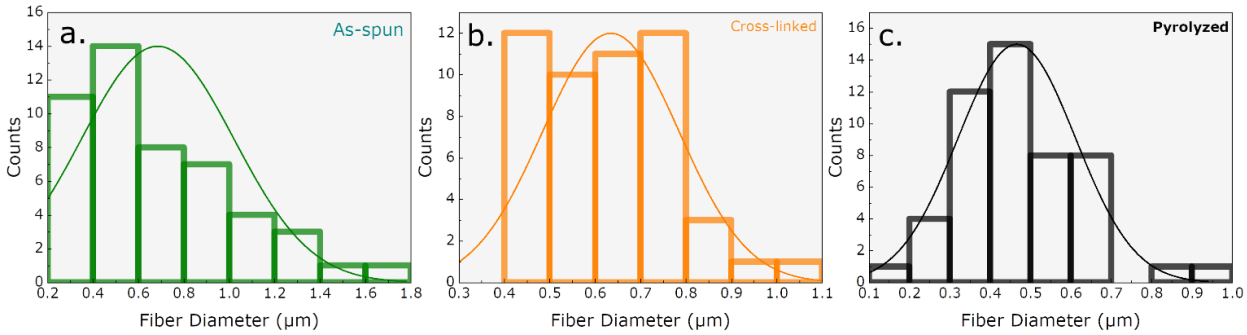


Figure 5.8: *Fiber diameter distribution plot of (a) As-spun; (b) Cross-linked; and (c) Pyrolyzed fibermats.*

Table 5.1: *Elemental Composition of the fibermats by XPS*

Pyrolyzed	Elements (Atomic wt.%)				
Fibermats	W4f	S2p	Si2p	C1s	O1s
WS_2NT/SiOC	3.10	3.43	12.86	53.65	26.35

Table 5.2: *Elemental Composition of the spent electrode by XPS*

Pyrolyzed	Elements (Atomic wt.%)						
Fibermats	W4f	S2p	Si2p	C1s	O1s	Na2s	Na1s
WS_2NT/SiOC	4.17	4.69	4.50	18.48	43.66	3.31	20.47

Table 5.3: *Summary and comparison of electrochemical performance for Na^+ storage of other nanomaterial-based structures with this work.*

Anode Materials	Rate Capability	Reference
WS_2/SiOC	454 mAh g^{-1} @100 mA g^{-1}	This work
001 oriented 2D WS_2	195.7 mAh g^{-1} @1000 mA g^{-1}	250
WS_2/3D rGO microspheres	334 mAh g^{-1} @200 mA g^{-1}	1
Porous WS_2/C nanocomposite	219 mAh g^{-1} @1000 mA g^{-1}	100
D-TiS_2	100 mAh g^{-1} @100 mA g^{-1}	293
WS_2/NC	320 mAh g^{-1} @200 mA g^{-1}	331
WS_2/3DCD	392.1 mAh g^{-1} @200 mA g^{-1}	249
$W_0 \cdot 9\,Mo_0 \cdot 1\,S_2$	262 mAh g^{-1} @1000 mA g^{-1}	372
MXene@Co_9S_8/$CoMO_2S_4$	325 mAh g^{-1} @100 mA g^{-1}	136
	309 mAh g^{-1} @200 mA g^{-1}	
	284 mAh g^{-1} @100 mA g^{-1}	
2H-WS_2	353.2 mAh g^{-1} @200 mA g^{-1}	195
MoS_2/graphene paper	240 mAh g^{-1} @25 mA g^{-1}	183
	214 mAh g^{-1} @100 mA g^{-1}	
	173 mAh g^{-1} @200 mA g^{-1}	
DODA-WS_2	318 mAh g^{-1} @1000 mA g^{-1}	66
WS_2@MoS_2@C/rGO	411.8 mAh g^{-1} @500 mA g^{-1}	176
	311.4 mAh g^{-1} @100 mA g^{-1}	
	302.8 mAh g^{-1} @200 mA g^{-1}	
WS_2/CNT-rGO ordered 3D aerogel	289 mAh g^{-1} @500 mA g^{-1}	24
MoS_2/RGO	253.1 mAh g^{-1} @100 mA g^{-1}	353
1T-MoS_2	324 mAh g^{-1} @1000 mA g^{-1}	326

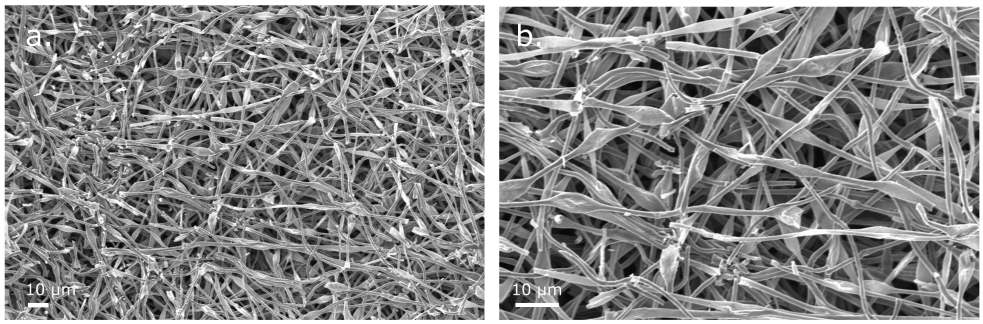


Figure 5.9: *SEM micrograph of SiOC pyrolyzed fibers at (a) lower magnification and (b) higher magnification exhibiting some irregularities (bead-like formation) in the fiber geometry.*

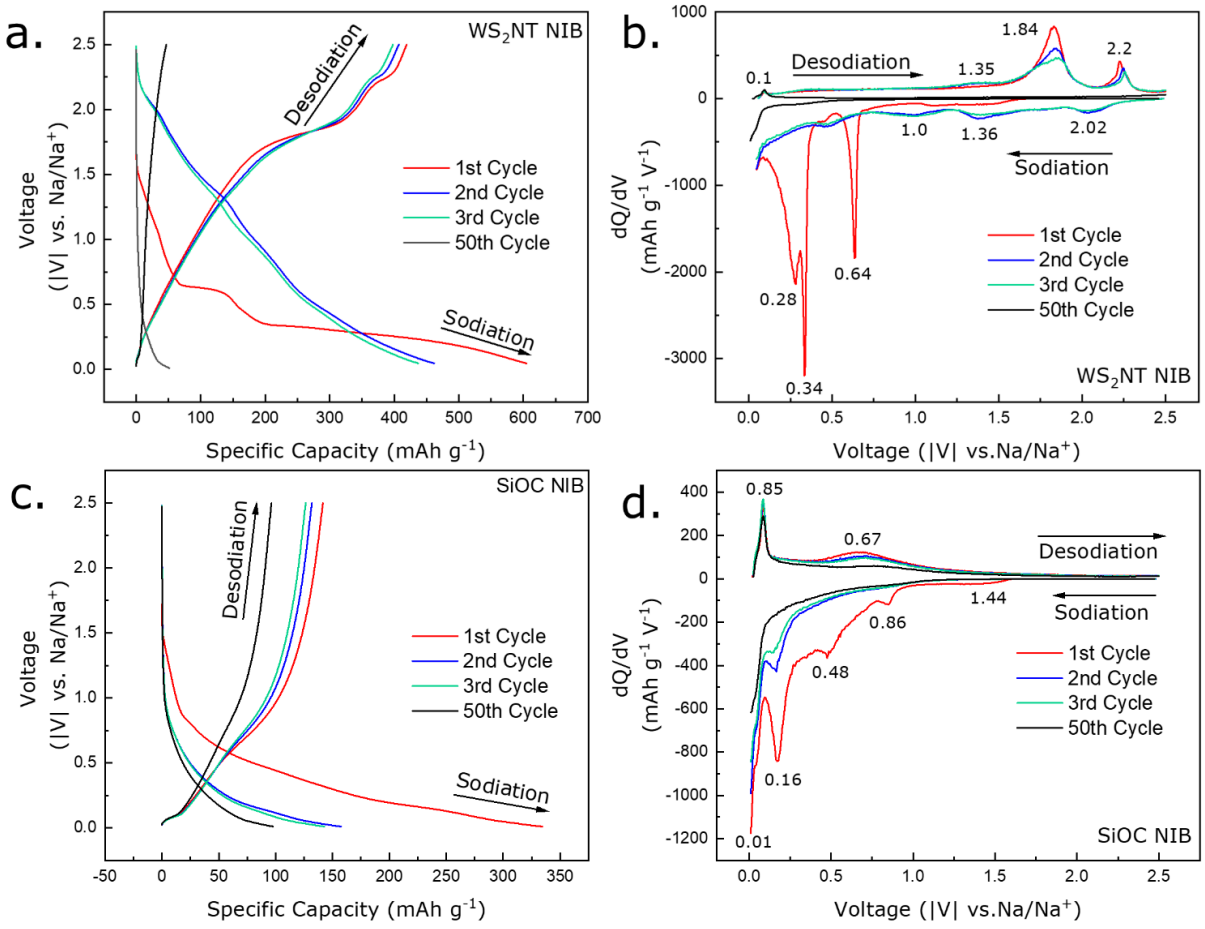


Figure 5.10: *(a) GCD profile of WS_2NT electrode tested in a sodium-ion half-cell setup; (b) Differential Capacity Curves obtained from the GCD profile of WS_2NT electrode; (c) GCD profile of SiOC electrode tested in a sodium-ion half-cell setup; (d) Differential Capacity Curves obtained from the GCD profile of SiOC electrode*

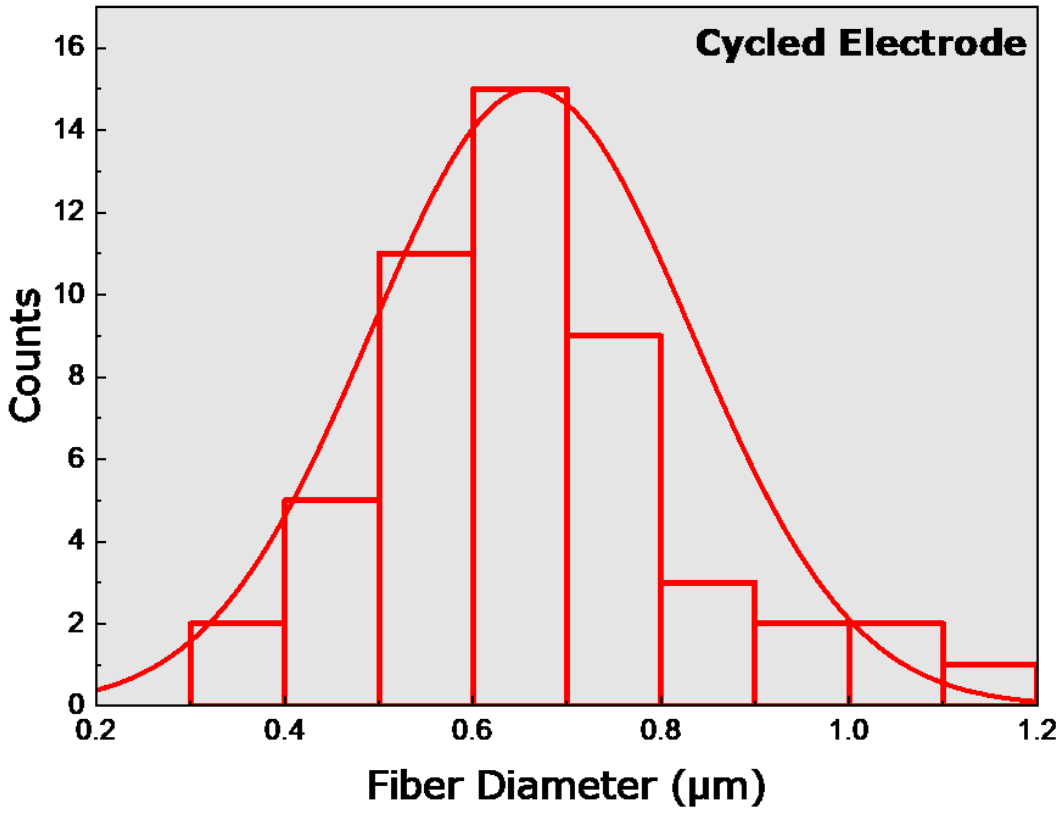


Figure 5.11: *Fiber diameter distribution plot of the cycled electrode.*

Chapter 6

Addressing Irreversibility and Structural Distortion in Quantum-Confined WS_2IF nanoparticles: Effects of Voltage Cut-off Experiments in Beyond Li^+-ion storage Applications[1]

6.1 Preface

While large interlayer spacing allows for Na^+ and K^+ ion storage in transition metal dichalcogenide (TMD) based electrodes, side reactions, and volume change leading to pulverization of crystalline structure are persistent challenges for employing these materials in next-generation devices. Here in this study, we first investigate if irreversibility due to struc-

[1]Reprinted from Dey, S., Manjunath, K., Zak, A., and Singh, G. (2023). WS_2 Nanotube-Embedded SiOC Fibermat Electrodes for Sodium-Ion Batteries. ACS omega, 8(11), 10126-10138.

tural distortion resulting in poor cycling stability is also apparent in the case of quantum confined fullerene-like tungsten disulfide (WS_2) nanocages (WS_2IF). To address these problems, we propose upper and lower voltage cut-off experiments to limit specific reactions. Three-dimensional (3D) differential capacity curves and derived surface plots highlight the continuation of reactions when a high upper cut-off technique is applied, indirectly suggesting the restriction of structural dissolution. Furthermore, structural preservation in half-cell electrodes during Li^+, Na^+, or K^+ storage delivered better capacity retention with stable performance and higher coulombic efficiency, laying the ground for future works.

6.2 Introduction

In 1985, the discovery of a highly symmetrical and stable C_{60} − fullerene-like hollow nanostructure inaugurated a new paragon in chemistry[150]. Initial concerns about chemical bonding limitations arising due to hollow spaces led to the hesitancy of the C_{60}'s use − nevertheless, it was effortlessly overcome by the discovery of manifold applications in environmental sensing, biosensing, and optoelectronics[388]. Much like C_{60}, layered compounds of TMDs, generally coined as $MX_2\neg$, where M represents a transition metal hexagonally packed with X or chalcogen atoms, can also form hollow cage-like structures with a combination of hexagons and triangles or/and rhombi being arranged as symmetric tetrahedron or octahedron[302]. The extensive scalability of such zero-dimensional (0D) supramolecules driven and guided by R. Tenne et al. has been capitalized in various fields: light-matter interactions, bulk electrical transport[182], solid lubricants[254], biomarkers, drug delivery vehicles, coatings for orthodontic wires, endodontic files, and so on[72]. Interestingly, current literature still lacks in exploring the electrochemical properties of inorganic fullerene-like nanophase materials, although the efficacy of nanomaterials cannot be disregarded. Specifically, nanomaterials, in general, present a mechanical advantage over traditional materials mainly due to their reduced size, as strain mismatch between particles is overcome as the particle size is equal to or below the typical crack size during charge storage[133].

Concerning rechargeable secondary alkali metal ion batteries, distinct WS_2 structures

with wide dimensional variety (a versatile TMD family member) have been investigated broadly. Specifically, investigation of Li^+-ion storage behavior inside nanostructures of WS_2, including nanosheets[145], nanohoneycombs[253], nanoflowers[253], nanotubes[321], and onion-like structures[160], are up to date. In comparison, electrochemical charge storage of earth-abundant alkali metal ions, such as Na^+ and K^+-ions, is rarely found in existing literature, especially in the case of WS_2IF supramolecular structures. Although Zak et al. explored the intercalation of alkali-metal ions into WS_2IF structures, the study extensively highlighted the transport properties, elaborating on the deviation of conductivity and magnetism before and after the experiment – utilizing vapor transport method quite different from electrochemical storage techniques[358]. Previous investigations highlight the existing drawbacks of WS_2, namely, low electronic conductivity, nanosheet reaggregation phenomena, chalcogen species dissolution, and extreme volume change, which are more apparent during reversible Na^+ and K^+ ion storage, as Na^+ and K^+ions are bulkier in size and present slower diffusion kinetics[40]. Usual strategies to curb the inherent deficiencies of TMD-based electrodes include hybrid structure formation with carbon additives – providing required conductivity to the nanofillers[84], enhancing the interlayer spacing[10], and inducing regional disorder[36] to facilitate higher alkali metal ion storage sites. Nevertheless, such strategies require convoluted synthesis parameters, instigate impurities within the crystal, and additionally bring down the cell's energy density as a whole. Therefore, a dearth necessity of complementary and/or alternative engineering strategies is imperative more than ever.

In this investigation, we applied the upper and lower voltage cut-off techniques to accomplish efficient and reversible electrochemical storage beyond Li^+-ions in 0D WS_2IF quantum confinement structures as a continuation of our previous study[142]. Like the typical TMD nanosheets, such WS_2IFs also suffer from volume expansion and subsequent structural distortion, for which inefficiency in cycling behavior was observed – leading to capacity fading. Therefore, we utilized upper and lower voltage cut-off techniques to suspend conversion reactions at various stages and scrutinize the structural evolution via differential capacity with evolving cycling conditions. The kinetics and subtle differences in Na^+ and K^+ ion storage within WS_2IFs were further explored by employing rigorous electrochemical analysis tech-

niques − rendering the preference of charge storage mechanism: faradaic or non-faradaic. With higher capacity achievement in the case of Na^+ ion storage and higher coulombic efficiency realization in $Li^+/Na^+/K^+$ ion storage, this study lays the ground for future studies concerning efficient storage within cage-bound like 0D fullerene supramolecules.

6.3 Materials and Methods

6.3.1 Morphologic and spectroscopic characterization

This study utilized Hitachi SU8010 for collecting the scanning electron microscopy (SEM) images of the neat WS_2IF material and the spent electrodes. The IXRF system was additionally used to obtain the corresponding X-ray fluorescence (XRF) spectrum. Phillips CM100 obtained the transmission electron microscopy (TEM) images of the bulk WS_2IF material. Raman spectra of the neat material and spent electrodes were obtained using a Renishaw Invia Raman microscope using a 532 nm laser. X-ray photoelectron spectroscopy (XPS) data were obtained using a thermo scientific equipped with a monochromatic Al anode Kα (hν = 1486.6 eV) with in situ sputtering of Ar^+ at 3.0 keV for 120s. X-ray diffraction (XRD) data were collected utilizing PANalytical Empyrean with 45 kV, 40 mA power setting, and a step size of 0.02 °. WS_2IF preparation.

6.3.2 Electrochemical Measurements

The working electrode for all three cell types was prepared with 70 wt.% of the active material (WS_2IF), 15 wt.% of carbon black as conducting agent (Alfa Aesar, Haverhill, MA, USA), and 15 wt % of polyvinylidene fluoride (PVDF) as a binder (Alfa Aesar, Haverhill, MA, USA). After preparing a homogenous slurry by dissolving the materials in 1-methyl-2-pyrrolidinone (Sigma-Aldrich, Missouri, MA, USA), acting as a solvent for PVDF, a coating (125µm) on top of 125 µm thick copper foil was deposited. The slurry coating was dried at 80 °C overnight and punched into 14.29 mm dia circles to be utilized as working electrodes. CR-2032 type coin cells were then assembled using the working electrode and Li/Na/K

metals as reference and counter electrodes in the case of LIB/NIB/KIB cells. The assembly of the half-cells was conducted inside a high-precision ultra-pure Ar glovebox with O_2 and H_2O contents below 0.1 ppm. The electrolyte for LIB/NIB/KIB half-cells consisted of $LiPF_6/NaClO_4/KPF_6$ salt in a common solvent: (1:1 v/v) Ethylene Carbonate (EC): Dimethyl Carbonate (DMC) (anhydrous, 99% Sigma Aldrich). A glass separator soaked with electrolyte separated the two electrodes in half-cells. Assembled half-cells were cycled at a constant 100 mA g^{-1} current density for 100 cycles in the Arbin BT 2000 test unit. Cyclic voltammetry (CV) tests were conducted in CH instruments (model 600 E) electrochemical analyzer at different scan rates. After cycling the half-cells in specific conditions, cycled electrodes were de-crimped in an inert Ar atmosphere and washed with DMC solvent to dispose of the separator fibers attached to the electrodes for further spectroscopic and microscopic analysis.

6.4 Results and Discussions

6.4.1 Spectroscopic and Microscopic Analysis

The morphology of the WS_2IF nanoparticles was investigated using SEM and TEM. SEM images (Figure 6.1a) of the WS_2IF showed the agglomerated nature of the nanoparticles. The high-magnification image of the WS_2IF showed that the shape of the fullerene-like nanoparticle was nearly isotropic and synonymous with the SEMs in previously published articles[75;178]. The TEM also shows the typical fullerene-like structure of the WS_2IF[124]. As shown in Figure 6.1e, the nanoparticle showed an onion-like nested arrangement of several closed layers of WS_2. According to TEM, the sub-globular nanoparticles mostly have closed structures with an average diameter of 100 nm. A selected area electron diffraction (SAED) pattern obtained from one of the WS_2IF nanoparticles showed the characteristic electron pattern of WS_2 at (002) and (101)[362].

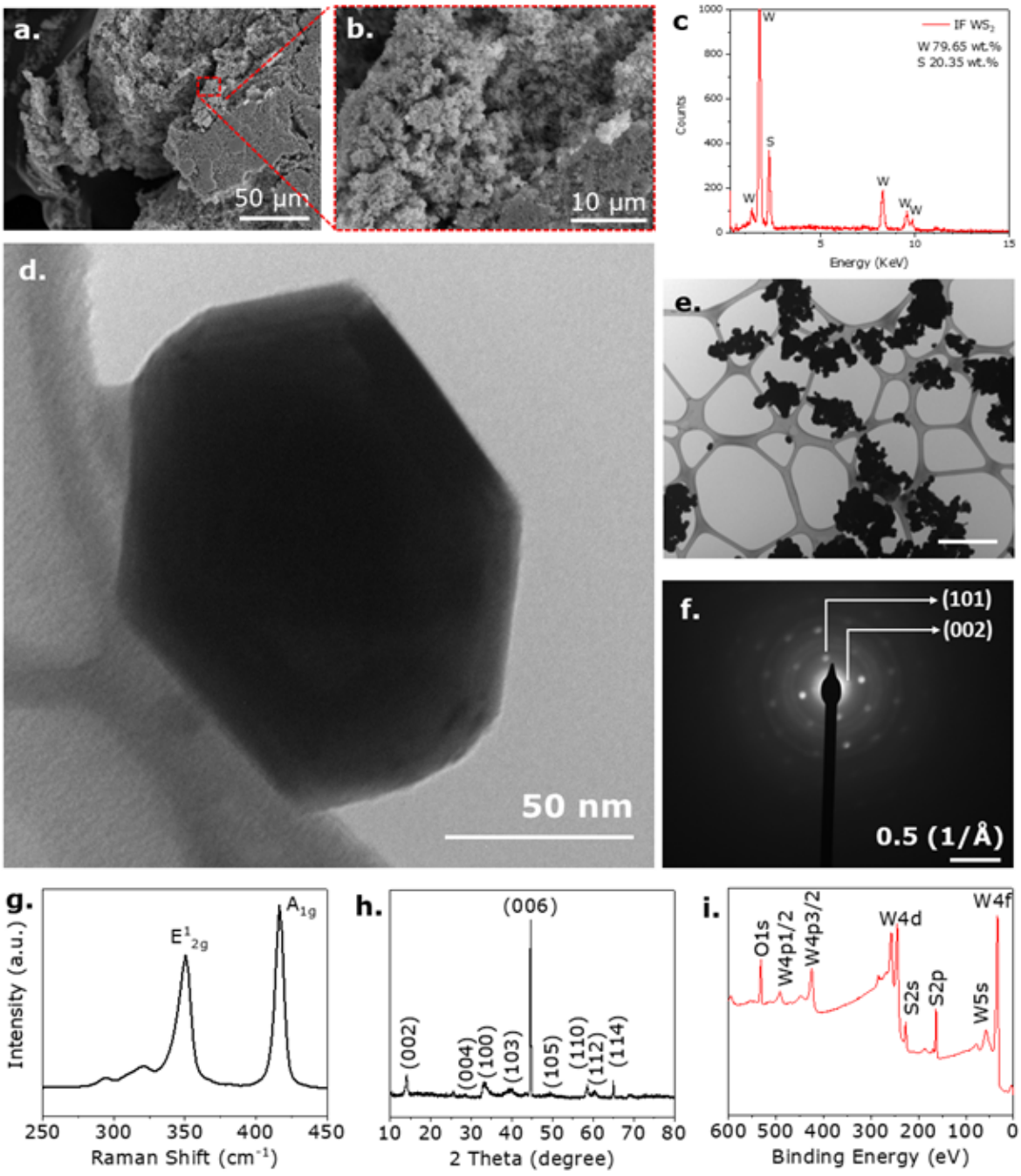


Figure 6.1: *(a) SEM micrograph of the agglomerated WS_2IF nanoparticles; (b) Magnified view of the fullerene-like WS_2 nanoparticles; (c) XRF spectra shows the characteristic elements present in WS_2IF; (d) TEM micrograph of the WS_2IF and (e) magnified view of individual WS_2IF; (f) SAED pattern of the individual WS_2IF particle; (g) Raman spectra of WS_2IF powder shows typical position of the WS_2 peaks; (h) X-ray diffractogram and (i) XPS survey spectra of the WS_2IF.*

Figure 6.1g shows the Raman spectrum of the WS_2IF nanoparticles. Two intense peaks in

the Raman spectrum of crystalline particles were observed at 349 and 416 cm-1. These peaks were assigned to characteristic E^1_{2g} and A_{1g} modes of WS_2IF[19], corresponding to molecules' in-plane and out-of-plane vibration, respectively[189]. XRD was also utilized to determine the crystallinity of the WS_2IF. The XRD patterns in Figure 1h had been assigned to the hexagonal phase of WS_2 with lattice constant: a = 3.153, c = 12.323 Å (ICDD Card No. 08-0237)[48;355]. Raman spectroscopy and XRD confirmed the presence of the pristine WS_2IF. In addition, XPS was performed to determine the chemical composition of the nanoparticles. As shown in Figure 6.1i, the XPS survey scan showed the presence of W, S, and O in the WS_2IF particles. The presence of oxygen was attributed to the surface oxidation of the particles. According to XPS, the W and S atomic percentages in the WS_2IF nanoparticles were 31.95 and 36.89 at.%, respectively.

6.4.2 Electrochemical Analysis

Galvanostatic charge-discharge curves (GCD), (Figures 6.6-a1, a2) and derived differential capacity curves (Figures 6.6-b1, b2) offer insight into various reactions happening at the charging and discharging of the half-cells. Figures 6.2 (a1-a4) denote GCD curves for the NIB and KIB cells. For the 0.01-2.5 V LIB cell, the first lithiation includes sharp peaks at 1.7, 0.79, 0.67, and 0.01 V (Figure 6.6-b2). The responses at lower voltage ranges might be ascribed to a combination of reactions: insertion of Li^+ ions into WS_2IF layers, additional conversion reaction of WS_2 and Li^+ ions to form W and Li_2S matrix, irreversible electrolyte decomposition, and the formation of a solid electrolyte interface layers[393;396;398]. Apart from the 0.01 V peak, the other peaks do not appear in the subsequent second and third cycles − indicating the irreversibility of the reactions. On the other hand, the delithiation curves present a significant peak at 2.3 V and a shoulder peak at 2.0 V − possibly originating from the extraction of Li^+ ions from the $LixWS_2$ host. Additional reversible peaks observed in the second and third lithiation cycles may be attributed to further insertion of Li^+ ions into the interlayers of WS_2IF. For the LIB cells cycled at 0.01-1.5 V range (Figure 6.6-b1), the same reactions indicated by the same peaks were present, suggesting no material

contamination. However, in the second and third cycles, a partial peak appeared from the 1.7 V peak. The continuation of intercalation and conversion reactions could be realized from the 3D differential capacity curves, plotted as a function of the cycle index illustrated in Figures S1-(c1,c2). For further examining the reaction continuity or polarization of the peaks, individual lithiation/delithiation 3D differential curves (Figures 6.6-c1, c2) are demonstrated as surface plots in Figures 6.7(a1-b4). As seen for LIB 0.01-2.5 V cells (Figure 6.7-a1), during delithiation, specific reactions at approx. 1.8 V continues only up to 20-25 cycles. The only long-term reaction during continuous cycling is observed at 2.3 V, which gradually loses intensity − indicating lesser electron transfer and fading after the 80th cycle. In the reverse lithiation process (Figure 6.7-a2), specific peaks at 1.7, 0.79, and 0.67 V diminish away at the 40th cycle − indicating the discontinuation of the reactions. Shoulder peaks around 1.5 V region discontinues at 40th cycle, which starts fading out starting from 15th cycle. Major 2.0 V peaks also gradually fade away starting from the 20th cycle and disappear entirely after the 80th cycle. Slight hysteresis is also observed from the 2.0 V peak. Only the low-voltage region 0.01 V peak continues up to the 100th cycle. This behavior is nonetheless ascribed to mechanical stress generation within the WS_2IFs and structure pulverization upon repeated Li^+ion insertion/extraction[59;263;322]. A possible explanation is that the structure completely changes after specific cycles due to repeated cycling, and therefore no reaction proceeds further as there are no available sites. On the contrary, for the 0.01-1.5 V cell, specific peaks at 0.01 V during delithiation are more prominent (Figure 6.7-b1), and no peak plummeting behavior is observed. Partial reaction originating from the 1.7 V − limited to 1.5 V due to voltage cut-off continues up to 100th cycle. Similar behavior in the case of lithiation is also observed (Figure 6.7-b2) − indicating the efficiency of a higher upper voltage cut-off technique, as the 3D differential capacity curves indirectly suggest that the inherent structure is preserved as the repeated insertion/extraction of Li^+ ions continues.

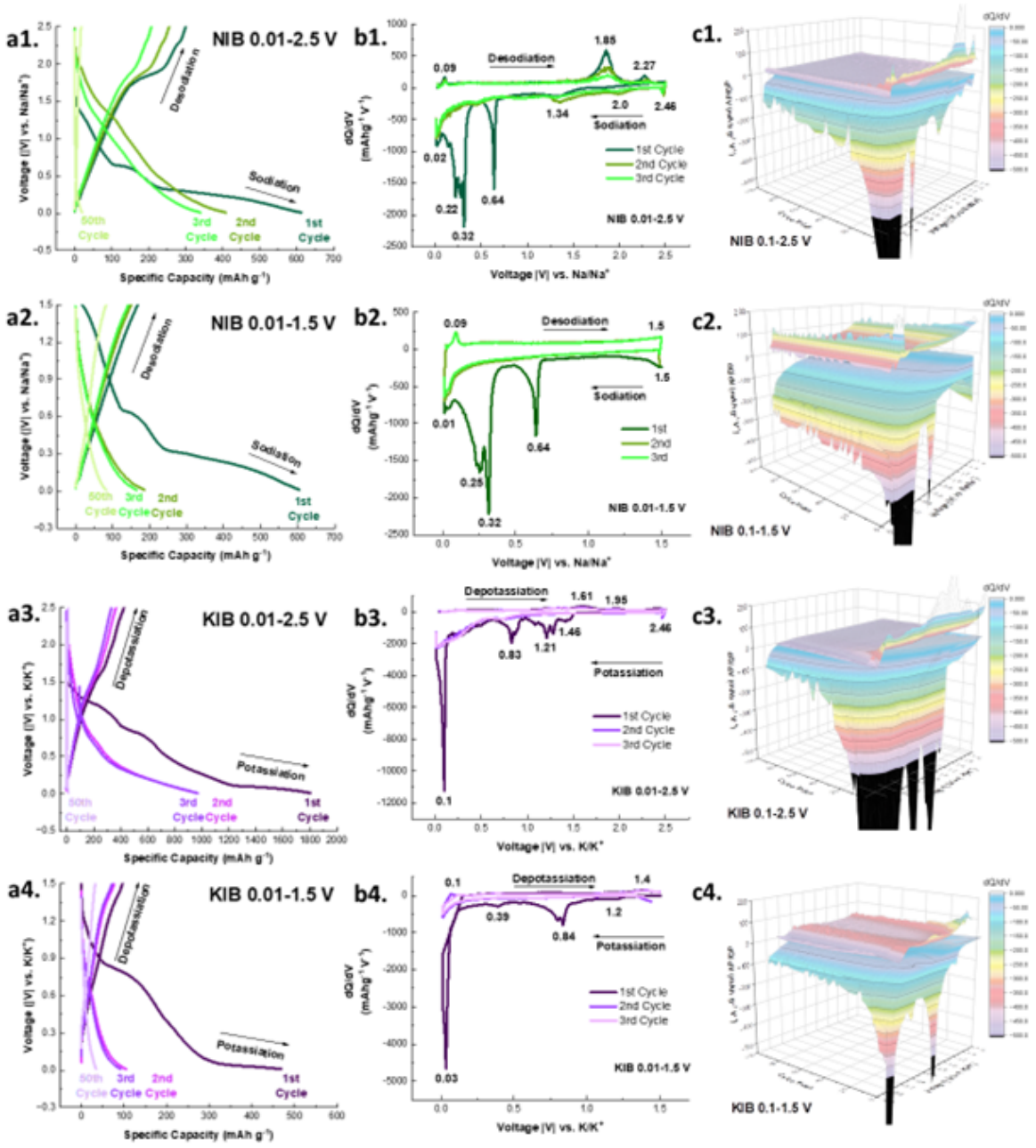


Figure 6.2: *GCD curves of: a1. NIB 0.01-2.5 V, a2. NIB 0.01-1.5 V, a3. KIB 0.01-2.5 V, a4. KIB 0.01-1.5 V half-cells; differential capacity curves of: b1. NIB 0.01-2.5 V, b2. NIB 0.01-1.5 V, b3. KIB 0.01-2.5 V, b4. KIB 0.01-1.5 V half-cells; differential capacity curves plotted as a function of cycle index for c1. NIB 0.01-2.5 V, c2. NIB 0.01-1.5 V, c3. KIB 0.01-2.5 V, c4. KIB 0.01-1.5 V half-cells.*

2D differential capacity curves Figures 6.2(a1-a4) derived from the GCD curves demonstrate the multistep first cycle sodiation process (Figure 6.2-b1) at $0.01 - 0.32$ V and 1.34 V.

The combination of significant peaks and peaks lying in the shoulder at 0.01-0.64 V region might be ascribed to several reactions taking place: insertion of Na^+ ions, conversion reaction of WS_2IF with Na^+ ions into metallic nanoparticles in the Na_2S matrix, and the formation of SEI layer[266]. Most of the reactions mentioned above are irreversible − predicted due to the disappearance of such peaks in the consecutive cycles. Reversible sodiation in WS_2IF nanoparticles was observed as peaks visible in the second and third cycles in 1.34, 2.0, and 2.46 V regions − indicating the possibility of similar insertions. In the reverse desodiation process, significant peaks were found in the 1.7-1.9, 2.27, and 2.5 V region − might be due to the extraction of Na^+ ions from the WS_2IF particles and the reconversion of W into WS_2[24]. In the cell cycle at 0.01-1.5 V (Figure 6.2-b2), the same reactions were observed apart from the half peak at 1.5 V, which could be a partial reaction from the 1.7 V peak. To assess the continuation and structural distortion of the electrode material, we further investigate the differential capacity curves as a function of the cycle index, illustrated in Figures 6.2(c1-c4). Figures 6.8 (a1-b2) are derived surface plots from the 3D differential capacity curves. As seen from the sodiation and desodiation surface plots in Figures (S6-8:a1-a2) for NIB 0.01-2.5 V cells, all the peaks disappeared within the 20th cycle apart from the ones in the lower voltage region. However, NIB cells cycled within the 0.01-1.5 V range conveys an exciting trait − peaks in the 0.01 V and 0.25 V region in the desodiation cycle continue up to a prolonged cycling period (Figure 6.8-b1). Similarly, during sodiation (Figure 6.8-b2), 0.09 V, and 1.5 V peak retain their intensity through 100 cycles, thereby bolstering our initial hypothesis: voltage cut-off restricts WS_2IF structure pulverization, even in case of repeated large Na^+ ion insertion/extraction, the result of which will be highlighted in the following section. Overall, when compared with LIB chemistry, NIB cells cycled up to 2.5 V conveyed even lesser reaction continuation. Nevertheless, NIB cells cycled up to 1.5 V retained even the lower amount of reactions happening within the WS_2IFs − indirectly indicating the structure preservation in the case of cells where higher voltage cut-off was utilized.

Similar to the sodiation/desodiation process, the potassiation/depotassiation process of the WS_2IF electrodes is demonstrated in GCD plots illustrated in Figures 6.2-(a1, a2). Differential capacity curves derived from the GCD graphs elucidate the specific reaction

at particular voltages. In the first potassiation process (Figure 6.2-b3), major peaks are observed at 0.1, 0.83, 1.0-1.5, and 2.46 V region. Previous investigations have assigned the peaks above the 0.75 V region to the intercalation process, and the peaks below the 0.75 V region to a mixture of reactions from the interaction of K^+ ions with WS_2 material, conversion reactions, and the formation of SEI layers[9;56;297]. Another school of thought exists where the interaction of K^+ ions with WS_2-based materials were assigned to be purely intercalation-based as no trace of metallic W was found due to conversion reaction products[6;316]. As there exists no direct evidence present to move in a certain direction, in this investigation we refrain from assigning the peaks to certain reactions. However, the peak at 0.1 V for the 0.01-2.5 V cell displayed the highest intensity – indicating greater electron transfer taking place, which can be ascribed to the SEI layer formation reaction in general. In earlier reports where MoS_2 was utilized as anode material utilizing KPF_6 as an electrolyte salt, unstable, potassium fluoride deficient, organic species-rich SEI layer formation was observed – leading to poor capacity retention[170]. The continuation of the peaks was further examined in 3D differential capacity curves, presented in Figures 6.2(c3, c4). Further elucidation of the 3D differential capacity curves are provided in Figures 6.9-(a1-b2) of potassiation/depotassiation processes for two different cells cycled at separate voltage ranges. From Figures 6.9(a1, a2) of the potassiation/depotassiation processes of the cell cycle at 0.01-2.5 V range, no continuation of reactions arising from higher voltage ranges are observed – peaks at 1.0-1.5 V region discontinues after the 10th cycle. The only reactions continuing are present in the lower voltage region (0.01 V peak in potassiation cycle – fading gradually after 50th cycle: Figure 6.9-a2). On the contrary, for the KIB 0.01-1.5 V cell, where the upper voltage cut-off technique was utilized, we observe the continuity of a 1.4 V peak, arising from a partial reaction of 1.7 V peak, up to the 100th cycle during depotassiation. Furthermore, the peak at 0.1 V maintained it's intensity throughout the depotassiation process (Figure 6.9-b1). In the reverse potassiation step, the only peak pursuing similar intensity during the prolonged process was the 0.01 V peak (Figure 6.9-b2) – indirectly indicating the structural preservation of the WS_2IF particles in KIB 0.01-1.5 V cells.

Cycling performance derived from the GCD experiments for all three alkali metal ion

systems was measured at similar conditions: constant current density of 100 mA g^{-1}. The specific capacity achieved from the LIB cells at different potential ranges was plotted as a function of the cycle index (Figures 6.10), from which the coulombic efficiency of the electrode material was also calculated. Similar graphs were obtained for the NIB and KIB cells demonstrated in Figures 6.3 (a, and b), respectively. The LIB cell cycled within 0.01-2.5 V demonstrated 349.67 mAh g^{-1} first cycle specific charge capacity with a coulombic efficiency of 42%. A consistent capacity degradation behavior was observed starting from the second cycle, perpetuating throughout the long-term cycling process. Capacity fading of the 0.01-2.5 V cell could be well correlated with the observations from the 3D differential capacity plots, where cessation of specific reactions suggesting structural distortion was observed. The first cycle capacity loss can be ascribed to inevitable SEI layer formation and a combination of side reactions through which Li^+ ions were irreversibly consumed[103]. Noticeably, the coulombic efficiency of the 0.01-2.5 V LIB cell was always around 60-70%. Interestingly, the LIB cell cycled at a higher upper cut-off voltage displayed 233.62 mAh g^{-1} initial capacity with a coulombic efficiency of 30.52%. The lower coulombic efficiency can be correlated with the higher intensity of the SEI layer formation peak (Figure 6.6-b2), where more Li^+ ion consumption could be predicted and, as a result, the 1st cycle discharge capacity was very high (Figure 6.6-1-a1). Nevertheless, the coulombic efficiency of the 0.01-1.5 V LIB cell was persistently near 100% from the 6th cycle, as a result, better capacity retention was observed with no fading behavior − also easy to be correlated with the prolongation of reaction peaks from 3D differential capacity Figure 6.7(b1, b2).

Similarly, Figure 6.3a depicts the cycling of two NIB cells at different voltage ranges under the same conditions as the LIB cells. The 0.01-2.5 V NIB cell displayed a first cycle charge capacity of 299 mAh g^{-1} with a coulombic efficiency of 48.94%, much higher than the 0.01-1.5 V cell residing at 167.65 mAh g^{-1} with a coulombic efficiency of 27.69%. However, the NIB 0.01-2.5 V cell never reached a coulombic efficiency near 100%, whereas the 0.01-1.5 V cell reached coulombic efficiency near 100% after 10 cycles. As a result, capacity retention of the NIB cell with no voltage cut-off technique utilized was much lower (sudden capacity degradation was observed up to the 8th cycle), which was quickly overtaken by the NIB

0.01-1.5 V cell at the 5th cycle. The above-mentioned behaviors of the NIB 0.01-2.5 V cells were in harmony with the findings from the 3D differential capacity curves (Figures 6.2:c1-c2) and surface plots (Figures 6.8: a1-b2), where maintenance of specific peaks in case of the 0.01-1.5 V cell was perceived − a characteristic quite the opposite in case of the 0.01-2.5 V cell. This phenomenon suggests well that Na^+ ion insertion/extraction at higher voltage ranges might lead to permanent structure distortion for which lesser capacity is achieved at prolonged cycling processes, even in the case of WS_2IF materials with different quantum confinement effects than nanosheets − in the 100th cycle specific capacity of the 0.01-2.5 V cell was 16.97 mAh g^{-1}, compared to 81.63 mAh g^{-1} for the 0.01-1.5 V NIB cell.

Similar characteristics were observed from the two KIB cells from Figure 6.3b, where the first cycle-specific charge capacity for the 0.01-2.5 V cell stood at 423 mAh g^{-1} with a coulombic efficiency of 23.47%. For the 0.01-1.5 V KIB cell, a similar coulombic efficiency was perceived, the reason for which has already been highlighted in the previous section (KPF_6 electrolyte degradation). In the case of the KIB cells, much like the LIB and NIB cells, the coulombic efficiency of the cell with higher upper voltage cut-off dominated over the cell cycled up to 2.5 V − reaching nearly 100% but at a later stage (after the 20th cycle). Such a performance could also be well connected with the results obtained from the surface plots (S6-9:a1-b2). Although with higher capacity retention, the 0.01-2.5 V cell demonstrated higher specific capacity at the 100th cycle (32 mAh g^{-1}, compared to 9.43 mAh g^{-1} of the 0.01-2.5 V cell), the value was far lower than both the LIB and NIB cells − providing overall inefficiency of the large K^+ ion storage within closed cage structures of WS_2IF.

To test the effects of lower voltage cut-off with a combination of best results achieved from the upper voltage cut-off experiments, four additional cells were assembled and cycled in the potential range of 0.25-1.5 V and 0.5-1.5 V range for NIB and KIB systems. Assembled cells were cycled at the same conditions as before, and Figures 6.11(a1-b4) demonstrate the GCD curves of the NIB and KIB cells cycled at different lower cut-off voltages. As observed from the derived differential capacity curves S6-11(b1,b2) from the GCD curves, only the specific reactions at the mentioned potential range are present. Figures 6.12(a) represent

the cycling stability and coulombic efficiency data of the NIB 0.25-1.5 V and 0.5-1.5 V cells. Both the cells demonstrate lower capacity achievement throughout the cycling process when compared to the cells with no lower cut-off applied. Although the NIB 0.25-1.5 V cell's initial capacity (65 mAh g^{-1}) was higher than the other counterpart (52 mAh g^{-1}), lower coulombic efficiency (approx. 70%, compared to near 100% after 30th cycle for the NIB 0.5-1.5 V cell) throughout the cycling continuation dragged the capacity down. The difference in terms of capacity for lower voltage cut-off was more apparent in KIB cells cycled under the same conditions (Figures 6.11-b) in the cycling stability test. The 0.25-1.5 V KIB cell demonstrates higher capacity achievement (46 mAh g^{-1}, compared with 26 mAh g^{-1} of the 0.5-1.5 V KIB cell). This result is well expected as the restriction of the potential range to 0.5 V suppresses several key reactions apparent from the differential capacity curve (Figure 6.11). Noticeably, both the KIB cells displayed low coulombic efficiency, around 65%, even less than the NIB 0.5-1.5 V cell.

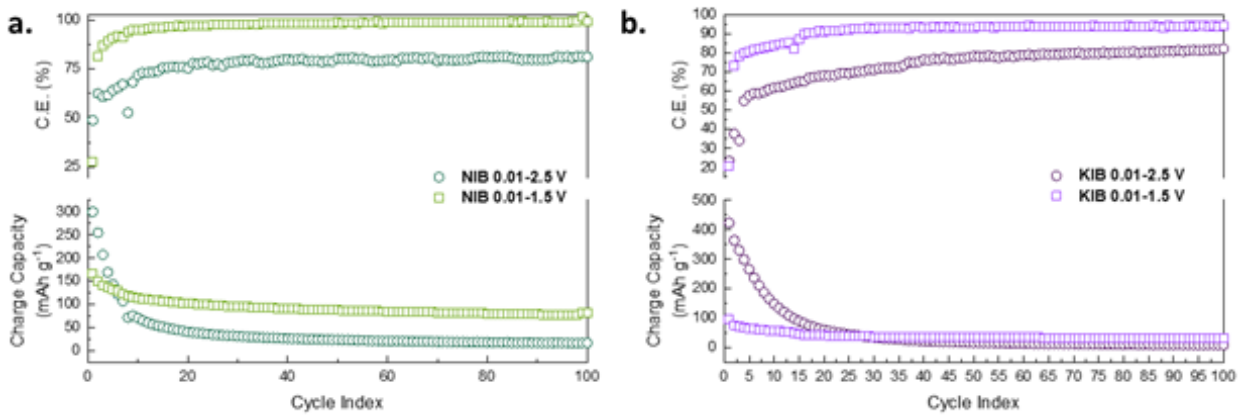


Figure 6.3: *Cycling stability and consecutive coulombic efficiency of a. NIB 0.01-2.5 V and NIB 0.01-1.5 V cells, b. KIB 0.01-2.5 V and KIB 0.01-1.5 V cells.*

The fast physical charge storage mechanism within WS_2IF material can be understood from the CV experiments performed at different scan rates[71]. Usually, the charge storage process relies on different scan rates (ν, mV s^{-1}) utilized in CV experiments, where the current response (i, amp) fluctuates as a function of voltage sweeps. Therefore, Figures 6.4 (a1-b2) denote the CV curves obtained for the NIB and KIB cells cycled at different volt-

age ranges, respectively. Supplementary Figures 6.13 (a_1 and a_2) illustrate the CV curves obtained from the LIB cells cycled at two different voltage ranges. Five different scan rates, such as 1, 2.5, 5, 7.5, and 10 mV s^{-1}, were utilized to investigate the charge storage mechanism. In the framework of this analysis, examination of the CV profiles enables quantitative differentiation of two different charge storage mechanisms: non-Faradaic surface capacitive effects and Faradaic diffusion-controlled insertion processes[187], according to equation (6.1).

$$i = k_1\nu + k_2\nu^{\frac{1}{2}} \tag{6.1}$$

The rearrangements of Equation 6.1 enable us to establish a relation in $i(V)/\nu^{1/2}$ vs. $\nu^{1/2}$ plots, as k_1 (slope) and k_2 (y-axis intercept) follow a linear behavior, illustrated in Figures 6.14 (a-c) for six different cell types cycled at different voltage ranges at fixed potentials, neglecting minimal peak shifts. Notably, $k_1\nu$ and $k_2\nu^{1/2}$ in the equation denote the surfaced capacitive and intercalation-based diffusive charge storage process − illustrated as bar graphs in Figures 6.4(b1-b4) for NIB and KIB cells cycled at two different potential ranges as a function of employed scan rates. We observe, while LIB cells cycled at 0.01-1.5 V illustrated 15, 10, 7, 6, and 5% pseudo-capacitive contributions (Figures 6.13:b1,b2), the cell cycled at 0.01-2.5 V demonstrated 65, 25, 19, 16, and 14% for scan rates of 1, 2.5, 4, 7.5 mV s^{-1}, respectively. Again, for NIB 0.01-1.5 V cells (Figure 6.4b1), 16, 11, 8, 6, and 6%, and for NIB 0.01-2.5 V cells (Figure 6.4b2), 56, 45, 37, 32, and 29% contributions were from pseudo-capacitive processes at scan rates of 1, 2.5, 4, 7.5 mV s^{-1}, respectively. Lastly, for KIB 0.01-1.5 V cells (Figure 6.4-b3), 56, 45, 37, 32, and 29%, and for KIB 0.01-2.5 V cells (Figure 6.4-b4), 44, 33, 26, 22, and 20% contributions were from pseudo-capacitive processes at scan rates of 1, 2.5, 4, 7.5 mV s^{-1}, respectively. To sum up, an increase in the capacitive contribution as a function of gradually increasing scan rate is common to all six cells. This behavior has been previously observed in the case of electrodes with fast reaction kinetics. Specifically, as the scan rate increases, alkali-metal ions experience decreased periods of complete diffusion inside the electrode material. Therefore, the cations prefer a surface adsorption-based storage mechanism rather than the formation of a solid solution. Domi-

nance in the capacitive contribution is observed from the LIB and NIB cells cycled at higher upper cut-off voltages[225;267;323]. Furthermore, another common trend is the dominance of the capacitive charge storage process over the faradaic process in the case of cells cycled at higher cut-off voltages. Firstly, as seen from the charge-discharge curves, higher cut-off voltages yield lesser capacity than the other cells −; therefore, the alkali-metal ions get less time to interact with the host WS_2IF electrode. Again, some of the reactions (intercalation and conversion) for LIB and NIB cells fall out of the 0.01-1.5 V range, apparent from both 2D and 3D differential capacity curves − pointing out that higher cut-off voltages might suppress specific reactions. Last but not least, the cage-like quantum confinement of WS_2IFs might also play a significant role in the case of a charge storage mechanism, as our previous works regarding WS_2NTs in LIB and NIB have shown better capacity achievement compared to WS_2IFs[189]. Nevertheless, further research efforts are required to come to this conclusion, which is currently underway. For the KIB cells, however, an opposing trend was observed − the cells with higher cut-off voltages demonstrated elevated diffusive charge storage characteristics. This can be explained by the partial reactions in the anodic cycle and complete reactions in the cathodic cycle in terms of 0.01-1.5 V cells. The height of the anodic peak (1.5 V) in the negative current axis for 0.01-1.5 V KIB cell is comparatively pronounced − indicating more electrons are transferred due to partial reactions than the complete reaction of 0.01-2.5 V cell. Therefore, this indirectly affirms our initial hypothesis that a higher voltage cut-off helps to protect the WS_2IF structure longer. This technique might be explored with a combination of composite structure formation to realize the full potential of voltage cut-off experiments, as some composite structure formation techniques have proven to enhance the capacity and stabilize the electrochemistry of TMD-based nanomaterials[97;303].

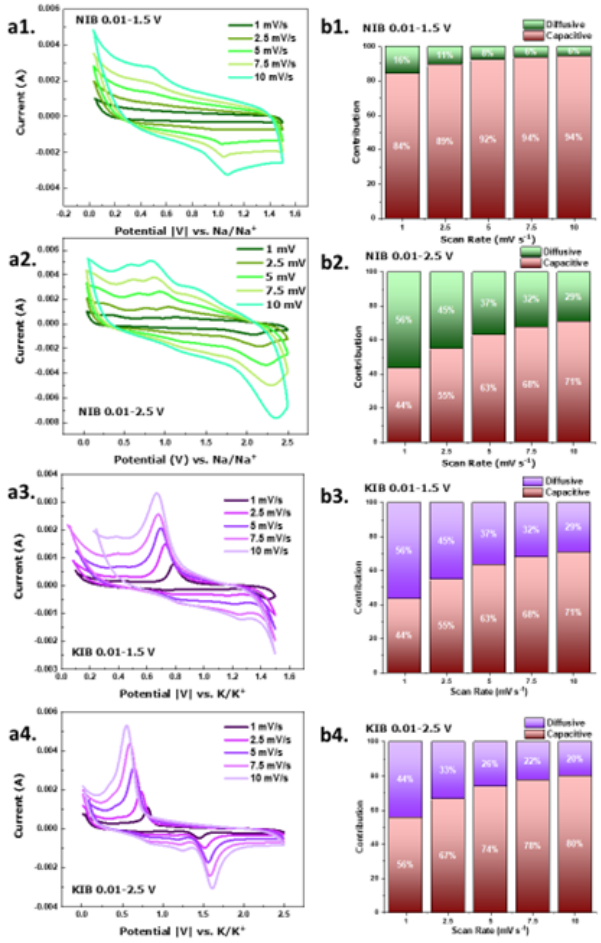


Figure 6.4: *CV curves of a1. NIB 0.01-1.5 V, a2. NIB 0.01-2.5 V, a3. KIB 0.01-1.5 V, a4. KIB 0.01-2.5 V half cells; capacitive and diffusion-controlled contribution ratios for different scan rates of b1. NIB 0.01-1.5 V, b2. NIB 0.01-2.5 V, b3. KIB 0.01-1.5 V, b4. KIB 0.01-2.5 V half cells.*

6.5 Post-Cycling Analysis

The upper voltage cut-off (up to 2.5V and 1.5 V) electrodes were disassembled after cycling, and they were analyzed using different characterization techniques as shown in Figure 6.5. Digital camera images of the recovered spent electrodes after cycling are shown in Figure 6.5(a-f). The spent electrodes, particularly NIB 0.01-2.5 V electrode showed disintegration in some parts, which had happened during the disassembly process. The presence

of an infrequent white substance on the electrodes was the residual waste of the glass fiber separators used in assembling the cells. However, the spent electrodes showed no visible color change or imperfections. The presence of glass fibers from the separator was confirmed by the SEM images (Figure 6.5a1-f1) of the spent electrodes. The SEM images of the 0.01-2.5 V electrodes showed increased microcracks compared to 0.01-1.5 V electrodes. This suggested the structural integrity and minimal stress development within the 0.01-1.5 V electrodes during cycling. Figure 6.5(a2-f2) shows the qualitative elemental analysis of the spent electrodes characterized by the XRF technique. The characteristic peaks for W and S spectral lines were observed for all the electrodes, suggesting the existence of WS_2IF after cycling. In addition, characteristic peaks for the electrolyte used in different cells, i.e., F for LIBs, Na, and Cl for NIBs, and K and F for KIBs were identified by XRF. Cu peaks were also detected, originating from the Cu foils. This study also utilized Raman spectroscopy to determine the spent electrode microstructure and designate the WS_2 phase from the carbon structure. Figures 6.5(a3-f3) show the Raman spectra of the electrodes after cycling. The two intense peaks at 1350 and 1599 cm-1 were assigned to the D and G carbon vibrations bands, respectively[295]. For the 2.5V spent electrodes (Figure 6.5:a3-c3), an additional Raman spectrum for crystalline WO_3 was observed. The intense peaks at 924, 808, and 305 cm-1¬ corresponded to the stretching vibrations of the bridging oxygen and were associated with W-O, W-O-W stretching (ν), and O-W-O bending (δ) vibrational modes[354]. By contrast, the 0.01-1.5 V spent electrodes (Figure 6.5(d3-f3)) showed the Raman peaks at 349 and 416 cm-1, which correspond to the in-plane mode $E^1{}_{2g}$ and out-of-plane mode A_{1g} mode for WS_2IF[19]. This also suggested that at higher voltage windows (0.01-2.5 V) WS_2IF electrodes were oxidized, contributing to the degradation of the cells. The Raman spectrum of the neat electrode before cycling is presented in the supplementary Figure S10. Figure 6.5(a4-f4) shows the XPS survey scan of the spent electrodes. C, O, F, and Cu elements were present, along with the base materials of W and S. For NIBs and KIBs, Na and K were detected, respectively, indicating the formation of the SEI layer.

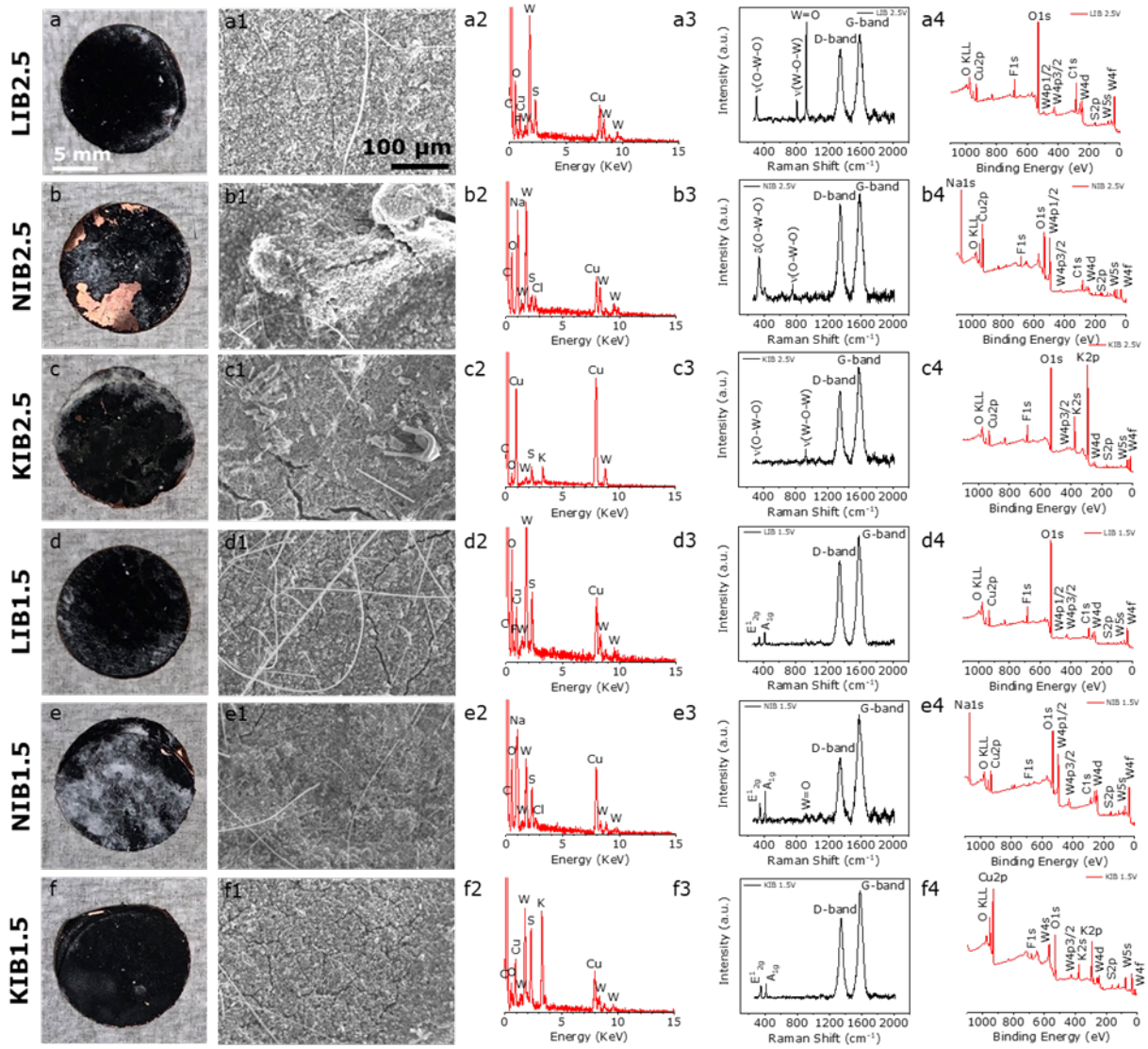


Figure 6.5: *Structural characterization of the spent (cycled) electrodes: (a-f) Digital camera image; (a1-f1) SEM micrographs showing structural integrity of the spent electrodes after cycling; (a2-f2) XRF spectra of the electrodes identify the characteristic elements; (a3-f3) Raman spectra show the distinctive peaks obtained for the spent electrodes; and (a4-f4) XPS survey scan of the electrodes representing the presence of individual elements after cycling.*

6.6 Conclusion

This research is the first work to study the alkali metal ion storage behavior of nanocage-like WS_2IF structure. Firstly, morphological and chemical characteristics of WS_2 polymorphs were studied via SEM, TEM, Raman spectroscopy, XPS, and XRD. We further investigated whether the drawbacks of traditional TMD-based materials in terms of alkali metal ion

storage, hold for quantum-confined 0D WS_2IF structures and found out that side reactions and significant volume change lead to structural distortion within. Therefore, we explored upper and lower voltage cut-off techniques to limit certain reactions. Upper voltage cut-off led to stable capacity achievement with minimal capacity fading and higher coulombic efficiency gain at prolonged cycling conditions in the case of Li^+/Na^+ ion storage, compared to cells with no voltage cut-off applied. Although K^+ ion storage in the upper voltage cut-off range resulted in higher coulombic efficiency achievement, no significant benefit in terms of higher capacity gain was apparent. The reason behind such phenomena was examined using 3D differential capacity curves and derived surface plots, where reactions for 0.01-2.5 V cells halted after certain cycles indicating structural pulverization resulting in capacity fading, also detectable from post-cycling analysis. Additionally, lower voltage cut-off combined with optimal upper voltage range yielded much lesser capacity gain as some reactions got restricted resulting in lesser electron transfer. Furthermore, when examining via CV experiments, LIB and NIB cells with higher upper voltage cut-off displayed preference in a non-faradaic charge storage mechanism, while K^+-ion storage inside WS_2IF was diffusion-dominated. Although the lesser capacity achievement of WS_2IF during Na^+ and K^+ ion storage is an issue evident in this investigation, this study nevertheless lays the ground for taking advantage of the composite formation in combination with voltage cut-off to harness next-generation electrochemical energy storage devices.

Table 6.1: *Elemental composition of the electrodes determined by XRF*

Samples	Elements (wt.%)					
	W	S	O	C	Li	P
Neat Electrode	33.3	13.59	6.99	36.46	-	-
LIB 2.5V	26.92	6.68	38.27	-	-	0.64
NIB 2.5V	30.23	2.31	35.66	-	-	-
KIB 2.5V	4.4	5.57	11.93	-	-	0.31
LIB 1.5V	20.33	8.14	50.05	-	-	0.32
NIB 1.5V	11.91	5.77	37.43	4.03	-	-
KIB 1.5V	17.01	10.43	19.5	18.94	-	0.45

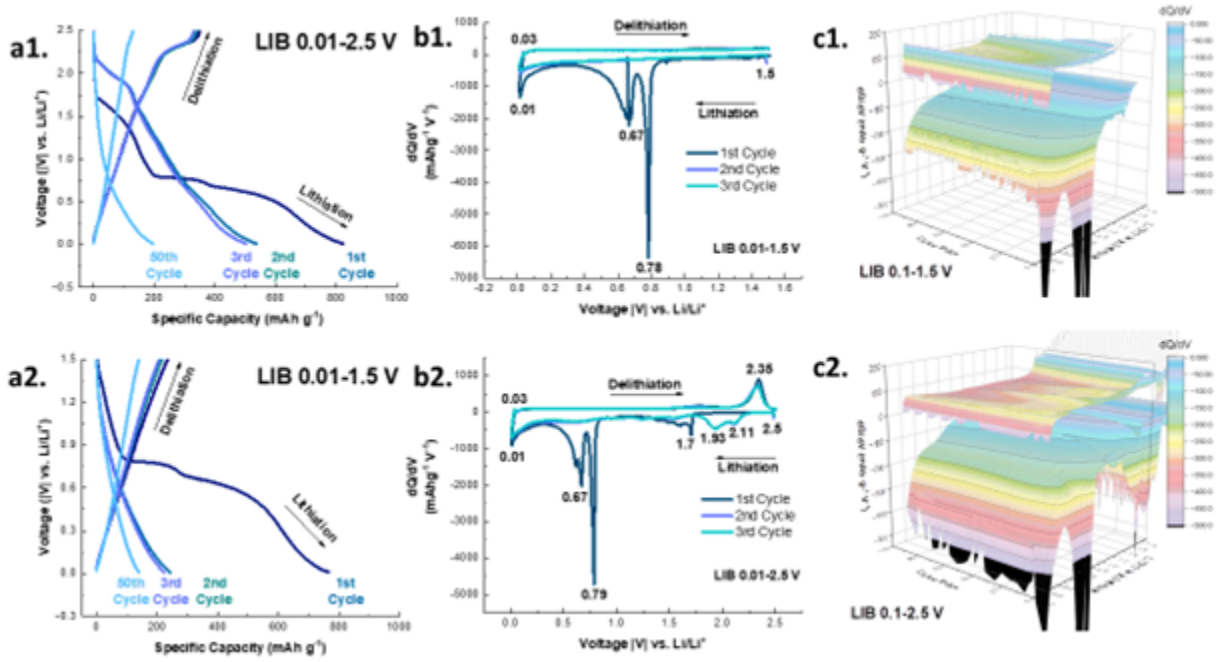


Figure 6.6: *GCD curves of a1. LIB 0.01-2.5 V, a2. LIB 0.01-1.5 V; differential capacity curves of b1. LIB 0.01-2.5 V, b2. LIB 0.01-1.5 V; differential capacity curves plotted as a function of cycle index for c1. LIB 0.01-2.5 V, c2. LIB 0.01-1.5 V half-cell.*

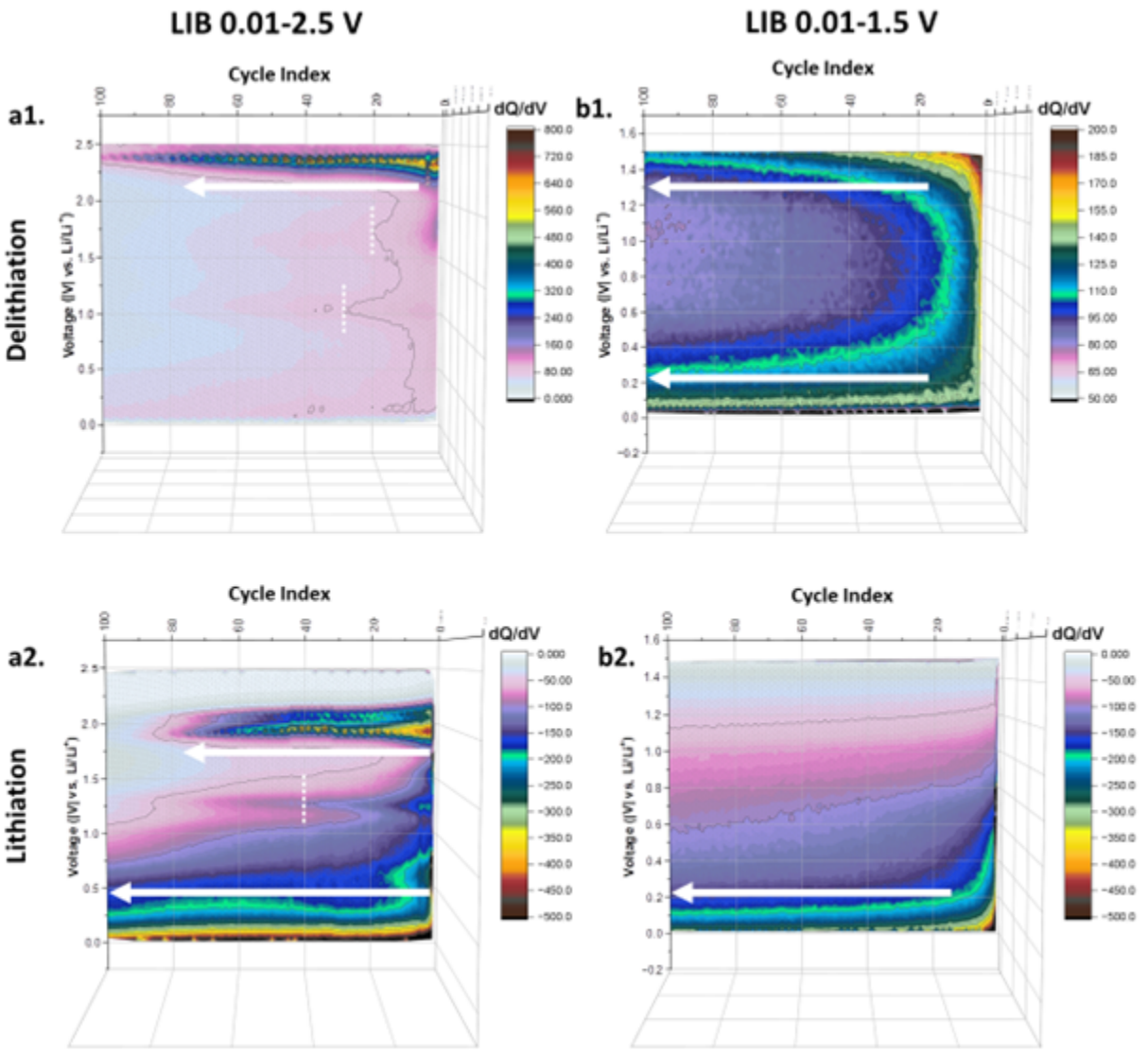


Figure 6.7: *Surface plots derived from the 3D differential capacity curves for LIB half-cells during a1. 0.01-2.5 V delithiation stage, a2. 0.01-1.5 V lithiation stage, b1. 0.01-1.5 V delithiation stage, b2. 0.01-1.5 V lithiation stage.*

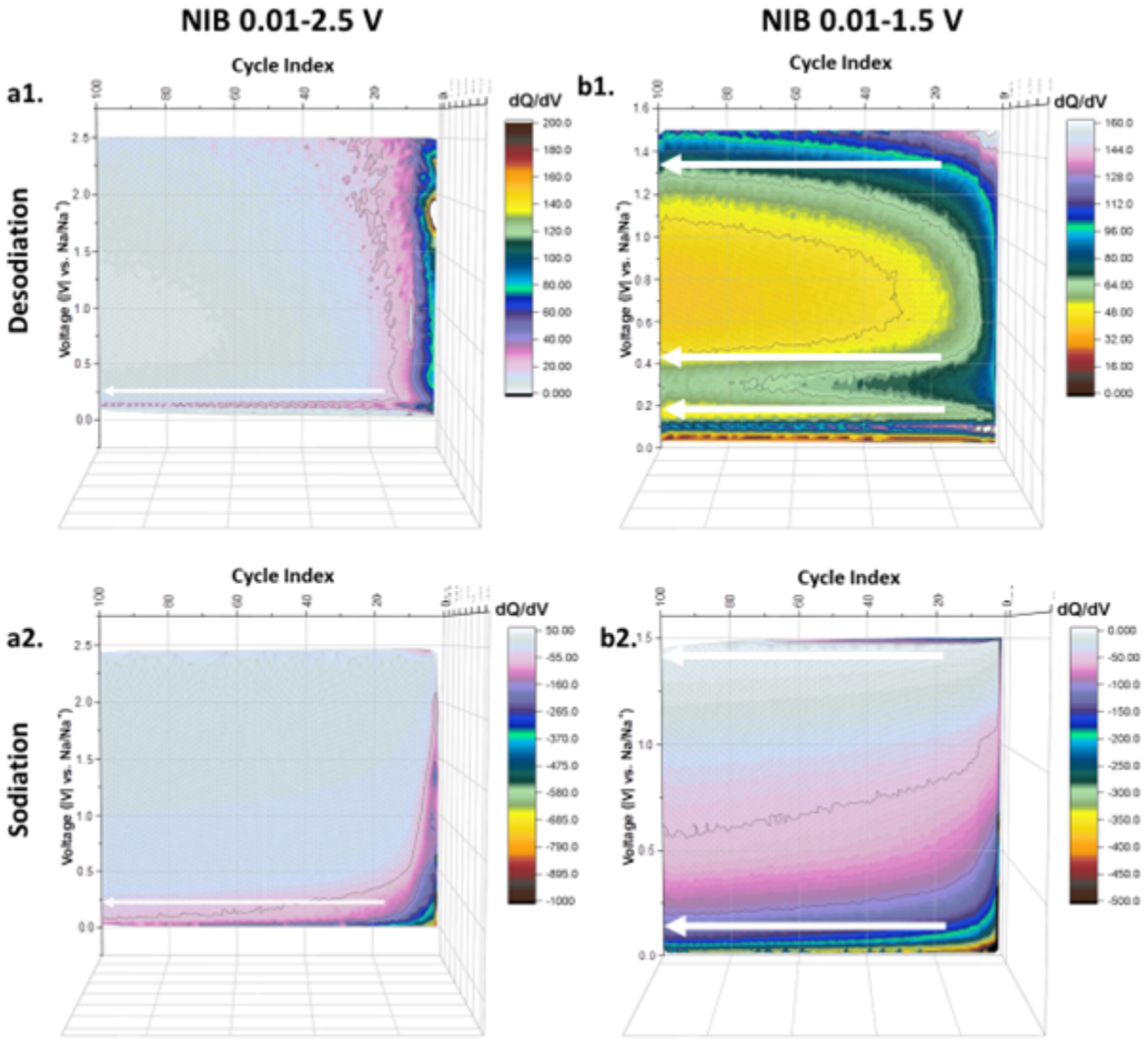


Figure 6.8: *Surface plots derived from the 3D differential capacity curves for NIB half-cells during a1. 0.01-2.5 V desodiation stage, a2. 0.01-1.5 V sodiation stage, b1. 0.01-1.5 V desodiation stage, b2. 0.01-1.5 V sodiation stage.*

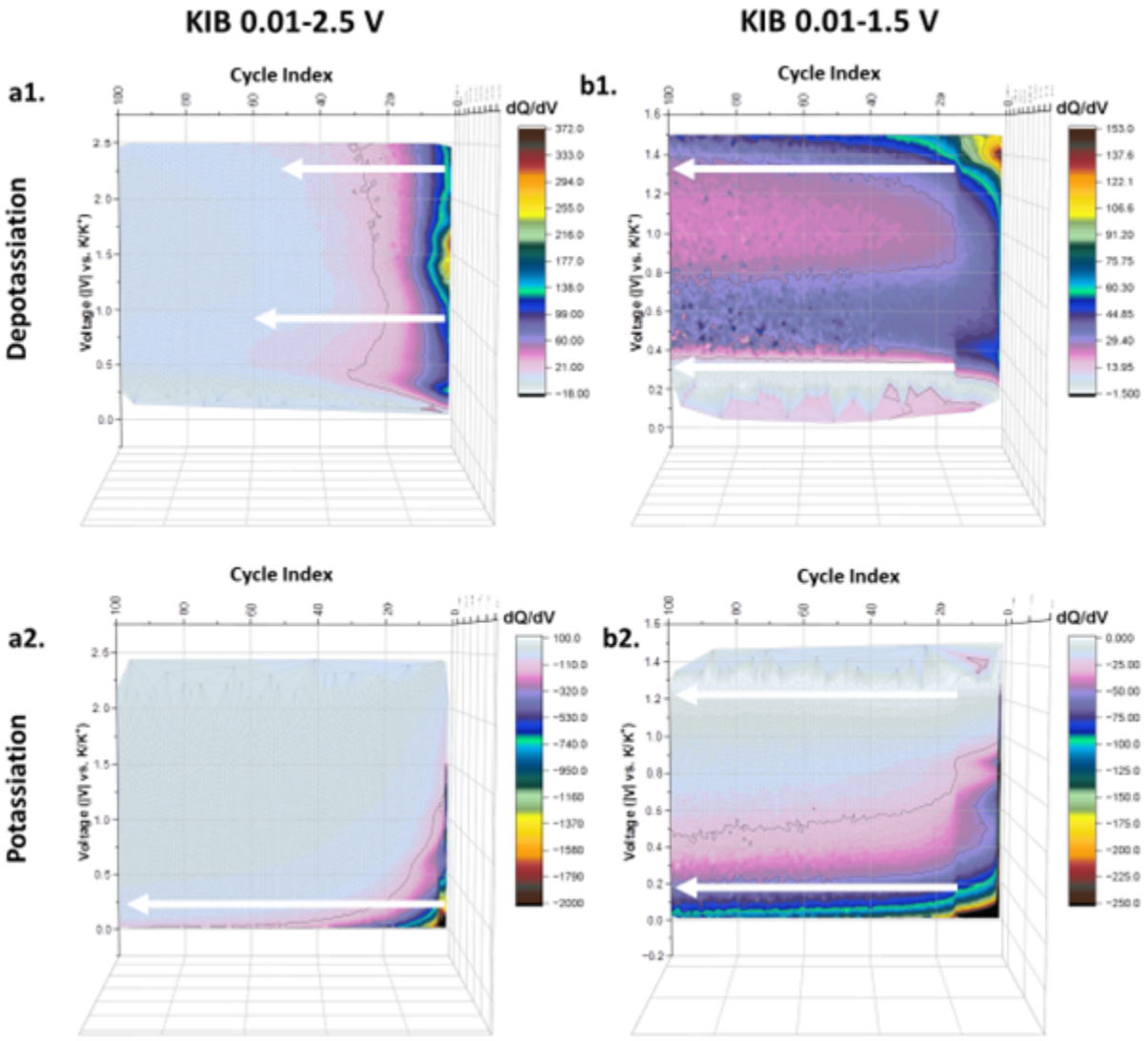


Figure 6.9: *Surface plots derived from the 3D differential capacity curves for KIB half-cells during a1. 0.01-2.5 V depotassiation stage, a2. 0.01-1.5 V potassiation stage, b1. 0.01-1.5 V depotassiation stage, b2. 0.01-1.5 V potassiation stage.*

Table 6.2: *Elemental composition determined by XPS*

Samples	Atomic (wt.%)					
	W	S	O	C	F	P
IF-WS_2 Powder	31.95	36.9	31.15	-	-	-
LIB 2.5V	3.12	2.19	42	46.66	4.74	0.48
NIB 2.5V	1.79	3.74	39.73	29.88	3.84	-
KIB 2.5V	0.27	0.91	13.73	65.24	2.57	0.57
LIB 1.5V	2.05	0.76	595.1	31.52	5	0.68
NIB 1.5V	10.31	-	54.33	15.96	0.97	-
KIB 1.5V	2.36	2.26	14.61	54.89	1.53	6.28

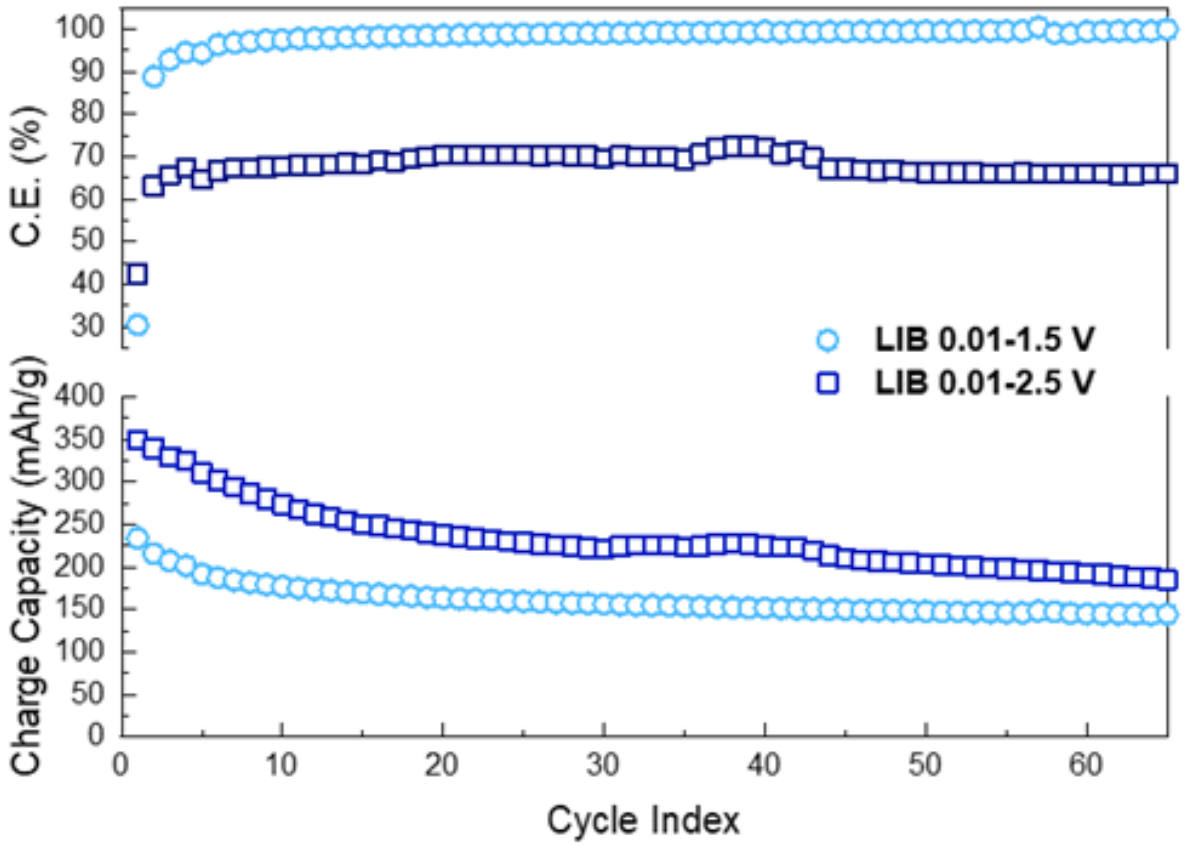


Figure 6.10: *Cycling stability test of LIB half-cells cycled at 0.01-1.5 V and 0.01-2.5 V range.*

Table 6.3: *Comparative electrochemical properties of different WS_2 quantum-confined structures.*

Electrodes	Properties	Half-cell Systems		
		LIB	NIB	KIB
WS_2NS	Charge Capacity (mAh g^{-1})	524.83	263.07	79.59
	Discharge Capacity (mAh g^{-1})	699.31	377.84	325.03
	C.E. (%)	75.37	69.63	24.49
WS_2NT	Charge Capacity (mAh g^{-1})	824.01	419.11	487.93
	Discharge Capacity (mAh g^{-1})	1126.81	604.96	1356.73
	C.E. (%)	73.13	69.28	35.96
WS_2IF	Charge Capacity (mAh g^{-1})	349.67	299.82	423.66
	Discharge Capacity (mAh g^{-1})	824.56	612.57	1805.15
	C.E. (%)	42.40	48.98	23.50

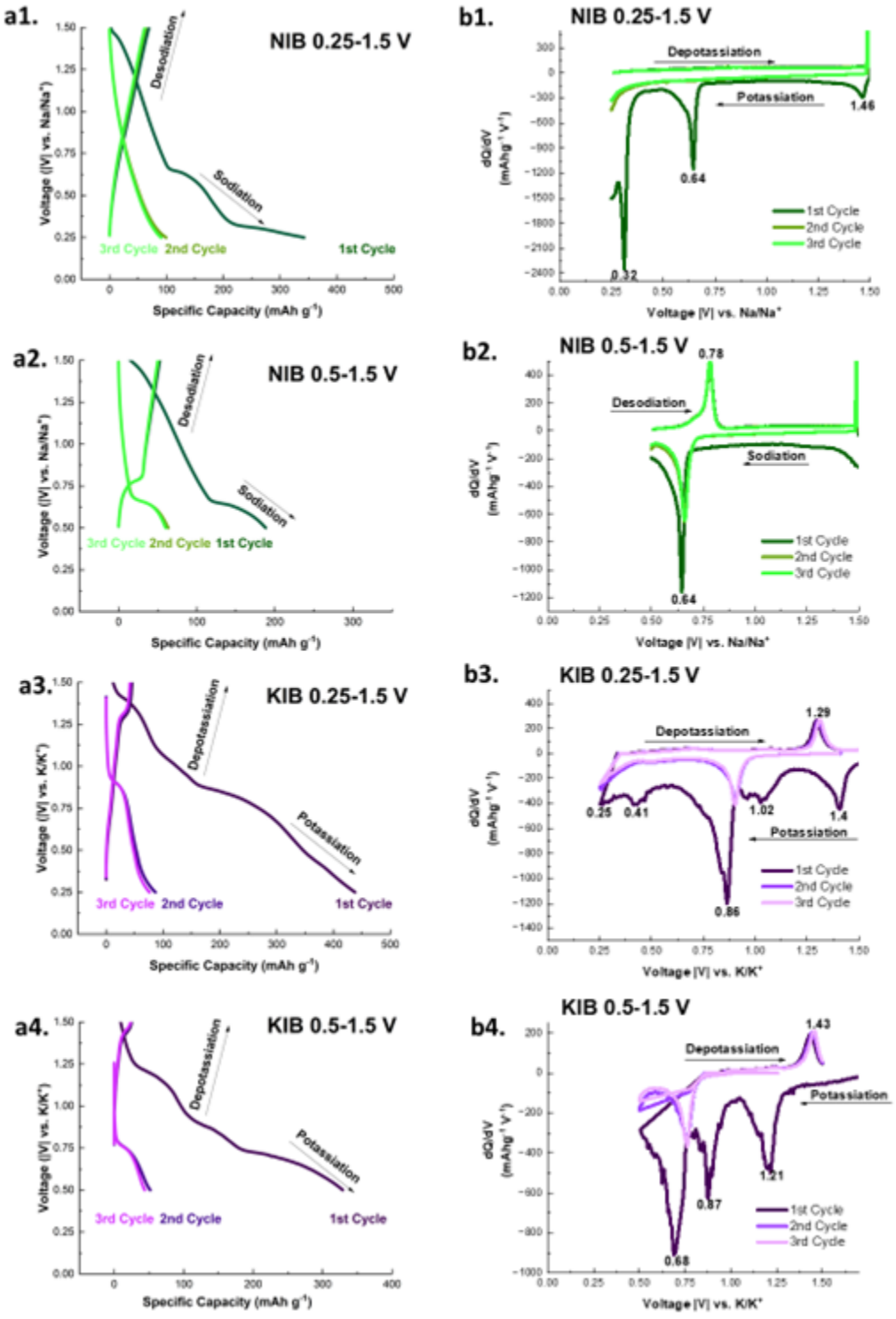


Figure 6.11: *GCD curves of a1. NIB 0.25-1.5 V, a2. NIB 0.5-1.5 V, a3. KIB 0.25-2.5 V, a4. KIB 0.5-1.5 V half-cells; differential capacity curves of: b1. NIB 0.25-1.5 V, b2. NIB 0.5-1.5 V, b3. KIB 0.25-2.5 V, b4. KIB 0.5-1.5 V half-cells.*

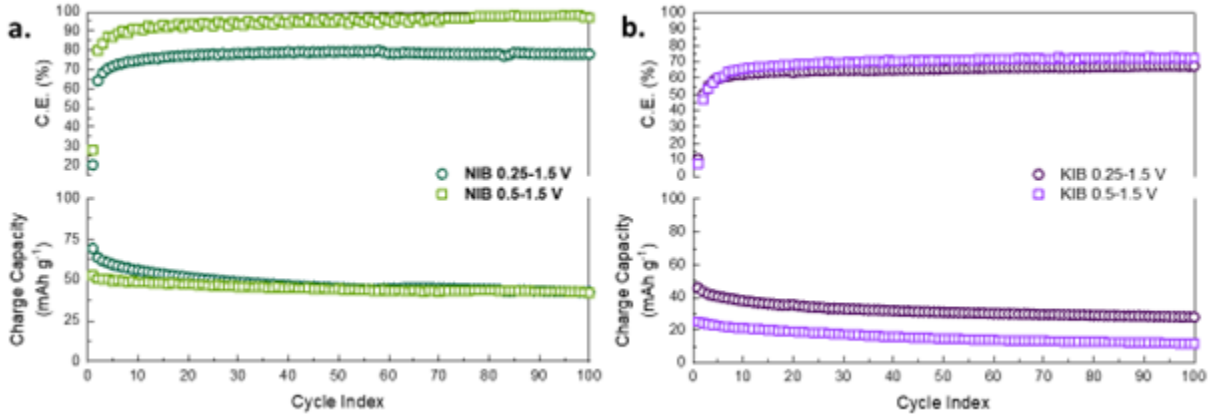


Figure 6.12: *Cycling stability test of a. NIB half-cells cycled at 0.25-1.5 V and 0.5-2.5 V range; b. KIB half-cells cycled at 0.25-1.5 V and 0.5-2.5 V range.*

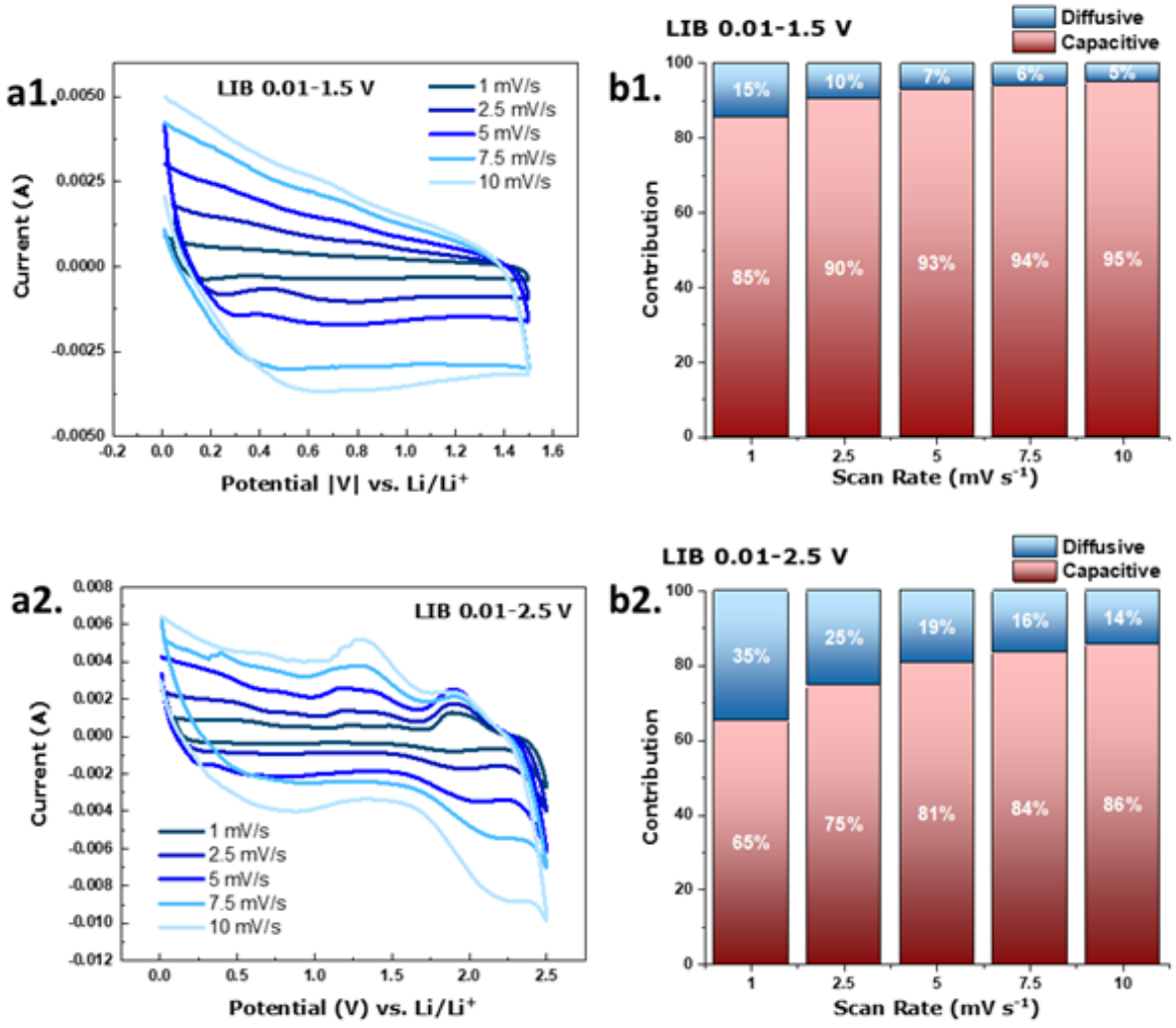


Figure 6.13: *CV curves of a1. LIB 0.01-1.5 V, a2. LIB 0.01-2.5 V half cells; capacitive and diffusion-controlled contribution ratios for different scan rates of b1. LIB 0.01-1.5 V, b2. LIB 0.01-2.5 V half-cells.*

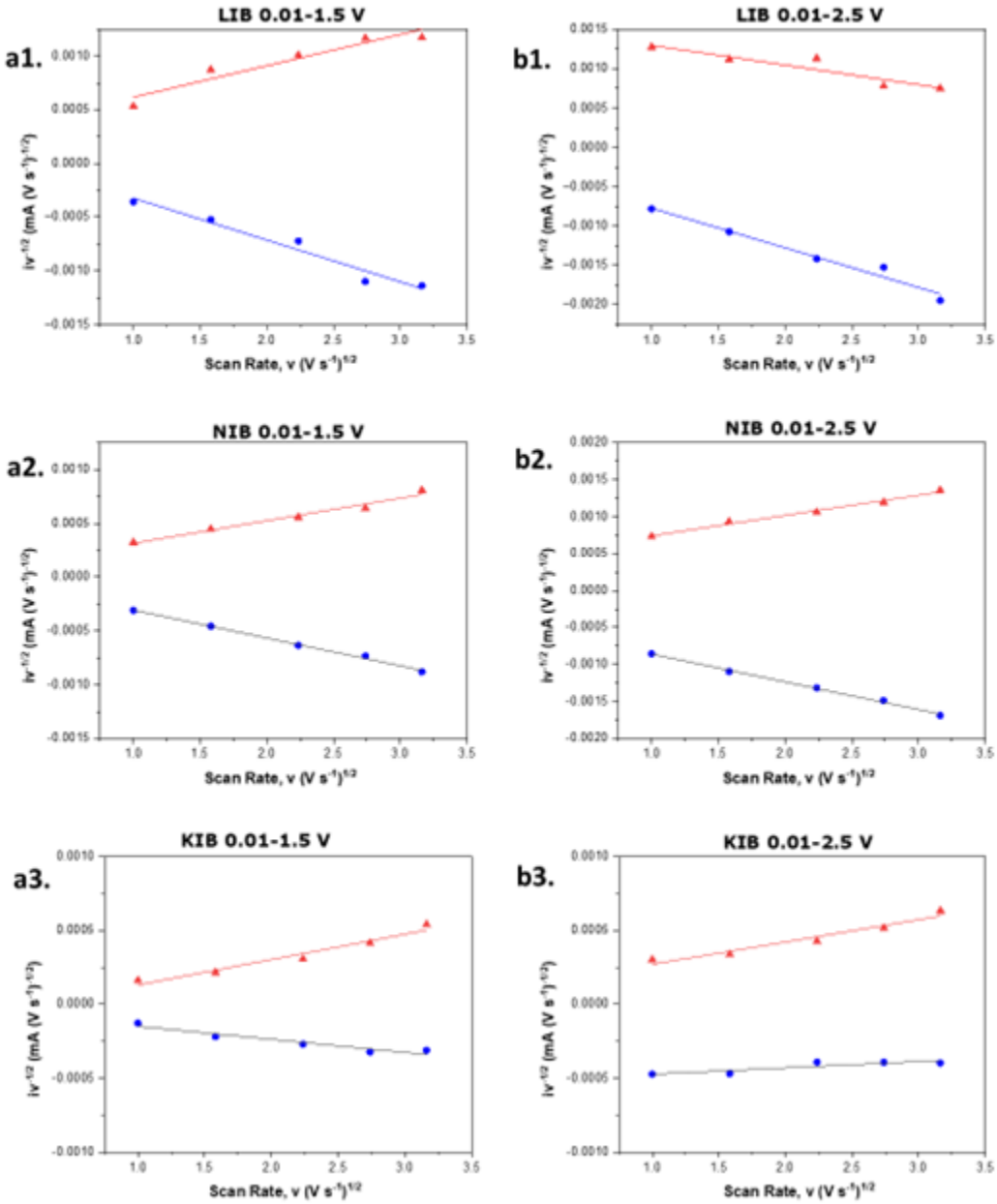


Figure 6.14: *Fitting of anodic and cathodic voltammetric sweep data of a1. LIB 0.01-1.5 V, a2. NIB 0.01-1.5 V, a3. KIB 0.01-1.5 V, b1. LIB 0.01-2.5 V, b2. NIB 0.01-2.5 V, b3. KIB 0.01-2.5 V half-cells.*

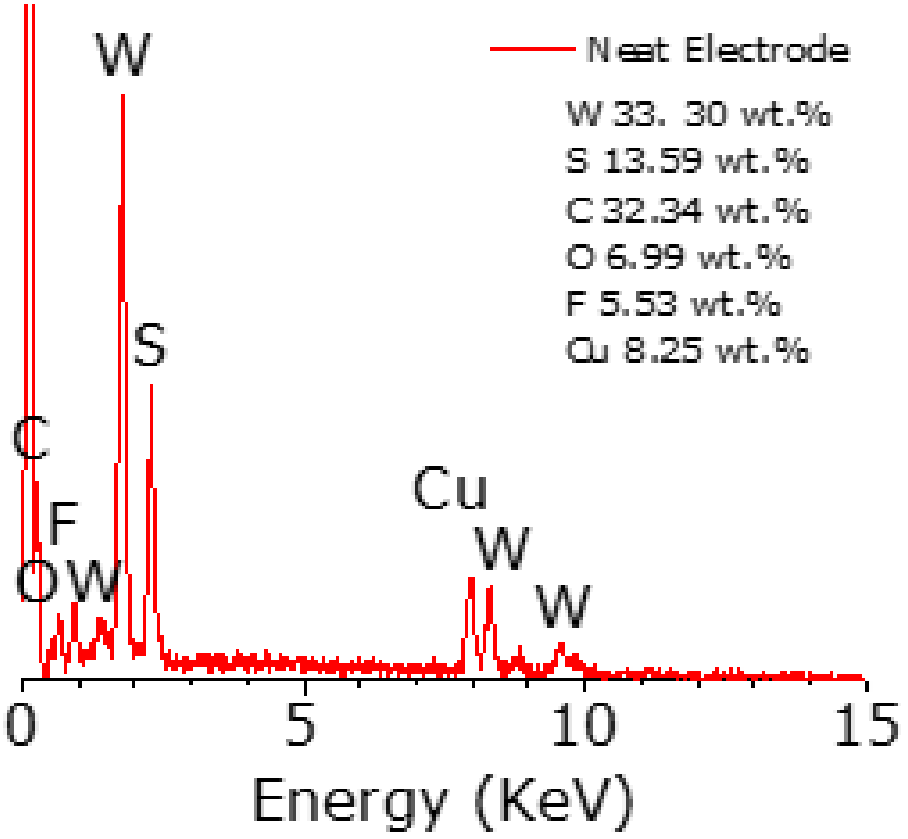


Figure 6.15: *XRF spectrum and elemental composition (determined by XRF) of the neat electrode (before cycling).*

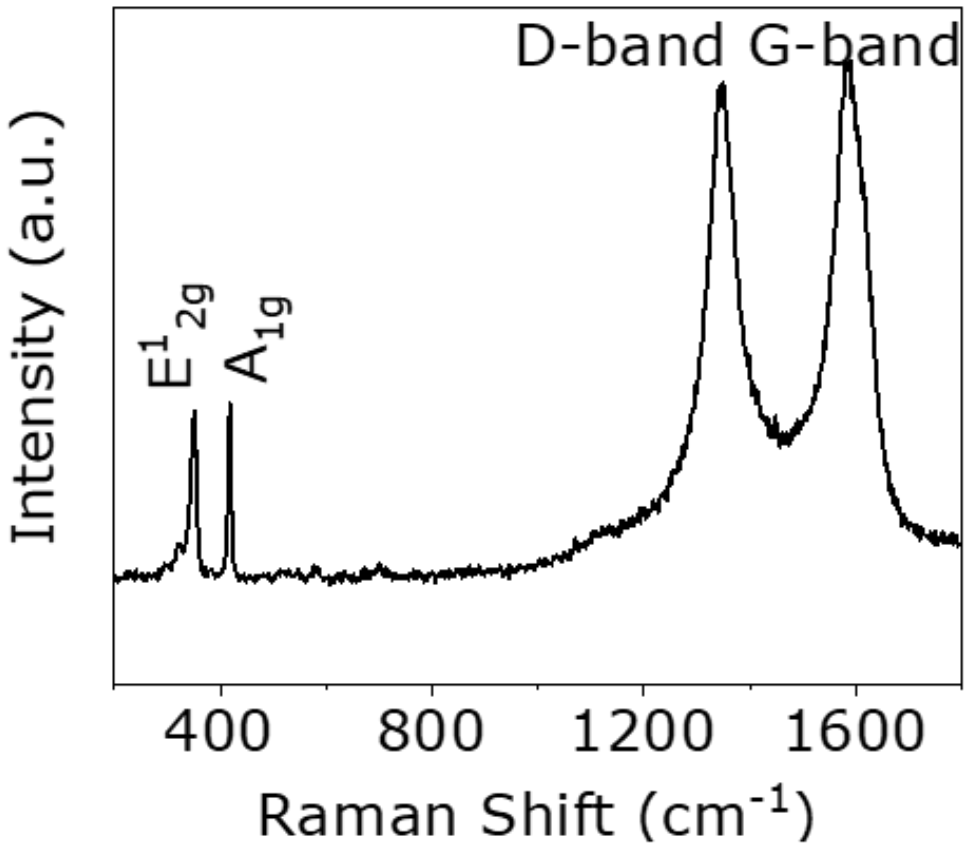


Figure 6.16: *Raman spectrum of the neat electrode (before cycling).*

Chapter 7

Sodium and Potassium ion storage in Cation Substituted 2D $MoWSe_2$: Insights into the Effects of Upper Voltage Cut-off[1]

7.1 Preface

The superior properties, such as large interlayer spacing and the ability to host large alkali-metal ions, of two-dimensional (2D) materials based on transition metal di-chalcogenides (TMDs) enable next-generation battery development beyond lithium-ion rechargeable batteries. In addition, compelling but rarely inspected TMD alloys provide additional opportunities to tailor bandgap and enhance thermodynamic stability. This study explores the sodium-ion (Na-ion) and potassium-ion (K-ion) storage behavior of cation-substituted molybdenum tungsten diselenide ($MoWSe_2$), a TMD alloy. This research also investigates upper potential suspension to overcome obstacles commonly associated with TMD materials,

[1] Dey, Sonjoy, and Gurpreet Singh. "Sodium and potassium ion storage in cation substituted 2D $MoWSe_2$: Insights into the effects of upper voltage cut-off." Nanotechnology (2023).

such as capacity fading at high current rates, prolonged cycling conditions, and voltage polarization during conversion reaction. The voltage cut-off was restricted to 1.5 V, 2.0 V, and 2.5 V to realize the material's Na^+ and K^+ ion storage behavior. Three-dimensional (3D) surface plots of differential capacity analysis up to prolonged cycles revealed the convenience of voltage suspension as a viable method for structural preservation. Moreover, the cells with higher potential cut-off values conveyed improved cycling stability, higher and stable coulombic efficiency for Na^+ and K^+ ion half-cells, and increased capacity retention for Na^+ ion half-cells, respectively, with half-cells cycled at higher voltage ranges.

7.2 Introduction

Investigations of TMDs that include MoS_2, $MoSe_2$, WS_2, and WSe_2 as electrodes in electrochemical energy storage devices have increased in recent years, encompassing practical research of traditional Li^+ ion-based rechargeable batteries and next-generation, earth-abundant sodium-ion batteries (NIBs) and potassium-ion batteries (KIBs)[77;292;351]. However, TMD's inherent drawbacks (low electronic conductivity and severe volume change during electrochemical redox reaction) yield undesirable outcomes, such as menial reaction kinetics, capacity fading, and intense polarization that decreases energy inefficiency[208]. Strategies such as the interlayer expansion of lamellae to enhance the intercalation reaction[47;300], improve reaction kinetics via conductive skeleton materials[129;183;204], and distinctive nanostructure formation to amplify rate capability and cycling efficiency[145;303;321] have been widely investigated. However, these modification procedures usually require a complicated synthesis route with convoluted parameters. Nevertheless, several intercalating agents introduce impurities within the material, further sacrificing the conductivity of TMDs[10], while other utilized techniques induce regional atomic disorder and generate a 1T phase[36;300]. In addition, coupling with conductive materials such as graphene paper and carbon additives supplementally reduces energy density. Therefore, future research should include deterministic methodical strategies.

Doping and alloying have been shown to effectively tailor the intrinsic properties of TMDs,

and a substitutional alloying strategy can engineer TMD bandgaps. For example, the substitution of anion and cation sites within MoS_2 to fabricate $Mo_xW_{1-x}S_2$, $MoS_{2x}Se_{2(1-x)}$ has resulted in a tuned bandgap of 1.8–2.0 eV and 1.6–1.9 eV, respectively[32;140]. In addition, an informed choice of transition metal alloying potentially increases the thermodynamic stability of ordered materials with a wide bandgap tuning ability of approx. 1 eV[83]. Because TMD materials have many atomic species, the versatile chemistry of TMD alloys increases their potential for engineering nanoscale applications. Consequently, TMD alloys have already been utilized in a wide range of practical devices, such as water splitting[21], photovoltaics[13], and gas sensing[192].

Overall, current research regarding electrochemical energy storage devices has focused on the application of TMD alloys, but most of the research has highlighted their usage in Li^+ ion-based storage technologies[116;126;155], with only a few investigations of earth-abundant, beyond lithium-ion (Li^+ ion)-based storage opportunities. For example, Mudgal et al. investigated MoSeTe as an anode for NIBs, but the study only investigated up to 10 cycles. Furthermore, few studies have utilized anion-substituted TMD alloys, such as MoSSe, with carbon additives, such as N-doped carbon[96], rGO[79], and carbon nanotubes[237]. The aforementioned techniques potentially decrease the energy density in a full cell, thereby significantly affecting the charge transport due to variations in bonding and relative position of TMD and carbon[383]. Hanna et al. created anion vacancies to investigate MoSSe in KIB storage applications by tediously optimizing the Se:S ratio during alloying to tailor particular properties[12]. Although a plethora of literature addresses anion-substituted TMD alloy for electrochemical energy storage devices, only a few investigations focus on cation-substituted TMD alloy and even less focus on NIBs and KIBs. For example, $MoWSe_2$ has been investigated as a potential LIB electrode, but the study considered using a three-electrode system, which exceeds the scope of practical application[?] .

This report investigates the applicability of $MoWSe_2$, a cation-substituted TMD alloy, beyond Li^+ ion storage application, specifically the Na^+ and K^+ ion storage properties of the $MoWSe_2$ alloy and subsequent internal reactions. This study also investigated the promise of $MoWSe_2$ in Na-ion and K-ion half-cells by reducing the upper potential values to prevent

structural distortion of the $MoWSe_2$ alloy. Although TMDs utilize both intercalation and conversion reactions during alkali-metal ion storage and their structural distortion occurs during prolonged cycling, previous studies have indicated that structural integrity preservation plays a decisive role in reaching the goal of stable capacity[6;188]. The structural disintegration is even more prominent beyond Li-ion storage technologies as Na^+ and K^+ ions are bulkier in size and possess slower diffusion kinetics than Li^+ ions. For cation-substituted TMD alloys such as $MoWSe_2$, a comparatively higher conversion reaction rate was expected than the neat TMDs, potentially leading to severe structure pulverization, as proven by broadened peaks of the differential capacity curves for both $MoSe_2$ and WSe_2. Therefore, the upper potential suspension strategy was utilized to preserve the crystal structure within the material-restricting pulverization of the $MoWSe_2$ alloy to achieve stability during rate capability and the long-term cyclability test. The upper potential cut-off approach revealed that $MoWSe_2$ electrodes cycled in a range of 0.01–1.5 V, with approximately 29% higher capacity retention for Na^+ ion half-cells due to the restriction of specific reactions. Moreover, higher coulombic efficiency was observed, reaching near 100% for a half-cell cycle at 0.01–1.5 V. Therefore, the upper potential restriction could be vital for studying Na^+ and K^+ ion storage in TMD alloys to improve cycling stability.

7.3 Materials, Methods, and Characterization

7.3.1 Morphologic and Spectroscopic Characterization

This study carried out transmission electron microscopy (TEM) and energy-dispersive x-ray spectroscopy (EDX) on an FEI Tecnai Osiris 200 kV. Selected area electron diffraction (SAED) image was obtained using Phillips CM100 TEM. Raman spectrum of the sample utilized a LabRAM ARAMIS Jobin Yvon Raman spectrometer with a HeNe laser ($\lambda = 633$ nm) as an excitation source. X-ray photoelectron spectroscopy (XPS) data were obtained using a thermo scientific equipped with a monochromatic Al anode Kα (hν = 1486.6 eV) with in-situ sputtering of Ar+ at 3.0 keV for 120 s. Scanning electron microscopy (SEM)

images of the disassembled cells were collected using Hitachi SU8010. The IXRF system obtained the corresponding X-ray fluorescence (XRF) spectrum.

7.3.2 Electrochemical Characterization

The preparation of electrodes included 70wt% of $MoWSe_2$ powder as received (Ossila, 99.9%), 15 wt.% of carbon black (Alfa Aesar, 99.9%), and 15 wt.% poly (vinylidene fluoride) (Alfa Aesar) mixed with a few drops of 1-Methyl-2-pyrrolidinone (Sigma Aldrich) until a homogenous slurry was achieved. The obtained slurry was coated onto a copper foil with a thickness of 9 µm and dried at 80 °C overnight. The obtained coating on the copper foil (125 µm thick) was cut into circular sections with diameters of 14.29 mm, which were used as working electrodes in Na^+ ion and K^+ ion half-cells, where the counter electrodes were Na and K metal, respectively. The electrolytes for Na^+ ion and K^+ ion half-cells were 1.0 M $NaClO_4$ (Alfa Aesar) in (1:1 v/v) Ethylene Carbonate (EC): Dimethyl Carbonate (DMC) (anhydrous, 99% Sigma Aldrich) and 1.0 M KPF_6 (Alfa Aesar) in (1:1 v/v) EC: DMC, respectively. All the half-cell assemblies utilized a high-precision argon atmosphere with O_2 and H_2O contents below 0.1 ppm. An Arbin BT 2000 test unit was used to investigate the electrochemical behavior of the assembled CR-2023 coin cells under potential ranges of 0.01–1.5 V, 0.01–2.0 V, and 0.01–2.5 V. A rate capability test was done under asymmetric cycling, in which sodiation and potassiation were carried out in 100 mA g^{-1} current density, and desodiation and depotassiation were carried out with stepwise increase and varying current densities. In addition, the cycling stability of electrodes was investigated under symmetric cycling conditions of 100 mA g^{-1} current density.

7.4 Results and Discussions

7.4.1 Microscopic and Spectroscopic Analysis

Figure 7.1a shows the low-resolution TEM micrograph of the $MoWSe_2$ sheets with a 120° edge angle, which is typical for TMD nanosheets. Figures 7.1b and 7-1c further illustrate

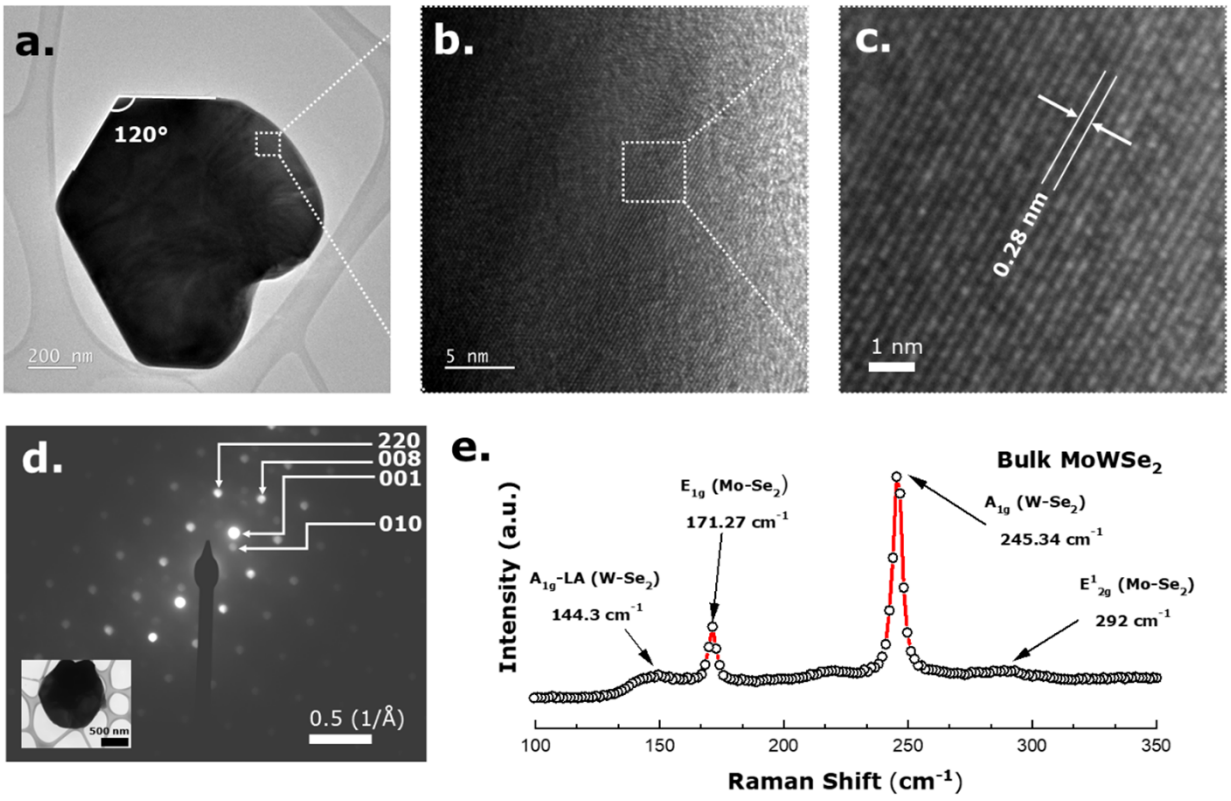


Figure 7.1: *a) Low-resolution TEM images of the $MoWSe_2$ flakes; b, c) high-resolution TEM images of $MoWSe_2$ nanosheets; d) six-fold symmetrical SAED spot pattern generated from the $MoWSe_2$ bulk flake shown in the index; e) Raman spectrum of bulk $MoWSe_2$ alloy depicting different vibrational modes.*

the sheet-like stacked structure of the $MoWSe_2$, confirming the existence of the bulk sheets. The fringes observed in Figure 7.1c were further analyzed to investigate the distance between them. Specifically, the fast Fourier transform (FFT) of Figure 7.1c, inverse FFT from the brightest spot, and finally, the fringe intensity profile (Figure 7.8a-c, respectively) were analyzed. The inter-fringe distance was found to be approx. 0.28 nm – in agreement with the interlayer lattice spacing value regarding (100) and (101) planes of hexagonal $MoSe_2$ and WSe_2[137]. Figure 7.1d shows the selected area electron diffraction pattern (SAED) of bulk $MoWSe_2$ powder. TEM micrograph on the inset of Figure 7.1d shows the flake from where the SAED was obtained. Specifically, the six-fold symmetrical spot pattern reflection from the SAED indicates the polycrystalline nature of the $MoWSe_2$ flake. Individual spots were assigned to the combination of (010), (220) planes of $MoSe_2$[318;379] and (001), (008) planes of

WSe_2 material[163].

Raman spectroscopy was used to characterize the bulk $MoWSe_2$ powder to confirm the presence of both Mo and W species bonded with Se. In addition, Raman spectra of the bulk $MoSe_2$ and WSe_2 powders were obtained and analyzed for comparison with bulk $MoWSe_2$ powder. The detailed analysis of the bands originating from the Raman spectra of $MoSe_2$ and WSe_2 bulk powders is provided in the supplementary information Figure 7.9(a-c). Figure 7.9c shows the schematic of various vibration modes originating from typical TMD materials. The A_{1g} vibration mode arises from the out-of-plane relative motion of the Se atoms concerning the Mo/W atom being stationary. In contrast, the E^1_{2g} vibration mode dictates the in-plane opposing vibration of Mo/W and Se atoms, and the E_{1g} mode defines the in-plane relative vibrational motion of the chalcogen atoms (Se)[14].

The as-obtained Raman spectrum of $MoWSe_2$ powder is illustrated in Figure 7.1e, which shows the intense and prominent out-of-plane A_{1g} mode of Mo bonded with Se[2]. For the $MoWSe_2$ alloy, the A_{1g} mode shifted from 240.1 to 249.3 cm-1, depending on the composition of W ranging from 0 to 1 in $Mo_{1-x}W_xSe_2$. This shift in A_{1g} mode originating due to linear dependence of W atoms indicates that the examined sample typically possesses x = 0.5 fraction - further indicating that the Mo : W ratio was 1:1 in the bulk material[305]. Noticeably, this peak may look broader due to the proximity of the A_{1g} and E^1_{2g} modes of WSe_2[202]. Peaks at 171.27 cm-1 and 292 cm-1 were also observed due to the E_{1g} and E^1_{2g} modes of $MoSe_2$, respectively[28;271]. Additionally, one weaker peak at 144.3 cm-1 originated from the A_{1g}-LA (longitudinal acoustic) mode of WSe_2 due to single degenerate vibrations of the lattice[110]. Modes such as E_{1g}+A_{1g}, E^1_{2g}+LA(M), and E^1_{2g} + E_{1g}, which are typically observed in monolayer and bilayer materials, were noticeably absent in the bulk $MoWSe_2$ with the Mo and W ratio of 1:1[305]. Moreover, in the bulk material, the B^1_{2g} mode was not visible for being Raman inactive, typically originating due to increased symmetry in the monolayer or bilayer materials[158;349].

Figure 7.2a shows the XPS survey scan of the $MoWSe_2$ powder, and Figures 7.2(b–d) present high-resolution scans of the Mo3d, W4f, and Se3d spectra, respectively. In addition to the desired Mo, W, and Se elements, other peaks were observed in the survey scan due to

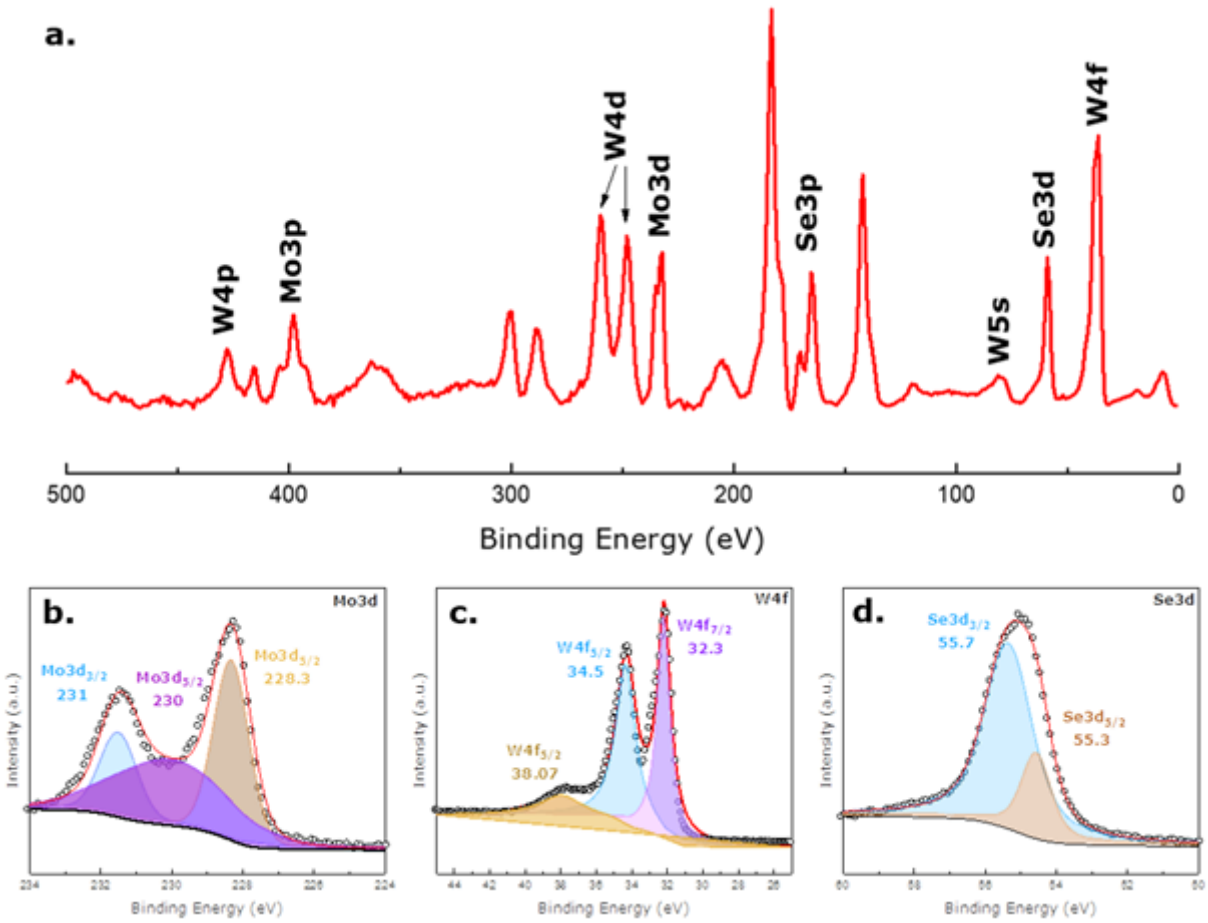


Figure 7.2: *a) XPS survey scan depicting the presence of different materials within $MoWSe_2$; high-resolution b) Mo3d; c) W4f; d) Se3d XPS spectra of the $MoWSe_2$ material illustrating the chemical bonding states.*

the sample preparation process. The atomic wt.% of the elements in the sample, specifically Mo (7.96), W (10.61), and Se (26.57) maintain close to a 1:1:2 stoichiometric ratio. The deconvolution of Mo3d high-resolution spectra in Figure 7.2b shows three distinct peaks: the Mo3d3/2 peak in the 231 eV region due to elemental Mo species[220] (possibly due to the sputtering process before XPS measurement) and two Mo3d5/2 peaks in the 230 eV and 228.3 eV regions, indicating the oxidized Mo species[264] (due to the sample preparation process) and Mo bonded with Se, respectively[390]. The peak-fitted W4f spectra revealed three peaks at 38.07 eV, 34.5 eV, and 32.3 eV (Figure 7.2c), with the first peak being the W4f5/2 peak from the oxidized WOx/W species[53] and the W4f5/2 and W4f7/2 peaks from the WSe_2 species[273], respectively. Finally, the deconvoluted Se3d spectra (Figure 7.2d) show

two Se3d3/2 peaks at 55.7 eV and 55.3 eV, with the former from the di-selenide moiety of $MoSe_2$ [120] and the latter from the WSe_2 [90].

7.4.2 Electrochemistry

Na^+ ion Storage

This study investigated Na^+ ion electrochemical reactions during sodiation/desodiation in the $MoWSe_2$ electrode using characteristic galvanostatic charge-discharge curves. The derived differential capacity curves from the charge-discharge curves provided the plateau regions of the charge-discharge curves as specific peaks at 100 mA g^{-1}. Figure 7.3a illustrates the sodiation/desodiation within the potential range of 0.01–2.5 V. As shown in the derived differential capacity curve in supplementary Figure 7.10a, several peaks indicate a mixture of reactions with $MoSe_2$ and WSe_2 within the TMD alloy ($MoWSe_2$) during the first-cycle sodiation. The first-cycle sodiation curve has major peaks at 0.59 V, 0.53 V, 0.16 V, and 0.01 V, possibly due to the Na/Se conversion reaction and the formation of the irreversible solid electrolyte layer (SEI) (0.01 V), as shown in Figure 7.10a with an intense peak only in the first cycle. Previous studies ascribed peaks near the approx. 0.5 V region to the irreversible conversion reaction of $MoSe_2$, and peaks ¡0.25 V were ascribed to the conversion reaction from the WSe_2 conversion product [45;139;235].

Although both reactions of the $MoWSe_2$ electrode appeared in the first-cycle sodiation curves, peaks in the 1.48 V and 1.87 V regions began to appear in the second cycle due to possible intercalation of Na^+ ions into the layers of $MoWSe_2$, as visible up to the 50th cycle (Figure 7.3b and Figure 7.10a). As mentioned, the peak intensity decreased from the first to the 50th cycle, potentially indicating fewer sites of $MoWSe_2$ to facilitate the gradual intercalation of Na^+ ions. A notable peak shift of the 1.48 V and 1.87 V reactions was observable in subsequent cycles to lower potential values, as shown in the surface plot (Figure 7.3b) and the 2D plot (Figure 7.10a). The shift for the 1.48 V peak was 0.03 V, while the observed shift for the 1.87 V peak was 0.06 V for the 0.01–2.5 V electrode (Figure 7.10a). Noticeable peaks were observed at 0.1 V, 1.73 V, and 2.1 V (Figure S3a) in the first-cycle

desodiation curve, of which the 1.73 V and 2.1 V peaks may be due to the reverse conversion and intercalation reactions, respectively. Previous literature has attributed the approx. 1.7 V peak to the extraction of Na^+ ions from WSe_2 electrodes or the reverse conversion reaction, but the 2.1 V is due to the reverse Na-Se reaction or the reverse intercalation reaction[98]. Although a shift of 0.04 V was observed for the 1.73 V peak up to the fifth cycle, the 2.1 V peak showed no such phenomenon (Figure 7.10a). Previous studies have suggested that the shift of peak locations to higher potential values during charge and lower potential values during discharge are due to resistive and diffusive polarization effects[230]. Because a lower voltage shift of peaks was discerned for the intercalation reaction, the conversion reaction may cause the most polarization effect. Moreover, the three-dimensional (3D) differential capacity curves of the desodiation cycle in Figure 3c show that the 0.1 V peak continues up to 140th cycle with slight polarization from the 100th cycle. In addition, the surface plot shows that the 2.1 V and the 1.73 V merge into one 1.73 V peak up to the 75th cycle and then eventually decrease in intensity, indicating a permanent structural change after the specific cycle.

The $MoWSe_2$ electrode was cycled within the potential range of 0.01–2.0 V in similar conditions. The characteristic differential capacity curve (Figure 7.10b) derived from the galvanostatic charge-discharge curve (Figure 7.3d) of the half-cell showed the same peaks, indicating no unique reactions due to upper voltage cut-off values. For the 0.01-2.0 V cell, several peaks typically due to conversion and intercalation reactions appeared at 1.25–2.0 V, with the center peak at 1.73 V (Figure 7.3e). The 1.73 V peak was visible up to the 90th cycle, as shown in the surface plot (Figure 7.3e) with a green peaked contour profile, comparatively better than the 0.1–2.5V cell, indicating the advantage of upper voltage suspension for structural stability. Although the peak shift of the desodiation curve (Figure 7.3f) showed values similar to the 0.01–2.5 V cell, higher values of the shift were observed for the peak at 1.73 V, indicating a change in 0.06 V up to five cycles.

When the $MoWSe_2$ electrode was cycled in the potential range of 0.01–1.5 V (Figure 7.3g), the derived differential capacity curve (Figure 7.10c) showed no prominent peaks except the conversion reaction peaks of the first-cycle desodiation, indicating that voltage restriction

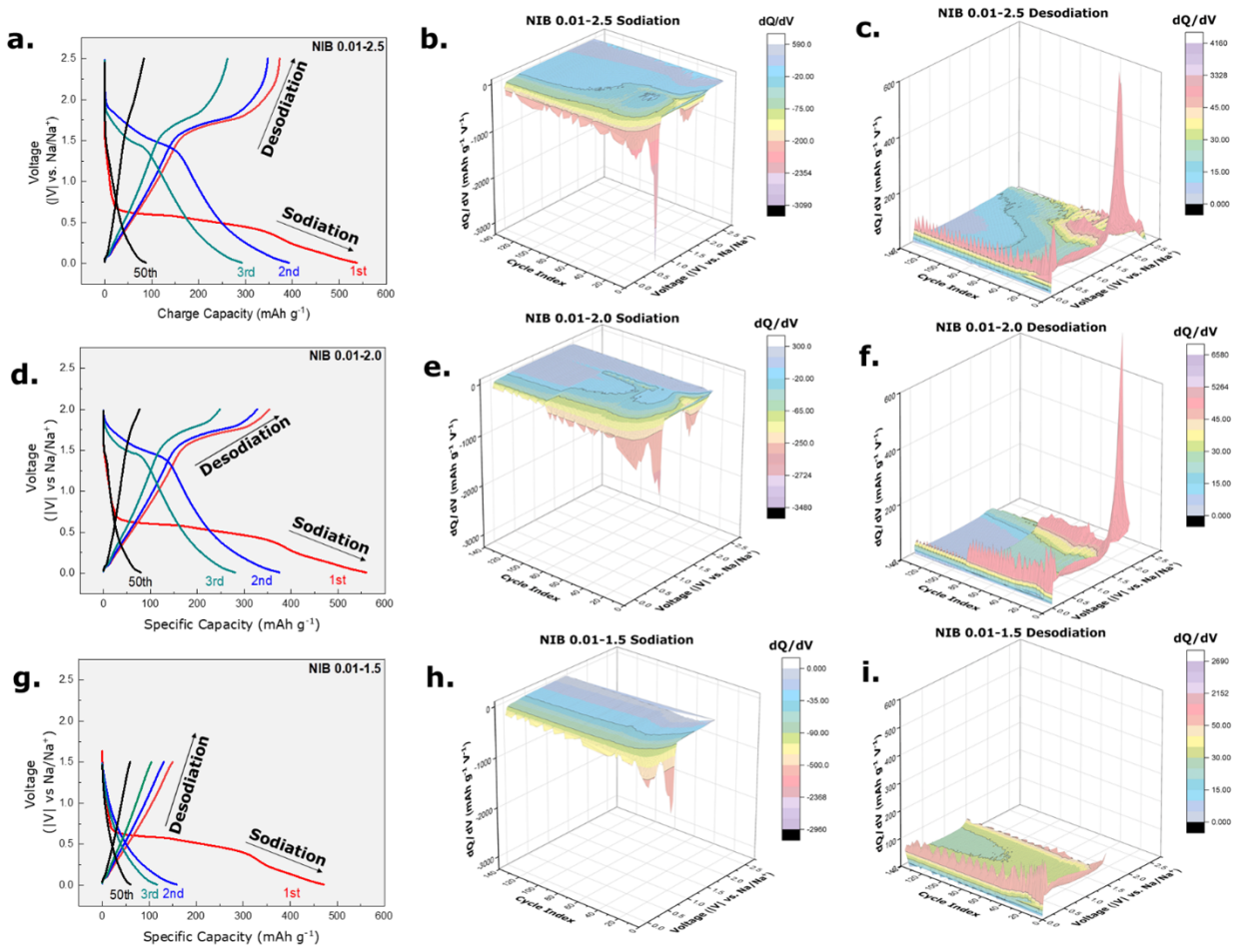


Figure 7.3: *: Investigation of Na^+ ion storage behavior: a) Galvanostatic charge-discharge curves of $MoWSe_2$ electrode cycled within 0.01-2.5 V; differential capacity curves of b) 1st-140th sodiation cycles, c) 1st-140th desodiation cycles of 0.01-2.5V $MoWSe_2$ electrode; d) Galvanostatic charge-discharge curves of $MoWSe_2$ electrode cycled within 0.01-2.0 V; differential capacity curves of e) 1st-140th sodiation cycles, f) 1st-140th desodiation cycles of 0.01-2.0V $MoWSe_2$ electrode; g) Galvanostatic charge-discharge curves of $MoWSe_2$ electrode cycled within 0.01-1.5 V; differential capacity curves of h) 1st-140th sodiation cycles, i) 1st-140th desodiation cycles of 0.01-1.5V $MoWSe_2$ electrode.*

prevents most of the redox reaction. However, a low intense peak was observed in the 1.5 V region in the desodiation curve, potentially due to a partial intercalation reaction at a lower voltage that does not fade away until the 50th cycle. Although the peaks in the sodiation (Figure 7.3h) and desodiation (Figure 7.3i) curves originating from the cell cycled at 0.01–1.5 V range were less intense than the other two cells cycled within different potential ranges, they were apparent up to the 140th cycle with consistent height (yellow for the sodiation

curve and red for the desodiation curve in Figures 7.3h and 7-3i, respectively), indicating possible structure retention in harsh and prolonged cycling. Furthermore, the conversion reactions (< 0.7 V region in green in the 3D surface plot in Figure 3h) inside the material were also visible up to the 140th cycle, with high intensity (shown in red in Figure 7.3i) for the first 20 cycles and lower intensity (shown in green in Figure 7.3i) for the remaining 120 cycles.

The performances of the three electrodes at different voltage ranges were tested in gradually increasing current densities of 100, 200, 400, 600, and 800 mA g^{-1} for five cycles and then returned to original current densities, as shown in Figure 7.3a. Both the 0.01–2.5 V and 0.01–2.0 V cells showed higher charge capacity (353 mAh g^{-1} and 372 mAh g^{-1}, respectively) than the 0.01–1.5 V cycled cell (149 mAh g^{-1}) in the initial cycles, but as shown in Figure 7.4a, in higher current densities, the 0.01–2.5 V cycled cell and the 0.01–2.0 V cycled cell showed gradual capacity fading. Less capacity fading was observed in the 0.01–1.5 V cycled cell. In the 5th, 10th, 15th, 20th, and 25th cycles, the 0.01–1.5 V cell showed 70%, 86%, 91%, 93%, and 95% capacity retention, respectively, constantly approx. 20%–30% higher than the other two electrodes, indirectly suggesting that the upper cut-off voltage significantly restricts capacity fading, leading to increased capacity retention and decreased structural distortion of the $MoWSe_2$ material. Following the rate capability test, the same cells were cycled at 100 mA g^{-1} current density for 100 cycles. As illustrated in Figure 7.4a, the capacity of the 0.01–2.5 V, and 0.01–2.0 V cells almost overlapped with the 0.01–1.5 V cells showed robust capacity up to the 140th cycle. In order to further emphasize the merits of voltage cut-off technique, three additional cells were assembled and cycled at 100 mA g^{-1}, for performance evaluation at a fixed cycling current. All three cells displayed low coulombic efficiency at the initial cycle, possibly due to the side reactions from electrolyte reduction in the initial cycle[252].

Figure 7.4a also shows that the high coulombic efficiency of the 0.01–1.5 V cycled cell exceeded 90% during the rate capability test at the seventh cycle for the Na^+ ion half-cell, while the coulombic efficiency was 4%–5% lower for the other two cells. A similar trend of coulombic efficiency was observed for the newly assembled cells cycled at three

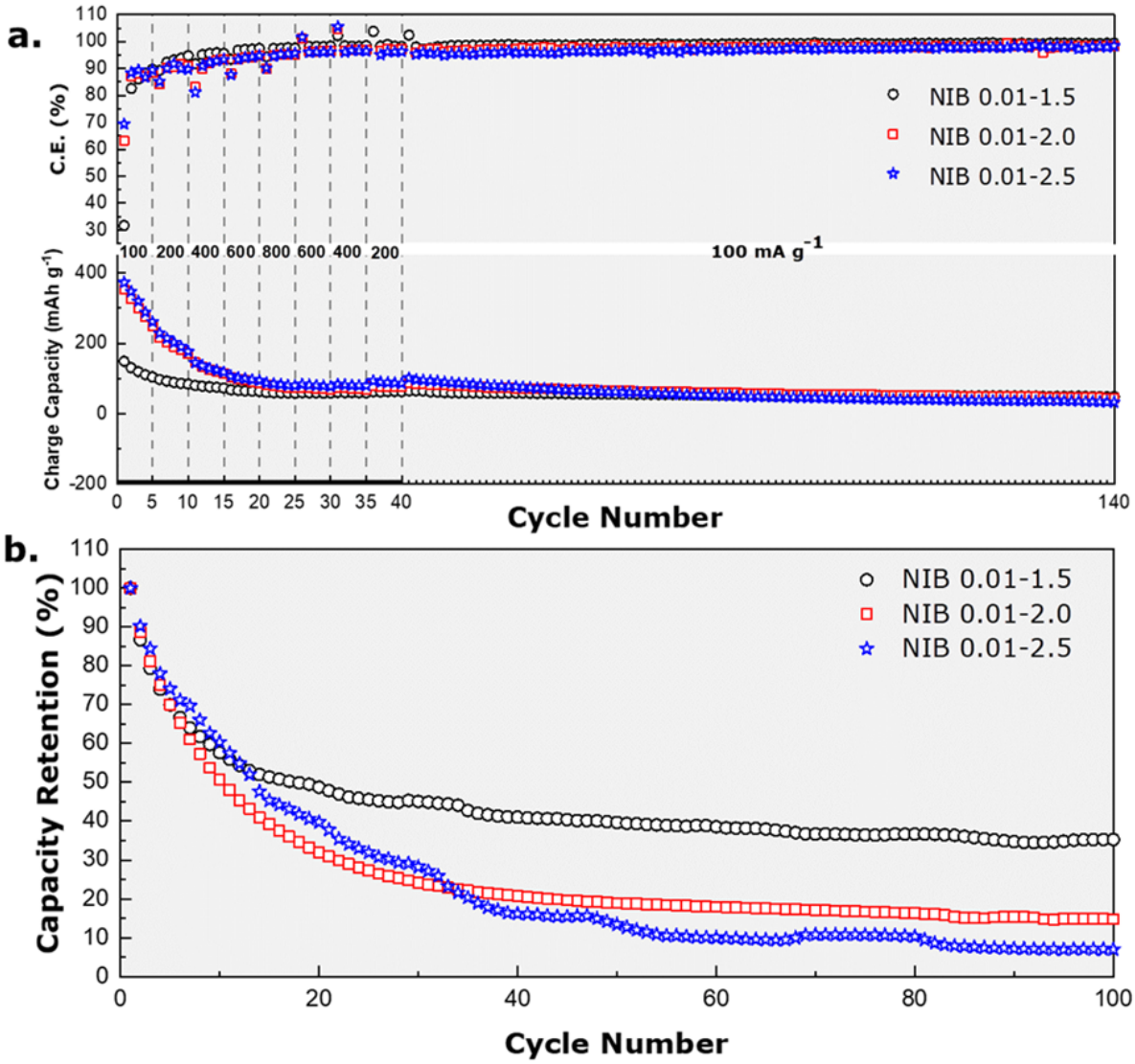


Figure 7.4: *: a) Rate capability and consecutive cycling stability tests for investigating Na^+ ion storage behavior of half-cells cycled within different potential ranges; b) capacity retention during Na^+ ion storage of different half-cells cycled at various potential ranges throughout cycling stability test derived from Figure S4.*

potential ranges during the stability test (Figure 7.11). In such conditions, the merit of upper voltage cut-off experiment was more apparent as the 0.01-2.5 V cell showed the most capacity degradation (starting from second cycle onwards), while the 0.01-1.5 V was relatively stable. Figure 7.4b shows capacity retention (derived from Figure 7.11) during the prolonged cycling period, where the cells with lower cut-off values (0.01-2.5 V) degrade fast - reaching 6.98% capacity retention in the 100th cycle. On the other hand in the 100th cycle, the

capacity retention of the 0.01–1.5 V cell was 16% and 29% higher than the 0.01–2.0 V cell and 0.01–2.5V cell, respectively, highlighting the benefits of the upper voltage cut-off for stable cycling conditions. Noticeably, capacity fading was also observed in case of the 0.01-1.5 V cell till the 14th cycle.

K^+ ion storage

K^+ ion storage behavior within the $MoWSe_2$ electrodes was investigated similarly. The differential capacity curve (Figure 7.12a) derived from the charge-discharge curve (Figure 7.5a) of the $MoWSe_2$ electrode cycled within the potential range 0.01-2.5 V indicated a combined reaction of $MoSe_2$ and WSe_2 material. Noticeably in Figure 7.5a, two prominent voltage plateaus were observed for KIB cells, while in NIB cells, one prominent plateau existed. The differential capacity curves further highlight the assignment of such plateaus. As shown in Figure 7.12a, the first cycle potassiation differential capacity curve reveals four prominent peaks and broad features below the 1 V region. These four peaks, which occur at 0.19 V, 0.36 V, 0.4 V, and 0.79 V and then disappear in subsequent cycles, were likely due to the irreversible conversion reaction associated with structural change and SEI layer formation. The peak at 0.79 V was attributed to K^+ ions interacting with $MoSe_2$ within the $MoWSe_2$ alloy[351]. In comparison, the broadening of the peak at 0.36 V to 0.5 V was correlated with the K^+ ion interaction with the WSe_2 layer of the $MoWSe_2$ alloy. The peak at 0.17 V was ascribed to an irreversible conversion reaction of WSe_2 regions within the $MoWSe_2$ alloy and the formation of the SEI layer[141;221]. Therefore, all the metals were assumed to participate in different electrochemical reactions with K^+ ions. After the first-cycle reactions, one peak at 1.24 V appeared from the second cycle onwards primarily due to the reduction of Se from the $MoWSe_2$ to K_2Se (Figure 7.12a), otherwise known as the reduction of metal selenide particles to form ultrafine crystals[229]. However, this peak shifted 0.05 V from the last place in the fifth cycle, potentially leading to polarization (Figure 7.12a). The peak at 0.79 V continued until 0–20 and 40–60 cycles with decreasing intensity (shown in blue in Figure 7.5b), thereby skipping the harsh current rates. Similar behavior was observed in the

1.24V peak, in which a broad peak from 1.3 V to 2.0 V was observed in the first to the fifth depotassiation cycle (Figure 7.12a), with a prominence at 1.59 V in the first cycle, indicating a multistep reaction. Previous studies have identified peaks at 1.68 V and 2.06 V as phase transformations of K_2Se to K_2Se_n and Se[141], and the high voltage 1.73 V peak has been associated with the oxidation reaction of metallic Mo to reform $MoSe_2$[67]. The prominent 1.73 V peak showed a shift of 0.02 V up to five cycles (Figure 7.12a), and peaks at 1.3–2.0 V became less prominent as the cycling continued, partially disappearing midway during high current density cycling (shown in blue in Figure 7.5c), losing their prominence in the 90th cycle (red to yellow on Figure 7.5c), and continuing as a single, less intense peak up to the 140th cycle, as shown in Figure 7.5c. The 0.36 V peak showed polarization behavior moving up to 0.5 V at the end of the cycling.

For the half-cell cycled in the 0.01–2.0 V potential range (charge-discharge curve of Figure 5d transformed into the differential capacity curve in Figure 7.12b), all the same reactions as 0.01-2.5 V cell occurred since no other reactions were observed, thereby confirming the logic of restricting the potential range to 2.0 V for K^+ ion storage. A similar behavior was observed in the potassiation cycle (Figure 7.5e) for the 0.01–2.0 V cell compared to the 0.01-2.5 V cell (Figure 7.5b), where, for the depotassiation cycle, the 3D differential capacity curve in Figure 5f shows that the 0.36 V curve maintains its intensity to the 140th cycle while undergoing a slight voltage shift and reaching 0.5 V. Although the peaks at the 1.3–2.0 V region survived the harsh cycling conditions, shown by the reactions up to the 140th cycle in Figure 7.5f which highlights the benefit of upper voltage suspension, the peaks narrow in size at 1.6–2.0 V in the last cycles.

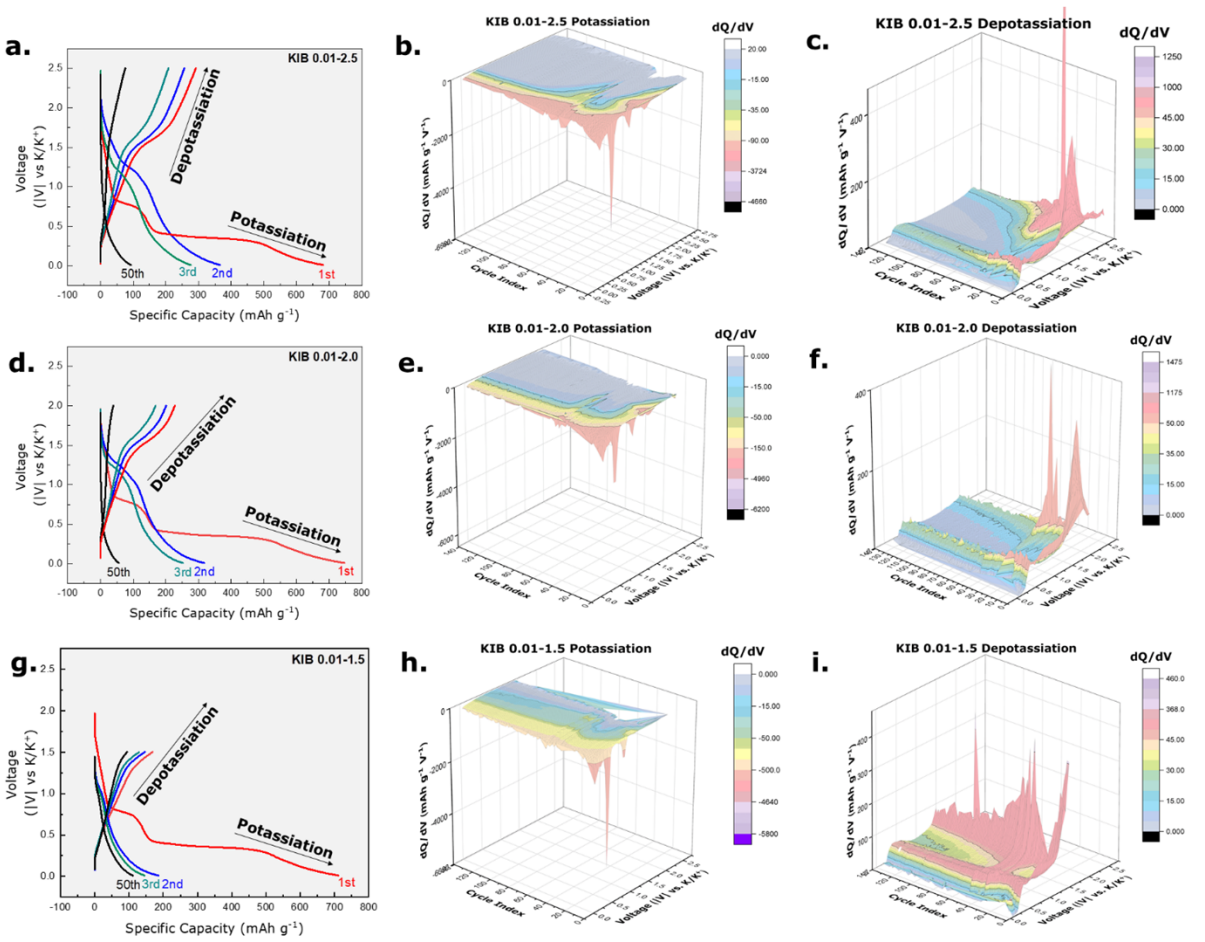


Figure 7.5: *: Investigation of K^+ ion storage behavior: a) Galvanostatic charge-discharge curves of $MoWSe_2$ electrode cycled within 0.01-2.5 V; differential capacity curves of b) 1st-140th potassiation cycles, c) 1st-140th depotassiation cycles of 0.01-2.5 V $MoWSe_2$ electrode; d) Galvanostatic charge-discharge curves of $MoWSe_2$ electrode cycled within 0.01-2.0 V; differential capacity curves of e) 1st-140th potassiation cycles, f) 1st-140th depotassiation cycles of 0.01-2.0 V $MoWSe_2$ electrode; g) Galvanostatic charge-discharge curves of $MoWSe_2$ electrode cycled within 0.01-1.5 V; differential capacity curves of h) 1st-140th potassiation cycles, i) 1st-140th depotassiation cycles of 0.01-1.5 V $MoWSe_2$ electrode.*

For the cell cycled in the potential range of 0.01–1.5 V (Figure 7.5g), the potassiation differential capacity curve presented the conversion reactions in the first cycle. The potassiation curve for cycles 2–140 contained only one peak at 1.06 V and then gradually became less intense, indicating the possible continuation of the intercalation reaction and subsequent preservation of the crystal structure (Figure 7.5h). In the depotassiation curve (Figure 7.5i), the peak at 1.5 V occurred until the 140th cycle, indirectly proving that upper voltage sus-

pension leads to longer reaction preservation in TMD alloys. The 0.36 V depotassiation peak also maintained uniform intensity throughout the harsh and prolonged cycling, showing hysteresis behavior during cycling at high current densities in which the peak moved to 0.5 V at the highest current density of 800 mA g^{-1}, implying that hysteresis may also increase at higher current densities (Figure 7.5i).

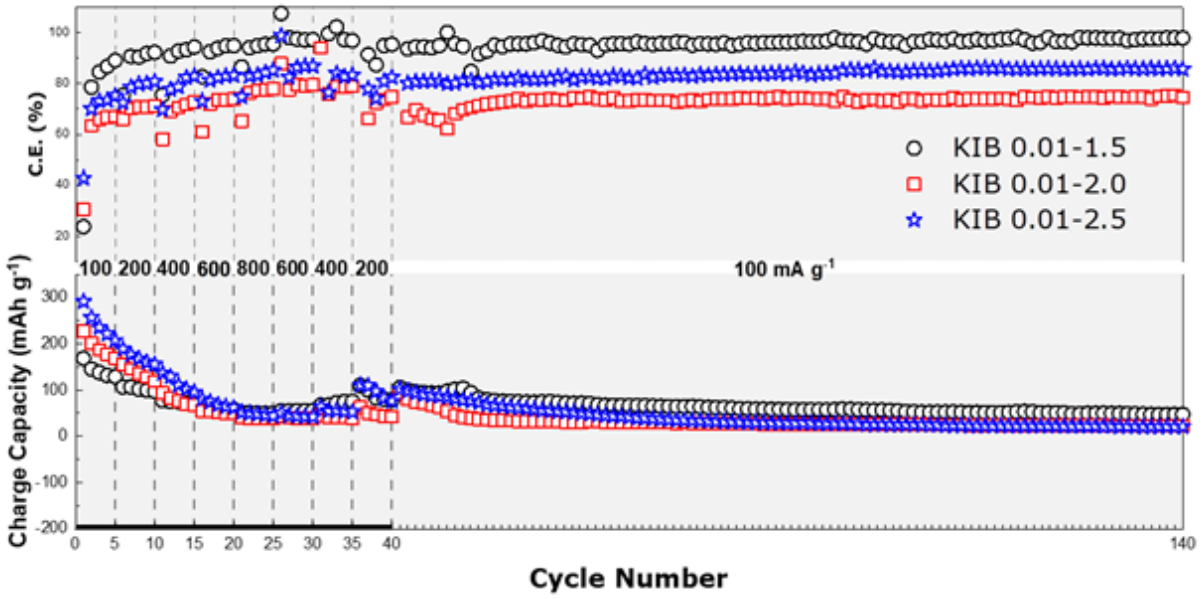


Figure 7.6: *Rate capability and consecutive cycling stability tests for investigating K^+ ion storage behavior of half-cells cycled within different potential ranges.*

The performances of the three electrodes were tested at different voltage ranges in gradually increasing and decreasing current densities of 100, 200, 400, 600, and 800 mA g^{-1} for five cycles up to the 25th cycle and then returned to the original current densities, as shown in Figure 7.6. In the initial five cycles, both the 0.01–2.5 V and 0.01–2.0 V cells showed higher charge capacity (291 mAh g^{-1} and 227 mAh g^{-1}, respectively) than the 0.01–1.5 V cycled cell (168 mAh g^{-1}). However, as shown in Figure 7.6, in higher current densities, the 0.01–2.5 V cycled cell and the 0.01–2.0 V cycled cell showed gradual capacity fading. In comparison, less capacity fading was observed in the 0.01–1.5 V cycled cell. In cycles 26, 31, 36, and 41 the cell cycled up to 1.5 V showed 76%, 91%, 93%, and 95% capacity retention, respectively, consistently approx. 10–20% higher than the other two electrodes, suggesting

that upper cut-off voltage restricts capacity fading. Higher voltage cut-off values may also decrease structural distortion of the $MoWSe_2$ material for K^+ ion storage.

After the rate capability test, the cells were cycled at 100 mA g^{-1} current density for additional 100 cycles. As illustrated in Figure 7.6, although the charge capacity of 0.01–2.5 V and 0.01–2.0 V cells overlapped, the 0.01–1.5 V cell showed stable and slightly higher charge capacity. However, the benefits of upper voltage restriction were more apparent in coulombic efficiency chart, where the 0.01-1.5 V cell demonstrated high cycling efficiency (near 100%) during stability test after the rate capability. In contrast, the 0.1-2.0 V cell constantly showed much lower (approx. 80%) coulombic efficiency during rate capability and consequent stability test, while the coulombic efficiency of the 0.01-2.5 V cell was the lowest at approx. 70% (Figure 7.6). This can be correlated with possible electrolyte consumption and structural degradation of the cells cycled at lower cut-off voltages.

7.5 Post-Cycling Analysis

To investigate the possible reasons for capacity fading of cells cycled at certain voltage range and consecutive higher capacity gain of cells cycled at higher cut-off voltages, selective spent cells were disassembled in an inert atmosphere, washed with DMC solvent for separator fiber and electrolyte contaminant desolvation. Digital camera images of electrodes cycled in 0.01-1.5 V and 0.01-2.5 V range are shown in Figures 7.13(a-d). The recovered electrodes for the 0.01-2.5 V range (Figures 7.13 a, b) showed signs of significant damage. This damage can be correlated to the substantial volume change experienced by traditional TMD during alkali-metal ion accommodation, conversion reactions, and subsequent loss of adhesion (peel-off) of active materials from the current collector[44;262;281]. Hence, SEM analysis of such electrodes was avoided.

On the other hand, the electrodes cycled in the 0.01-1.5 V range experienced significantly less damage (Figures 7.13 c, d) – the active material was still retained on the copper current collector. The above electrodes were further analyzed using SEM and XRF (elemental analysis) and compared with the uncycled $MoWSe_2$ electrode. As can be seen in Figures 7.7(a-c),

the neat electrodes possessed smooth geometrical features with somewhat homogeneous dispersion of micron-size $MoWSe_2$ particles. The XRF spectra of the electrode (Figure 7.14a) showed the presence of Mo, W, Se, and C (originating from the binder and conductive agent particles) elements. The SEM micrograph (Figure 7.7d) of the disassembled electrode, cycled in the 0.01-1.5 V (v/s Na^+) range, shows a relatively smooth surface geometry similar to the uncycled electrode. Insertion of Na^+ ions into the $MoWSe_2$ sheets may be realized from Figures 7.7(e, f), which resembles textbook page-like puffy flakes with dimensions in the micrometer range. The corresponding XRF spectrum in Figure 7.14b shows the presence of Mo, W, and Se peaks (elemental composition similar to the neat electrode for the alloy TMD) –the Na and O peaks and traces of Cl and C are mainly attributed to $NaClO_4$ salt in organic electrolyte. Compared to the Na^+ ion half-cells, the K^+ ion disassembled half-cell electrodes showed surface cracks (marked in Figure 7.7g) – approximately micrometer in dimension (marked in Figure 7.7h), with traces of separator fibers on the surface. These surface cracks can be correlated to the strain induced within the $MoWSe_2$ flakes during prolonged cycling. The XRF spectra in Figure 7.14c of 0.01-1.5 V cycled K^+ ion half-cells show the Mo, W, and Se elements along with large amounts of K (due to K^+ ion insertion into the material) and traces of electrolyte elements (e.g., P and F arising from the salt, and C arising from the solvent, conducting agent and binder). The lower capacity of K^+ ion half-cells at different voltage ranges in comparison with Na^+ ion half-cells can be well correlated with the higher ionic radius of K^+ ions and the surface cracks visible from the post-cycled electrodes likely originating during repeated potassiation and depotassiation. Overall, the usefulness of the voltage cut-off technique in determining the optimum charge/discharge voltage potentials (for maximum capacity retention for a given class of electrode materials) is further emphasized by post-cycling analysis. The electrodes charged to 2.5V reveal significant damages in contrast with the electrodes charged to 1.5V, which maintained the 10–20% higher than the other two electrodes, suggesting that upper cut-off voltage restricts capacity fading. Higher voltage cut-off values may also decrease structural distortion of the $MoWSe_2$ material for K^+ ion storage.

After the rate capability test, the cells were cycled at 100 mA g^{-1} current density for

additional 100 cycles. As illustrated in Figure 7.6, although the charge capacity of 0.01–2.5 V and 0.01–2.0 V cells overlapped, the 0.01–1.5 V cell showed stable and slightly higher charge capacity. However, the benefits of upper voltage restriction were more apparent in coulombic efficiency chart, where the 0.01-1.5 V cell demonstrated high cycling efficiency (near 100%) during stability test after the rate capability. In contrast, the 0.1-2.0 V cell constantly showed much lower (approx. 80%) coulombic efficiency during rate capability and consequent stability test, while the coulombic efficiency of the 0.01-2.5 V cell was the lowest at approx. 70% (Figure 7.6). This can be correlated with possible electrolyte consumption and structural degradation of the cells cycled at lower cut-off voltages.

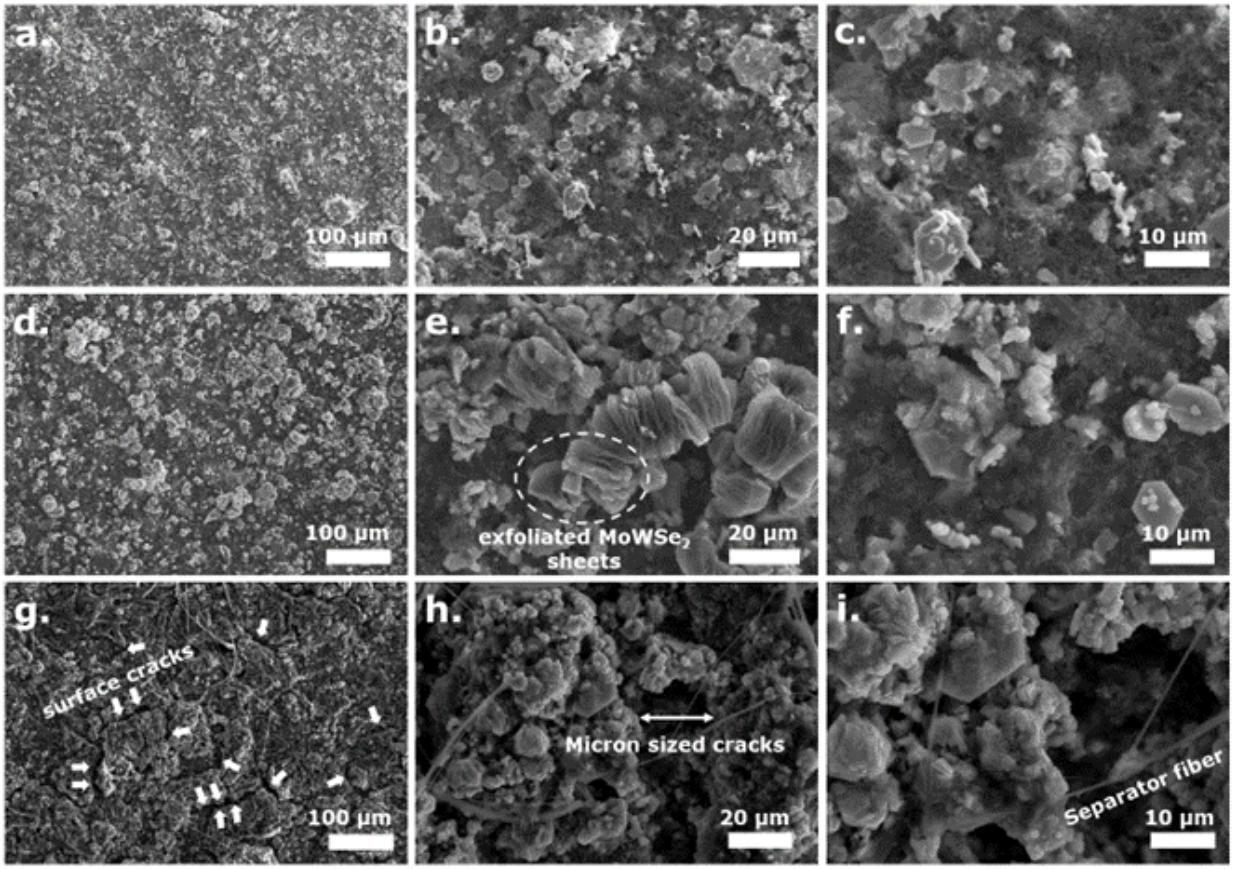


Figure 7.7: *:SEM micrographs of (a-c) Neat $MoWSe_2$ electrode showing smooth surface with $MoWSe_2$ sheet dispersion; (d-f) disassembled $MoWSe_2$ Na^+ ion half-cell electrode cycled within 0.01-1.5 V showing exfoliated flakes; (g-i) disassembled $MoWSe_2$ K^+ ion half-cell electrode cycled within 0.01-1.5 V showing microcracks generated due to cycling.*

7.6 Conclusion

This research is the first work to study the Na^+ and K^+ ion storage behavior of cation-substituted $MoWSe_2$ alloy. Because traditional TMDs experience side reactions and significant volume changes that lead to capacity fading and instability during prolonged cycling in LIB, similar or more significant material degradation for long cycling for beyond lithium alkali metal-ions was expected from cation-substituted TMD alloys such as the $MoWSe_2$. Therefore, this study restricted the potential range for charge-discharge to prevent structural disorientation. When cycled at potential ranges of 0.01–2.5 V, the $MoWSe_2$ showed continuous capacity degradation during rate capability and cycling stability tests, indicating structural and chemical degradation, as confirmed by 3D differential capacity surface plots and electron microscopy. Suspension of the potential range to 0.01–2.0 V led to 16% better capacity retention for Na^+ ion half-cells, and additional potential range restriction to 0.01–1.5 V resulted in approx. 29% higher capacity retention than the 2.5 V cycled cell. High coulombic efficiency was observed in the cell with a potential range of 0.01–1.5 V, especially in the K^+ ion half-cells. Reaction analysis of the differential curve showed that high upper voltage suspension restricts specific undesirable reactions during sodiation/desodiation or potassiation/depotassiation and therefore helps preserve the crystal structure of the TMD alloy. The intercalation and conversion reaction occurred for the cells cycled within high potential ranges (0.01–2.0 V and 0.01–2.5 V), and crystal structure distortion occurred at the initial cycling stages, leading to capacity fading, shown in the 3D differential capacity curve. Noticeably, the benefits of upper voltage cut-off were more apparent in case of Na^+ ion half-cells in contrast to the K^+ ion half-cells during long-term cycling. SEM micrographs of cycled cells with higher voltage cut-off showed smooth geometry retention in the case of Na^+ ion half-cell electrodes and microcracks evolution due to potassiation/depotassiation, which is indirect evidence of strain-induced within. Therefore, this study demonstrated that regulating the operating potential range strongly influences structural preservation, thereby expediting electrochemical performance, specifically cycling stability, capacity retention, and coulombic efficiency of layered $MoWSe_2$. Although full capacity retention from higher voltage

cut-off (or cycling within a lower potential range) was not realized, this study nevertheless lays the ground for utilizing the upper voltage cut-off technique combined with composite electrode formation for future investigations regarding the search of next-generation NIB and KIB anodes.

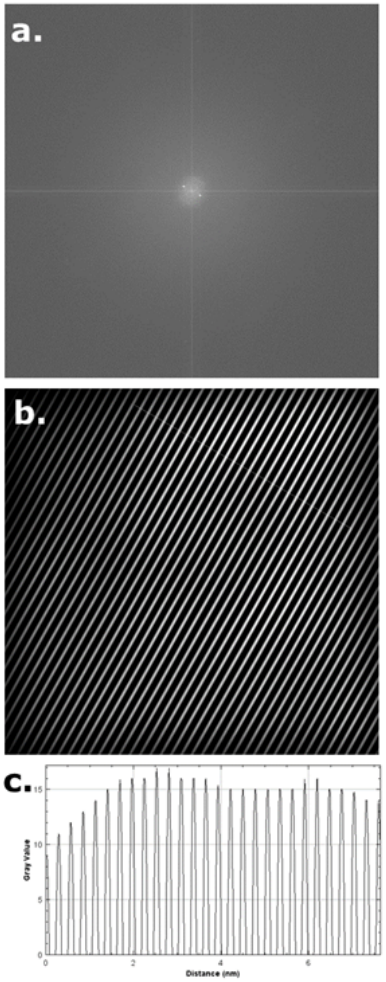


Figure 7.8: *Fringe distance determination from TEM image of Figure 1c. a) FT image, b) Inverse FT image, and c) Fringe profile plot from the inverse FT image derived from Figure 7.1c.*

Figure 7.9a shows the Raman spectra of the $MoSe_2$ bulk powders. The most prominent modes observable from the spectra are the A_{1g}, E^1_{2g}, and E^1_{2g}-LA vibrational modes at 239 cm-1, 284 cm-1, and 146 cm-1, respectively. A few additional peaks are also observed in the spectra at 113 cm-1, 124 cm-1, 195 cm-1, and 336 cm-1, which are yet not specified in the literature[65;175;223].

On the other hand, from Figure 7.9b, the most intense peak from the WSe_2 bulk powder is centered at 251 cm-1. This peak is attributed to the overlap of A_{1g} and E^1_{2g} vibrational modes originating from the WSe_2 bulk powder. Another peak at 175 cm-1 can be attributed

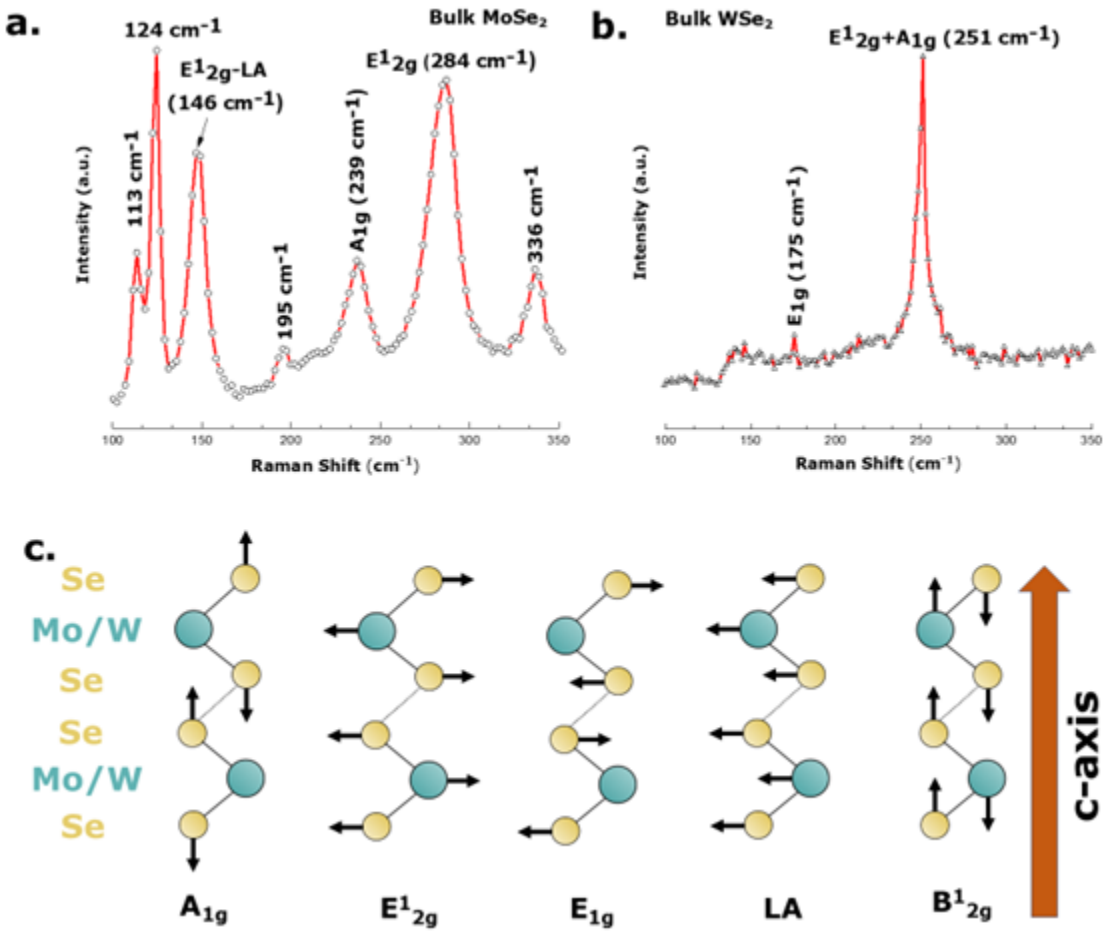


Figure 7.9: *Raman spectra of bulk a) $MoSe_2$ and b) WSe_2 powders for clear comparison with bulk $MoWSe_2$ powder; c) schematic of vibrational modes typically obtained from TMDs.*

to the E_{1g} vibrational modes[151;214;349;389].

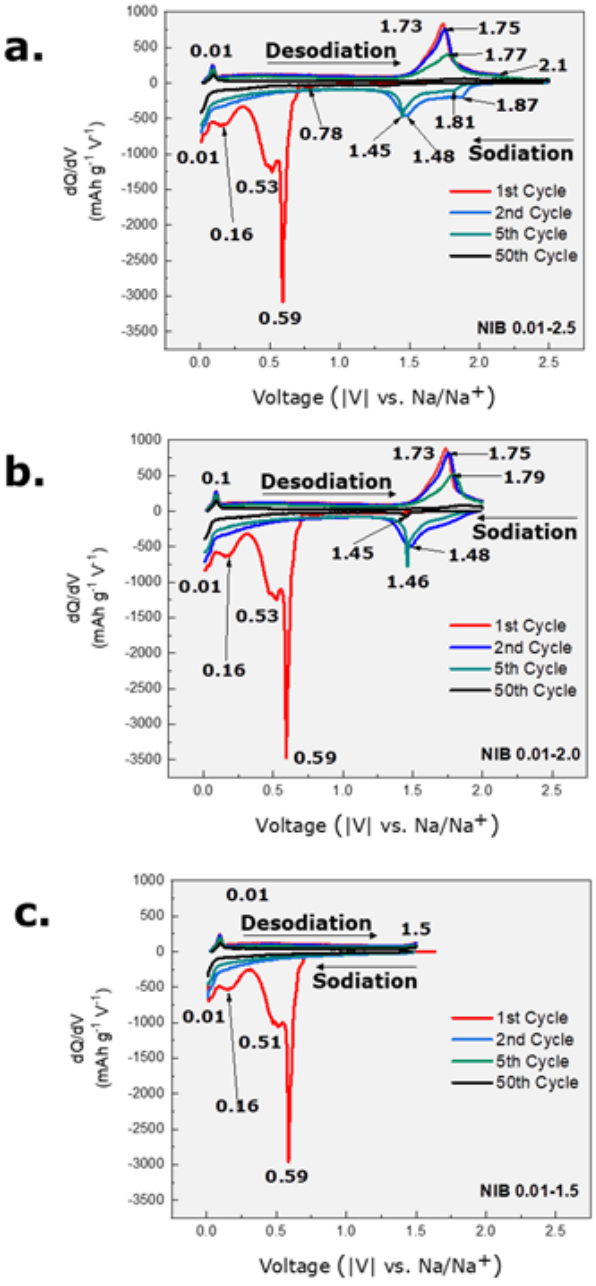


Figure 7.10: *Differential capacity curves of Na^+ ion half-cells of $MoWSe_2$ electrode cycled within potential ranges: a) 0.01-2.5 V; b) 0.01-2.0 V; c) 0.01-1.5 V.*

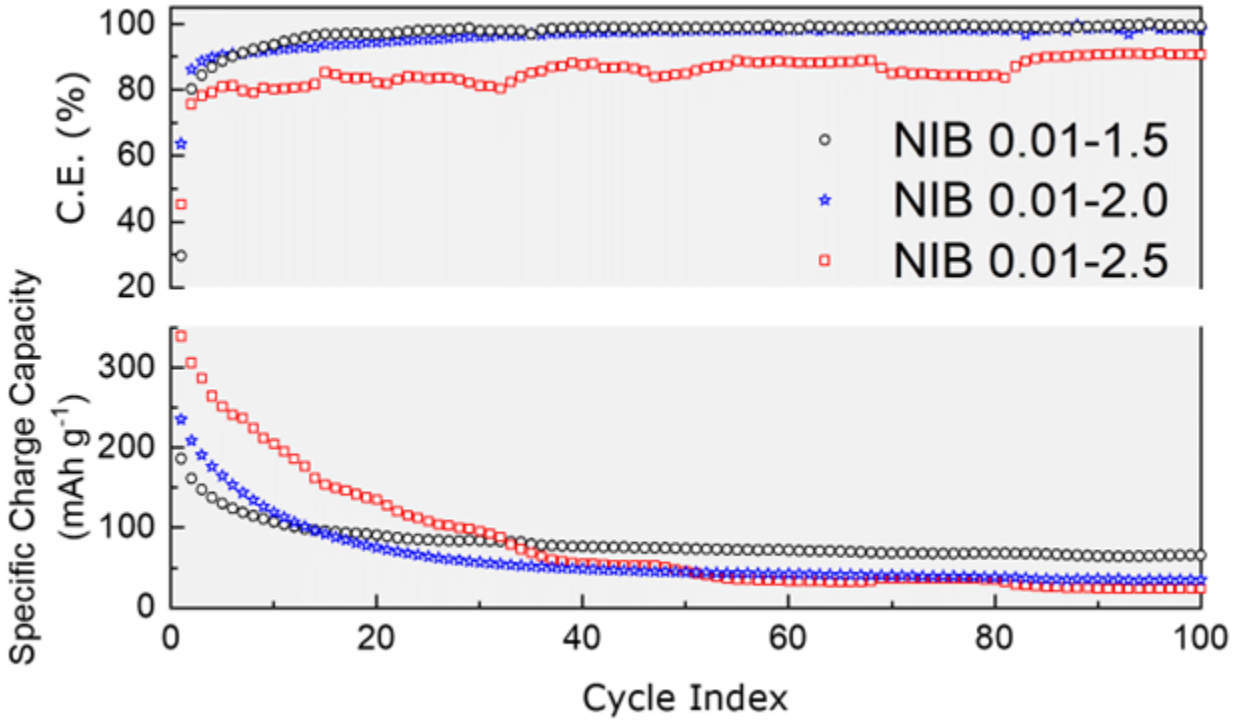


Figure 7.11: *Cycling stability test of $MoWSe_2$ electrodes cycled within the potential range of 0.01-1.5 V, 0.01-2.0 V, 0.01-2.5 V in Na^+ ion half-cells.*

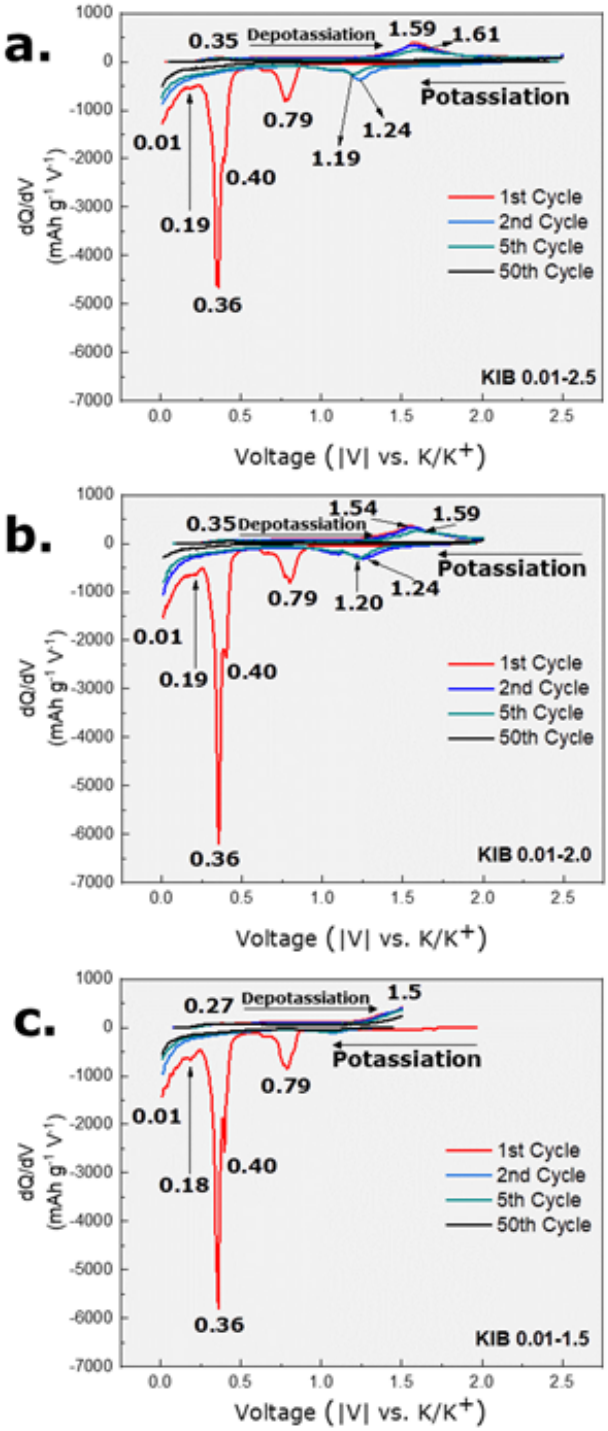


Figure 7.12: *Differential capacity curves of K^+ ion half-cells of $MoWSe_2$ electrode cycled within potential ranges: a) 0.01-2.5 V; b) 0.01-2.0 V; c) 0.01-1.5 V.*

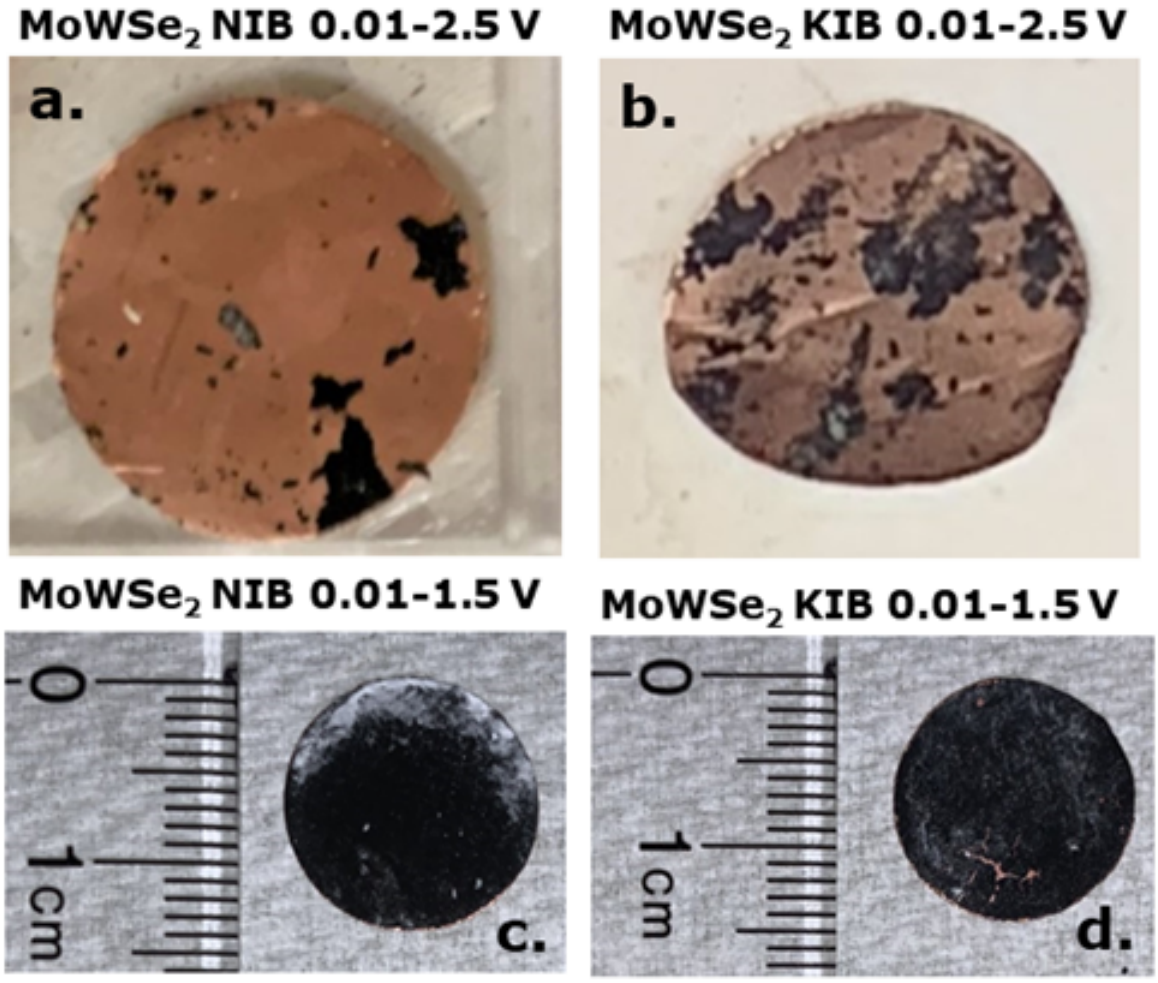


Figure 7.13: *Digital camera photographs of disassembled electrodes from a) $MoWSe_2$ 0.01-2.5 V Na^+ ion half-cell, b) $MoWSe_2$ 0.01-2.5 V K^+ ion half-cell; c) $MoWSe_2$ 0.01-1.5 V Na^+ ion half-cell, d) $MoWSe_2$ 0.01-1.5 V K^+ ion half-cell.*

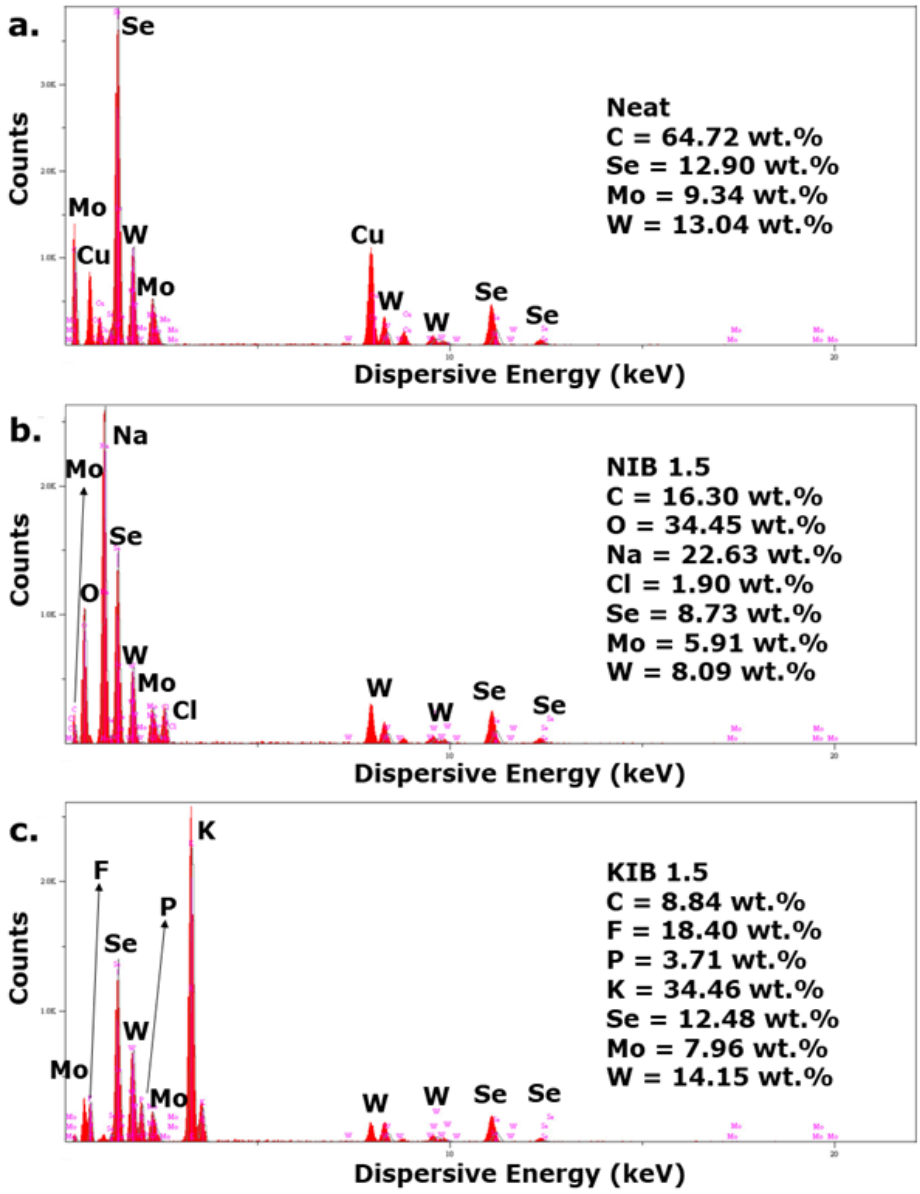


Figure 7.14: *XRF plots and corresponding elemental composition of a) neat $MoWSe_2$ electrode, b) 0.01-1.5 V $MoWSe_2$ Na^+ ion half-cell, and c) 0.01-1.5 V $MoWSe_2$ K^+ ion half-cell.*

Chapter 8

Enhanced Li-Ion Rate Capability and Stable Efficiency Enabled by $MoSe_2$ Nanosheets in Polymer-Derived Silicon Oxycarbide Fiber Electrodes[1]

8.1 Preface

Transition metal dichalcogenides (TMDs) such as $MoSe_2$ have continued to generate interest in the engineering community because of their unique layered morphology—the strong in-plane chemical bonding between transition metal atoms sandwiched between two chalcogen atoms and the weak physical attraction between adjacent TMD layers provides them with not only chemical versatility but also a range of electronic, optical, and chemical properties that can be unlocked upon exfoliation into individual TMD layers. Such a layered morphology is particularly suitable for ion intercalation as well as for conversion chemistry with alkali metal ions for electrochemical energy storage applications. Nonetheless, host of issues

[1]Dey, Sonjoy, Shakir Bin Mujib, and Gurpreet Singh. "Enhanced Li-Ion Rate Capability and Stable Efficiency Enabled by $MoSe_2$ Nanosheets in Polymer-Derived Silicon Oxycarbide Fiber Electrodes." Nanomaterials 12.3 (2022): 553.

including fast capacity decay arising due to volume changes and from TMD's degradation reaction with electrolyte at low discharge potentials have restricted use in commercial batteries. One approach to overcome barriers associated with TMDs' chemical stability functionalization of TMD surfaces by chemically robust precursor-derived ceramics or PDC materials, such as silicon oxycarbide (SiOC). SiOC-functionalized TMDs have shown to curb capacity degradation in TMD and improve long term cycling as Li-ion battery (LIBs) electrodes. Herein, we report synthesis of such a composite in which $MoSe_2$ nanosheets are in SiOC matrix in a self-standing fiber mat configuration. This was achieved via electrospinning of TMD nanosheets suspended in pre-ceramic polymer followed by high-temperature pyrolysis. The morphology and chemical composition of synthesized material was established by use of electron microscopy and spectroscopic technique. When tested as LIB electrode, the SiOC/$MoSe_2$ fiber mats showed improved cycling stability over neat $MoSe_2$ and neat SiOC electrodes. The freestanding composite electrode delivered a high charge capacity of 586 mAh g^{-1}electrode with an initial coulombic efficiency of 58%. The composite electrode also showed good cycling stability over SiOC fiber mat electrode for over 100 cycles.

8.2 Introduction

The most recent advancement in energy storage and conversion systems was the instigation of flexible or bendable systems that were fabricated to be portable, lightweight, and wearable while being mechanically flexible and having a high-energy density[49]. However, the preparation methods, assembly process, and selection of proper electrolytes to transform traditional energy storage devices remains a challenging task. Conventional LIBs usually consist of a carbon-based anode, a transition metal oxide-based cathode, a polymer separator, and an organic liquid electrolyte. In such devices, heavy metal foils are always used as both a conductive substrate and structural support with a slurry of active materials, binders, and conductive additives coated on its surface. However, such electrode designs have certain drawbacks—for example, as the metal foil possesses a smooth surface, the active materials can easily become detached from the current collector. Additionally, there is an increase in

the internal impedance and passivation of active materials due to relatively poor chemical stability. Lastly, the conductive additives such as carbon black, carbon nanotubes (CNTs), and graphite account for the 10–20 wt.% of the whole slurry make no or little contribution to the capacity of the cell. Polymer binders such as polyvinylidene fluoride (PVDF) are electrochemically inactive or even insulating, making their presence a hindrance to the transportation of lithium ions and electrons.

Flexible conducting and self-supporting electrodes replace traditional metal-foil-based heavy current collectors and standard binders with lightweight substrates or embedded current collectors. The approach is to make a combination of active materials and flexible substrates by taking advantage of the conductive and flexible matrix embedded in the current collector or the substrates with functional materials firmly entrapped on them through novel methods such as coating, spraying, or depositing[333]. Although the use of CNT and graphene as both active materials and current collectors has been widely studied, other forms of carbon materials and some novel metal-based current collectors are now becoming more popular. For example, an effective chemical oxidation and reduction method to increase the surface area of carbon materials using a carbon cloth-based solid-state supercapacitor was prepared by Wang et al.[317]. A novel bamboo-like structure was reported in 2005, which showed excellent mechanical flexibility, foldability, and electrochemical performance. In dimethylformamide, polyacrylonitrile and tetraethyl orthosilicate were used to create nanofibers via electrospinning[298].

In recent years, the application of polymer-derived ceramic (PDC) materials and compounds with CNTs and graphene as free-standing electrodes in electrochemical devices has been studied. Due to desirable properties such as high stability during cyclic loading and structure preservation during very high C-rates, PDCs have become materials of increasing interest[4;107;314]. Interestingly, studies from David et al.[76] and Davi et al.[134] showed that the chemical functionalization of polymer-derived ceramics (PDC) with Transition Metal Dichalcogenide (TMD) materials leads to stable Li^+ and Na+ cycling in the fabricated TMD-electrodes. Specifically, the presence of PDC nanolayers on TMD surfaces prevented the loss of sulfur species from the TMD surfaces during a conversion-type reaction.

In the present work, our primary motivation is to exploit the chemical functionalization of TMDs with PDCs and to demonstrate the fabrication of a new kind of freestanding electrode consisting of exfoliated $MoSe_2$ TMD that offers Li ions stable cyclability, high energy density, and rate capability. This was achieved via a single-step electrospinning process in which a combination of liquid-phase organic/inorganic preceramic polymer and exfoliated TMD nanosheets were used as the spinning solution to fabricate non-woven fiber mats followed by pyrolysis to achieve a composite fiber mat of $MoSe_2$ embedded in a SiOC matrix. The microscopy and spectroscopy images confirmed the presence of $MoSe_2$ in the SiOC matrix, and electrochemical tests of the SiOC/$MoSe_2$ electrode in the LIBs showed enhanced performance over neat SiOC and bulk $MoSe_2$ electrodes. To the best of our knowledge, a combination of the TMD $MoSe_2$ and PDC in a free-standing form has not been reported for either battery or supercapacitor applications.

8.3 Materials and Methods

8.3.1 Materials

The preceramic silicon oligomer 1,3,5,7-tetramethyl, 1,3,5,7-tetravinyl cyclotetrasiloxane (denoted as 4-TTCS) was purchased from Gelest (Morrisville, PA, USA). Polyvinylpyrrolidone (PVP), which has an average molecular mass of 1,300,000 g mol^{-1}, was used as the spinning agent, and dicumyl peroxide (DCP) was the cross-linking agent. Both materials were purchased from Sigma-Aldrich (Missouri, MO, USA). Isopropyl alcohol (IPA), purchased from Fisher Chemical (Lenexa, KS, USA), was used as the solvent. This study also utilized ultra-high-purity and high-purity argon gas in the glove box and tube furnace, respectively. The gases were purchased from Matheson (Manhattan, KS, USA). Bulk molybdenum diselenide (99.9% pure) powder ($MoSe_2$) was purchased from Alfa Aesar (Haverhill, MA, USA) and had a dark grey appearance with a molecular weight of 253.87.

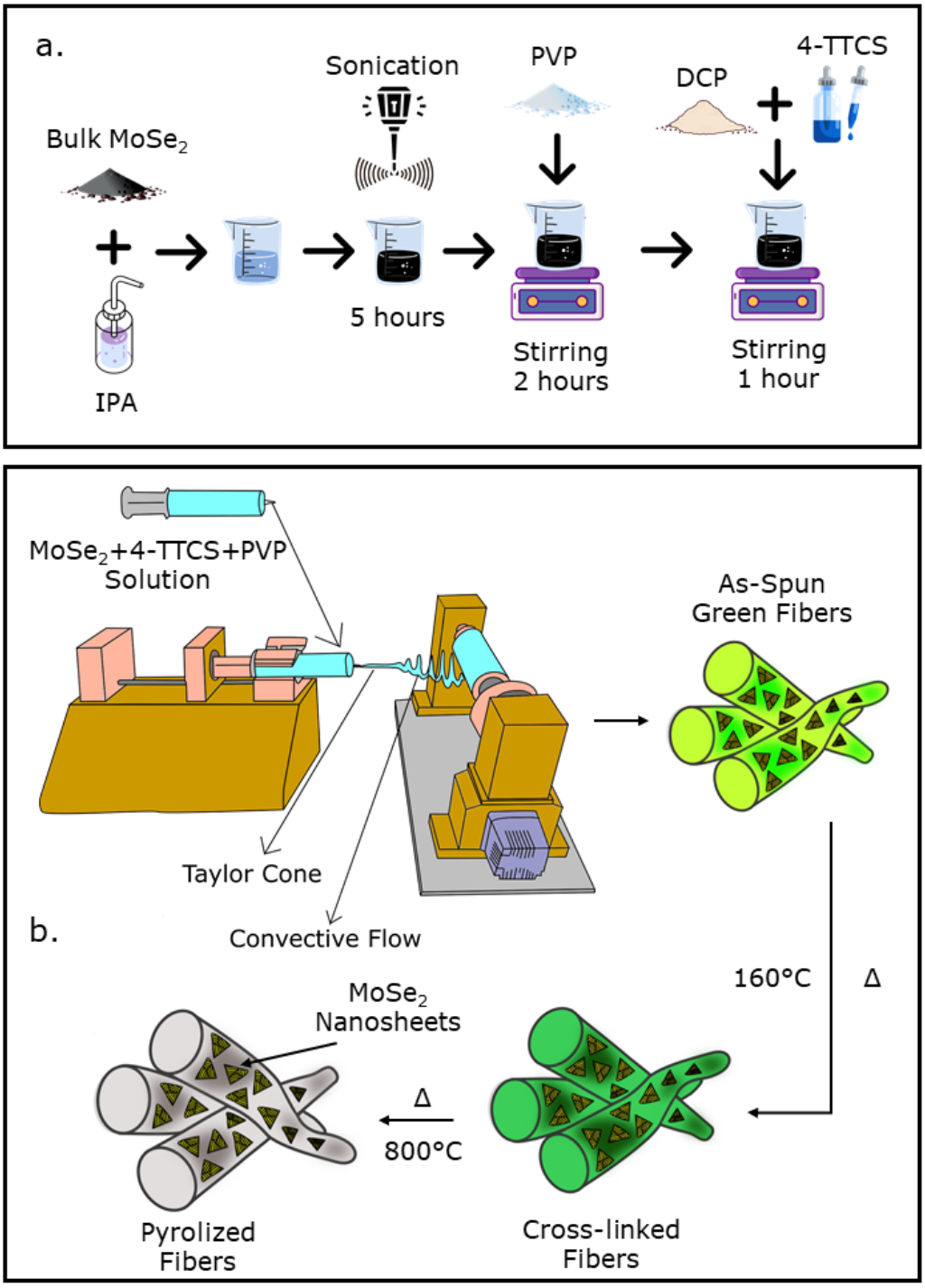


Figure 8.1: *Solution preparation process for (a) PVP/SiOC/$MoSe_2$ fiber mat; (b) schematic showing electrospinning process for the fabrication of the PVP/SiOC/$MoSe_2$ composite fiber mats.*

8.3.2 Methods

Preparation of Fiber Mats

PVP Fiber mat Preparation

In the solution preparation step for the PVP fiber mat, 800 mg of PVP powder was mixed with IPA to create a solution, and the ratio of PVP:IPA was kept at 1:9. A magnetic stirrer was used to create a homogenous mixture of the solution, which was stirred for 2 h. The resulting solution was loaded into a 10 mL syringe with a flat metallic needle for electrospinning purposes. The fiber mat that was produced with this solution is referred to as the PVP fiber mat in the following sections.

PVP/SiOC Fibermat Preparation

The solution preparation for the PVP/SiOC fiber mat involved creating a similar solution as the one for the PVP fiber mat followed by the addition of a polymeric precursor material. The polymeric precursor 4-TTCS (i.e., 2400 mg) was primarily mixed with 1 wt.% DCP (i.e., 24 mg), which worked as a cross-linking initiator. The resultant PVP + 4-TTCS + IPA solution was stirred until a homogeneous mixture was achieved. Finally, the above-mentioned solution was loaded in a 10 mL syringe with a flat metallic needle for electrospinning, and the fiber mat produced with this solution is referred to as the PVP/SiOC fiber mat in the following sections.

PVP/SiOC/$MoSe_2$ Fiber mat Preparation The first step for the preparation of the PVP/SiOC/$MoSe_2$ fiber mat involved the preparation of the nanosheet material from the bulk $MoSe_2$ powder. For this particular purpose, 10 wt.% $MoSe_2$ bulk powder compared to the amount of PVP (i.e., 80 mg) was added with IPA and was sonicated using a probe sonicator. In the next step, this solution was mixed with the same amounts of PVP and 4-TTCS as before and was stirred until a homogenous mixture was obtained. This solution preparation process is depicted in Figure 8.1a. The resultant solution was further loaded into a syringe and was electrospun to obtain PVP/SiOC/$MoSe_2$ fiber mat, as shown in Figure 8.1b. The feed rate for the fiber mat fabrication process was 5 mL h^{-1}. An alligator pin was connected to the metallic needle and was subject to a high voltage of 15–20 kV

depending on the viscosity of the solution, while the ground was connected to a cylindrical-shaped roller collector. The distance between the needle tip and the roller was kept at 15 cm. Thus, as-spun fiber mats that were 20 × 20 cm^2 in size were fabricated. After drying in the open air, the as-spun fiber mats were put into a low-temperature oven and cross-linked at 160 °C for 24 h. The cross-linked fiber mats were cut into small pieces, were fitted into small rectangular (30 × 25 mm^2) ceramic boats and put into a tube furnace in argon gas environment for high temperature pyrolysis. Two-step annealing was carried out at 400 °C for 1 h and at 800 °C for 30 min. The heating rate was kept at 2 °C per min. Thus, SiOC-functionalized $MoSe_2$ fiber mats were produced. In addition, one sample of PVP/SiOC/$MoSe_2$ fiber mat was fabricated by drop coating exfoliated $MoSe_2$ (using the same amount of $MoSe_2$ as before) onto a PVP/SiOC fiber mat followed by pyrolysis. This drop-coated PVP/SiOC/$MoSe_2$ sample was prepared to compare its electrochemical performance with the electrospun PVP/SiOC/$MoSe_2$ sample in which $MoSe_2$ was inherently introduced to SiOC in a single-step spinning process.

Electrochemistry

A 7.94 mm circular punch was used to punch out the composite pyrolyzed electrodes, which were then used as cathodes in the coin-like lithium half-cell setup. The weight of the PVP, PVP/SiOC, and PVP/SiOC/$MoSe_2$ electrodes were 1.6 mg, 1.1 mg, and 2.1 mg, respectively. Pure lithium metal (diameter of 14.3 mm and a thickness of 75) μm was used as the counter electrode. The electrolyte solution was a mixture of 1 M lithium hexafluorophosphate ($LiPF_6$) in 1:1 v/v dimethyl carbonate with ethylene carbonate (Sigma AldrichTM, St. Louis, MO, USA). This solution had an ionic conductivity of 10.7 mS cm^{-1}. A glass separator with a diameter of 19 mm and a thickness of 25 μm separated the two electrodes as they were pre-soaked with the electrolyte. The electrochemical measurements were taken using a multichannel BT 2000 Arbin test unit (College Station, TX, USA) between 2.5 V and 10 mV at current densities of 50, 100, 200, 400, 600, and 800 mA g^{-1}.

Characterization Techniques

Scanning electron microscopy (SEM) was used to illustrate the morphology of the fiber mat samples. The SEM used was a Carl Zeiss EVO MA10 (White Plains, NY, USA) system with a 5–30 kV impinging voltage. Transmission electron microscopy (TEM) images of the samples were obtained using Phillips CM100 TEM (Nashville, TN, USA) under an accelerating voltage of 100 kV. The X-ray photoemission spectroscopy (XPS) spectra were obtained with a PHI Quantera SXM (Chanhassen, MN, USA) using monochromatic Al-Ka with an energy of 1486.6 eV to analyze the chemical composition of the surface. Raman spectra were collected using a He-Ne laser (wavelength of 633 nm and power of 17 mW) on a confocal Raman imaging system (Horiba Jobin Yvon LabRam Aramis, Edison, NJ, USA). Fourier transform infrared spectroscopy (FTIR) spectra of the fiber mats were obtained using the Spectrum 400 FT-IR spectrometer, PerkinElmer (Waltham, MA, USA).

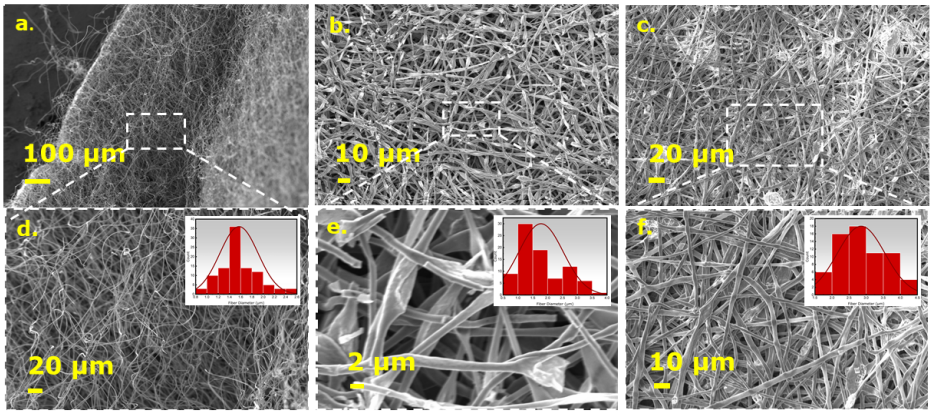


Figure 8.2: *SEM images of (a) PVP fiber mat carbonized at 800 °C, (b) PVP/SiOC fiber mat pyrolyzed at 800 °C, (c) PVP/SiOC/$MoSe_2$ fiber mat pyrolyzed at 8000 °C, and (d–f) corresponding high-magnification images of these fiber mats (inset shows diameter distribution of the fibers).*

8.4 Results and Discussions

8.4.1 Morphological Characterization

Because the fiber mats were first electrospun green and then cross-linked and pyrolyzed at elevated temperatures, the changes in the morphology of these fiber mats were investigated using SEM. Figure 8.2a–c illustrate the fiber-like morphology retention of the PVP, PVP/SiOC, and PVP/SiOC/$MoSe_2$ fiber mats after the cross-linking process at 160 °C and pyrolysis at 800 °C. Figure 8.2d–f reveals the images taken for the pyrolyzed fiber mats at a higher magnification from which the average fiber diameters were calculated using a distribution plot, as shown in the inset of the respective images. From the distribution plots, the mean fiber diameters for the PVP, PVP/SiOC, and PVP/SiOC/$MoSe_2$ fibers were identified as approx. 1.2 to 1.8 μm, approx. 1.2 to 2.75 μm, and approx. 2.25 to 3.75 μm, respectively. Compared to results in the literature, Wang et al. found that the average diameter of the PVDF/PVP nanofibers used in their experiment was in the range of 121–305 nm[328]. Additionally, the nanofibers fabricated by Newsome et al., which contained 9, 10, and 11 wt.% PVP in the silica/PVP electrospinning solution, possessed an average diameter in the range of 380–430 nm[78]. However, because the solution used and the electrospinning parameters differed from those used in the current research, the values cannot be directly compared. Ren et al. found that the average fiber diameter of the 4-TTCS fibers was 1 to 3 μm, which falls within the diameter range reported here[165]. Additionally, some irregularities such as microbeads and particles (likely to be $MoSe_2$ in case of the SiOC/$MoSe_2$ fiber mat) can be observed in the SEM images of the PVP/SiOC and PVP/SiOC/$MoSe_2$ fiber mats. It can be inferred from the above information that the addition of polymeric precursor 4-TTCS turned into a silicon oxycarbide (SiOC) ceramic material, and the sonicated nanosheets composed of the TMD material ($MoSe_2$) in the linear polymeric PVP fibers (transformed to carbon during pyrolysis) increased the diameters of the fibers sequentially. Thus, the presence of these materials in the fibers can be primarily confirmed and will be further validated by the other characterization techniques described in the following sections.

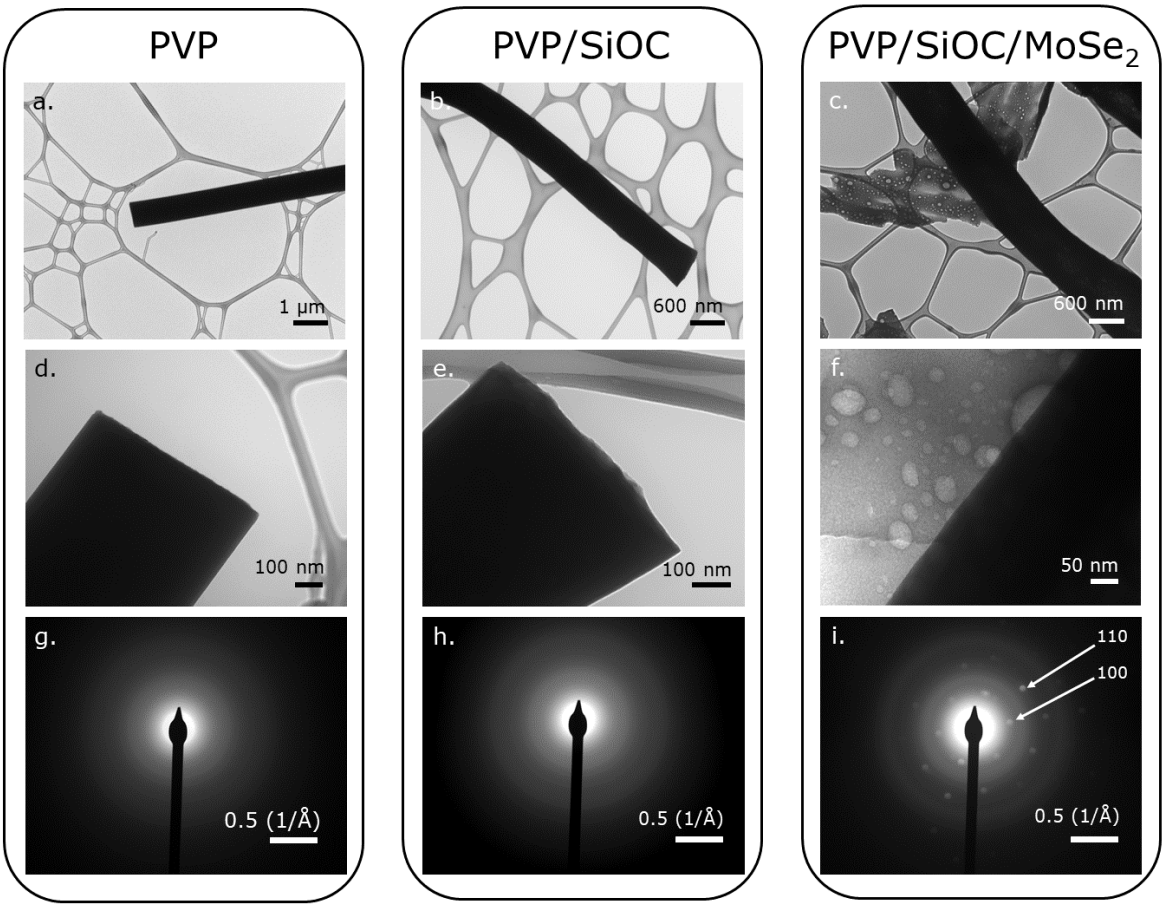


Figure 8.3: *TEM images of (a) PVP fibers carbonized at 800 °C, (b) PVP/SiOC fibers pyrolyzed at 800 °C, (c) PVP/SiOC/$MoSe_2$ fibers pyrolyzed at 800 °C, and corresponding HRTEM (d–f) and diffraction pattern (g–i) images of these fibers. Diffraction pattern of pyrolyzed PVP/SiOC/$MoSe_2$ indicates the presence of $MoSe_2$ particles in the pyrolyzed fiber mat.*

Figure 8.3a–c illustrates the low-mag TEM images of the PVP, PVP/SiOC, and PVP/SiOC/$MoSe_2$ fibers carbonized or pyrolyzed at 800 °C, respectively, while the high-resolution TEM (HRTEM) images are shown in Figure 8.3d–f. From the lower and higher magnification TEM images of the fibers, it can be inferred that all of the fibers have dense cores, as the electrons could not pass through the fibers in the TEM instrument. The diameters of the pyrolyzed PVP, PVP/SiOC, and PVP/SiOC/$MoSe_2$ fibers correspond well with the diameters in the SEM image, which validated the experiment. The carbonized PVP fibers seem to be uniform in diameter in both the higher and lower magnification images. Although mostly uniform along the cross-section, higher magnification images of the pyrolyzed PVP/SiOC

and PVP/SiOC/$MoSe_2$ fibers reveal the porosity and irregularity of the fibers. The beads seen from the SEM images of the PVP/SiOC and PVP/SiOC/$MoSe_2$ fibers were thus further validated by the anomalies observed in the TEM images of the fibers. The fiber porosity was as expected because it is this porosity that enhances the use of such fiber mats as electrodes in energy storage devices. The irregularities and beads in these fibers can be attributed to the processing conditions of the fiber mats. During the cross-linking and pyrolysis steps, the long-chain polymeric compound PVP decomposes and forms the long chain.

The release of volatile compounds from the preceramic polymer resin during cross-linking and pyrolysis leads to irregular geometries similar to those observed in the investigation by Mujib et al.[307]. The non-regular features of the fibers[234] can also be ascribed to solution parameters such as the molecular mass of the polymers used, correlating to the concentration of the polymer solution and viscosity and the effect of the solvent used, which has been widely studied in the literature[299]. Figure 8.3g–i represent the diffraction patterns of the pyrolyzed PVP, SiOC, and SiOC/$MoSe_2$ fibers taken in the position previously seen in Figure 8.3d–f, respectively. Figure 8.3g,h, respectively, reveal the amorphous structure of the carbonized PVP and PVP/SiOC fibers, which correspond well with the investigation by Ren et al.[165]. The diffraction pattern of Figure 8.3i elucidates the crystalline nature of $MoSe_2$ seen in the pyrolyzed PVP/SiOC/$MoSe_2$ fiber mats by possessing an interplanar spacing of 2.9 Å, which corresponds to (100) planes with six diffraction spots[143].

Spectrocopic Analysis

Raman spectroscopy is a fast and non-destructive ubiquitous method that was used to detect the microstructural features of the pyrolyzed fiber mats. The microstructural information of the fiber mats, including the free carbon phase and the presence of the TMD materials in the fiber mat, was determined using this versatile tool. Figure 8.4a,b,d elucidate the presence of the free carbon phase in the peak-fitted Raman spectra of the carbonized PVP fiber mat and pyrolyzed PVP/SiOC fiber mat and a definite region of the pyrolyzed PVP/SiOC/$MoSe_2$ fiber mat, respectively. The convoluted plots above revealed the D band for all of fiber mats

at approximately 1336 cm^{-1}, which appeared because of the disorganization or disorder in the carbon phase[340]. The G band was observed in the region of approximately 1602 cm^{-1} due to the in-plane bond stretching of the sp2 carbons. Additionally, peaks were also observed at 1213 cm^{-1} and 1495 cm^{-1}, which can be ascribed to the T and D" bands, respectively. While the T band can be ascribed to the presence of sp2-sp3 (C-C and C=C) bonds, the D" band corresponds to the presence of amorphous carbon in the sample. These two bands usually originate from graphene edges, from pores in the samples, and from sp3 hybridized carbon atoms. Riedel and co-workers found similar results with the micro-Raman spectroscopy of SiOC materials[212]. The Raman spectra obtained from other studies also indicate that the D and G bands are in similar positions[112;217]. Figure 8.4c illustrates the Raman spectra in the region of 200–320 cm^{-1} for both the bulk $MoSe_2$ powder and pyrolyzed PVP/SiOC/$MoSe_2$ fiber mats. For the bulk $MoSe_2$ powder, two peaks appear at 239.29 cm^{-1} and 282.14 cm^{-1}, among which the former shows a distinct sharp peak, and the latter has a dull one, indicating the A_{1g} and E^1_{2g} modes, respectively. While the A_{1g} mode signifies the out-of-plane vibrations of the chalcogen (selenium) species, the E^1_{2g} mode demonstrates the in-plane vibration mode of the transition metal (molybdenum) and chalcogen (selenium) atoms. In Raman-active A_{1g} mode, the Mo atom stays stationary, while the subsequent Se atoms that are present in all layers vibrate in phase with the subsequent Mo atoms[327]. The spectra obtained from the pyrolyzed PVP/SiOC/$MoSe_2$ fiber mat in the region mentioned earlier shows A_{1g} and E^1_{2g} modes that have two similar peaks in the slightly shifted region of 236.94 cm^{-1} and 287.03 cm^{-1}, respectively. The slight shift to the lower wavelength is usually observed because of the softening of the A_{1g} mode (redshift), with a decrease in the thickness of the material. While the A_{1g} peak was much more intense than the E^1_{2g} peak in the bulk sample, the same peaks on the $MoSe_2$ present in the material[276;378]. Similar peaks in the same position have been observed in several other studies as well[138;357;370]. The intensity ratio of the D and G peaks from the plots for pyrolyzed PVP, PVP/SiOC, and PVP/SiOC/$MoSe_2$ fiber mats were 1.02, 1.54, and 1.11, respectively, which revealed a higher degree of disorder-induced carbons in all of the samples.

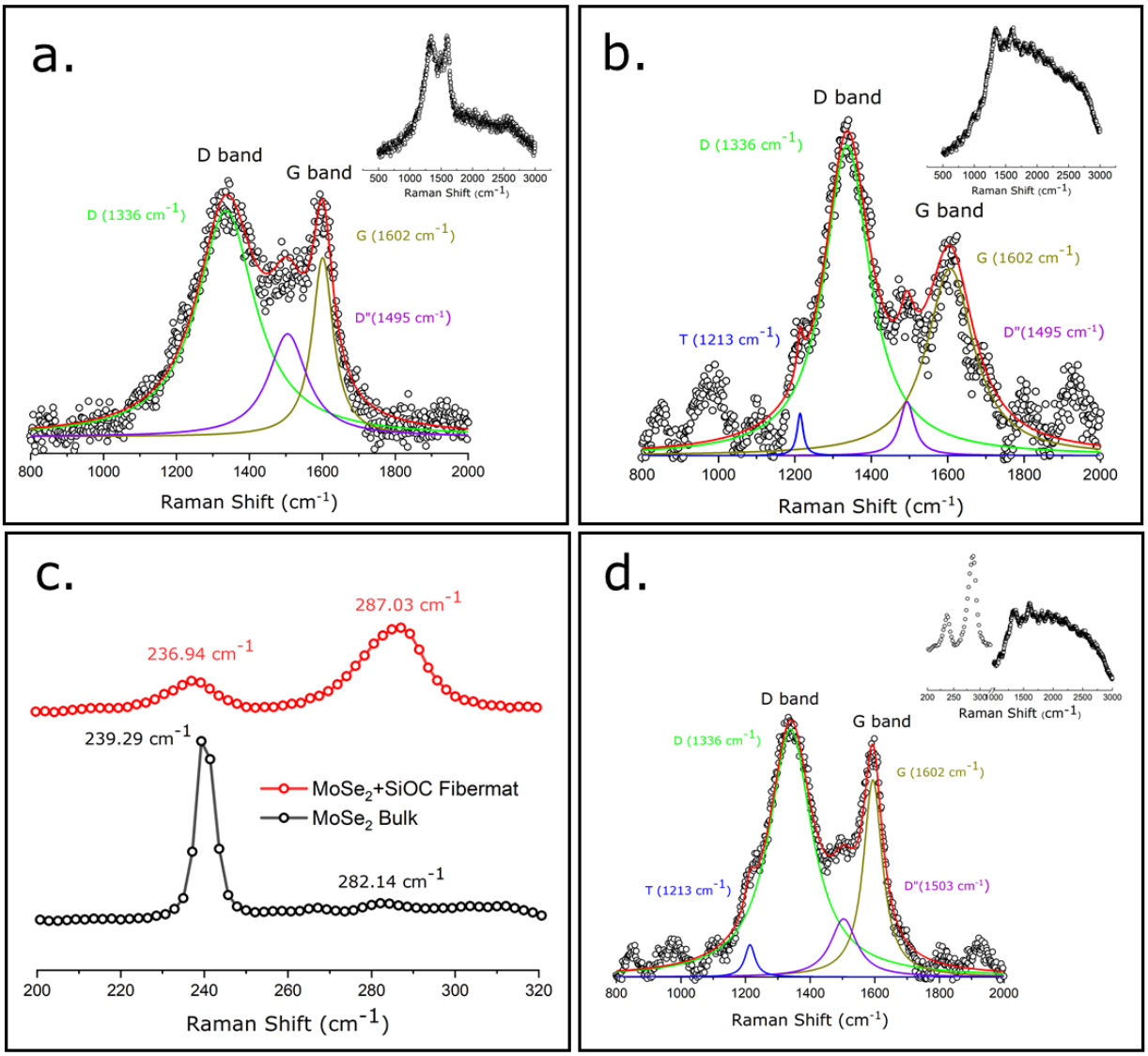


Figure 8.4: *Raman spectra of carbonized PVP fiber mat with integrated peaks; (b) Raman spectra of pyrolyzed PVP/SiOC fiber mat with integrated peaks; (c) Raman spectra of bulk $MoSe_2$ powder and the region of 200–300 cm^{-1} from the pyrolyzed SiOC/$MoSe_2$ fiber mat; (d) Raman Spectra of pyrolyzed PVP/SiOC/$MoSe_2$ fiber mat with integrated peaks in the region of 800–2000 cm^{-1}.*

Figure 8.5 illustrates the XPS survey scan of the carbonized/pyrolyzed PVP, PVP/SiOC, and PVP/SiOC/$MoSe_2$ fiber mats. C 1s, O 1s, and N 1s peaks were visible in the survey scan of the carbonized PVP fiber mat, which validated the presence of these molecules, even

after the pyrolysis stage. The survey scan of the pyrolyzed PVP/SiOC fiber mat revealed the presence of Si 2p, O 1s, and C 1s. For the pyrolyzed PVP/SiOC/$MoSe_2$ fiber mat, two additional peaks, Mo 3d and Se 3d, were observed, which again substantiates the presence of $MoSe_2$ in the pyrolyzed fiber mat. The PVP fiber mat showed the highest amount of carbon present in the pyrolyzed stage, with a percentage of 93.06%. Some nitrogen was also found in the fiber mat (2.1%), which originated from the pyrrolidinone structure of the PVP. The elemental analysis of the PVP/SiOC fiber mats shows the presence of carbon, silicone, and oxygen. The high amount of carbon (70.46%) visible in the pyrolyzed fiber mat resembles the data obtained from the Raman analysis well. The presence of high amounts of oxygen (17.36%) in this fiber mat is likely due to the cross-linking process conducted in the presence of air. The surface analysis of the pyrolyzed PVP/SiOC/$MoSe_2$ fiber mat reveals the presence of molybdenum and selenium particles in the fiber mat. The comparatively low amount of such particles only points to the elements present on the surface of the fiber mat or the fibers but not in the whole fiber mat. The nitrogen found in the pyrolyzed PVP/SiOC and PVP/SiOC/$MoSe_2$ fiber mats was low compared to the PVP fiber mat, which did not contribute significantly to the total elemental analysis.

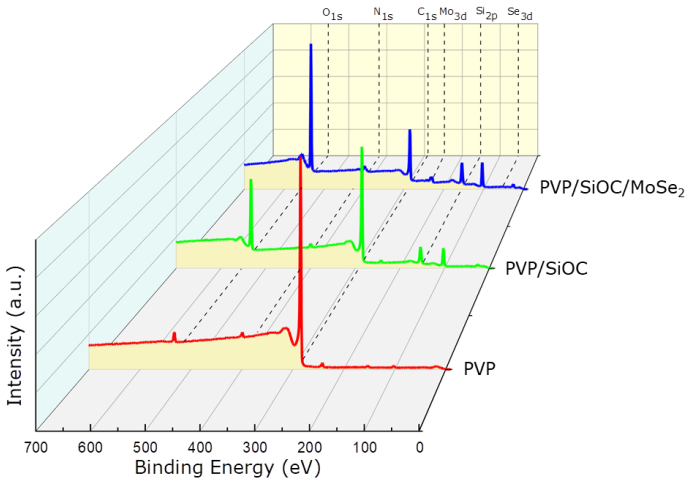


Figure 8.5: *XPS survey scan of pyrolyzed PVP, PVP/SiOC, and PVP/SiOC/$MoSe_2$ fiber mats.*

Figure 8.6 depicts the high-resolution scans of the XPS spectra for each element, elu-

cidating the individual peaks obtained from the survey scan. Multiple peak fittings of the high-resolution XPS spectra reveal the elements being differently bonded with other elements (hybridization). The high-resolution N 1s spectra (Figure 8.6a) of the pyrolyzed PVP fiber mat disclose the presence of pyridinic, pyrrolic, graphitic, and oxidized nitrogen with binding energies of 398.2 ± 0.1 eV, 399.4 ± 0.1 eV, 400.8 ± 0.1 eV, and 402.7 ± 0.1 eV, respectively, which correspond well with the literature[113]. The peak fitting of the O 1s high-resolution spectra (Figure 8.6b) of the carbonized PVP fiber mat divulged the bonding states C-O, C=O, NO, and O-C=O at 535 ± 0.1 eV, 533.5 ± 0.1 eV, 532.5 ± 0.1 eV, and 531.5 ± 0.1 eV, respectively[213;343]. Additionally, the deconvolution of the C 1s high-resolution spectra (Figure 8.6c) uncovered peaks in the binding energy region of 287.5 ± 0.1 eV, 285.8 ± 0.1 eV, and 284.5 ± 0.1 eV, which can be ascribed to the bonding states of O=C-N, C-N, and C-C, respectively[347]. From the deconvoluted C 1s spectra of the pyrolyzed PVP/SiOC and PVP/SiOC/$MoSe_2$ fiber mats, the C=O, C-C, and C-Si bonding states were observed in the regions of 287.1 ± 0.1 eV, 284.9 ± 0.1 eV, and 284.0 ± 0.1 eV, respectively. From the Si 2p spectra of the PVP/SiOC (Figure 8.6d) and PVP/SiOC/$MoSe_2$ (Figure 8.6g) fiber mats, the $SiCO_3$ and SiC_2O_2 bonding states were discovered in the 103.5 ± 0.1 eV and 102.9 ± 0.1 eV regions of the spectra. Finally, the O-Si and SiO_2 bonding states were discerned from the O 1s spectra of the PVP/SiOC (Figure 8.6e) and PVP/SiOC/$MoSe_2$ (Figure 8.6h) pyrolyzed fiber mats. The corresponding peaks align well with previous studies conducted regarding SiOC-based materials[37;369;394]. The high-resolution spectra also imparted the dominance of C-Si bonds over the C-C bonds. Furthermore, the deconvolution of the Mo 3d spectra of the pyrolyzed PVP/SiOC/$MoSe_2$ fiber mats presented the 3d5/2 and 3d3/2 peaks in the region 228 ± 0.1 eV and, 231.1 ± 0.1 eV, respectively, signifying the 2H polymorph of $MoSe_2$[148;268]. In addition to this, two other peaks at around 229.8 ± 0.1 eV and 232.9 ± 0.1 eV were identified and were thought to have originated from 2H-$MoSe_2$[400]. Another peak at around 235.4 ± 0.1 eV was located and was determined to correspond to Mo-O-C bonds with low intensity values[85]. The spectra of the Se 3d spectra can be deconvoluted into two peaks of 3d5/2 and 3d3/2 in the regions of 54.1 ± 0.1 eV and 55.0 ± 0.1 eV for the 1T and 2H phases, respectively[23;30].

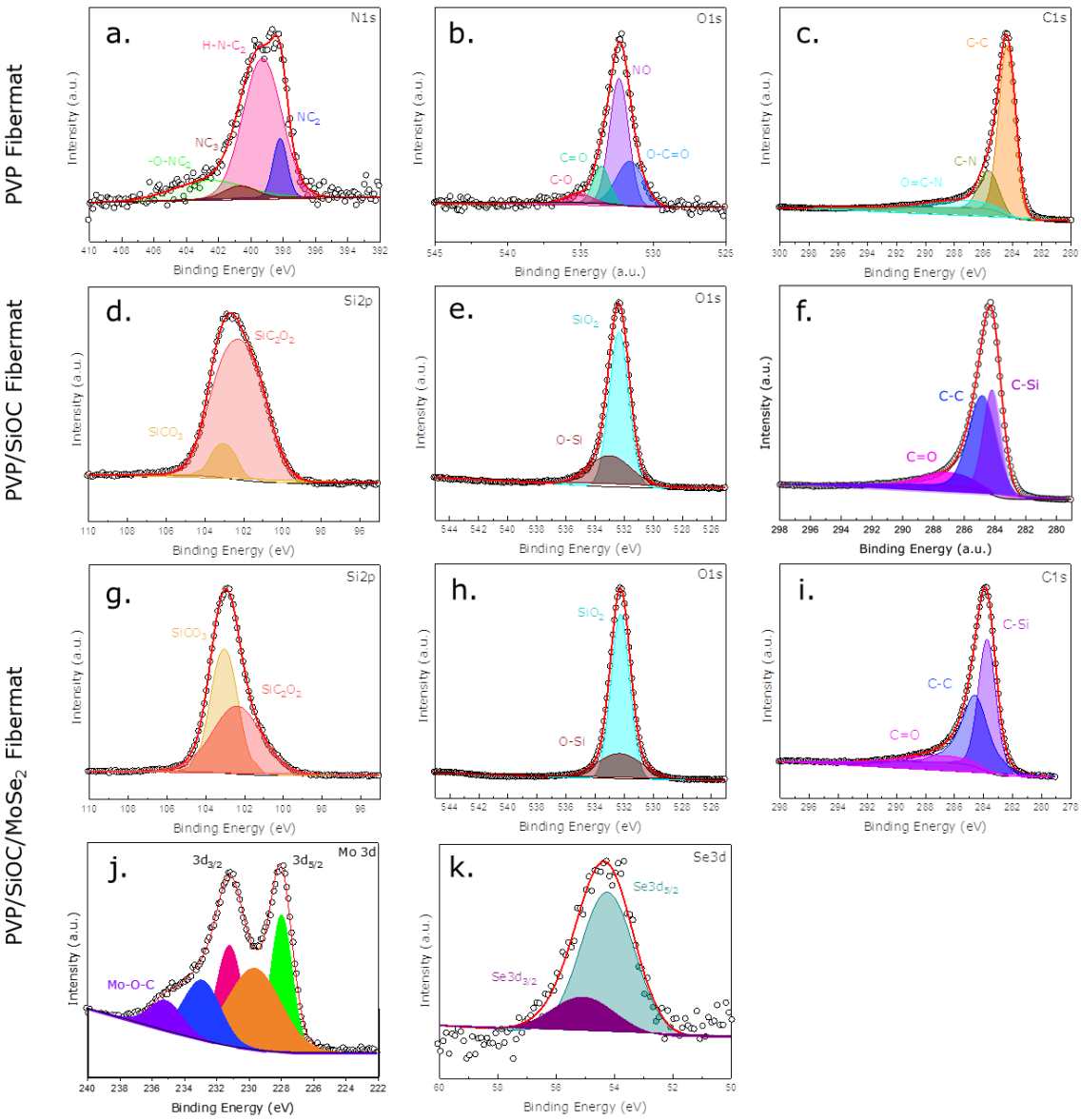


Figure 8.6: *High-resolution XPS spectra of three pyrolyzed fiber mats: (a–c) PVP fiber mat; (d–f) PVP/SiOC fiber mat; (g–k) PVP/SiOC/$MoSe_2$ fiber mat.*

Figure 8.7a–c illustrates the FTIR absorption bands of the PVP, PVP/SiOC, and PVP/SiOC/$MoSe_2$ fiber mats in their as spun, cross-linked, and pyrolyzed forms. From the FTIR spectra of the as-spun PVP fiber mat, absorption bands at 570, 841, 1018, 1288, 1422, 1663, 2923, and 3399 cm^{-1} were observed. These peaks can be assigned to N-C=O bond bending, CH2 bond bending, the rocking motion of CH2 bonds, C-N bond stretching, C-H bond stretching, C=O bond stretching, and symmetric stretching of the CH2 chain, respectively[20;122]. In

the cross-linked fiber mats, similar peaks were observed at 160 °C, demonstrating meager changes indicative of the small cross-linking reactions of the polymer chains. Finally, from the bottom of Figure 8.7c in the PVP fiber mat carbonized at 800 °C, the peaks mentioned above were not visible, which indicates the presence of only carbon. From Figure 8.7a, the FTIR spectra in the middle are for the PVP/SiOC as-spun fiber mats from which the dedicated absorption bands for SiOC materials can be observed. The peak observed at 797 cm^{-1} can be ascribed to the Si-C deformation vibration originating from the Si-CH3 bond. The peak at 1059 cm^{-1} is indicative of the Si-O-Si asymmetric stretching.

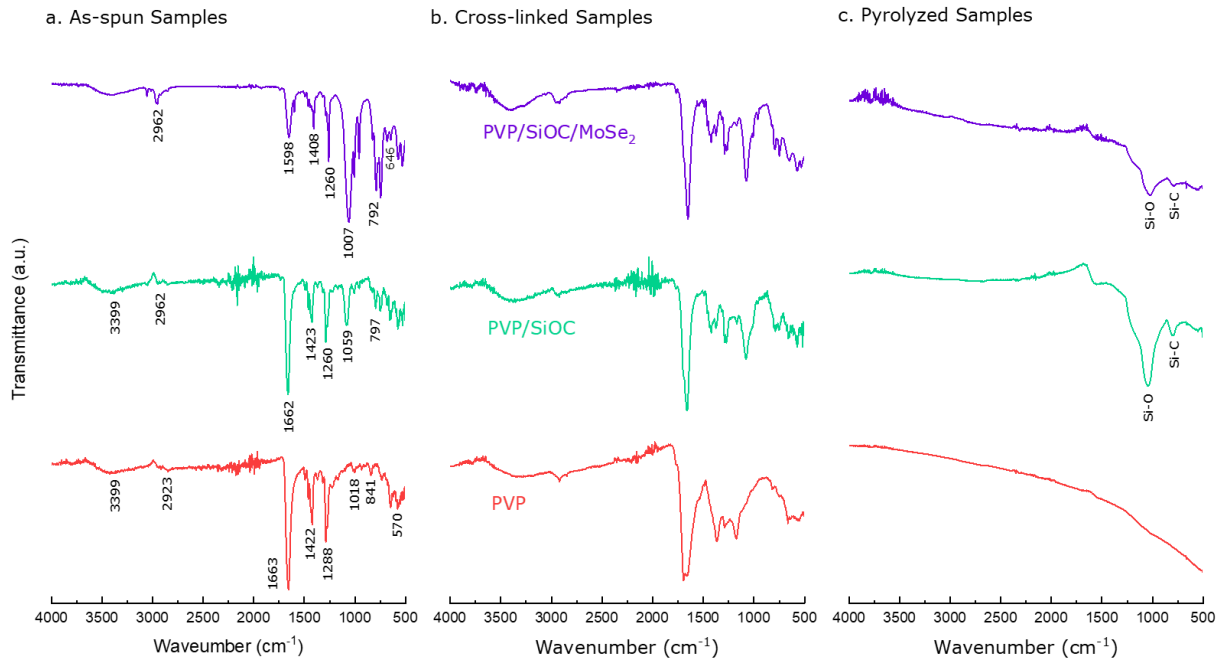


Figure 8.7: *FTIR spectra of (a) as-spun, (b) cross-linked, and (c) pyrolyzed fiber mats. Each figure consists of the FTIR spectra shown for PVP, PVP/SiOC and PVP/SiOC/$MoSe_2$ fiber mats from bottom to top.*

Additionally, the peak at 1260 and 1423 cm^{-1} originated from the C-H symmetric and asymmetric bending vibration from the Si-CH3 bonds, respectively. The peak at 1662 cm^{-1} is thought to originate from C=C double bond stretching. The absorption bands over the 2900 cm^{-1} can be allotted to the C-H asymmetric stretching originating from Si-CH3 and Si-CH=CH2 bonds. All of these bonds are in accordance with the previous literature and are suggestive of the presence of pre-ceramic polymers present in the as-spun fiber mats[43;215;243].

No significant changes were evident from the cross-linked fiber mat. However, the pyrolyzed fiber mat only represented the Si-O and Si-C bonds present in the 1060 and 800 cm^{-1} regions, which confirms the progressive degradation of the SiOC network as the temperature increases. Similar peaks were observed in the as spun, cross-linked, and pyrolyzed PVP/SiOC/$MoSe_2$ fiber mats and showed no additional peaks for $MoSe_2$.

Electrochemical Analysis

Figure 8a–d illustrates the electrochemical charge–discharge behavior of the carbonized PVP, pyrolyzed PVP/SiOC, $MoSe_2$ drop-coated pyrolyzed PVP/SiOC, and pyrolyzed PVP/SiOC/$MoSe_2$ electrodes in the lithium half-cell setup over a voltage window of 0.01–2.5 V. In addition, Figure 8.8e–h denotes the differential curves of the same fiber mats in the previously mentioned order, where the plateaus of the charge–discharge profile are clearly visible with the corresponding peaks. From the charge–discharge behavior of the carbonized PVP fiber mat electrode presented in Figure 8.8a, for the first cycle, which took place at a current density of 50 mA g^{-1}, a specific charge capacity of 569.96 mAh g^{-1} and a specific discharge capacity of 269.95 mAh g^{-1} are observed. Thus, high irreversible capacity loss can be observed, which is not visible in the consecutive cycles. It is possible to analyze this behavior with the help of the differential capacity curve from Figure 8.8e, where a sharp peak at 0.53 V is seen in the first cycle. However, this peak was not present in the consecutive cycles, which is indicative of an irreversible layer of materials, generally called solid electrolyte interface (SEI) forming, on the interface of the electrolyte and electrode. Similar peaks in can be observed in the 0.75–0.85 V region in various studies of hard carbons, which can be assigned to pore lithiation as well as SEI formation[193]. The peak below the 0.5V region can be attributed to the lithium ions interacting with the functional oxygen groups that are present in the fiber mat[319]. This peak was also irreversible in the delithiation cycle because the working voltage window does not fall into the range[62]. The peaks observed at around the 1 V region originated from the nitrogen-containing carbon present in the fiber mat, which was confirmed by the XPS analysis[168].

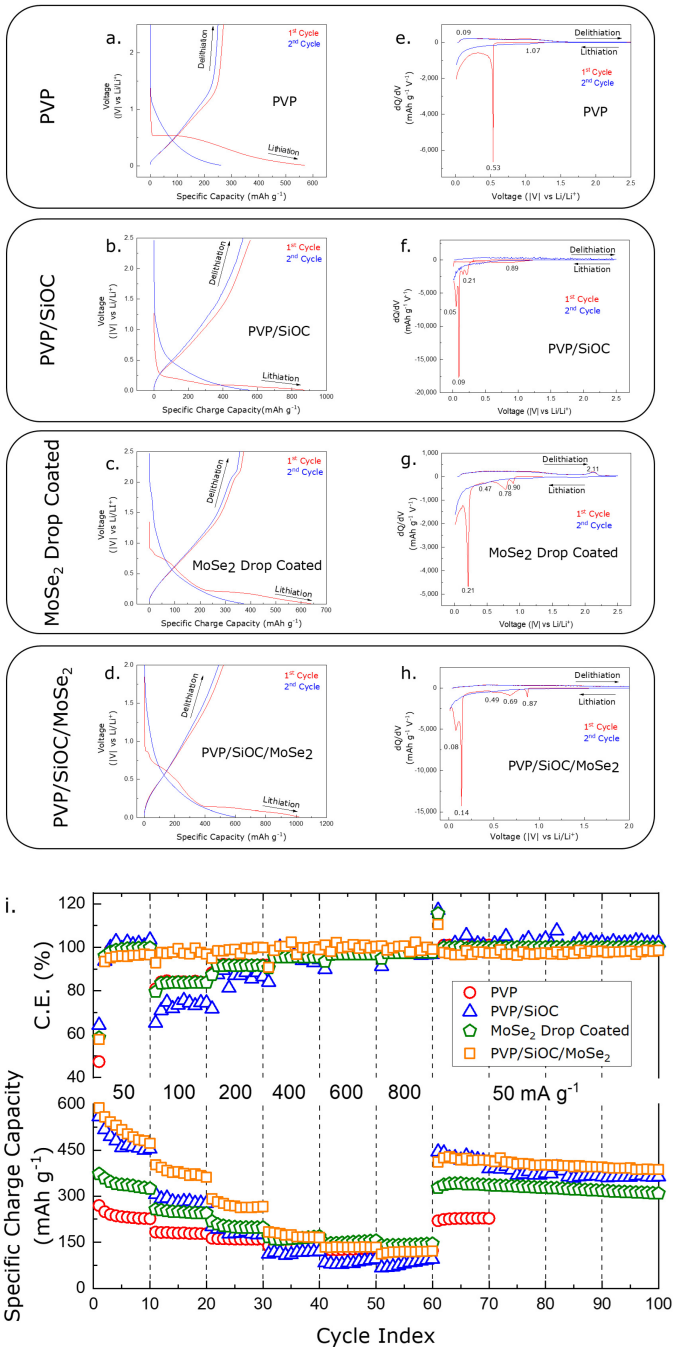


Figure 8.8: *Charge–discharge profile of (a) PVP fiber mat electrode; (b) PVP/SiOC fiber mat electrode; (c) $MoSe_2$ drop coated fiber mat electrode; (d) PVP/SiOC/$MoSe_2$ electrode and differential capacity curves of (e) PVP fiber mat electrode; (f) PVP/SiOC fiber mat electrode; (g) $MoSe_2$ drop coated fiber mat electrode; (h) PVP/SiOC/$MoSe_2$ electrode; (i) cycle performance comparison for PVP, PVP/SiOC, PVP/SiOC/$MoSe_2$ electrode at different current densities.*

Figure 8b,f shows the charge–discharge profiles and the differential capacity curves for the pyrolyzed PVP/SiOC fiber mat electrode. Fukui et al. demonstrated that the lithium ion storage mechanism of the SiOC material is via the intercalation/deintercalation reaction, which is quite similar to hard carbon materials. The peaks seen in between 0.5–1.5 V can be assigned to the electrolyte decomposition and the formation of the SEI layer. In addition to these peaks, some other peaks can be observed in a low-lying potential region, which can be assigned to lithium being irreversibly trapped in a region where oxygen is present or where dangling bonds and defects are present. However, the delithiation curve obtained in Figure 8.8b is uniform and straight, showing neither any plateaus nor any peaks, which is indicative of the porous nature of the SiOC material[106;152].

Figure 8.8c,g shows the charge–discharge profiles and differential capacity curves of $MoSe_2$ that was drop coated onto the electrode of the SiOC fiber mat—which was prepared for comparison purposes with the electrospun SiOC/$MoSe_2$ fiber mat. Due to similarities in the structure of $MoSe_2$ and MoS2, they go through the similar initial lithium ion intercalation[123]. As the $MoSe_2$ material was introduced by creating a coating on top of the fibers, the lithium ions were more exposed to it, and thus, the peaks related to the reaction with the $MoSe_2$ material were more pronounced. For instance, the peak observed in the first cycle near the 1 V region can be ascribed to the irreversible crystal structure change in $MoSe_2$ from trigonal prismatic 2H-$MoSe_2$ to octahedral 2T-Li$x$$MoSe_2$ 103. The latter coordination is more stable, and the phase change was confirmed by previous studies[244]. The peak assignment is based on the following lithiation process: The first cycle lithiation peak at approx. 0.7 V can thus be assigned to the following conversion process:

$$Li_xMoSe_2 + (4-x)Li \longrightarrow Mo + 2Li_2Se \tag{8.1}$$

$$MoSe_2 + 4Li \longrightarrow Mo + Li_2Se \tag{8.2}$$

These two equations can be combinedly expressed as follows, and the formula has been

confirmed by previous studies[320]:

$$Se + 2Li \longrightarrow Li_2Se \tag{8.3}$$

The peaks below the 0.4 V potential region are indicative of SEI formation by the SiOC material. Furthermore, one more peak situated in the 0.47 V can be assigned to the SEI formation that occurs due to the $MoSe_2$ material. Finally, the oxidation peak visible in the 2.1 V region can be accredited to the following equation confirmed by Cui et al., which appears in consecutive cycles as well[61].

For the pyrolyzed PVP/SiOC/$MoSe_2$ fiber mat electrode (Figure 8.8h), three reduction peaks in the potential region of 0.4–1 V can be similarly credited to the lithiation process happening due to $MoSe_2$, while the peak below this region is due to the SEI formation happening because of the SiOC material. Interestingly, no delithiation or oxidation peaks were observed in the first and second cycles, which is indicative of the dominance of the SiOC material in the fiber mat.

Figure 8.8i shows the comparison of the three fiber mat electrodes of the PVP PVP/SiOC mats and the PVP/SiOC/$MoSe_2$ electrodes when they are cycled at increasingly higher current densities (100, 200, 400, 600, 800 mA g^{-1}) in a rate capability test, thus leading to faster lithium ion insertion and extraction. The $MoSe_2$ drop-coated electrode is not included in this comparison. The comparison of the first cycle charge capacity of the fiber mat electrodes show a dominance of the pyrolyzed PVP/SiOC/$MoSe_2$ electrode, with a value of 586.96 mAh g^{-1} over the other electrodes. At higher current densities at which the electrodes were tested, the PVP/SiOC fiber mat electrode showed a clear capacity advantage over the carbonized PVP fiber mat electrode. The reason for this good performance can be attributed to the porous nature of the SiOC materials and the fiber mats, which facilitate lithium-ion storage by decreasing the distance required for ion diffusion when the electrolytes penetrate inside the deep pores. These pores also work as protection against the large volume expansion that takes place during the insertion and extraction of lithium ions[93;153;169]. From the investigation of Fukui et al., it can be confirmed that the SiOC materials store lithium

ion on interstitial spaces or graphene edges[93]. Further improvements can be seen at even higher current densities for the pyrolyzed PVP/SiOC/$MoSe_2$ electrode. Although the charge capacity of the pyrolyzed PVP/SiOC/$MoSe_2$ electrode was slightly less than the PVP/SiOC electrode when cycled back to the initial 50 mA g^{-1} current density from 800 mA g^{-1}, the fast recovery was achieved in the 71st cycle, and the specific charge capacity improved in the later cycles while cycling at the same current density.

The coulombic efficiency of the lithium half-cell for all of the electrodes is presented in Figure 8.8i. From figure, it is evident that all of the fiber mat electrodes suffered from a low coulombic efficiency in the first cycle, which is due to the formation of irreversible SEI formation. It is also evident that the pyrolyzed PVP/SiOC/$MoSe_2$ fiber mat electrode was more stable while charging and discharging at the higher current densities, which indicates that the fast and reversible insertion and extraction of lithium ions into the fibers was maintained in all of the cycles. The pyrolyzed PVP/SiOC/$MoSe_2$ electrode showed a stable response with a coulombic efficiency of 100% for 100 cycles, whereas carbonized PVP and pyrolyzed PVP/SiOC electrodes showed poor reversibility when the current density was increased to 100 and 200 mA g^{-1}. This further elucidates that the SiOC-functionalized $MoSe_2$ fiber mat kept its structure intact, even after going through harsh testing conditions, making this fiber mat electrode superior to the other electrodes tested.

8.5 Summary and Conclusion

In summary, this work is the first to present $MoSe_2$ nano-sheets combined with polymer-derived PVP/SiOC fiber mats to yield a free-standing electrode, providing stable cycling in higher current densities in LIB half-cell configuration. The ceramic mats were prepared via the electrospinning of chemically exfoliated $MoSe_2$ that had been dispersed in a preceramic polymer solution. A small quantity of PVP was used as a spinning agent, mainly to facilitate fiber spinnability. In addition to this, the evolution of the fibers from as spun to cross-linked and finally to the pyrolyzed form was confirmed by the FTIR spectroscopy. Raman and XPS spectroscopic studies revealed the presence of the free carbon phase present

in the fibers and the mixture of bonds between Si-O-C, respectively. The PVP/SiOC/$MoSe_2$ fiber mat electrode showed stable coulombic efficiency and a higher capacity than the fiber mats fabricated without the $MoSe_2$ material when cycled at progressively increasing current densities. Therefore, a self-supporting SiOC-functionalized $MoSe_2$ composite electrode possessing such stable performance during harsh cycling conditions can be suitable for a wide range of energy storage applications.

8.6 Mechanical Testing of Fibermats

Mechanical properties of the neat fibermats and TMD nanofiller-reinforced fibermats were determined using a tensile testing approach. Different fibermats were punched out by a metallic punch with a width and thickness of 5.8 mm and 20 mm, respectively. To test the delicate cross-linked fibers specialized grips were designed using Solidworks and then machined using aluminum. Specific dimensions of the grips and digital camera image are shown in Figure 8.10 illustrated by Solidworks 3D drawing.

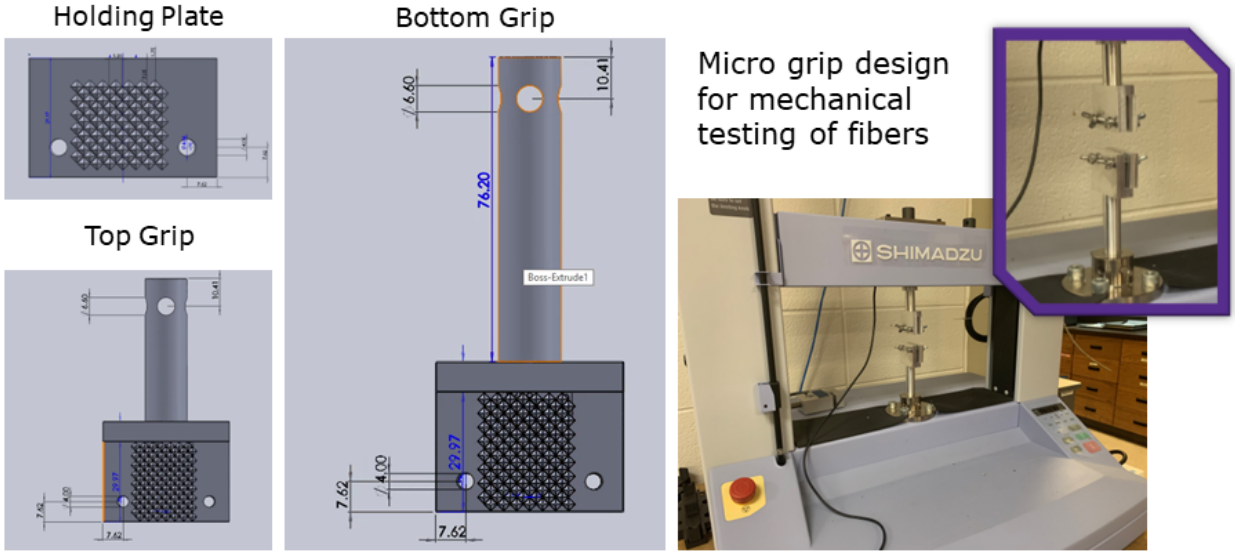


Figure 8.9: *Solidworks 3D model of the grip designed for tensile testing of x-linked fibermats with digital camera images.*

Figures **??**(a-f) show the stress-strain plots of different fibermats, and the results are reported in Table 8.1. PVP fibers showed the highest strain to failure, while $MoSe_2$/SiOC

fibers had the lowest strain. SiOC ceramic inclusion on PVP resulted in comparatively similar strength but less strain to failure. This behavior is as per expectation from ceramic-based composites. Different further nanofiller reinforcements resulted in variability in stress and strain. For instance, $MoSe_2$/SiOC fibers were the strongest among the measured samples, with 2.28 MPa strength at failure. The most insufficient strength was realized from WS2NS-reinforced SiOC fibers with 0.43 MPa. When compared amongst the same TMDs with different polymorph-reinforced fibers, WS2NT reinforcement led to higher strength than WS2NS reinforcement. Specific mechanical properties of the fibers with and without nanofiller reinforcements are listed in Table 8.1.

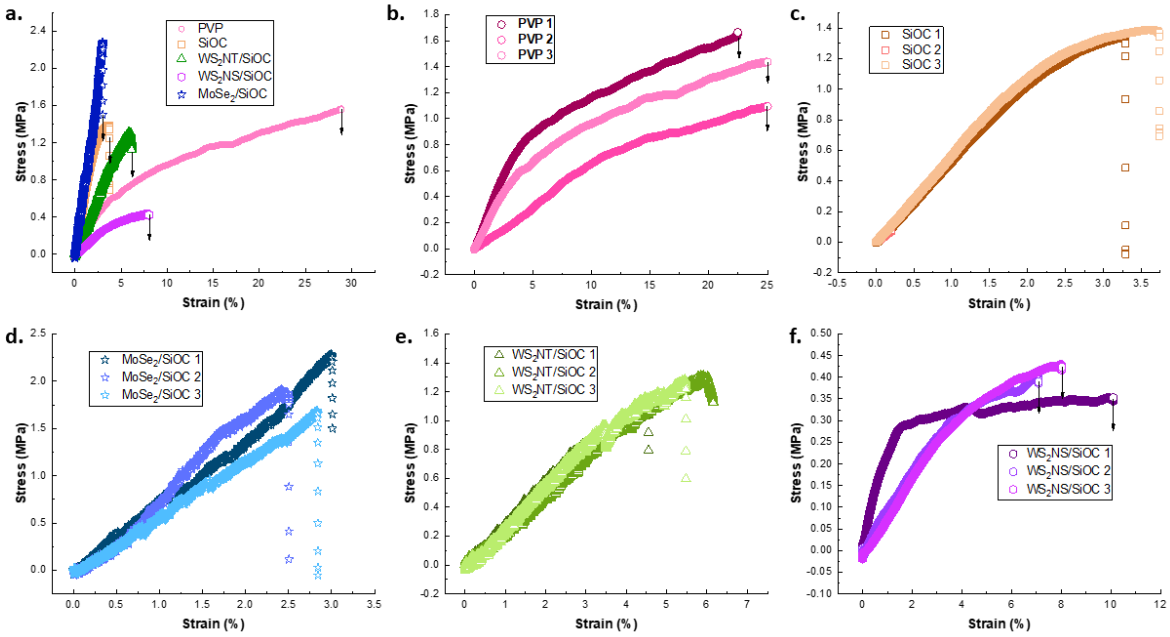


Figure 8.10: *Stress-strain plots of a. best performing fibermats from all samples; b. PVP; c. SiOC; d. $MoSe_2$/SiOC; e.WS2NT/SiOC; f. WS2NS/SiOC fibermats.*

Table 8.1: *Tensile properties of fibermats with or without reinforcement.*

Sample	Strain to Failure (%)	Strength at failure (MPa)	Young's Modulus
PVP 1	22.47	1.66	0.24
PVP 2	24.95	1.09	0.06
PVP 3	24.92	1.44	0.19
SiOC 1	3.29	1.30	0.54
SiOC 2	3.21	1.30	0.39
SiOC 3	3.73	1.37	0.57
$MoSe_2$/SiOC 1	2.98	2.28	0.82
$MoSe_2$/SiOC 2	2.42	1.92	0.56
$MoSe_2$/SiOC 3	2.82	1.69	0.59
WS2NS/SiOC 1	10.11	0.35	0.12
WS2NS/SiOC 2	7.09	0.39	0.12
WS2NS/SiOC 3	7.99	0.43	0.12
WS2NT/SiOC 1	4.46	1.1	0.27
WS2NT/SiOC 2	5.85	1.32	0.23
WS2NS/SiOC 3	5.45	1.29	0.30

Chapter 9

Conclusion and Future Direction

Research thrust for electrochemical energy storage in TMDs reached its zenith due to high interlayer spacing, metal ion hosting ability, and higher amount of electron transfer for hosting multiple ions per molecule. Most research in reversible electrochemical energy storage of TMDs focuses on Li^+ ion

−

based technologies. Yet, the most recent pandemic has underscored the urgency to search for complementary battery technologies. With an identical number of valence electrons in the outermost shell, Na and K−based battery technologies present an immense opportunity with similar chemical properties, but are barely studied in reversible storage inside TMD layers. Therefore, in this thesis, we examine how size in alkali metal influences the storage properties in traditional TMD nanosheets. Realizing large interlayer expansion and subsequent structure pulverization, we further looked into the influence of TMD structure modification by utilizing nanotubes and nanocage−like quantum−confined polymorphs in terms of bulky alkali−metal ion storage. To overcome existing drawbacks in TMD nanostructures, we utilize them as nanofillers to form composite high aspect ratio structures with chemically robust PDCs. Nevertheless, we employ a voltage cut−off technique in neat TMD polymorphs to suppress side reactions and observe stable cycling behavior.

Motivated by applying distinct nanostructures of TMDs, this thesis curiously inves-

tigated the change of Na^+ and K^+-ion storage inside TMD alloys, where a transition metal is arbitrarily substituted with another transition metal, and suggested methodology to revamp their electrochemical properties. Being successful in composite formation with sulfide−based TMD materials and PDCs in fibermat form, the dissertation further implemented selenide−based TMDs and PDCs − scrutinized the feasibility of fibermat fabrication and highlighted utilizing fibermats as electrically conducting and self−supporting electrodes. Finally, the mechanical properties of such fibermats were investigated, fulfilling the search for bendable systems fabricated to be lightweight and wearable while mechanically flexible. The upcoming section provides a concise overview of each chapter's key findings and significance, while a connection is established between various topics.

9.1 Dissertation Summary

The introduction (Chapter 1) of this thesis highlighted the worldwide transition from fossil fuel−based energy production to renewable energy systems and afterward delved into the deficiencies of current renewable energy generation technologies. Building upon that, the role of electrochemical energy storage systems in preserving produced energy via renewable sources is demonstrated next. The superiority of LIB systems in modern technology is presented next. With adversities of current LIB systems, such as uneven distribution of resources, supply chain risks, difficulties associated with the mining process, and surging demand for Lithium − the chapter established the need for alternative battery systems. Expanding on the abovementioned case, the benefits of NIB and KIB were demonstrated. As this thesis sheds light on using different nanostructured materials, the proliferation of other nanomaterials driven by the surge in nanotechnology was highlighted, and their benefits upon use as electrode materials were stressed. The contribution of this thesis can be classified into the following objectives: the first objective was to find out how different nanostructures of 2D TMD materials influence larger than conventional alkali metal ion storage, find out their deficiencies, and address novel and innovative procedures to overcome the shortcomings. Two such ways were discovered: composite structure formation with chemically robust PDC

materials and use of voltage cut−off techniques − building upon which such materials can be better utilized in NIB and KIB applications. The second objective was to apply such processes in other TMD−based nanostructures, observe the consistency of such techniques, and suggest ways towards practical application of specific fibermats.

Chapter 2 first highlights the historical development of different battery chemistries (LIBs/NIBs/KIBs), the working principle of each, and then the most recent developments in negative electrode materials for each system. The chapter then introduces the investigated nanomaterial, specifically the different nanostructures of TMDs and their alkali metal−ion storage properties. This chapter also highlights the matrix material used for the composition of composite structures, namely PDCs, and existing literature on their electrochemical properties. Progressing on that, different microscopical techniques for visual identification of nanoparticles and hybrid networks, spectroscopic methods for elemental and chemical structure identification and re−verification of fabricated structures, and finally, popular electrochemical probing tools for identification of reversible ion storage mechanism, electrode kinetics, and performance metrics were pointed out in chapter 3.

Chapters 4 and 5 investigated the alkali metal ion storage within distinctive nanostructures of WS_2, namely nanosheets and nanotubes − pointing out their inadequacy of stable electrochemical performance due to energy inefficiency resulting from conversion reactions, extreme volume change leading to pulverization and associated side reactions. Carrying forward, these chapters shed light on the successful functionalization and composite formation with chemically robust PDCs in fibermat form. The optimization of the nanofiller (TMD nanotube) to matrix (PDCs) material ratio in fiber form led to a synergistic performance of the composite structure − displaying robust performance in terms of harsh cycling conditions. Such a performance of the composite system assisted in building upon the case that the PDC matrix might buffer the volume change of such materials during reversible sodiation/potassiation, helping the nanomaterials to survive for a longer time and provide stable performance.

Chapter 6 progressed on applying WS_2 fullerene−like nanoparticles with closed cage−like structures. Here, a different technique, namely, upper and lower voltage cut−off, was em-

ployed to curb reversible sodiation/potassiation fatality. The restriction of upper voltage led to the most stable performance of the electrode with enhanced coulombic efficiency. In contrast, suspension of lower voltage along with upper voltage proved to halt essential chemical reactions taking place − the result of which was the reflection of poor performance in half−cells. Furthermore, the electrode kinetics was identified with several electrochemical techniques pointing to different cells' diffusive vs capacitive charge storage mechanisms with distinct cut−off voltages. Being motivated by this study, chapter 7 assessed the efficiency of the voltage cut−off technique in arbitrarily transition metal substituted selenide−based TMD alloy, which offers much intense conversion reaction and the possibility of pronounced voltage hysteresis leading to energy inefficiency. After careful investigation, the efficiency of the upper−voltage cut−off techniques proved to be vital for the structural preservation of $MoWSe_2$. In this chapter, the predominance of 3D differential capacity curves, which extend the plotting process as a function of progressing cycles, also guides the researchers to a new, readily accessible in−situ data analysis technique. Nevertheless, such investigations might inspire researchers to combine such methods with composite formation to best use existing materials beyond LIB application.

As previous composite fibers were produced with sulfide−based TMDs, chapter 8 inquires about applying this facile technique in selenide−based TMDs ($MoSe_2$). This study underscored the versatility of such a technique and pushed us toward using pyrolyzed fibermats in free−standing form without the support of a copper current collector. Only a small quantity of nanofilled ($MoSe_2$) containing PDC fibers displayed stable coulombic efficiency and higher capacity (higher than the robust anode material of LIBs, Graphite 372 mAh g^{-1}) compared to the neat materials. To assess the load bearing and controlled deformation capability of such self−supporting fibermats ($MoSe_2$/SiOC), customized grippers were designed, mechanical tests were performed and compared with fibermats fabricated and described in the previous chapters (WS_2NS/SiOC, and WS_2NT/SiOC).

9.2 Direction of Future Work

Although this thesis developed new tools, employed novel methods, and emphasized innovative techniques and specific findings leading to electrochemical performance enhancements, it undeniably opened the door to additional research opportunities. This section, therefore, lists some of the areas that can be possibly explored in advancing on this line of research:

- This thesis showcased the kinetics of alkali metal ion storage inside TMDs and composite fibermats nanostructures via different electrochemical analysis techniques. A push for novel characterization techniques might lead to using operando or in−situ techniques where reversible alkali−metal ion insertion can be measured either in real operating time or on−site, referring to a distinct variable against relevant system parameters.

- All the work presented in this thesis was conducted experimentally, gathering knowledge from the existing literature. However, theoretical work regarding the charge storage mechanism of different TMD quantum confinement structures is still missing. Therefore, geometry optimization to measure optimized lattice structure, density of states calculation to measure the electronic conductivity, charge density calculation for investigating the interaction of SiOC with TMD nanomaterials and the existing chemical environment, and transition state search of Na^+/K^+−ions for mapping preferable storage sites can be performed utilizing density functional theory.

- Although this thesis presents the primary mechanical properties of randomly aligned electrospun fibers, how the alignment of fibers affects the mechanical strength of fibers has not yet been investigated, especially with nanomaterial reinforcement. Therefore, further study regarding specific instrumental setups for vertical and horizontal alignment of nanofibers is necessary, which can be compared with randomly aligned ones to provide a better basis for next−generation fiber electrode utilization.

- Fabricated composite fibermats showed a random dispersion of materials. For example, while most of the WS_2NTs were found inside the SiOC fibers, some chunks were

observed, and WS_2NS and $MoSe_2$NS were found to be randomly dispersed within the fibers. Literature suggests the distribution of charges under high voltage influences the arrangement of nanofillers and polymers inside the spinneret before forming a Taylor Cone. An electrical field simulation analysis might be performed to optimize the nanomaterial dispersion and further improve the versatility of electrospinning.

- This thesis is the first work to show the possibility of TMD nanofiller−reinforced ceramic fiber composite formation and its application in reversible electrochemical energy storage devices. This work utilized only one precursor out of more than a hundred to fabricate PDC fibermat, which nevertheless accentuated the countless possibilities of fiber production techniques. Furthermore, substituting O from SiOC yields SiCN−based PDC fibers (a process generally carried out in the absence of ambient) that have not yet been electrospun with nanofillers, for which an electrospinning setup can be utilized in an inert atmosphere. Additionally, complementary, cost−effective, and faster methods for fiber production, such as force−spinning, can be explicitly explored for ceramic fibers.

- Ceramics are ubiquitously high−temperature withstanding materials − providing further basis for applying them as electrode materials for batteries operating at a wider range of temperatures. For such applications, ionic liquid or dual salt−based electrolytes can be employed, promoting a higher ionic conduction rate. Such electrolytes can also be investigated with the electrode setup utilized in this study, as a minor capacity decay is observed at the 50^{th} cycle in the rate capability test.

- The SEI formation procedure of the fabricated electrodes on copper foils or in free−standing form can be an exciting field to investigate further. Specific flame retardant materials or additives preventing HF formation, which stops corrosion of current collectors, are now widely applied in LIB systems. Their application in NIB and KIB systems is another exciting prospect.

- So far, 40 different TMDs exist, consisting of Group VI−X transition metals. Among

them, Group VI transition metals containing TMDs are widely known for their semiconducting properties. Although traditional electrodes are fabricated with conductive materials, they might not provide enough electrically conducting paths for electrons to pass and move to the outer circuit. Therefore, the application of conductive binder materials replacing traditional insulating PVDF−based binders might be explored.

Bibliography

[1] A. R. Adini, Meir Redlich, and Reshef Tenne. Medical applications of inorganic fullerene-like nanoparticles. *Journal of materials chemistry*, 21(39):15121–15131, 2011. doi: 10.1039/C1JM11799H. URL http://dx.doi.org/10.1039/C1JM11799H.

[2] H. Ahmad, S. A. Reduan, S. N. Aidit, N. Yusoff, M. J. Maah, M. F. Ismail, and Z. C. Tiu. Ternary mowse2 alloy saturable absorber for passively q-switched yb-, er- and tm-doped fiber laser. *Optics Communications*, 437:355–362, 2019. ISSN 0030-4018. doi: https://doi.org/10.1016/j.optcom.2019.01.009. URL https://www.sciencedirect.com/science/article/pii/S0030401819300094.

[3] Dongjoon Ahn. Electrochemical insertion of lithium into polymer derived silicon oxycarbide and oxycarbonitride ceramics. 2010. ISSN 110977964X. URL https://www.proquest.com/dissertations-theses/electrochemical-insertion-lithium-into-polymer/docview/504852781/se-2?accountid=11789.

[4] Dongjoon Ahn and Rishi Raj. Cyclic stability and c-rate performance of amorphous silicon and carbon based anodes for electrochemical storage of lithium. *Journal of Power Sources*, 196(4):2179–2186, 2011. ISSN 0378-7753. doi: https://doi.org/10.1016/j.jpowsour.2010.09.086. URL https://www.sciencedirect.com/science/article/pii/S0378775310016927.

[5] Ata Akcil, Zhi Sun, and Sandeep Panda. Covid-19 disruptions to tech-metals supply are a wake-up call. *Nature*, 587(7834):365–367, 2020. ISSN 0028-0836. URL https://www.nature.com/articles/d41586-020-03190-8.

[6] Mohammed A. Al-Tahan, Yutao Dong, Aml E. Shrshr, Xiaobiao Liu, Ran Zhang,

Hui Guan, Xiyang Kang, Ruipeng Wei, and Jianmin Zhang. Enormous-sulfur-content cathode and excellent electrochemical performance of li-s battery accouched by surface engineering of ni-doped ws2@rgo nanohybrid as a modified separator. *Journal of Colloid and Interface Science*, 609:235–248, 2022. ISSN 0021-9797. doi: https://doi.org/10.1016/j.jcis.2021.12.035. URL https://www.sciencedirect.com/science/article/pii/S0021979721021640.

[7] José Luis Aleixandre-Tudó, Lourdes Castelló-Cogollos, José Luis Aleixandre, and Rafael Aleixandre-Benavent. Renewable energies: Worldwide trends in research, funding and international collaboration. *Renewable Energy*, 139:268–278, 2019. ISSN 0960-1481. doi: https://doi.org/10.1016/j.renene.2019.02.079. URL https://www.sciencedirect.com/science/article/pii/S0960148119302332.

[8] Michel Armand and J. M. Tarascon. Building better batteries. *nature*, 451(7179): 652–657, 2008. ISSN 0028-0836. doi: 10.1038/451652a. URL https://doi.org/10.1038/451652a.

[9] Veronica Augustyn, Jérémy Come, Michael A. Lowe, Jong Woung Kim, Pierre-Louis Taberna, Sarah H. Tolbert, Héctor D. Abruña, Patrice Simon, and Bruce Dunn. High-rate electrochemical energy storage through li+ intercalation pseudocapacitance. *Nature Materials*, 12(6):518–522, 2013. ISSN 1476-4660. doi: 10.1038/nmat3601. URL https://doi.org/10.1038/nmat3601.

[10] Doron Azulay, Frieda Kopnov, Reshef Tenne, Isaac Balberg, and Oded Millo. Observation of current reversal in the scanning tunneling spectra of fullerene-like ws2 nanoparticles. *Nano letters*, 6(4):760–764, 2006. ISSN 1530-6984.

[11] Seung-Ho Baek, Lukas Mirko Reinold, Magdalena Graczyk-Zajac, Ralf Riedel, Franziska Hammerath, Bernd Büchner, and Hans-Joachim Grafe. Lithium dynamics in carbon-rich polymer-derived sicn ceramics probed by nuclear magnetic resonance. *Journal of Power Sources*, 253:342–348, 2014. ISSN 0378-7753. doi:

https://doi.org/10.1016/j.jpowsour.2013.12.065. URL https://www.sciencedirect.com/science/article/pii/S0378775313020430.

[12] Jiaxi Bai, Lifeng Zhang, Shuai Li, Huijun Ren, Yi Liu, and Shouwu Guo. Self-assembled mote2 hierarchical nanoflowers with carbon coating as anode material for excellent sodium storage performance. *Chemical Engineering Journal*, 452:139111, 2023. ISSN 1385-8947. doi: https://doi.org/10.1016/j.cej.2022.139111. URL https://www.sciencedirect.com/science/article/pii/S1385894722045909.

[13] Gayatree Barik and Sourav Pal. Monolayer transition-metal dichalcogenide mo1–xwxs2 alloys as efficient anode materials for lithium-ion batteries. *The Journal of Physical Chemistry C*, 122(45):25837–25848, 2018. ISSN 1932-7447. doi: 10.1021/acs.jpcc.8b07876. URL https://doi.org/10.1021/acs.jpcc.8b07876.

[14] Vahid Barough, Esmaiel Saievar Iranizad, Amir Bayat, and Khadijeh Hemmati. Synthesis of binder-free mose2 nanoflakes as a new electrode for electrocatalytic hydrogen evolution. *Journal of Electroanalytical Chemistry*, 823:278–286, 2018. ISSN 1572-6657. doi: https://doi.org/10.1016/j.jelechem.2018.06.022. URL https://www.sciencedirect.com/science/article/pii/S1572665718304363.

[15] Rivka Ben Ishay, Yifat Harel, Ronit Lavi, and Jean-Paul Lellouche. Multiple functionalization of tungsten disulfide inorganic nanotubes by covalently grafted conductive polythiophenes. *RSC Advances*, 6(92):89585–89598, 2016. doi: 10.1039/C6RA19628D. URL http://dx.doi.org/10.1039/C6RA19628D.

[16] Ayse Berkdemir, Humberto R. Gutiérrez, Andrés R. Botello-Méndez, Néstor Perea-López, Ana Laura Elías, Chen-Ing Chia, Bei Wang, Vincent H. Crespi, Florentino López-Urías, Jean-Christophe Charlier, Humberto Terrones, and Mauricio Terrones. Identification of individual and few layers of ws2 using raman spectroscopy. *Scientific Reports*, 3(1):1755, 2013. ISSN 2045-2322. doi: 10.1038/srep01755. URL https://doi.org/10.1038/srep01755.

[17] Samuel Bernard, Koffi Fiaty, David Cornu, Philippe Miele, and Pierre Laurent. Kinetic modeling of the polymer-derived ceramics route: investigation of the thermal decomposition kinetics of poly[b-(methylamino)borazine] precursors into boron nitride. *The Journal of Physical Chemistry B*, 110(18):9048–9060, 2006. ISSN 1520-6106. doi: 10.1021/jp055981m. URL https://doi.org/10.1021/jp055981m.

[18] Simone Bertolazzi, Jacopo Brivio, and Andras Kis. Stretching and breaking of ultrathin mos2. *ACS Nano*, 5(12):9703–9709, 2011. ISSN 1936-0851. doi: 10.1021/nn203879f. URL https://doi.org/10.1021/nn203879f.

[19] R. Bhandavat, L. David, and G. Singh. Synthesis of surface-functionalized ws2 nanosheets and performance as li-ion battery anodes. *The Journal of Physical Chemistry Letters*, 3(11):1523–1530, 2012. doi: 10.1021/jz300480w. URL https://doi.org/10.1021/jz300480w.

[20] Dhrubajyoti Bhattacharjya, Hyean-Yeol Park, Min-Sik Kim, Hyuck-Soo Choi, Shaukatali N. Inamdar, and Jong-Sung Yu. Nitrogen-doped carbon nanoparticles by flame synthesis as anode material for rechargeable lithium-ion batteries. *Langmuir*, 30(1):318–324, 2014. ISSN 0743-7463. doi: 10.1021/la403366e. URL https://doi.org/10.1021/la403366e.

[21] Sanket Bhoyate, Bumsu Park, Sang Ho Oh, and Wonbong Choi. Defect engineered mows alloy catalyst boost the polysulfide conversion in lithium–sulfur battery. *Journal of Power Sources*, 511:230426, 2021. ISSN 0378-7753. doi: https://doi.org/10.1016/j.jpowsour.2021.230426. URL https://www.sciencedirect.com/science/article/pii/S0378775321009319.

[22] P. Biloen and G. T. Pott. X-ray photoelectron spectroscopy study of supported tungsten oxide. *Journal of Catalysis*, 30(2):169–174, 1973. ISSN 0021-9517. doi: https://doi.org/10.1016/0021-9517(73)90063-8. URL https://www.sciencedirect.com/science/article/pii/0021951773900638.

[23] Lee Bok-Hee, Kim Ki-Bok, and Kim You-Ha. Measurement of the ground resistance using the fall-of-potential method with the vertically-placed current and potential auxiliary electrodes. *Journal of the Korean Institute of Illuminating and Electrical Installation Engineers*, 26(3):53–60, 2012. ISSN 1229-4691. URL http://www.dbpia.co.kr/journal/articleDetail?nodeId=NODE01815912.

[24] Liliane Bokobza, Jean-Luc Bruneel, and Michel Couzi. Raman spectra of carbon-based materials (from graphite to carbon black) and of some silicone composites. *C*, 1(1): 77–94, 2015. ISSN 2311-5629. doi: 10.3390/c1010077.

[25] J. Both. The modern era of aluminum electrolytic capacitors. *IEEE Electrical Insulation Magazine*, 31(4):24–34, 2015. ISSN 1558-4402. doi: 10.1109/MEI.2015.7126071.

[26] K. Brandt and F. C. Laman. Reproducibility and reliability of rechargeable lithium/molybdenum disulfide batteries. *Journal of power sources*, 25(4):265–276, 1989. ISSN 0378-7753.

[27] M. Broussely, Ph Biensan, and B. Simon. Lithium insertion into host materials: the key to success for li ion batteries. *Electrochimica Acta*, 45(1-2):3–22, 1999. ISSN 0013-4686.

[28] B. Brox and I. Olefjord. Esca studies of moo2 and moo3. *Surface and Interface Analysis*, 13(1):3–6, 1988. ISSN 0142-2421. doi: https://doi.org/10.1002/sia.740130103. URL https://doi.org/10.1002/sia.740130103.

[29] Rayna Bryaskova, Daniela Pencheva, Stanislav Nikolov, and Todor Kantardjiev. Synthesis and comparative study on the antimicrobial activity of hybrid materials based on silver nanoparticles (agnps) stabilized by polyvinylpyrrolidone (pvp). *Journal of Chemical Biology*, 4(4):185, 2011. ISSN 1864-6166. doi: 10.1007/s12154-011-0063-9. URL https://doi.org/10.1007/s12154-011-0063-9.

[30] L. G. Bulusheva, A. V. Okotrub, A. G. Kurenya, H. Zhang, H. Zhang, X. Chen, and H. Song. Electrochemical properties of nitrogen-doped car-

bon nanotube anode in li-ion batteries. *Carbon*, 49(12):4013–4023, 2011. doi: 10.1016/j.carbon.2011.05.043. URL https://www.scopus.com/inward/record.uri?eid=2-s2.0-79959964900&doi=10.1016%2fj.carbon.2011.05.043&partnerID=40&md5=3192f755529684e21a36a63f7060c5d4.

[31] Gary T. Burns, Timothy P. Angelotti, Larry F. Hanneman, Grish Chandra, and John A. Moore. Alkyl- and arylsilsesquiazanes: effect of the r group on polymer degradation and ceramic char composition. *Journal of Materials Science*, 22 (7):2609–2614, 1987. ISSN 1573-4803. doi: 10.1007/BF01082152. URL https://doi.org/10.1007/BF01082152.

[32] Guohui Cai, Lei Peng, Shiyong Ye, Yucheng Huang, Guangfeng Wang, and Xiaojun Zhang. Defect-rich mos2(1-x)se2x few-layer nanocomposites: a superior anode material for high-performance lithium-ion batteries. *Journal of Materials Chemistry A*, 7(16): 9837–9843, 2019. ISSN 2050-7488. doi: 10.1039/C8TA11583D. URL http://dx.doi.org/10.1039/C8TA11583D.

[33] Christian Chandra and Jaehoon Kim. Silicon oxycarbide produced from silicone oil for high-performance anode material in sodium ion batteries. *Chemical Engineering Journal*, 338:126–136, 2018. ISSN 1385-8947. doi: https://doi.org/10.1016/j.cej.2018.01.032. URL https://www.sciencedirect.com/science/article/pii/S1385894718300329.

[34] Christian Chandra, Handi Setiadi Cahyadi, Stevanus Alvin, Winda Devina, Jae-Ho Park, Wonyoung Chang, Kyung Yoon Chung, Sang Kyu Kwak, and Jaehoon Kim. Revealing the sodium storage mechanism in high-temperature-synthesized silicon oxycarbides. *Chemistry of Materials*, 32(1):410–423, 2020. ISSN 0897-4756. doi: 10.1021/acs.chemmater.9b04018. URL https://doi.org/10.1021/acs.chemmater.9b04018.

[35] Christian Chandra, Winda Devina, Handi Setiadi Cahyadi, Sang Kyu Kwak, and Jaehoon Kim. Understanding lithium, sodium, and potassium storage mechanisms in silicon oxycarbide. *Chemical Engineering Journal*, 428:131072, 2022. ISSN 1385-8947.

doi: https://doi.org/10.1016/j.cej.2021.131072. URL https://www.sciencedirect.com/science/article/pii/S1385894721026541.

[36] Lianxia Chang, Haibin Yang, Wuyou Fu, Nan Yang, Jiuju Chen, Minghui Li, Guangtian Zou, and Jixue Li. Synthesis and thermal stability of w/ws2 inorganic fullerene-like nanoparticles with core–shell structure. *Materials research bulletin*, 41(7):1242–1248, 2006. ISSN 0025-5408.

[37] Yung-Huang Chang, Wenjing Zhang, Yihan Zhu, Yu Han, Jiang Pu, Jan-Kai Chang, Wei-Ting Hsu, Jing-Kai Huang, Chang-Lung Hsu, Ming-Hui Chiu, Taishi Takenobu, Henan Li, Chih-I. Wu, Wen-Hao Chang, Andrew Thye Shen Wee, and Lain-Jong Li. Monolayer mose2 grown by chemical vapor deposition for fast photodetection. *ACS Nano*, 8(8):8582–8590, 2014. ISSN 1936-0851. doi: 10.1021/nn503287m. URL https://doi.org/10.1021/nn503287m.

[38] Kudakwashe Chayambuka, Grietus Mulder, Dmitri L. Danilov, and Peter H. L. Notten. From li-ion batteries toward na-ion chemistries: Challenges and opportunities. *Advanced Energy Materials*, 10(38):2001310, 2020. ISSN 1614-6832. doi: https://doi.org/10.1002/aenm.202001310. URL https://doi.org/10.1002/aenm.202001310.

[39] Biao Chen, Dongliang Chao, Enzuo Liu, Mietek Jaroniec, Naiqin Zhao, and Shi-Zhang Qiao. Transition metal dichalcogenides for alkali metal ion batteries: engineering strategies at the atomic level. *Energy & Environmental Science*, 13(4):1096–1131, 2020. ISSN 1754-5692. doi: 10.1039/C9EE03549D. URL http://dx.doi.org/10.1039/C9EE03549D.

[40] Ding Chen, Santosh K. Tiwari, Zhiyuan Ma, Jiahao Wen, Song Liu, Jiewei Li, Feng Wei, Kunyapat Thummavichai, Zhuxian Yang, and Yanqiu Zhu. Phase behavior and thermo-mechanical properties of if-ws2 reinforced pp–pet blend-based nanocomposites. *Polymers*, 12(10):2342, 2020. ISSN 2073-4360.

[41] Jun Chen, Nobuhiro Kuriyama, Huatang Yuan, Hiroyuki T. Takeshita, and Tet-

suo Sakai. Electrochemical hydrogen storage in mos2 nanotubes. *Journal of the American Chemical Society*, 123(47):11813–11814, 2001. ISSN 0002-7863. doi: 10.1021/ja017121z. URL https://doi.org/10.1021/ja017121z.

[42] Mengyuan Chen, Xiaotu Ma, Bin Chen, Renata Arsenault, Peter Karlson, Nakia Simon, and Yan Wang. Recycling end-of-life electric vehicle lithium-ion batteries. *Joule*, 3(11):2622–2646, 2019. ISSN 2542-4785.

[43] Renjie Chen, Teng Zhao, Weiping Wu, Feng Wu, Li Li, Ji Qian, Rui Xu, Huiming Wu, Hassan M. Albishri, A. S. Al-Bogami, Deia Abd El-Hady, Jun Lu, and Khalil Amine. Free-standing hierarchically sandwich-type tungsten disulfide nanotubes/graphene anode for lithium-ion batteries. *Nano Letters*, 14(10):5899–5904, 2014. ISSN 1530-6984. doi: 10.1021/nl502848z. URL https://doi.org/10.1021/nl502848z.

[44] Shao-Yu Chen, Changxi Zheng, Michael S. Fuhrer, and Jun Yan. Helicity-resolved raman scattering of mos2, mose2, ws2, and wse2 atomic layers. *Nano Letters*, 15(4): 2526–2532, 2015. ISSN 1530-6984. doi: 10.1021/acs.nanolett.5b00092. URL https://doi.org/10.1021/acs.nanolett.5b00092.

[45] Xiaoxia Chen, Haliya Muheiyati, Xiuping Sun, Pan Zhou, Peican Wang, Xuyang Ding, Yitai Qian, and Liqiang Xu. Rational design of tungsten selenide @ n-doped carbon nanotube for high-stable potassium-ion batteries. *Small*, 18(5):2104363, 2022. ISSN 1613-6810. doi: https://doi.org/10.1002/smll.202104363. URL https://doi.org/10.1002/smll.202104363.

[46] Xinzhi Chen, Wenjun He, Liang-Xin Ding, Suqing Wang, and Haihui Wang. Enhancing interfacial contact in all solid state batteries with a cathode-supported solid electrolyte membrane framework. *Energy & Environmental Science*, 12(3):938–944, 2019.

[47] Yanfeng Chen, Jinyang Xi, Dumitru O. Dumcenco, Zheng Liu, Kazu Suenaga, Dong Wang, Zhigang Shuai, Ying-Sheng Huang, and Liming Xie. Tunable band gap photoluminescence from atomically thin transition-metal dichalcogenide alloys. *ACS*

Nano, 7(5):4610–4616, 2013. ISSN 1936-0851. doi: 10.1021/nn401420h. URL https://doi.org/10.1021/nn401420h.

[48] Yuning Chen, Lidong Li, and Lin Guo. Two-dimensional metal-containing nanomaterials for battery anode applications. *ChemElectroChem*, 7(15):3193–3210, 2020. ISSN 2196-0216. doi: https://doi.org/10.1002/celc.202000440. URL https://doi.org/10.1002/celc.202000440.

[49] Zuxin Chen, Huiqiang Liu, Xuechen Chen, Guang Chu, Sheng Chu, and Hang Zhang. Wafer-size and single-crystal mose2 atomically thin films grown on gan substrate for light emission and harvesting. *ACS Applied Materials & Interfaces*, 8(31):20267–20273, 2016. ISSN 1944-8244. doi: 10.1021/acsami.6b04768. URL https://doi.org/10.1021/acsami.6b04768.

[50] Xin-Bing Cheng and Qiang Zhang. Dendrite-free lithium metal anodes: stable solid electrolyte interphases for high-efficiency batteries. *Journal of Materials Chemistry A*, 3(14):7207–7209, 2015. ISSN 2050-7496.

[51] Manish Chhowalla, Hyeon Suk Shin, Goki Eda, Lain-Jong Li, Kian Ping Loh, and Hua Zhang. The chemistry of two-dimensional layered transition metal dichalcogenide nanosheets. *Nature Chemistry*, 5(4):263–275, 2013. ISSN 1755-4349. doi: 10.1038/nchem.1589. URL https://doi.org/10.1038/nchem.1589.

[52] Pallellappa Chithaiah, Saptarshi Ghosh, Alexander Idelevich, Lev Rovinsky, Tsachi Livneh, and Alla Zak. Solving the "mos2 nanotubes" synthetic enigma and elucidating the route for their catalyst-free and scalable production. *ACS Nano*, 14(3):3004–3016, 2020. ISSN 1936-0851. doi: 10.1021/acsnano.9b07866. URL https://doi.org/10.1021/acsnano.9b07866.

[53] Jung Sang Cho, Seung-Keun Park, Kyung Min Jeon, Yuanzhe Piao, and Yun Chan Kang. Mesoporous reduced graphene oxide/wse2 composite particles for efficient sodium-ion batteries and hydrogen evolution reactions. *Applied Surface*

Science, 459:309–317, 2018. ISSN 0169-4332. doi: https://doi.org/10.1016/j.apsusc.2018.07.200. URL https://www.sciencedirect.com/science/article/pii/S0169433218320956.

[54] Jang Wook Choi and Doron Aurbach. Promise and reality of post-lithium-ion batteries with high energy densities. *Nature Reviews Materials*, 1(4):16013, 2016. ISSN 2058-8437. doi: 10.1038/natrevmats.2016.13. URL https://doi.org/10.1038/natrevmats.2016.13.

[55] Seung Ho Choi and Yun Chan Kang. Sodium ion storage properties of ws2-decorated three-dimensional reduced graphene oxide microspheres. *Nanoscale*, 7(9):3965–3970, 2015. ISSN 2040-3364. doi: 10.1039/C4NR06880G. URL http://dx.doi.org/10.1039/C4NR06880G.

[56] Wonbong Choi, Nitin Choudhary, Gang Hee Han, Juhong Park, Deji Akinwande, and Young Hee Lee. Recent development of two-dimensional transition metal dichalcogenides and their applications. *Materials Today*, 20(3):116–130, 2017. ISSN 1369-7021. doi: https://doi.org/10.1016/j.mattod.2016.10.002. URL https://www.sciencedirect.com/science/article/pii/S1369702116302917.

[57] Jonathan N. Coleman, Mustafa Lotya, Arlene O'Neill, Shane D. Bergin, Paul J. King, Umar Khan, Karen Young, Alexandre Gaucher, Sukanta De, Ronan J. Smith, Igor V. Shvets, Sunil K. Arora, George Stanton, Hye-Young Kim, Kangho Lee, Gyu Tae Kim, Georg S. Duesberg, Toby Hallam, John J. Boland, Jing Jing Wang, John F. Donegan, Jaime C. Grunlan, Gregory Moriarty, Aleksey Shmeliov, Rebecca J. Nicholls, James M. Perkins, Eleanor M. Grieveson, Koenraad Theuwissen, David W. McComb, Peter D. Nellist, and Valeria Nicolosi. Two-dimensional nanosheets produced by liquid exfoliation of layered materials. *Science*, 331(6017):568–571, 2011. doi: 10.1126/science.1194975. URL https://doi.org/10.1126/science.1194975.

[58] Paolo Colombo, Gabriela Mera, Ralf Riedel, and Gian Domenico Sorarù. Polymer-derived ceramics: 40 years of research and innovation in advanced ceramics. *Jour-*

nal of the American Ceramic Society, 93(7):1805–1837, 2010. ISSN 0002-7820. doi: https://doi.org/10.1111/j.1551-2916.2010.03876.x. URL https://doi.org/10.1111/j.1551-2916.2010.03876.x.

[59] John B. Cook, Hyung-Seok Kim, Terri C. Lin, Chun-Han Lai, Bruce Dunn, and Sarah H. Tolbert. Pseudocapacitive charge storage in thick composite mos2 nanocrystal-based electrodes. *Advanced Energy Materials*, 7(2):1601283, 2017. ISSN 1614-6832. doi: https://doi.org/10.1002/aenm.201601283. URL https://doi.org/10.1002/aenm.201601283.

[60] Jiang Cui, Shanshan Yao, and Jang-Kyo Kim. Recent progress in rational design of anode materials for high-performance na-ion batteries. *Energy Storage Materials*, 7: 64–114, 2017. ISSN 2405-8297. doi: https://doi.org/10.1016/j.ensm.2016.12.005. URL https://www.sciencedirect.com/science/article/pii/S2405829716302719.

[61] Yanjie Cui, Ali Abouimrane, Cheng-Jun Sun, Yang Ren, and Khalil Amine. Li–se battery: absence of lithium polyselenides in carbonate based electrolyte. *Chemical Communications*, 50(42):5576–5579, 2014. doi: 10.1039/C4CC00934G. URL http://dx.doi.org/10.1039/C4CC00934G.

[62] Yanjie Cui, Ali Abouimrane, Cheng-Jun Sun, Yang Ren, and Khalil Amine. Li–se battery: absence of lithium polyselenides in carbonate based electrolyte. *Chemical Communications*, 50(42):5576–5579, 2014. ISSN 1359-7345. doi: 10.1039/C4CC00934G. URL http://dx.doi.org/10.1039/C4CC00934G.

[63] Rebecca L. Dahlin, F. Kurtis Kasper, and Antonios G. Mikos. Polymeric nanofibers in tissue engineering. *Tissue Engineering Part B: Reviews*, 17(5):349–364, 2011. ISSN 1937-3368.

[64] P. Dan, E. Mengeritski, Y. Geronov, D. Aurbach, and I. Weisman. Performances and safety behaviour of rechargeable aa-size li/lixmno2 cell. *Journal of Power Sources*, 54(1):143–145, 1995. ISSN 0378-7753. doi: https://doi.org/10.1016/

0378-7753(94)02055-8. URL https://www.sciencedirect.com/science/article/pii/0378775394020558.

[65] L. David, R. Bhandavat, U. Barrera, and G. Singh. Polymer-derived ceramic functionalized mos2 composite paper as a stable lithium-ion battery electrode. *Scientific Reports*, 5(1):9792, 2015. ISSN 2045-2322. doi: 10.1038/srep09792. URL https://doi.org/10.1038/srep09792.

[66] Lamuel David, Romil Bhandavat, and Gurpreet Singh. Mos2/graphene composite paper for sodium-ion battery electrodes. *ACS Nano*, 8(2):1759–1770, 2014. ISSN 1936-0851. doi: 10.1021/nn406156b. URL https://doi.org/10.1021/nn406156b.

[67] Elena del Corro, Humberto Terrones, Ana Elias, Cristiano Fantini, Simin Feng, Minh An Nguyen, Thomas E. Mallouk, Mauricio Terrones, and Marcos A. Pimenta. Excited excitonic states in 1l, 2l, 3l, and bulk wse2 observed by resonant raman spectroscopy. *ACS Nano*, 8(9):9629–9635, 2014. ISSN 1936-0851. doi: 10.1021/nn504088g. URL https://doi.org/10.1021/nn504088g.

[68] Claude Delmas, Jean-Jacques Braconnier, Claude Fouassier, and Paul Hagenmuller. Electrochemical intercalation of sodium in naxcoo2 bronzes. *Solid State Ionics*, 3: 165–169, 1981. ISSN 0167-2738.

[69] Leqing Deng, Yuchuan Zhang, Ruiting Wang, Meiying Feng, Xiaogang Niu, Lulu Tan, and Yujie Zhu. Influence of kpf6 and kfsi on the performance of anode materials for potassium-ion batteries: A case study of mos2. *ACS Applied Materials & Interfaces*, 11 (25):22449–22456, 2019. ISSN 1944-8244. doi: 10.1021/acsami.9b06156. URL https://doi.org/10.1021/acsami.9b06156.

[70] Zongnan Deng, Hao Jiang, and Chunzhong Li. 2d metal chalcogenides incorporated into carbon and their assembly for energy storage applications. *Small*, 14(22):1800148, 2018. ISSN 1613-6810. doi: https://doi.org/10.1002/smll.201800148. URL https://doi.org/10.1002/smll.201800148.

[71] Sonjoy Dey and Gurpreet Singh. Ws2 nanosheet loaded silicon-oxycarbide electrode for sodium and potassium batteries, 2022. URL https://www.mdpi.com/2079-4991/12/23/4185.

[72] Sonjoy Dey and Gurpreet Singh. Sodium and potassium ion storage in cation substituted 2d mowse2: insights into the effects of upper voltage cut-off. *Nanotechnology*, 34(38):385401, 2023. ISSN 0957-4484. doi: 10.1088/1361-6528/acdf66. URL https://dx.doi.org/10.1088/1361-6528/acdf66.

[73] Sonjoy Dey, Shakir Bin Mujib, and Gurpreet Singh. Enhanced li-ion rate capability and stable efficiency enabled by mose2 nanosheets in polymer-derived silicon oxycarbide fiber electrodes, 2022. URL https://www.mdpi.com/2079-4991/12/3/553.

[74] Sonjoy Dey, Shakir Bin Mujib, and Gurpreet Singh. Enhanced li-ion rate capability and stable efficiency enabled by mose2 nanosheets in polymer-derived silicon oxycarbide fiber electrodes, 2022. URL https://www.mdpi.com/2079-4991/12/3/553.

[75] Sonjoy Dey, Krishnappa Manjunath, Alla Zak, and Gurpreet Singh. Ws2 nanotube-embedded sioc fibermat electrodes for sodium-ion batteries. *ACS omega*, 8(11):10126–10138, 2023. ISSN 2470-1343.

[76] Binbin Dong, Yehu Han, Ting Wang, Zhanwu Lei, Yawei Chen, Feihong Wang, Hamidreza Abadikhah, Sayed Ali Khan, Luyuan Hao, Xin Xu, Ruiguo Cao, Liangjun Yin, and Simeon Agathopoulos. Hard sioc microbeads as a high-performance lithium-ion battery anode. *ACS Applied Energy Materials*, 3(10):10183–10191, 2020. doi: 10.1021/acsaem.0c0191010.1021/acsaem.0c01910⟨/p⟩. URL https://doi.org/10.1021/acsaem.0c01910.

[77] Huishuang Dong, Yang Xu, Chenglin Zhang, Yuhan Wu, Min Zhou, Long Liu, Yulian Dong, Qun Fu, Minghong Wu, and Yong Lei. Mos2 nanosheets with expanded interlayer spacing for enhanced sodium storage. *Inorganic Chemistry Frontiers*, 5(12):

3099–3105, 2018. doi: 10.1039/C8QI00969D. URL http://dx.doi.org/10.1039/C8QI00969D.

[78] Litian Dong, Guowen Wang, Xifei Li, Dongbin Xiong, Bo Yan, Baoxian Chen, Dejun Li, and Yanhua Cui. Pvp-derived carbon nanofibers harvesting enhanced anode performance for lithium ion batteries. *RSC Advances*, 6(5):4193–4199, 2016. doi: 10.1039/C5RA23924A. URL http://dx.doi.org/10.1039/C5RA23924A.

[79] Yulian Dong, Yang Xu, Wei Li, Qun Fu, Minghong Wu, Eberhard Manske, Jörg Kröger, and Yong Lei. Insights into the crystallinity of layer-structured transition metal dichalcogenides on potassium ion battery performance: A case study of molybdenum disulfide. *Small*, 15(15):1900497, 2019. ISSN 1613-6810. doi: https://doi.org/10.1002/smll.201900497. URL https://doi.org/10.1002/smll.201900497.

[80] Zak C. Eckel, Chaoyin Zhou, John H. Martin, Alan J. Jacobsen, William B. Carter, and Tobias A. Schaedler. Additive manufacturing of polymer-derived ceramics. *Science*, 351(6268):58–62, 2016. doi: 10.1126/science.aad2688. URL https://doi.org/10.1126/science.aad2688.

[81] Ali Eftekhari. Potassium secondary cell based on prussian blue cathode. *Journal of Power Sources*, 126(1):221–228, 2004. ISSN 0378-7753. doi: https://doi.org/10.1016/j.jpowsour.2003.08.007. URL https://www.sciencedirect.com/science/article/pii/S0378775303008954.

[82] Ali Eftekhari. Molybdenum diselenide (mose2) for energy storage, catalysis, and optoelectronics. *Applied Materials Today*, 8:1–17, 2017. ISSN 2352-9407. doi: https://doi.org/10.1016/j.apmt.2017.01.006. URL https://www.sciencedirect.com/science/article/pii/S2352940716302475.

[83] Fatih Ersan, Gökhan Gökoğlu, and Ethem Aktürk. Adsorption and diffusion of lithium on monolayer transition metal dichalcogenides (mos2(1–x)se2x) alloys. *The Journal of*

Physical Chemistry C, 119(51):28648–28653, 2015. ISSN 1932-7447. doi: 10.1021/acs.jpcc.5b09034. URL https://doi.org/10.1021/acs.jpcc.5b09034.

[84] Robert A. Evarestov, Andrei V. Bandura, Vitaly V. Porsev, and Alexey V. Kovalenko. Phonon spectra, electronic, and thermodynamic properties of ws2 nanotubes. *Journal of Computational Chemistry*, 38(30):2581–2593, 2017. ISSN 0192-8651. doi: https://doi.org/10.1002/jcc.24916. URL https://doi.org/10.1002/jcc.24916.

[85] Ling Fan and Bingan Lu. Reactive oxygen-doped 3d interdigital carbonaceous materials for li and na ion batteries. *Small*, 12(20):2783–2791, 2016. ISSN 1613-6810. doi: https://doi.org/10.1002/smll.201600565. URL https://doi.org/10.1002/smll.201600565.

[86] Xiangpeng Fang, Chunxiu Hua, Xianwei Guo, Yongsheng Hu, Zhaoxiang Wang, Xueping Gao, Feng Wu, Jiazhao Wang, and Liquan Chen. Lithium storage in commercial mos2 in different potential ranges. *Electrochimica Acta*, 81:155–160, 2012. ISSN 0013-4686. doi: https://doi.org/10.1016/j.electacta.2012.07.020. URL https://www.sciencedirect.com/science/article/pii/S001346861201136X.

[87] Chuanqi Feng, Lunfeng Huang, Zaiping Guo, and Huakun Liu. Synthesis of tungsten disulfide (ws2) nanoflakes for lithium ion battery application. *Electrochemistry Communications*, 9(1):119–122, 2007. ISSN 1388-2481. doi: https://doi.org/10.1016/j.elecom.2006.08.048. URL https://www.sciencedirect.com/science/article/pii/S1388248106003821.

[88] Jeffrey W. Fergus. Ceramic and polymeric solid electrolytes for lithium-ion batteries. *Journal of Power Sources*, 195(15):4554–4569, 2010. ISSN 0378-7753.

[89] S. Flandrois and B. Simon. Carbon materials for lithium-ion rechargeable batteries. *Carbon*, 37(2):165–180, 1999. ISSN 0008-6223.

[90] A. Fly and R. Chen. Rate dependency of incremental capacity analysis (dq/dv) as a diagnostic tool for lithium-ion batteries. *Journal of Energy Storage*, 29:101329, 2020.

ISSN 2352-152X. doi: https://doi.org/10.1016/j.est.2020.101329. URL https://www.sciencedirect.com/science/article/pii/S2352152X19308175.

[91] G. L. Frey, R. Tenne, M. J. Matthews, M. S. Dresselhaus, and G. Dresselhaus. Optical properties of ms2 (m = mo, w) inorganic fullerenelike and nanotube material optical absorption and resonance raman measurements. *Journal of Materials Research*, 13 (9):2412–2417, 1998. ISSN 0884-2914. doi: 10.1557/JMR.1998.0335. URL https://doi.org/10.1557/JMR.1998.0335.

[92] Li Fu, Tian Xia, Yuhong Zheng, Jun Yang, Aiwu Wang, and Zhong Wang. Preparation of wo3-reduced graphene oxide nanocomposites with enhanced photocatalytic property. *Ceramics International*, 41(4):5903–5908, 2015. ISSN 0272-8842. doi: https://doi.org/10.1016/j.ceramint.2015.01.022. URL https://www.sciencedirect.com/science/article/pii/S0272884215000619.

[93] Hiroshi Fukui, Hisashi Ohsuka, Takakazu Hino, and Kiyoshi Kanamura. A si-o-c composite anode: High capability and proposed mechanism of lithium storage associated with microstructural characteristics. *ACS Applied Materials & Interfaces*, 2(4):998–1008, 2010. ISSN 1944-8244. doi: 10.1021/am100030f. URL https://doi.org/10.1021/am100030f.

[94] Hiroshi Fukui, Hisashi Ohsuka, Takakazu Hino, and Kiyoshi Kanamura. Polysilane/acenaphthylene blends toward si–o–c composite anodes for rechargeable lithium-ion batteries. *Journal of The Electrochemical Society*, 158(5):A550, 2011. ISSN 1945-7111 0013-4651. doi: 10.1149/1.3567956. URL https://dx.doi.org/10.1149/1.3567956.

[95] Hiroshi Fukui, Katsuya Eguchi, Hisashi Ohsuka, Takakazu Hino, and Kiyoshi Kanamura. Structures and lithium storage performance of si–o–c composite materials depending on pyrolysis temperatures. *Journal of Power Sources*, 243:152–158, 2013. ISSN 0378-7753. doi: https://doi.org/10.1016/j.jpowsour.2013.05.124. URL https://www.sciencedirect.com/science/article/pii/S0378775313009142.

[96] Yang Gao, Kai Liu, Yingjun Wu, Caijuan Li, Qiang Lü, and Guomei Zu. A strategy of combination reaction to improve electrochemical performance in two-dimensional mo1-xwxse2 battery-type electrode materials. *Ceramics International*, 49(5):7196–7207, 2023. ISSN 0272-8842. doi: https://doi.org/10.1016/j.ceramint.2021.12.116. URL https://www.sciencedirect.com/science/article/pii/S0272884221038979.

[97] JunMin Ge, Ling Fan, Jue Wang, Qingfeng Zhang, Zhaomeng Liu, Erjin Zhang, Qian Liu, Xinzhi Yu, and Bingan Lu. Mose2/n-doped carbon as anodes for potassium-ion batteries. *Advanced Energy Materials*, 8(29):1801477, 2018. ISSN 1614-6832. doi: https://doi.org/10.1002/aenm.201801477. URL https://doi.org/10.1002/aenm.201801477.

[98] Peng Ge, Hongshuai Hou, Craig E. Banks, Christopher W. Foster, Sijie Li, Yun Zhang, Jianyong He, Chenyang Zhang, and Xiaobo Ji. Binding mose2 with carbon constrained in carbonous nanosphere towards high-capacity and ultrafast li/na-ion storage. *Energy Storage Materials*, 12:310–323, 2018. ISSN 2405-8297. doi: https://doi.org/10.1016/j.ensm.2018.02.012. URL https://www.sciencedirect.com/science/article/pii/S2405829718300631.

[99] A. K. Geim. Graphene: Status and prospects. *Science*, 324(5934):1530–1534, 2009. doi: 10.1126/science.1158877. URL https://doi.org/10.1126/science.1158877.

[100] Shitao Geng, Tong Zhou, Minyu Jia, Xiangyan Shen, Peibo Gao, Shuang Tian, Pengfei Zhou, Bo Liu, Jin Zhou, Shuping Zhuo, and Feng Li. Carbon-coated ws2 nanosheets supported on carbon nanofibers for high-rate potassium-ion capacitors. *Energy & Environmental Science*, 14(5):3184–3193, 2021. ISSN 1754-5692. doi: 10.1039/D1EE00193K. URL http://dx.doi.org/10.1039/D1EE00193K.

[101] Mahdi Ghorbani-Asl, Nourdine Zibouche, Mohammad Wahiduzzaman, Augusto F. Oliveira, Agnieszka Kuc, and Thomas Heine. Electromechanics in mos2 and ws2: nanotubes vs. monolayers. *Scientific Reports*, 3(1):2961, 2013. ISSN 2045-2322. doi: 10.1038/srep02961. URL https://doi.org/10.1038/srep02961.

[102] S. Ghosh, V. Brüser, I. Kaplan-Ashiri, R. Popovitz-Biro, S. Peglow, J. I. Martínez, J. A. Alonso, and A. Zak. Cathodoluminescence in single and multiwall ws2 nanotubes: Evidence for quantum confinement and strain effect. *Applied Physics Reviews*, 7(4): 041401, 2020. doi: 10.1063/5.0019913. URL https://doi.org/10.1063/5.0019913.

[103] Sourav Ghosh, V. Kiran Kumar, S. Krishna Kumar, Sanjay Biswas, and Surendra K. Martha. An insight of sodium-ion storage, diffusivity into tio2 nanoparticles and practical realization to sodium-ion full cell. *Electrochimica Acta*, 316:69–78, 2019. ISSN 0013-4686. doi: https://doi.org/10.1016/j.electacta.2019.05.109. URL https://www.sciencedirect.com/science/article/pii/S0013468619310424.

[104] Sourav Ghosh, Zhimin Qi, Haiyan Wang, Surendra K. Martha, and Vilas G. Pol. Ws2 anode in na and k-ion battery: Effect of upper cut-off potential on electrochemical performance. *Electrochimica Acta*, 383:138339, 2021. ISSN 0013-4686. doi: https://doi.org/10.1016/j.electacta.2021.138339. URL https://www.sciencedirect.com/science/article/pii/S0013468621006290.

[105] Eider Goikolea, Verónica Palomares, Shijian Wang, Idoia Ruiz de Larramendi, Xin Guo, Guoxiu Wang, and Teofilo Rojo. Na-ion batteries—approaching old and new challenges. *Advanced Energy Materials*, 10(44):2002055, 2020. ISSN 1614-6832. doi: https://doi.org/10.1002/aenm.202002055. URL https://doi.org/10.1002/aenm.202002055.

[106] M. Graczyk-Zajac, L. Toma, C. Fasel, and R. Riedel. Carbon-rich sioc anodes for lithium-ion batteries: Part i. influence of material uv-pre-treatment on high power properties. *Solid State Ionics*, 225:522–526, 2012. ISSN 0167-2738. doi: https://doi.org/10.1016/j.ssi.2011.12.007. URL https://www.sciencedirect.com/science/article/pii/S0167273811005996.

[107] Magdalena Graczyk-Zajac, Lukas Mirko Reinold, Jan Kaspar, Pradeep Vallachira Warriam Sasikumar, Gian-Domenico Soraru, and Ralf Riedel. New insights into under-

standing irreversible and reversible lithium storage within sioc and sicn ceramics, 2015. URL https://www.mdpi.com/2079-4991/5/1/233.

[108] Magdalena Graczyk-Zajac, Dragoljub Vrankovic, Philipp Waleska, Christian Hess, Pradeep Vallachira Sasikumar, Stefan Lauterbach, Hans-Joachim Kleebe, and Gian Domenico Sorarù. The li-storage capacity of sioc glasses with and without mixed silicon oxycarbide bonds. *Journal of Materials Chemistry A*, 6(1):93–103, 2018. ISSN 2050-7488. doi: 10.1039/C7TA09236A. URL http://dx.doi.org/10.1039/C7TA09236A.

[109] Alessandro Grillo, Maurizio Passacantando, Alla Zak, Aniello Pelella, and Antonio Di Bartolomeo. Ws2 nanotubes: Electrical conduction and field emission under electron irradiation and mechanical stress. *Small*, 16(35):2002880, 2020. ISSN 1613-6810. doi: https://doi.org/10.1002/smll.202002880. URL https://doi.org/10.1002/smll.202002880.

[110] Samuel O Grim and Luis J Matienzo. X-ray photoelectron spectroscopy of inorganic and organometallic compounds of molybdenum. *Inorganic chemistry*, 14(5):1014–1018, 1975. ISSN 0020-1669.

[111] Dan Guo, Kaike Yang, Cai-Xin Zhang, Tao Shen, and Hui-Xiong Deng. Electronic structures and band alignment transition in double-wall mos2/ws2 nanotubes for optoelectronic applications. *Journal of Physics D: Applied Physics*, 54(9):095105, 2020.

[112] Carissa Hampton, Dustin Demoin, and Rainer E Glaser. Vibrational spectroscopy tutorial: sulfur and phosphorus. *University of missouri, fall*, 2010.

[113] Meikang Han, Xiaowei Yin, Wenyan Duan, Sa Ren, Litong Zhang, and Laifei Cheng. Hierarchical graphene/sic nanowire networks in polymer-derived ceramics with enhanced electromagnetic wave absorbing capability. *Journal of the European Ceramic Society*, 36(11):2695–2703, 2016. ISSN 0955-2219. doi: https://doi.org/10.

1016/j.jeurceramsoc.2016.04.003. URL https://www.sciencedirect.com/science/article/pii/S0955221916301686.

[114] Oliver Hardick, Bob Stevens, and Daniel G. Bracewell. Nanofibre fabrication in a temperature and humidity controlled environment for improved fibre consistency. *Journal of materials science*, 46:3890–3898, 2011. ISSN 0022-2461.

[115] Saurabh Jyoti Hazarika and Dambarudhar Mohanta. Inorganic fullerene-type ws2 nanoparticles: processing, characterization and its photocatalytic performance on malachite green. *Applied Physics A*, 123(5):381, 2017. ISSN 1432-0630. doi: 10.1007/s00339-017-0965-7. URL https://doi.org/10.1007/s00339-017-0965-7.

[116] Hanna He, Dan Huang, Qingmeng Gan, Junnan Hao, Sailin Liu, Zhibin Wu, Wei Kong Pang, Bernt Johannessen, Yougen Tang, Jing-Li Luo, Haiyan Wang, and Zaiping Guo. Anion vacancies regulating endows mosse with fast and stable potassium ion storage. *ACS Nano*, 13(10):11843–11852, 2019. ISSN 1936-0851. doi: 10.1021/acsnano.9b05865. URL https://doi.org/10.1021/acsnano.9b05865.

[117] Markus Heim, David Keerl, and Thomas Scheibel. Spider silk: From soluble protein to extraordinary fiber. *Angewandte Chemie International Edition*, 48(20):3584–3596, 2009. ISSN 1433-7851. doi: https://doi.org/10.1002/anie.200803341. URL https://doi.org/10.1002/anie.200803341.

[118] Hayley S. Hirsh, Yixuan Li, Darren H. S. Tan, Minghao Zhang, Enyue Zhao, and Y. Shirley Meng. Sodium-ion batteries paving the way for grid energy storage. *Advanced Energy Materials*, 10(32):2001274, 2020. ISSN 1614-6832. doi: https://doi.org/10.1002/aenm.202001274. URL https://doi.org/10.1002/aenm.202001274.

[119] J. Ho, T. R. Jow, and S. Boggs. Historical introduction to capacitor technology. *IEEE Electrical Insulation Magazine*, 26(1):20–25, 2010. ISSN 1558-4402. doi: 10.1109/MEI.2010.5383924.

[120] Young Hoe Seon, Yun Chan Kang, and Jung Sang Cho. One-dimensional porous nanostructure composed of few-layered mose2 nanosheets and highly densified-entangled-n-doped cnts as anodes for na ion batteries. *Chemical Engineering Journal*, 425: 129051, 2021. ISSN 1385-8947. doi: https://doi.org/10.1016/j.cej.2021.129051. URL https://www.sciencedirect.com/science/article/pii/S1385894721006422.

[121] Yuhai Hu and Xueliang Sun. Flexible rechargeable lithium ion batteries: advances and challenges in materials and process technologies. *Journal of Materials Chemistry A*, 2 (28):10712–10738, 2014.

[122] Yuhai Hu, Xifei Li, Andrew Lushington, Mei Cai, Dongsheng Geng, Mohammad Norouzi Banis, Ruying Li, and Xueliang Sun. Fabrication of mos2-graphene nanocomposites by layer-by-layer manipulation for high-performance lithium ion battery anodes. *ECS Journal of Solid State Science and Technology*, 2(10):M3034–M3039, 2013. ISSN 2162-8769 2162-8777. doi: 10.1149/2.007310jss. URL http://dx.doi.org/10.1149/2.007310jss.

[123] Yuhai Hu, Xifei Li, Andrew Lushington, Mei Cai, Dongsheng Geng, Mohammad Norouzi Banis, Ruying Li, and Xueliang Sun. Fabrication of mos2-graphene nanocomposites by layer-by-layer manipulation for high-performance lithium ion battery anodes. *ECS Journal of Solid State Science and Technology*, 2(10):M3034, 2013. doi: 10.1149/2.007310jss. URL https://dx.doi.org/10.1149/2.007310jss.

[124] Feng Huang, JiKang Jian, and Rong Wu. Few-layer thick ws2 nanosheets produced by intercalation/exfoliation route. *Journal of Materials Science*, 51(22):10160–10165, 2016. ISSN 1573-4803. doi: 10.1007/s10853-016-0243-7. URL https://doi.org/10.1007/s10853-016-0243-7.

[125] Kai Huang, Hamada Elsayed, Giorgia Franchin, and Paolo Colombo. Complex sioc ceramics from 2d structures by 3d printing and origami. *Additive Manufacturing*, 33:101144, 2020. ISSN 2214-8604. doi: https://doi.org/10.1016/

j.addma.2020.101144. URL https://www.sciencedirect.com/science/article/pii/S2214860419320998.

[126] Yongxin Huang, Ziheng Wang, Minrong Guan, Feng Wu, and Renjie Chen. Toward rapid-charging sodium-ion batteries using hybrid-phase molybdenum sulfide selenide-based anodes. *Advanced Materials*, 32(40):2003534, 2020. ISSN 0935-9648. doi: https://doi.org/10.1002/adma.202003534. URL https://doi.org/10.1002/adma.202003534.

[127] M. Hughes, N. A. Hampson, and S. A. G. R. Karunathilaka. A review of cells based on lithium negative electrodes (anodes). *Journal of Power Sources*, 12(2):83–144, 1984. ISSN 0378-7753. doi: https://doi.org/10.1016/0378-7753(84)80044-0. URL https://www.sciencedirect.com/science/article/pii/0378775384800440.

[128] Jang-Yeon Hwang, Seung-Taek Myung, and Yang-Kook Sun. Sodium-ion batteries: present and future. *Chemical Society Reviews*, 46(12):3529–3614, 2017. ISSN 0306-0012. doi: 10.1039/C6CS00776G. URL http://dx.doi.org/10.1039/C6CS00776G.

[129] M. Idrees, H. U. Din, R. Ali, G. Rehman, T. Hussain, C. V. Nguyen, Iftikhar Ahmad, and B. Amin. Optoelectronic and solar cell applications of janus monolayers and their van der waals heterostructures. *Physical Chemistry Chemical Physics*, 21(34):18612–18621, 2019. ISSN 1463-9076. doi: 10.1039/C9CP02648G. URL http://dx.doi.org/10.1039/C9CP02648G.

[130] Takafumi Ishii and Jun-ichi Ozaki. Understanding the chemical structure of carbon edge sites by using deuterium-labeled temperature-programmed desorption technique. *Carbon*, 161:343–349, 2020. ISSN 0008-6223.

[131] Ashraf A. Ismail, Frederick R. van de Voort, and Jacqueline Sedman. *Fourier transform infrared spectroscopy: principles and applications*, volume 18, pages 93–139. Elsevier, 1997. ISBN 0167-9244.

[132] W. Jaegermann, F. S. Ohuchi, and B. A. Parkinson. Interaction of cu, ag and au with van der waals faces of ws, and sns2. *Surface Science*, 201(1):211–227, 1988. ISSN 0039-6028. doi: https://doi.org/10.1016/0039-6028(88)90607-3. URL https://www.sciencedirect.com/science/article/pii/0039602888906073.

[133] Rishabh Jain, Aniruddha Singh Lakhnot, Kevin Bhimani, Shyam Sharma, Varad Mahajani, Reena A. Panchal, Mithil Kamble, Fudong Han, Chunsheng Wang, and Nikhil Koratkar. Nanostructuring versus microstructuring in battery electrodes. *Nature Reviews Materials*, 7(9):736–746, 2022. ISSN 2058-8437. doi: 10.1038/s41578-022-00454-9. URL https://doi.org/10.1038/s41578-022-00454-9.

[134] Liwen Ji, Zhan Lin, Andrew J. Medford, and Xiangwu Zhang. Porous carbon nanofibers from electrospun polyacrylonitrile/sio2 composites as an energy storage material. *Carbon*, 47(14):3346–3354, 2009. ISSN 0008-6223. doi: https://doi.org/10.1016/j.carbon.2009.08.002. URL https://www.sciencedirect.com/science/article/pii/S0008622309004965.

[135] Zelang Jian, Wei Luo, and Xiulei Ji. Carbon electrodes for k-ion batteries. *Journal of the American Chemical Society*, 137(36):11566–11569, 2015. ISSN 0002-7863. doi: 10.1021/jacs.5b06809. URL https://doi.org/10.1021/jacs.5b06809.

[136] Zelang Jian, Zhenyu Xing, Clement Bommier, Zhifei Li, and Xiulei Ji. Hard carbon microspheres: Potassium-ion anode versus sodium-ion anode. *Advanced Energy Materials*, 6(3):1501874, 2016. ISSN 1614-6832. doi: https://doi.org/10.1002/aenm.201501874. URL https://doi.org/10.1002/aenm.201501874.

[137] Qingqing Jiang, Yongfeng Lu, Zhengxi Huang, and Juncheng Hu. Facile solvent-thermal synthesis of ultrathin mose2 nanosheets for hydrogen evolution and organic dyes adsorption. *Applied Surface Science*, 402:277–285, 2017. ISSN 0169-4332. doi: https://doi.org/10.1016/j.apsusc.2017.01.049. URL https://www.sciencedirect.com/science/article/pii/S0169433217300491.

[138] Yifeng Jiang, Dawei Fang, Guoqiang Song, Jun Nie, Binling Chen, and Guiping Ma. Fabrication of core–shell nanofibers by single capillary electrospinning combined with vapor induced phase separation. *New Journal of Chemistry*, 37(9):2917–2924, 2013. ISSN 1144-0546. doi: 10.1039/C3NJ00654A. URL http://dx.doi.org/10.1039/C3NJ00654A.

[139] Xiaojuan Jiao, Xiaojie Liu, Beibei Wang, Gang Wang, Xiujuan Wang, and Hui Wang. A controllable strategy for the self-assembly of wm nanocrystals/nitrogen-doped porous carbon superstructures (m = o, c, p, s, and se) for sodium and potassium storage. *Journal of Materials Chemistry A*, 8(4):2047–2065, 2020. ISSN 2050-7488. doi: 10.1039/C9TA11312F. URL http://dx.doi.org/10.1039/C9TA11312F.

[140] Cui Jin, Xiao Tang, Xin Tan, Sean C. Smith, Ying Dai, and Liangzhi Kou. A janus mosse monolayer: a superior and strain-sensitive gas sensing material. *Journal of Materials Chemistry A*, 7(3):1099–1106, 2019. ISSN 2050-7488. doi: 10.1039/C8TA08407F. URL http://dx.doi.org/10.1039/C8TA08407F.

[141] Mingge Jin, Wei Zheng, Ying Ding, Yanming Zhu, Weiliang Wang, and Feng Huang. Raman tensor of van der waals mose2. *The Journal of Physical Chemistry Letters*, 11 (11):4311–4316, 2020. doi: 10.1021/acs.jpclett.0c01183. URL https://doi.org/10.1021/acs.jpclett.0c01183.

[142] L. Joly-Pottuz, J. M. Martin, F. Dassenoy, M. Belin, G. Montagnac, B. Reynard, and N. Fleischer. Pressure-induced exfoliation of inorganic fullerene-like ws2 particles in a hertzian contact. *Journal of Applied Physics*, 99(2), 2006. ISSN 0021-8979. doi: 10.1063/1.2165404. URL https://doi.org/10.1063/1.2165404.

[143] Chulseung Jung, Seung Min Kim, Hyunseong Moon, Gyuchull Han, Junyeon Kwon, Young Ki Hong, Inturu Omkaram, Youngki Yoon, Sunkook Kim, and Jozeph Park. Highly crystalline cvd-grown multilayer mose2 thin film transistor for fast photodetector. *Scientific Reports*, 5(1):15313, 2015. ISSN 2045-2322. doi: 10.1038/srep15313. URL https://doi.org/10.1038/srep15313.

[144] Jan Kaspar, Caglar Terzioglu, Emanuel Ionescu, Magdalena Graczyk-Zajac, Stefania Hapis, Hans-Joachim Kleebe, and Ralf Riedel. Stable sioc/sn nanocomposite anodes for lithium-ion batteries with outstanding cycling stability. *Advanced Functional Materials*, 24(26):4097–4104, 2014. ISSN 1616-301X. doi: https://doi.org/10.1002/adfm.201303828. URL https://doi.org/10.1002/adfm.201303828.

[145] Jan Kaspar, Mathias Storch, Cristina Schitco, Ralf Riedel, and Magdalena Graczyk-Zajac. Sioc(n)/hard carbon composite anodes for na-ion batteries: Influence of morphology on the electrochemical properties. *Journal of The Electrochemical Society*, 163 (2):A156–A162, 2015. ISSN 0013-4651 1945-7111. doi: 10.1149/2.0391602jes. URL http://dx.doi.org/10.1149/2.0391602jes.

[146] Jan Kaspar, Magdalena Graczyk-Zajac, Soumyadip Choudhury, and Ralf Riedel. Impact of the electrical conductivity on the lithium capacity of polymer-derived silicon oxycarbide (sioc) ceramics. *Electrochimica Acta*, 216:196–202, 2016. ISSN 0013-4686. doi: https://doi.org/10.1016/j.electacta.2016.08.121. URL https://www.sciencedirect.com/science/article/pii/S0013468616318576.

[147] Brian Kihun Kim, Serubbable Sy, Aiping Yu, and Jinjun Zhang. *Electrochemical Supercapacitors for Energy Storage and Conversion*, pages 1–25. 2015. ISBN 9781118991978. doi: https://doi.org/10.1002/9781118991978.hces112. URL https://doi.org/10.1002/9781118991978.hces112.

[148] C. Kim, K. S Yang, M. Kojima, K. Yoshida, Y. J Kim, Y. A Kim, and M. Endo. Fabrication of electrospinning-derived carbon nanofiber webs for the anode material of lithium-ion secondary batteries. *Advanced Functional Materials*, 16(18):2393–2397, 2006. ISSN 1616-301X. doi: https://doi.org/10.1002/adfm.200500911. URL https://doi.org/10.1002/adfm.200500911.

[149] Dowon Kim, Hyeongwoo Kim, Hyojun Lim, Ki Jae Kim, Hun-Gi Jung, Dongjin Byun, Changsam Kim, and Wonchang Choi. A facile control in free-carbon domain with divinylbenzene for the high-rate-performing sb/sioc composite anode ma-

terial in sodium-ion batteries. *International Journal of Energy Research*, 44(14): 11473–11486, 2020. ISSN 0363-907X. doi: https://doi.org/10.1002/er.5769. URL https://doi.org/10.1002/er.5769.

[150] Inha Kim, Sung-Woo Park, and Dong-Wan Kim. Onion-like crystalline ws2 nanoparticles anchored on graphene sheets as high-performance anode materials for lithium-ion batteries. *Chemical Engineering Journal*, 375:122033, 2019. ISSN 1385-8947. doi: https://doi.org/10.1016/j.cej.2019.122033. URL https://www.sciencedirect.com/science/article/pii/S1385894719314275.

[151] Jeong F. Kim, Ji Hoon Kim, Young Moo Lee, and Enrico Drioli. Thermally induced phase separation and electrospinning methods for emerging membrane applications: A review. *AIChE Journal*, 62(2):461–490, 2016. ISSN 0001-1541.

[152] Min-Sik Kim, Dhrubajyoti Bhattacharjya, Baizeng Fang, Dae-Soo Yang, Tae-Sung Bae, and Jong-Sung Yu. Morphology-dependent li storage performance of ordered mesoporous carbon as anode material. *Langmuir*, 29(22):6754–6761, 2013. ISSN 0743-7463. doi: 10.1021/la401150t. URL https://doi.org/10.1021/la401150t.

[153] Min-Sik Kim, Dhrubajyoti Bhattacharjya, Baizeng Fang, Dae-Soo Yang, Tae-Sung Bae, and Jong-Sung Yu. Morphology-dependent li storage performance of ordered mesoporous carbon as anode material. *Langmuir*, 29(22):6754–6761, 2013. doi: https://doi.org/10.1021/la401150t. URL https://doi.org/10.1021/la401150t.

[154] Taewhan Kim, Woosung Choi, Heon-Cheol Shin, Jae-Young Choi, Ji Man Kim, Min-Sik Park, and Won-Sub Yoon. Applications of voltammetry in lithium ion battery research. *J. Electrochem. Sci. Technol*, 11(1):14–25, 2020. ISSN 2093-8551. doi: 10.33961/jecst.2019.00619. URL https://doi.org/10.33961/jecst.2019.00619http://www.jecst.org/journal/view.php?number=318.

[155] Yena Kim, Sujung Kim, Misun Hong, and Hye Ryung Byon. Tubular mosse/carbon nanotube electrodes for hybrid-ion capacitors. *Electrochimica Acta*, 374:137971, 2021.

ISSN 0013-4686. doi: https://doi.org/10.1016/j.electacta.2021.137971. URL https://www.sciencedirect.com/science/article/pii/S0013468621002619.

[156] Brij Kishore, Venkatesh G, and N. Munichandraiah. K2ti4o9: A promising anode material for potassium ion batteries. *Journal of The Electrochemical Society*, 163(13): A2551, 2016. ISSN 1945-7111. doi: 10.1149/2.0421613jes. URL https://dx.doi.org/10.1149/2.0421613jes.

[157] Philippe Knauth. Inorganic solid li ion conductors: An overview. *Solid State Ionics*, 180(14):911–916, 2009. ISSN 0167-2738. doi: https://doi.org/10.1016/j.ssi.2009.03.022. URL https://www.sciencedirect.com/science/article/pii/S0167273809001179.

[158] Isao Kojima and Masayasu Kurahashi. Application of asymmetrical gaussian/lorentzian mixed function for x-ray photoelectron curve synthesis. *Journal of Electron Spectroscopy and Related Phenomena*, 42(2):177–181, 1987. ISSN 0368-2048. doi: https://doi.org/10.1016/0368-2048(87)85018-1. URL https://www.sciencedirect.com/science/article/pii/0368204887850181.

[159] F. Kopnov, A. Yoffe, G. Leitus, and R. Tenne. Transport properties of fullerene-like ws2 nanoparticles. *physica status solidi (b)*, 243(6):1229–1240, 2006. ISSN 0370-1972. doi: https://doi.org/10.1002/pssb.200541170. URL https://doi.org/10.1002/pssb.200541170.

[160] Frieda Kopnov, Alexander Yoffe, Gregory Leitus, and Reshef Tenne. Transport properties of fullerene-like ws2 nanoparticles. *physica status solidi (b)*, 243(6):1229–1240, 2006. ISSN 0370-1972.

[161] H. W. Kroto, J. R. Heath, S. C. O'Brien, R. F. Curl, and R. E. Smalley. C60: Buckminsterfullerene. *Nature*, 318(6042):162–163, 1985. ISSN 1476-4687. doi: 10.1038/318162a0. URL https://doi.org/10.1038/318162a0.

[162] Gustavo Larsen, Raffet Velarde-Ortiz, Kevin Minchow, Antonio Barrero, and Ignacio G. Loscertales. A method for making inorganic and hybrid (organic/inorganic) fibers and vesicles with diameters in the submicrometer and micrometer range via sol-gel chemistry and electrically forced liquid jets. *Journal of the American Chemical Society*, 125(5):1154–1155, 2003. ISSN 0002-7863. doi: 10.1021/ja028983i. URL https://doi.org/10.1021/ja028983i.

[163] Dattatray J. Late, Sharmila N. Shirodkar, Umesh V. Waghmare, Vinayak P. Dravid, and C. N. R. Rao. Thermal expansion, anharmonicity and temperature-dependent raman spectra of single- and few-layer mose2 and wse2. *ChemPhysChem*, 15(8):1592–1598, 2014. ISSN 1439-4235. doi: https://doi.org/10.1002/cphc.201400020. URL https://doi.org/10.1002/cphc.201400020.

[164] M. Lazzari and B. Scrosati. A cyclable lithium organic electrolyte cell based on two intercalation electrodes. *Journal of The Electrochemical Society*, 127(3):773, 1980. ISSN 1945-7111.

[165] Byoung-Sun Lee, Seoung-Bum Son, Kyu-Min Park, Geunsung Lee, Kyu Hwan Oh, Se-Hee Lee, and Woong-Ryeol Yu. Effect of pores in hollow carbon nanofibers on their negative electrode properties for a lithium rechargeable battery. *ACS Applied Materials & Interfaces*, 4(12):6702–6710, 2012. ISSN 1944-8244. doi: 10.1021/am301873d. URL https://doi.org/10.1021/am301873d.

[166] Changgu Lee, Qunyang Li, William Kalb, Xin-Zhou Liu, Helmuth Berger, Robert W. Carpick, and James Hone. Frictional characteristics of atomically thin sheets. *Science*, 328(5974):76–80, 2010. doi: 10.1126/science.1184167. URL https://doi.org/10.1126/science.1184167.

[167] Hun Lee, Meltem Yanilmaz, Ozan Toprakci, Kun Fu, and Xiangwu Zhang. A review of recent developments in membrane separators for rechargeable lithium-ion batteries. *Energy & Environmental Science*, 7(12):3857–3886, 2014.

[168] K. T Lee, J. C Lytle, N. S Ergang, S. M Oh, and A. Stein. Synthesis and rate performance of monolithic macroporous carbon electrodes for lithium-ion secondary batteries. *Advanced Functional Materials*, 15(4):547–556, 2005. ISSN 1616-301X. doi: https://doi.org/10.1002/adfm.200400186. URL https://doi.org/10.1002/adfm.200400186.

[169] Kyu T Lee, Justin C Lytle, Nicholas S Ergang, Seung M Oh, and Andreas Stein. Synthesis and rate performance of monolithic macroporous carbon electrodes for lithium-ion secondary batteries. *Advanced Functional Materials*, 15(4):547–556, 2005. doi: https://doi.org/10.1002/adfm.200400186. URL https://onlinelibrary.wiley.com/doi/abs/10.1002/adfm.200400186.

[170] Yongho Lee, Kwan Young Lee, and Wonchang Choi. One-pot synthesis of antimony-embedded silicon oxycarbide materials for high-performance sodium-ion batteries. *Advanced Functional Materials*, 27(43):1702607, 2017. ISSN 1616-301X. doi: https://doi.org/10.1002/adfm.201702607. URL https://doi.org/10.1002/adfm.201702607.

[171] Tianyu Lei, Wei Chen, Jianwen Huang, Chaoyi Yan, Haoxuan Sun, Chao Wang, Wanli Zhang, Yanrong Li, and Jie Xiong. Multi-functional layered ws2 nanosheets for enhancing the performance of lithium–sulfur batteries. *Advanced Energy Materials*, 7(4): 1601843, 2017. ISSN 1614-6832. doi: https://doi.org/10.1002/aenm.201601843. URL https://doi.org/10.1002/aenm.201601843.

[172] Ting Leng, Khaled Parvez, Kewen Pan, Junaid Ali, Daryl McManus, Kostya S. Novoselov, Cinzia Casiraghi, and Zhirun Hu. Printed graphene/ws2 battery-free wireless photosensor on papers. *2D Materials*, 7(2):024004, 2020. ISSN 2053-1583. doi: 10.1088/2053-1583/ab602f. URL https://dx.doi.org/10.1088/2053-1583/ab602f.

[173] Dan Li and Younan Xia. Electrospinning of nanofibers: reinventing the wheel? *Advanced materials*, 16(14):1151–1170, 2004. ISSN 0935-9648.

[174] Dan Li, Yuliang Wang, and Younan Xia. Electrospinning of polymeric and ceramic

nanofibers as uniaxially aligned arrays. *Nano letters*, 3(8):1167–1171, 2003. ISSN 1530-6984.

[175] Hongfei Li, Zijie Tang, Zhuoxin Liu, and Chunyi Zhi. Evaluating flexibility and wearability of flexible energy storage devices. *Joule*, 3(3):613–619, 2019. ISSN 2542-4785.

[176] Peng Li, Xiaobo Zheng, Haoxiang Yu, Guoqiang Zhao, Jie Shu, Xun Xu, Wenping Sun, and Shi Xue Dou. Electrochemical potassium/lithium-ion intercalation into tise2: Kinetics and mechanism. *Energy Storage Materials*, 16:512–518, 2019. ISSN 2405-8297. doi: https://doi.org/10.1016/j.ensm.2018.09.014. URL https://www.sciencedirect.com/science/article/pii/S2405829718309243.

[177] Wangda Li, Bohang Song, and Arumugam Manthiram. High-voltage positive electrode materials for lithium-ion batteries. *Chemical Society Reviews*, 46(10):3006–3059, 2017.

[178] Xiao-Lin Li, Jian-Ping Ge, and Ya-Dong Li. Atmospheric pressure chemical vapor deposition: An alternative route to large-scale mos2 and ws2 inorganic fullerene-like nanostructures and nanoflowers. *Chemistry – A European Journal*, 10(23):6163–6171, 2004. ISSN 0947-6539. doi: https://doi.org/10.1002/chem.200400451. URL https://chemistry-europe.onlinelibrary.wiley.com/doi/abs/10.1002/chem.200400451.

[179] Xin Li, Jinying Zhang, Zechen Liu, Chengcheng Fu, and Chunming Niu. Ws2 nanoflowers on carbon nanotube vines with enhanced electrochemical performances for lithium and sodium-ion batteries. *Journal of Alloys and Compounds*, 766:656–662, 2018. ISSN 0925-8388. doi: https://doi.org/10.1016/j.jallcom.2018.07.008. URL https://www.sciencedirect.com/science/article/pii/S0925838818325088.

[180] Xiu Li, Yonggang Sun, Xun Xu, Yun-Xiao Wang, Shu-Lei Chou, Anmin Cao, Libao Chen, and Shi-Xue Dou. Lotus rhizome-like s/n–c with embedded ws2 for superior sodium storage. *Journal of Materials Chemistry A*, 7(45):25932–25943, 2019.

ISSN 2050-7488. doi: 10.1039/C9TA09373G. URL http://dx.doi.org/10.1039/C9TA09373G.

[181] Yan Li, Renheng Wang, Zhinan Guo, Zhe Xiao, Huide Wang, Xiaoling Luo, and Han Zhang. Emerging two-dimensional noncarbon nanomaterials for flexible lithium-ion batteries: opportunities and challenges. *Journal of Materials Chemistry A*, 7(44): 25227–25246, 2019. ISSN 2050-7488. doi: 10.1039/C9TA09377J. URL http://dx.doi.org/10.1039/C9TA09377J.

[182] Yifei Li, Yanliang Liang, Francisco C. Robles Hernandez, Hyun Deog Yoo, Qinyou An, and Yan Yao. Enhancing sodium-ion battery performance with interlayer-expanded mos2–peo nanocomposites. *Nano Energy*, 15:453–461, 2015. ISSN 2211-2855. doi: https://doi.org/10.1016/j.nanoen.2015.05.012. URL https://www.sciencedirect.com/science/article/pii/S221128551500227X.

[183] Youpeng Li, Chenghao Yang, Fenghua Zheng, Qichang Pan, Yanzhen Liu, Gang Wang, Tiezhong Liu, Junhua Hu, and Meilin Liu. Design of tio2ec hierarchical tubular heterostructures for high performance potassium ion batteries. *Nano Energy*, 59:582–590, 2019. ISSN 2211-2855. doi: https://doi.org/10.1016/j.nanoen.2019.03.002. URL https://www.sciencedirect.com/science/article/pii/S2211285519301909.

[184] Yu Li, Jiawei Zhang, Qingguo Chen, Xinhui Xia, and Minghua Chen. Emerging of heterostructure materials in energy storage: A review. *Advanced Materials*, 33(27): 2100855, 2021. ISSN 0935-9648. doi: https://doi.org/10.1002/adma.202100855. URL https://doi.org/10.1002/adma.202100855.

[185] Yunchao Li, Ryan A. Adams, Anjela Arora, Vilas G. Pol, Alan M. Levine, Richard J. Lee, Kokouvi Akato, Amit K. Naskar, and Mariappan Parans Paranthaman. Sustainable potassium-ion battery anodes derived from waste-tire rubber. *Journal of The Electrochemical Society*, 164(6):A1234, 2017. ISSN 1945-7111. doi: 10.1149/2.1391706jes. URL https://dx.doi.org/10.1149/2.1391706jes.

[186] Zhe Li, Jun Huang, Bor Yann Liaw, Viktor Metzler, and Jianbo Zhang. A review of lithium deposition in lithium-ion and lithium metal secondary batteries. *Journal of power sources*, 254:168–182, 2014. ISSN 0378-7753.

[187] Zheling Li, Libo Deng, Ian A. Kinloch, and Robert J. Young. Raman spectroscopy of carbon materials and their composites: Graphene, nanotubes and fibres. *Progress in Materials Science*, 135:101089, 2023. ISSN 0079-6425. doi: https://doi.org/10.1016/j.pmatsci.2023.101089. URL https://www.sciencedirect.com/science/article/pii/S007964252300021X.

[188] Fang Liang, Hejun Xu, Xing Wu, Chaolun Wang, Chen Luo, and Jian Zhang. Raman spectroscopy characterization of two-dimensional materials*. *Chinese Physics B*, 27 (3):037802, 2018. ISSN 1674-1056. doi: 10.1088/1674-1056/27/3/037802. URL https://dx.doi.org/10.1088/1674-1056/27/3/037802.

[189] Yew Von Lim, Zhi Xiang Huang, Ye Wang, Fei Hu Du, Jun Zhang, Tu Pei Chen, L. K. Ang, and Hui Ying Yang. Ws2–3d graphene nano-architecture networks for high performance anode materials of lithium ion batteries. *RSC Advances*, 6(109): 107768–107775, 2016. doi: 10.1039/C6RA21141K. URL http://dx.doi.org/10.1039/C6RA21141K.

[190] Yew Von Lim, Ye Wang, Dezhi Kong, Lu Guo, Jen It Wong, L. K. Ang, and Hui Ying Yang. Cubic-shaped ws2 nanopetals on a prussian blue derived nitrogen-doped carbon nanoporous framework for high performance sodium-ion batteries. *Journal of Materials Chemistry A*, 5(21):10406–10415, 2017. ISSN 2050-7488. doi: 10.1039/C7TA01821E. URL http://dx.doi.org/10.1039/C7TA01821E.

[191] David Linden. Handbook of batteries. volume 4, page 265. ISBN 0140-6701.

[192] Beibei Liu, Yangjie Liu, Xiang Hu, Guobao Zhong, Junwei Li, Jun Yuan, and Zhenhai Wen. N-doped carbon modifying mosse nanosheets on hollow cubic carbon for high-performance anodes of sodium-based dual-ion batteries. *Advanced Functional*

Materials, 31(31):2101066, 2021. ISSN 1616-301X. doi: https://doi.org/10.1002/adfm.202101066. URL https://doi.org/10.1002/adfm.202101066.

[193] Chen Liu, Xianyu Meng, Xinghong Zhang, Changqing Hong, Jiecai Han, Wenbo Han, Baosheng Xu, Shun Dong, and Shanyi Du. High temperature structure evolution of macroporous sioc ceramics prepared by a sol–gel method. *Ceramics International*, 41(9, Part A):11091–11096, 2015. ISSN 0272-8842. doi: https://doi.org/10.1016/j.ceramint.2015.05.056. URL https://www.sciencedirect.com/science/article/pii/S0272884215009852.

[194] Na Liu, Paul Kim, Ji Heon Kim, Jun Ho Ye, Sunkook Kim, and Cheol Jin Lee. Large-area atomically thin mos2 nanosheets prepared using electrochemical exfoliation. *ACS Nano*, 8(7):6902–6910, 2014. ISSN 1936-0851. doi: 10.1021/nn5016242. URL https://doi.org/10.1021/nn5016242.

[195] Tingting Liu, Xikun Zhang, Maoting Xia, Haoxiang Yu, Na Peng, Cheng Jiang, Miao Shui, Ying Xie, Ting-Feng Yi, and Jie Shu. Functional cation defects engineering in tis2 for high-stability anode. *Nano Energy*, 67:104295, 2020. ISSN 2211-2855. doi: https://doi.org/10.1016/j.nanoen.2019.104295. URL https://www.sciencedirect.com/science/article/pii/S221128551931002X.

[196] Yongchang Liu, Ning Zhang, Hongyan Kang, Minghui Shang, Lifang Jiao, and Jun Chen. Ws2 nanowires as a high-performance anode for sodium-ion batteries. *Chemistry – A European Journal*, 21(33):11878–11884, 2015. ISSN 0947-6539. doi: https://doi.org/10.1002/chem.201501759. URL https://doi.org/10.1002/chem.201501759.

[197] Yuping Liu, Xiaoyun He, Damien Hanlon, Andrew Harvey, Umar Khan, Yanguang Li, and Jonathan N. Coleman. Electrical, mechanical, and capacity percolation leads to high-performance mos2/nanotube composite lithium ion battery electrodes. *ACS Nano*, 10(6):5980–5990, 2016. ISSN 1936-0851. doi: 10.1021/acsnano.6b01505. URL https://doi.org/10.1021/acsnano.6b01505.

[198] Y. Lu, Y. Y. Lu, Z. Q. Niu, and J. Chen. Graphene-based nanomaterials for sodium-ion batteries. *ADVANCED ENERGY MATERIALS*, 8(17), 2018. ISSN 1614-6832 1614-6840. doi: 10.1002/aenm.201702469.

[199] Maria R. Lukatskaya, Bruce Dunn, and Yury Gogotsi. Multidimensional materials and device architectures for future hybrid energy storage. *Nature communications*, 7(1): 12647, 2016. ISSN 2041-1723.

[200] Wei Luo, Jiayu Wan, Burak Ozdemir, Wenzhong Bao, Yanan Chen, Jiaqi Dai, Hao Lin, Yue Xu, Feng Gu, Veronica Barone, and Liangbing Hu. Potassium ion batteries with graphitic materials. *Nano Letters*, 15(11):7671–7677, 2015. ISSN 1530-6984. doi: 10.1021/acs.nanolett.5b03667. URL https://doi.org/10.1021/acs.nanolett.5b03667.

[201] Xiaomin Luo, Jianfeng Huang, Yixuan Huang, Liyun Cao, Jiayin Li, Yuhang Wang, Zhanwei Xu, Shiying Wei, and Koji Kajiyoshi. Self-templated induced carbon-supported hollow ws2 composite structure for high-performance sodium storage. *Journal of Materials Chemistry A*, 9(37):21366–21378, 2021. ISSN 2050-7488. doi: 10.1039/D1TA04858A. URL http://dx.doi.org/10.1039/D1TA04858A.

[202] Xin Luo, Yanyuan Zhao, Jun Zhang, Minglin Toh, Christian Kloc, Qihua Xiong, and Su Ying Quek. Effects of lower symmetry and dimensionality on raman spectra in two-dimensional wse_2. *Physical Review B*, 88(19):195313, 2013. doi: 10.1103/PhysRevB.88.195313. URL https://link.aps.org/doi/10.1103/PhysRevB.88.195313.

[203] Lu Ma, Zan Liu, and Zhi-Lin Cheng. Scalable exfoliation and friction performance of few-layered ws2 nanosheets by microwave-assisted liquid-phase sonication. *Ceramics International*, 46(3):3786–3792, 2020. ISSN 0272-8842. doi: https://doi.org/10.1016/j.ceramint.2019.10.101. URL https://www.sciencedirect.com/science/article/pii/S0272884219329645.

[204] Xiangchao Ma, Xin Wu, Haoda Wang, and Yucheng Wang. A janus mosse monolayer: a

potential wide solar-spectrum water-splitting photocatalyst with a low carrier recombination rate. *Journal of Materials Chemistry A*, 6(5):2295–2301, 2018. ISSN 2050-7488. doi: 10.1039/C7TA10015A. URL http://dx.doi.org/10.1039/C7TA10015A.

[205] Gábor Zsolt Magda, János Pető, Gergely Dobrik, Chanyong Hwang, László P. Biró, and Levente Tapasztó. Exfoliation of large-area transition metal chalcogenide single layers. *Scientific Reports*, 5(1):14714, 2015. ISSN 2045-2322. doi: 10.1038/srep14714. URL https://doi.org/10.1038/srep14714.

[206] Eimear Magee, Fengzai Tang, Esra Ozdemir, Marc Walker, Tiziana Di Luccio, Julia A. Kornfield, Alla Zak, Reshef Tenne, and Tony McNally. Ws2 nanotubes as a 1d functional filler for melt mixing with poly(lactic acid):implications for composites manufacture. *ACS Applied Nano Materials*, 5(5):6385–6397, 2022. doi: 10.1021/acsanm.2c00489. URL https://doi.org/10.1021/acsanm.2c00489.

[207] Kin Fai Mak, Changgu Lee, James Hone, Jie Shan, and Tony F. Heinz. Atomically thin mos_2: A new direct-gap semiconductor. *Physical Review Letters*, 105(13):136805, 2010. doi: 10.1103/PhysRevLett.105.136805. URL https://link.aps.org/doi/10.1103/PhysRevLett.105.136805.

[208] John Mann, Quan Ma, Patrick M. Odenthal, Miguel Isarraraz, Duy Le, Edwin Preciado, David Barroso, Koichi Yamaguchi, Gretel von Son Palacio, Andrew Nguyen, Tai Tran, Michelle Wurch, Ariana Nguyen, Velveth Klee, Sarah Bobek, Dezheng Sun, Tony F. Heinz, Talat S. Rahman, Roland Kawakami, and Ludwig Bartels. 2-dimensional transition metal dichalcogenides with tunable direct band gaps: Mos2(1–x)se2x monolayers. *Advanced Materials*, 26(9):1399–1404, 2014. ISSN 0935-9648. doi: https://doi.org/10.1002/adma.201304389. URL https://doi.org/10.1002/adma.201304389.

[209] GE McGuire, G Kk Schweitzer, and Thomas A Carlson. Core electron binding energies in some group iiia, vb, and vib compounds. *Inorganic Chemistry*, 12(10):2450–2453, 1973. ISSN 0020-1669.

[210] Beatriz Mendoza-Sánchez, João Coelho, Anuj Pokle, and Valeria Nicolosi. A study of the charge storage properties of a mose2 nanoplatelets/swcnts electrode in a li-ion based electrolyte. *Electrochimica Acta*, 192:1–7, 2016. ISSN 0013-4686. doi: https://doi.org/10.1016/j.electacta.2016.01.114. URL https://www.sciencedirect.com/science/article/pii/S0013468616301153.

[211] E. Mengeritsky, P. Dan, I. Weissman, A. Zaban, and D. Aurbach. Safety and performance of tadiran tlr-7103 rechargeable batteries. *Journal of the Electrochemical Society*, 143(7):2110, 1996. ISSN 1945-7111.

[212] Gabriela Mera, Alexandra Navrotsky, Sabyasachi Sen, Hans-Joachim Kleebe, and Ralf Riedel. Polymer-derived sicn and sioc ceramics – structure and energetics at the nanoscale. *Journal of Materials Chemistry A*, 1(12):3826–3836, 2013. ISSN 2050-7488. doi: 10.1039/C2TA00727D. URL http://dx.doi.org/10.1039/C2TA00727D.

[213] E. Minni and F. Werfel. Oxygen interaction with mo(100) studied by xps, aes and eels. *Surface and Interface Analysis*, 12(7):385–390, 1988. ISSN 0142-2421. doi: https://doi.org/10.1002/sia.740120704. URL https://doi.org/10.1002/sia.740120704.

[214] Shakir Bin Mujib, Riccardo Cuccato, Santanu Mukherjee, Giorgia Franchin, Paolo Colombo, and Gurpreet Singh. Electrospun sioc ceramic fiber mats as freestanding electrodes for electrochemical energy storage applications. *Ceramics International*, 46(3):3565–3573, 2020. ISSN 0272-8842. doi: https://doi.org/10.1016/j.ceramint.2019.10.074. URL https://www.sciencedirect.com/science/article/pii/S0272884219329207.

[215] Shakir Bin Mujib, François Ribot, Christel Gervais, and Gurpreet Singh. Self-supporting carbon-rich sioc ceramic electrodes for lithium-ion batteries and aqueous supercapacitors. *RSC Advances*, 11(56):35440–35454, 2021. doi: 10.1039/D1RA05968H. URL http://dx.doi.org/10.1039/D1RA05968H.

[216] Santanu Mukherjee, Zhongkan Ren, and Gurpreet Singh. Molecular polymer-derived

ceramics for applications in electrochemical energy storage devices. *Journal of Physics D: Applied Physics*, 51(46):463001, 2018. ISSN 0022-3727 1361-6463. doi: 10.1088/1361-6463/aadb18. URL http://dx.doi.org/10.1088/1361-6463/aadb18.

[217] Santanu Mukherjee, Jonathan Turnley, Elisabeth Mansfield, Jason Holm, Davi Soares, Lamuel David, and Gurpreet Singh. Exfoliated transition metal dichalcogenide nanosheets for supercapacitor and sodium ion battery applications. *Royal Society Open Science*, 6(8):190437, 2019. doi: doi:10.1098/rsos.190437. URL https://royalsocietypublishing.org/doi/abs/10.1098/rsos.190437.

[218] D. R. Mullins and P. F. Lyman. Sulfur-induced changes in the w(001) surface core level shift. *Surface Science Letters*, 285(1):L473–L478, 1993. ISSN 0167-2584. doi: https://doi.org/10.1016/0167-2584(93)90336-H. URL https://www.sciencedirect.com/science/article/pii/016725849390336H.

[219] Lucia Muscuso, Sara Cravanzola, Federico Cesano, Domenica Scarano, and Adriano Zecchina. Optical, vibrational, and structural properties of mos2 nanoparticles obtained by exfoliation and fragmentation via ultrasound cavitation in isopropyl alcohol. *The Journal of Physical Chemistry C*, 119(7):3791–3801, 2015. ISSN 1932-7447. doi: 10.1021/jp511973k. URL https://doi.org/10.1021/jp511973k.

[220] Leyla Najafi, Sebastiano Bellani, Reinier Oropesa-Nuñez, Alberto Ansaldo, Mirko Prato, Antonio Esau Del Rio Castillo, and Francesco Bonaccorso. Engineered mose2-based heterostructures for efficient electrochemical hydrogen evolution reaction. *Advanced Energy Materials*, 8(16):1703212, 2018. ISSN 1614-6832. doi: https://doi.org/10.1002/aenm.201703212. URL https://doi.org/10.1002/aenm.201703212.

[221] Dahyun Nam, Jae-Ung Lee, and Hyeonsik Cheong. Excitation energy dependent raman spectrum of mose2. *Scientific Reports*, 5(1):17113, 2015. ISSN 2045-2322. doi: 10.1038/srep17113. URL https://doi.org/10.1038/srep17113.

[222] C. Nethravathi, A. Anto Jeffery, Michael Rajamathi, Naoyuki Kawamoto, Reshef

Tenne, Dmitri Golberg, and Yoshio Bando. Chemical unzipping of ws2 nanotubes. *ACS Nano*, 7(8):7311–7317, 2013. ISSN 1936-0851. doi: 10.1021/nn4029635. URL https://doi.org/10.1021/nn4029635.

[223] Toni E. Newsome and Susan V. Olesik. Electrospinning silica/polyvinylpyrrolidone composite nanofibers. *Journal of Applied Polymer Science*, 131(21), 2014. ISSN 0021-8995.

[224] Yoshio Nishi. The development of lithium ion secondary batteries. *The Chemical Record*, 1(5):406–413, 2001. ISSN 1527-8999.

[225] Feier Niu, Jing Yang, Nana Wang, Dapeng Zhang, Weiliu Fan, Jian Yang, and Yitai Qian. Mose2-covered n,p-doped carbon nanosheets as a long-life and high-rate anode material for sodium-ion batteries. *Advanced Functional Materials*, 27(23):1700522, 2017. ISSN 1616-301X. doi: https://doi.org/10.1002/adfm.201700522. URL https://doi.org/10.1002/adfm.201700522.

[226] Abolhassan Noori, Maher F. El-Kady, Mohammad S. Rahmanifar, Richard B. Kaner, and Mir F. Mousavi. Towards establishing standard performance metrics for batteries, supercapacitors and beyond. *Chemical Society Reviews*, 48(5):1272–1341, 2019. ISSN 0306-0012. doi: 10.1039/C8CS00581H. URL http://dx.doi.org/10.1039/C8CS00581H.

[227] Vaclav Novotny, Vit Basta, Petr Smola, and Jan Spale. Review of carnot battery technology commercial development, 2022.

[228] Joyce A. Ober. Mineral commodity summaries 2018. Report, US Geological Survey, 2018.

[229] Maria O'Brien, Niall McEvoy, Damien Hanlon, Kangho Lee, Riley Gatensby, Jonathan N. Coleman, and Georg S. Duesberg. Low wavenumber raman spectroscopy of highly crystalline mose2 grown by chemical vapor deposition. *physica status solidi*

(b), 252(11):2385–2389, 2015. ISSN 0370-1972. doi: https://doi.org/10.1002/pssb.201552225. URL https://doi.org/10.1002/pssb.201552225.

[230] Hong Geun Oh and Seung-Keun Park. Co-mof derived mose2@cose2/n-doped carbon nanorods as high-performance anode materials for potassium ion batteries. *International Journal of Energy Research*, 46(8):10677–10688, 2022. ISSN 0363-907X. doi: https://doi.org/10.1002/er.7866. URL https://doi.org/10.1002/er.7866.

[231] T. Oshima, M. Kajita, and A. Okuno. Development of sodium-sulfur batteries. *INTERNATIONAL JOURNAL OF APPLIED CERAMIC TECHNOLOGY*, 1(3):269–276, 2004. ISSN 1546-542X.

[232] Kazunori Ozawa. Lithium-ion rechargeable batteries with licoo2 and carbon electrodes: the licoo2/c system. *Solid State Ionics*, 69(3-4):212–221, 1994. ISSN 0167-2738.

[233] Bhavya Padha, Sonali Verma, Prerna Mahajan, Vinay Gupta, Ajit Khosla, and Sandeep Arya. Role of electrochemical techniques for photovoltaic and supercapacitor applications. *Critical Reviews in Analytical Chemistry*, pages 1–35, 2022. ISSN 1040-8347. doi: 10.1080/10408347.2022.2096401. URL https://doi.org/10.1080/10408347.2022.2096401.

[234] Han Pan, Hongwei Chu, Ying Li, Shengzhi Zhao, and Dechun Li. Comprehensive study on the nonlinear optical properties of few-layered mose2 nanosheets at 1 microm. *Journal of Alloys and Compounds*, 806:52–57, 2019. ISSN 0925-8388. doi: https://doi.org/10.1016/j.jallcom.2019.07.268. URL https://www.sciencedirect.com/science/article/pii/S0925838819327835.

[235] Huilin Pan, Xia Lu, Xiqian Yu, Yong-Sheng Hu, Hong Li, Xiao-Qing Yang, and Liquan Chen. Sodium storage and transport properties in layered na2ti3o7 for room-temperature sodium-ion batteries. *Advanced Energy Materials*, 3(9):1186–1194, 2013. ISSN 1614-6832. doi: https://doi.org/10.1002/aenm.201300139. URL https://doi.org/10.1002/aenm.201300139.

[236] Jeongeun Park, Minjun Kim, Minsu Choi, Minkyeong Ku, Dayoung Kam, Sang-Ok Kim, and Wonchang Choi. Sb/c composite embedded in sioc buffer matrix via dispersion property control for novel anode material in sodium-ion batteries. *Journal of Power Sources*, 568:232908, 2023. ISSN 0378-7753. doi: https://doi.org/10.1016/j.jpowsour.2023.232908. URL https://www.sciencedirect.com/science/article/pii/S0378775323002835.

[237] Alkesh B. Patel, Hiren K. Machhi, Payal Chauhan, Som Narayan, Vijay Dixit, Saurabh S. Soni, Prafulla K. Jha, Gunvant K. Solanki, Kireetkumar D. Patel, and Vivek M. Pathak. Electrophoretically deposited mose2/wse2 heterojunction from ultrasonically exfoliated nanocrystals for enhanced electrochemical photoresponse. *ACS Applied Materials & Interfaces*, 11(4):4093–4102, 2019. ISSN 1944-8244. doi: 10.1021/acsami.8b18177. URL https://doi.org/10.1021/acsami.8b18177.

[238] Nathalie Pereira, Glenn G. Amatucci, M. Stanley Whittingham, and Robert Hamlen. Lithium–titanium disulfide rechargeable cell performance after 35 years of storage. *Journal of power sources*, 280:18–22, 2015. ISSN 0378-7753.

[239] Renate Petry, Michael Schmitt, and Jürgen Popp. Raman spectroscopy—a prospective tool in the life sciences. *chemphyschem*, 4(1):14–30, 2003. ISSN 1439-4235.

[240] Raquel Peña-Alonso, Gino Mariotto, Christel Gervais, Florence Babonneau, and Gian Domenico Soraru. New insights on the high-temperature nanostructure evolution of sioc and b-doped siboc polymer-derived glasses. *Chemistry of Materials*, 19(23):5694–5702, 2007. ISSN 0897-4756. doi: 10.1021/cm071203q. URL https://doi.org/10.1021/cm071203q.

[241] Sergei Piskunov, Oleg Lisovski, Yuri F. Zhukovskii, Pavel N. D'yachkov, Robert A. Evarestov, Stephane Kenmoe, and Eckhard Spohr. First-principles evaluation of the morphology of ws2 nanotubes for application as visible-light-driven water-splitting photocatalysts. *ACS Omega*, 4(1):1434–1442, 2019. doi: 10.1021/acsomega.8b03121. URL https://doi.org/10.1021/acsomega.8b03121.

[242] V. S. Pradeep, D. G. Ayana, M. Graczyk-Zajac, G. D. Soraru, and R. Riedel. High rate capability of sioc ceramic aerogels with tailored porosity as anode materials for li-ion batteries. *Electrochimica Acta*, 157:41–45, 2015. ISSN 0013-4686. doi: https://doi.org/10.1016/j.electacta.2015.01.088. URL https://www.sciencedirect.com/science/article/pii/S0013468615001085.

[243] M. A. Py and R. R. Haering. Structural destabilization induced by lithium intercalation in mos2 and related compounds. *Canadian Journal of Physics*, 61(1):76–84, 1983. ISSN 0008-4204. doi: 10.1139/p83-013. URL https://doi.org/10.1139/p83-013.

[244] MA Py and RR Haering. Structural destabilization induced by lithium intercalation in mos2 and related compounds. *Canadian Journal of Physics*, 61(1):76–84, 1983. doi: 10.1139/p83-013. URL https://doi.org/10.1139/p83-013.

[245] F. Qin, W. Shi, T. Ideue, M. Yoshida, A. Zak, R. Tenne, T. Kikitsu, D. Inoue, D. Hashizume, and Y. Iwasa. Superconductivity in a chiral nanotube. *Nature Communications*, 8(1):14465, 2017. ISSN 2041-1723. doi: 10.1038/ncomms14465. URL https://doi.org/10.1038/ncomms14465.

[246] Furong Qin, Hongxing Hu, Yongjia Jiang, Kai Zhang, Zhao Fang, Yanqing Lai, and Jie Li. Mesoporous mose2/c composite as anode material for sodium/lithium ion batteries. *Journal of Electroanalytical Chemistry*, 823:67–72, 2018. ISSN 1572-6657. doi: https://doi.org/10.1016/j.jelechem.2018.05.023. URL https://www.sciencedirect.com/science/article/pii/S1572665718303692.

[247] Eliana Quartarone and Piercarlo Mustarelli. Electrolytes for solid-state lithium rechargeable batteries: recent advances and perspectives. *Chemical Society Reviews*, 40(5):2525–2540, 2011.

[248] Ranjusha Rajagopalan, Yougen Tang, Xiaobo Ji, Chuankun Jia, and Haiyan Wang. Advancements and challenges in potassium ion batteries: A comprehensive review.

Advanced Functional Materials, 30(12):1909486, 2020. ISSN 1616-301X. doi: https://doi.org/10.1002/adfm.201909486. URL https://doi.org/10.1002/adfm.201909486.

[249] Yu Rao, Jing Wang, Penghua Liang, Hongjuan Zheng, Meng Wu, Jiatao Chen, Feng Shi, Kang Yan, Jinsong Liu, Kan Bian, Chuanxiang Zhang, and Kongjun Zhu. Heterostructured ws2/mos2@carbon hollow microspheres anchored on graphene for high-performance li/na storage. *Chemical Engineering Journal*, 443:136080, 2022. ISSN 1385-8947. doi: https://doi.org/10.1016/j.cej.2022.136080. URL https://www.sciencedirect.com/science/article/pii/S1385894722015789.

[250] L. Rapoport, V. Leshchinsky, M. Lvovsky, O. Nepomnyashchy, Yu Volovik, and Reshef Tenne. Friction and wear of powdered composites impregnated with ws2 inorganic fullerene-like nanoparticles. *Wear*, 252(5-6):518–527, 2002. ISSN 0043-1648.

[251] Omid Razbani and Mohsen Assadi. Artificial neural network model of a short stack solid oxide fuel cell based on experimental data. *Journal of Power Sources*, 246:581–586, 2014. ISSN 0378-7753. doi: https://doi.org/10.1016/j.jpowsour.2013.08.018. URL https://www.sciencedirect.com/science/article/pii/S0378775313013578.

[252] Michelle D. Regulacio, Dan-Thien Nguyen, Raymond Horia, and Zhi Wei Seh. Designing nanostructured metal chalcogenides as cathode materials for rechargeable magnesium batteries. *Small*, 17(25):2007683, 2021. ISSN 1613-6810. doi: https://doi.org/10.1002/smll.202007683. URL https://doi.org/10.1002/smll.202007683.

[253] Maja Remskar, Ales Mrzel, Marko Virsek, Matjaz Godec, Matthias Krause, Andreas Kolitsch, Amol Singh, and Alan Seabaugh. The mos2 nanotubes with defect-controlled electric properties. *Nanoscale Res Lett*, 6(1):26, 2010. ISSN 1556-276X. doi: 10.1007/s11671-010-9765-0. URL https://doi.org/10.1007/s11671-010-9765-0.

[254] Xiaodi Ren, Qiang Zhao, William D. McCulloch, and Yiying Wu. Mos2 as a long-life host material for potassium ion intercalation. *Nano Research*, 10(4):1313–1321, 2017.

ISSN 1998-0000. doi: 10.1007/s12274-016-1419-9. URL https://doi.org/10.1007/s12274-016-1419-9.

[255] Zhongkan Ren, Christel Gervais, and Gurpreet Singh. Fabrication and characterization of silicon oxycarbide fibre-mats via electrospinning for high temperature applications. *RSC Advances*, 10(63):38446–38455, 2020. doi: 10.1039/D0RA04060F. URL http://dx.doi.org/10.1039/D0RA04060F.

[256] Ralf Riedel, Gabriela Mera, Ralf Hauser, and Alexander Klonczynski. Silicon-based polymer-derived ceramics: synthesis properties and applications-a review dedicated to prof. dr. fritz aldinger on the occasion of his 65th birthday. *Journal of the Ceramic Society of Japan*, 114(1330):425–444, 2006.

[257] J. Riga, Ph Snauwaert, A. De Pryck, R. Lazzaroni, J. P. Boutique, J. J. Verbist, J. L. Brédas, J. M. André, and C. Taliani. Electronic structure of sulphur-containing conducting polymers. *Synthetic Metals*, 21(1):223–228, 1987. ISSN 0379-6779. doi: https://doi.org/10.1016/0379-6779(87)90090-7. URL https://www.sciencedirect.com/science/article/pii/0379677987900907.

[258] Chantal Robillard. Lithium-metal-polymer batteries. pages 1223–1227. IEEE. ISBN 0780391578.

[259] Felix Rosenburg, Emanuel Ionescu, Norbert Nicoloso, and Ralf Riedel. High-temperature raman spectroscopy of nano-crystalline carbon in silicon oxycarbide. *Materials*, 11(1), 2018. ISSN 1996-1944. doi: 10.3390/ma11010093.

[260] A. Rothschild, R. Popovitz-Biro, O. Lourie, and R. Tenne. Morphology of multiwall ws2 nanotubes. *The Journal of Physical Chemistry B*, 104(38):8976–8981, 2000. ISSN 1520-6106. doi: 10.1021/jp001783d. URL https://doi.org/10.1021/jp001783d.

[261] Atanu Saha, Rishi Raj, and Don L. Williamson. A model for the nanodomains in polymer-derived sico. *Journal of the American Ceramic Society*, 89(7):2188–2195,

2006. ISSN 0002-7820. doi: https://doi.org/10.1111/j.1551-2916.2006.00920.x. URL https://doi.org/10.1111/j.1551-2916.2006.00920.x.

[262] H. Sahin, S. Tongay, S. Horzum, W. Fan, J. Zhou, J. Li, J. Wu, and F. M. Peeters. Anomalous raman spectra and thickness-dependent electronic properties of wse_2. *Physical Review B*, 87(16):165409, 2013. doi: 10.1103/PhysRevB.87.165409. URL https://link.aps.org/doi/10.1103/PhysRevB.87.165409.

[263] Ramkrishna Sahoo, Monika Singh, and Tata Narasinga Rao. A review on the current progress and challenges of 2d layered transition metal dichalcogenides as li/na-ion battery anodes. *ChemElectroChem*, 8(13):2358–2396, 2021. ISSN 2196-0216. doi: https://doi.org/10.1002/celc.202100197. URL https://doi.org/10.1002/celc.202100197.

[264] G. Salitra, G. Hodes, E. Klein, and R. Tenne. Highly oriented wse2 thin films prepared by selenization of evaporated wo3. *Thin Solid Films*, 245(1):180–185, 1994. ISSN 0040-6090. doi: https://doi.org/10.1016/0040-6090(94)90896-6. URL https://www.sciencedirect.com/science/article/pii/0040609094908966.

[265] Pedro E. Sanchez-Jimenez and Rishi Raj. Lithium insertion in polymer-derived silicon oxycarbide ceramics. *Journal of the American Ceramic Society*, 93(4):1127–1135, 2010. ISSN 0002-7820. doi: https://doi.org/10.1111/j.1551-2916.2009.03539.x. URL https://doi.org/10.1111/j.1551-2916.2009.03539.x.

[266] Zhiyuan Sang, Dong Su, Jinsong Wang, Yue Liu, and Huiming Ji. Bi-continuous nanoporous carbon sphere derived from sioc as high-performance anodes for pibs. *Chemical Engineering Journal*, 381:122677, 2020. ISSN 1385-8947. doi: https://doi.org/10.1016/j.cej.2019.122677. URL https://www.sciencedirect.com/science/article/pii/S1385894719320807.

[267] Clara Santato, Marek Odziemkowski, Martine Ulmann, and Jan Augustynski. Crystallographically oriented mesoporous wo3 films: synthesis, characterization, and appli-

cations. *Journal of the American Chemical Society*, 123(43):10639–10649, 2001. ISSN 0002-7863. doi: 10.1021/ja011315x. URL https://doi.org/10.1021/ja011315x.

[268] A. L. Saroj, R. K. Singh, and S. Chandra. Studies on polymer electrolyte poly(vinyl) pyrrolidone (pvp) complexed with ionic liquid: Effect of complexation on thermal stability, conductivity and relaxation behaviour. *Materials Science and Engineering: B*, 178(4):231–238, 2013. ISSN 0921-5107. doi: https://doi.org/10.1016/j.mseb.2012.11.007. URL https://www.sciencedirect.com/science/article/pii/S0921510712005648.

[269] Riccardo Scarfiello, Elisabetta Mazzotta, Davide Altamura, Concetta Nobile, Rosanna Mastria, Simona Rella, Cinzia Giannini, Pantaleo Davide Cozzoli, Aurora Rizzo, and Cosimino Malitesta. An insight into chemistry and structure of colloidal 2d-ws2 nanoflakes: combined xps and xrd study, 2021. URL https://www.mdpi.com/2079-4991/11/8/1969.

[270] Anastasiya Sedova, Bojana Višić, Victor Vega-Mayoral, Daniele Vella, Christoph Gadermaier, Hanna Dodiuk, Samuel Kenig, Reshef Tenne, Raz Gvishi, and Galit Bar. Silica aerogels as hosting matrices for ws2 nanotubes and their optical characterization. *Journal of Materials Science*, 55(18):7612–7623, 2020. ISSN 1573-4803. doi: 10.1007/s10853-020-04562-1. URL https://doi.org/10.1007/s10853-020-04562-1.

[271] G. Seifert, J. Finster, and H. Müller. Sw xα calculations and x-ray photoelectron spectra of molybdenum(ii) chloride cluster compounds. *Chemical Physics Letters*, 75(2):373–377, 1980. ISSN 0009-2614. doi: https://doi.org/10.1016/0009-2614(80)80534-3. URL https://www.sciencedirect.com/science/article/pii/0009261480805343.

[272] Bora Seo, Hu Young Jeong, Sung You Hong, Alla Zak, and Sang Hoon Joo. Impact of a conductive oxide core in tungsten sulfide-based nanostructures on the hydrogen evolution reaction. *Chemical Communications*, 51(39):8334–8337, 2015. ISSN 1359-7345. doi: 10.1039/C5CC02472B. URL http://dx.doi.org/10.1039/C5CC02472B.

[273] Keith Share, John Lewis, Landon Oakes, Rachel E. Carter, Adam P. Cohn, and Cary L. Pint. Tungsten diselenide (wse2) as a high capacity, low overpotential conversion electrode for sodium ion batteries. *RSC Advances*, 5(123):101262–101267, 2015. doi: 10.1039/C5RA19717A. URL http://dx.doi.org/10.1039/C5RA19717A.

[274] Keith Share, Adam P. Cohn, Rachel Carter, Bridget Rogers, and Cary L. Pint. Role of nitrogen-doped graphene for improved high-capacity potassium ion battery anodes. *ACS Nano*, 10(10):9738–9744, 2016. ISSN 1936-0851. doi: 10.1021/acsnano.6b05998. URL https://doi.org/10.1021/acsnano.6b05998.

[275] Mark Shneider, Hanna Dodiuk, Samuel Kenig, and Reshef Tenne. The effect of tungsten sulfide fullerene-like nanoparticles on the toughness of epoxy adhesives. *Journal of Adhesion Science and Technology*, 24(6):1083–1095, 2010. ISSN 0169-4243. doi: 10.1163/016942409X12584625925268. URL https://doi.org/10.1163/016942409X12584625925268.

[276] Zhuang Shuxian, W. Keith Hall, Gerhard Ertl, and Helmut Knözinger. X-ray photoemission study of oxygen and nitric oxide adsorption on mos2. *Journal of Catalysis*, 100(1):167–175, 1986. ISSN 0021-9517. doi: https://doi.org/10.1016/0021-9517(86)90082-5. URL https://www.sciencedirect.com/science/article/pii/0021951786900825.

[277] Surajudeen Sikiru, Temidayo Lekan Oladosu, Sanusi Yekinni Kolawole, Lawal Adeyemi Mubarak, Hassan Soleimani, Lukmon Owolabi Afolabi, and Afolabi-Owolabi Oluwafunke Toyin. Advance and prospect of carbon quantum dots synthesis for energy conversion and storage application: A comprehensive review. *Journal of Energy Storage*, 60:106556, 2023. ISSN 2352-152X. doi: https://doi.org/10.1016/j.est.2022.106556. URL https://www.sciencedirect.com/science/article/pii/S2352152X22025452.

[278] P. Simon and Y. Gogotsi. *Nanoscience and technology: a collection of reviews from nature journals, world scientific*, pages 320–329. Macmillan publishers UK, 2010.

[279] Sudarson S. Sinha, Lena Yadgarov, Sokhrab B. Aliev, Yishay Feldman, Iddo Pinkas, Pallellappa Chithaiah, Saptarshi Ghosh, Alexander Idelevich, Alla Zak, and Reshef Tenne. Mos2 and ws2 nanotubes: Synthesis, structural elucidation, and optical characterization. *The Journal of Physical Chemistry C*, 125(11):6324–6340, 2021. ISSN 1932-7447. doi: 10.1021/acs.jpcc.0c10784. URL https://doi.org/10.1021/acs.jpcc.0c10784.

[280] Davi Marcelo Soares and Gurpreet Singh. Sioc functionalization of mos¡sub¿2¡/sub¿ as a means to improve stability as sodium-ion battery anode. *Nanotechnology*, 31 (14):145403, 2020. ISSN 0957-4484 1361-6528. doi: 10.1088/1361-6528/ab6480. URL http://dx.doi.org/10.1088/1361-6528/ab6480.

[281] Davi Marcelo Soares, Santanu Mukherjee, and Gurpreet Singh. Tmds beyond mos2 for electrochemical energy storage. *Chemistry – A European Journal*, 26(29):6320–6341, 2020. ISSN 0947-6539. doi: https://doi.org/10.1002/chem.202000147. URL https://doi.org/10.1002/chem.202000147.

[282] Yaochen Song, Jiaxuan Liao, Cheng Chen, Jian Yang, Jinchen Chen, Feng Gong, Sizhe Wang, Ziqiang Xu, and Mengqiang Wu. Controllable morphologies and electrochemical performances of self-assembled nano-honeycomb ws2 anodes modified by graphene doping for lithium and sodium ion batteries. *Carbon*, 142:697–706, 2019. ISSN 0008-6223. doi: https://doi.org/10.1016/j.carbon.2018.07.060. URL https://www.sciencedirect.com/science/article/pii/S0008622318307103.

[283] C. Sourisseau, F. Cruege, M. Fouassier, and M. Alba. Second-order raman effects, inelastic neutron scattering and lattice dynamics in 2h-ws2. *Chemical Physics*, 150(2): 281–293, 1991. ISSN 0301-0104. doi: https://doi.org/10.1016/0301-0104(91)80136-6. URL https://www.sciencedirect.com/science/article/pii/0301010491801366.

[284] Andrea Splendiani, Liang Sun, Yuanbo Zhang, Tianshu Li, Jonghwan Kim, Chi-Yung Chim, Giulia Galli, and Feng Wang. Emerging photoluminescence in monolayer mos2.

Nano Letters, 10(4):1271–1275, 2010. ISSN 1530-6984. doi: 10.1021/nl903868w. URL https://doi.org/10.1021/nl903868w.

[285] Christina Stabler, Emanuel Ionescu, Magdalena Graczyk-Zajac, Isabel Gonzalo-Juan, and Ralf Riedel. Silicon oxycarbide glasses and glass-ceramics: "all-rounder" materials for advanced structural and functional applications. *Journal of the American Ceramic Society*, 101(11):4817–4856, 2018. ISSN 0002-7820. doi: https://doi.org/10.1111/jace.15932. URL https://doi.org/10.1111/jace.15932.

[286] A. M. Stacy and D. T. Hodul. Raman spectra of ivb and vib transition metal disulfides using laser energies near the absorption edges. *Journal of Physics and Chemistry of Solids*, 46(4):405–409, 1985. ISSN 0022-3697. doi: https://doi.org/10.1016/0022-3697(85)90103-9. URL https://www.sciencedirect.com/science/article/pii/0022369785901039.

[287] Matthias Staiger, Peter Rafailov, Konstantin Gartsman, Hagen Telg, Matthias Krause, Gal Radovsky, Alla Zak, and Christian Thomsen. Excitonic resonances in ws_2 nanotubes. *Physical Review B*, 86(16):165423, 2012. doi: 10.1103/PhysRevB.86.165423. URL https://link.aps.org/doi/10.1103/PhysRevB.86.165423.

[288] D. A. Stevens and J. R. Dahn. High capacity anode materials for rechargeable sodium-ion batteries. *JOURNAL OF THE ELECTROCHEMICAL SOCIETY*, 147(4):1271–1273, 2000. ISSN 0013-4651. doi: 10.1149/1.1393348.

[289] Fred A. Stevie and Carrie L. Donley. Introduction to x-ray photoelectron spectroscopy. *Journal of Vacuum Science & Technology A*, 38(6), 2020. ISSN 0734-2101.

[290] Dawei Su, Shixue Dou, and Guoxiu Wang. Ws2@graphene nanocomposites as anode materials for na-ion batteries with enhanced electrochemical performances. *Chemical Communications*, 50(32):4192–4195, 2014. ISSN 1359-7345. doi: 10.1039/C4CC00840E. URL http://dx.doi.org/10.1039/C4CC00840E.

[291] Anitha S. Subburaj, Bejoy N. Pushpakaran, and Stephen B. Bayne. Overview of grid connected renewable energy based battery projects in usa. *Renewable and Sustainable Energy Reviews*, 45:219–234, 2015. ISSN 1364-0321. doi: https://doi.org/10.1016/j.rser.2015.01.052. URL https://www.sciencedirect.com/science/article/pii/S1364032115000623.

[292] Ran Sui, Guangtao Zan, Ming Wen, Weina Li, Zihui Liu, Qingsheng Wu, and YongQing Fu. Dual carbon design strategy for anodes of sodium-ion battery: Mesoporous cos2/coo on open framework carbon-spheres with rgo encapsulating. *ACS Applied Materials & Interfaces*, 14(24):28004–28013, 2022. ISSN 1944-8244. doi: 10.1021/acsami.2c06551. URL https://doi.org/10.1021/acsami.2c06551.

[293] Irin Sultana, Thrinathreddy Ramireddy, Md Mokhlesur Rahman, Ying Chen, and Alexey M. Glushenkov. Tin-based composite anodes for potassium-ion batteries. *Chemical Communications*, 52(59):9279–9282, 2016. ISSN 1359-7345. doi: 10.1039/C6CC03649J. URL http://dx.doi.org/10.1039/C6CC03649J.

[294] Irin Sultana, Md Mokhlesur Rahman, Srikanth Mateti, Vahide Ghanooni Ahmadabadi, Alexey M. Glushenkov, and Ying Chen. K-ion and na-ion storage performances of co3o4–fe2o3 nanoparticle-decorated super p carbon black prepared by a ball milling process. *Nanoscale*, 9(10):3646–3654, 2017. ISSN 2040-3364. doi: 10.1039/C6NR09613A. URL http://dx.doi.org/10.1039/C6NR09613A.

[295] Dan Sun, Delai Ye, Ping Liu, Yougen Tang, Jun Guo, Lianzhou Wang, and Haiyan Wang. Mos2/graphene nanosheets from commercial bulky mos2 and graphite as anode materials for high rate sodium-ion batteries. *Advanced Energy Materials*, 8(10):1702383, 2018. ISSN 1614-6832. doi: https://doi.org/10.1002/aenm.201702383. URL https://doi.org/10.1002/aenm.201702383.

[296] Dan Sun, Dan Huang, Haiyan Wang, Gui-Liang Xu, Xiaoyi Zhang, Rui Zhang, Yougen Tang, Deia Abd Ei-Hady, Wael Alshitari, Abdullah Saad Al-Bogami, Khalil Amine, and Minhua Shao. 1t mos2 nanosheets with extraordinary sodium storage

properties via thermal-driven ion intercalation assisted exfoliation of bulky mos2. *Nano Energy*, 61:361–369, 2019. ISSN 2211-2855. doi: https://doi.org/10.1016/j.nanoen.2019.04.063. URL https://www.sciencedirect.com/science/article/pii/S2211285519303647.

[297] Hong Sun and Kejie Zhao. Atomistic origins of high capacity and high structural stability of polymer-derived sioc anode materials. *ACS Applied Materials & Interfaces*, 9(40):35001–35009, 2017. ISSN 1944-8244. doi: 10.1021/acsami.7b10906. URL https://doi.org/10.1021/acsami.7b10906.

[298] Yongming Sun, Ryan B. Sills, Xianluo Hu, Zhi Wei Seh, Xu Xiao, Henghui Xu, Wei Luo, Huanyu Jin, Ying Xin, Tianqi Li, Zhaoliang Zhang, Jun Zhou, Wei Cai, Yunhui Huang, and Yi Cui. A bamboo-inspired nanostructure design for flexible, foldable, and twistable energy storage devices. *Nano Letters*, 15(6):3899–3906, 2015. ISSN 1530-6984. doi: 10.1021/acs.nanolett.5b00738. URL https://doi.org/10.1021/acs.nanolett.5b00738.

[299] Zhenlu Sun, Hongwei Chu, Ying Li, Lijie Liu, Shengzhi Zhao, Guiqiu Li, and Dechun Li. Optical properties of mose2 nanosheets: characterization, simulation and application for q-switching. *Optical Materials Express*, 9(8):3494–3503, 2019. doi: 10.1364/OME.9.003494. URL http://opg.optica.org/ome/abstract.cfm?URI=ome-9-8-3494.

[300] Teck L. Tan, Man-Fai Ng, and Goki Eda. Stable monolayer transition metal dichalcogenide ordered alloys with tunable electronic properties. *The Journal of Physical Chemistry C*, 120(5):2501–2508, 2016. ISSN 1932-7447. doi: 10.1021/acs.jpcc.5b10739. URL https://doi.org/10.1021/acs.jpcc.5b10739.

[301] Huachao Tao, Jing Li, Jinhang Li, Zhenhua Hou, Xuelin Yang, and Li-Zhen Fan. Metallic phase w0.9mo0.1s2 for high-performance anode of sodium ion batteries through suppressing the dissolution of polysulfides. *Journal of Energy Chemistry*, 66:356–

365, 2022. ISSN 2095-4956. doi: https://doi.org/10.1016/j.jechem.2021.08.026. URL https://www.sciencedirect.com/science/article/pii/S2095495621004496.

[302] R. Tenne. Inorganic nanotubes and fullerene-like nanoparticles. *Journal of Materials Research*, 21(11):2726–2743, 2006. ISSN 0884-2914. doi: 10.1557/jmr.2006.0354. URL https://www.cambridge.org/core/article/inorganic-nanotubes-and-fullerenelike-nanoparticles/E45E73DDA400A8F3F6E9061020C833E6.

[303] R. Tenne, L. Margulis, M. Genut, and G. Hodes. Polyhedral and cylindrical structures of tungsten disulphide. *Nature*, 360(6403):444–446, 1992. ISSN 1476-4687. doi: 10.1038/360444a0. URL https://doi.org/10.1038/360444a0.

[304] Reshef Tenne. Advances in the synthesis of inorganic nanotubes and fullerene-like nanoparticles. *Angewandte Chemie International Edition*, 42(42):5124–5132, 2003. ISSN 1433-7851. doi: https://doi.org/10.1002/anie.200301651. URL https://doi.org/10.1002/anie.200301651.

[305] H. Terrones, E. Del Corro, S. Feng, J. M. Poumirol, D. Rhodes, D. Smirnov, N. R. Pradhan, Z. Lin, M. A. T. Nguyen, A. L. Elías, T. E. Mallouk, L. Balicas, M. A. Pimenta, and M. Terrones. New first order raman-active modes in few layered transition metal dichalcogenides. *Scientific Reports*, 4(1):4215, 2014. ISSN 2045-2322. doi: 10.1038/srep04215. URL https://doi.org/10.1038/srep04215.

[306] Michael M. Thackeray, Christopher Wolverton, and Eric D. Isaacs. Electrical energy storage for transportation—approaching the limits of, and going beyond, lithium-ion batteries. *Energy & Environmental Science*, 5(7):7854–7863, 2012.

[307] Philipp Tonndorf, Robert Schmidt, Philipp Böttger, Xiao Zhang, Janna Börner, Andreas Liebig, Manfred Albrecht, Christian Kloc, Ovidiu Gordan, Dietrich R. T. Zahn, Steffen Michaelis de Vasconcellos, and Rudolf Bratschitsch. Photoluminescence emission and raman response of monolayer mos2, mose2, and wse2. *Optics Express*, 21

(4):4908–4916, 2013. doi: 10.1364/OE.21.004908. URL http://opg.optica.org/oe/abstract.cfm?URI=oe-21-4-4908.

[308] Sergio Trasatti and Giovanni Buzzanca. Ruthenium dioxide: A new interesting electrode material. solid state structure and electrochemical behaviour. *Journal of Electroanalytical Chemistry and Interfacial Electrochemistry*, 29(2):A1–A5, 1971. ISSN 0022-0728. doi: https://doi.org/10.1016/S0022-0728(71)80111-0. URL https://www.sciencedirect.com/science/article/pii/S0022072871801110.

[309] Robert Usiskin, Yaxiang Lu, Jelena Popovic, Markas Law, Palani Balaya, Yong-Sheng Hu, and Joachim Maier. Fundamentals, status and promise of sodium-based batteries. *Nature Reviews Materials*, 6(11):1020–1035, 2021. ISSN 2058-8437.

[310] Christoph Vaalma, Daniel Buchholz, and Stefano Passerini. Non-aqueous potassium-ion batteries: a review. *Current Opinion in Electrochemistry*, 9:41–48, 2018. ISSN 2451-9103. doi: https://doi.org/10.1016/j.coelec.2018.03.031. URL https://www.sciencedirect.com/science/article/pii/S2451910318300358.

[311] Christoph Vaalma, Daniel Buchholz, Marcel Weil, and Stefano Passerini. A cost and resource analysis of sodium-ion batteries. *Nature reviews materials*, 3(4):1–11, 2018. ISSN 2058-8437.

[312] Marko Viršek, Adolf Jesih, Ivanka Milošević, Milan Damnjanović, and Maja Remškar. Raman scattering of the mos2 and ws2 single nanotubes. *Surface Science*, 601(13):2868–2872, 2007. ISSN 0039-6028. doi: https://doi.org/10.1016/j.susc.2006.12.050. URL https://www.sciencedirect.com/science/article/pii/S0039602806013458.

[313] Fritz Vollrath and David P. Knight. Liquid crystalline spinning of spider silk. *Nature*, 410(6828):541–548, 2001. ISSN 1476-4687. doi: 10.1038/35069000. URL https://doi.org/10.1038/35069000.

[314] Dragoljub Vrankovic, Magdalena Graczyk-Zajac, Constanze Kalcher, Jochen Rohrer, Malin Becker, Christina Stabler, Grzegorz Trykowski, Karsten Albe, and Ralf Riedel. Highly porous silicon embedded in a ceramic matrix: A stable high-capacity electrode for li-ion batteries. *ACS Nano*, 11(11):11409–11416, 2017. ISSN 1936-0851. doi: 10.1021/acsnano.7b06031. URL https://doi.org/10.1021/acsnano.7b06031.

[315] Bo Wang, Yi Peng, Fei Yuan, Qian Liu, Lizhi Sun, Pin Zhang, Qiujun Wang, Zhaojin Li, and Yimin A. Wu. A comprehensive review of carbons anode for potassium-ion battery: fast kinetic, structure stability and electrochemical. *Journal of Power Sources*, 484:229244, 2021. ISSN 0378-7753. doi: https://doi.org/10.1016/j.jpowsour.2020.229244. URL https://www.sciencedirect.com/science/article/pii/S0378775320315342.

[316] G. X. Wang, Steve Bewlay, Jane Yao, H. K. Liu, and S. X. Dou. Tungsten disulfide nanotubes for lithium storage. *Electrochemical and Solid-State Letters*, 7(10):A321, 2004. ISSN 1099-0062. doi: 10.1149/1.1788591. URL http://dx.doi.org/10.1149/1.1788591.

[317] Gongming Wang, Hanyu Wang, Xihong Lu, Yichuan Ling, Minghao Yu, Teng Zhai, Yexiang Tong, and Yat Li. Solid-state supercapacitor based on activated carbon cloths exhibits excellent rate capability. *Advanced Materials*, 26(17):2676–2682, 2014. ISSN 0935-9648. doi: https://doi.org/10.1002/adma.201304756. URL https://doi.org/10.1002/adma.201304756.

[318] Haotian Wang, Desheng Kong, Petr Johanes, Judy J. Cha, Guangyuan Zheng, Kai Yan, Nian Liu, and Yi Cui. Mose2 and wse2 nanofilms with vertically aligned molecular layers on curved and rough surfaces. *Nano Letters*, 13(7):3426–3433, 2013. ISSN 1530-6984. doi: 10.1021/nl401944f. URL https://doi.org/10.1021/nl401944f.

[319] Hui Wang, Xiaoyan Wang, Li Wang, Jin Wang, Danlu Jiang, Guopen Li, Yan Zhang, Honghai Zhong, and Yang Jiang. Phase transition mechanism and electrochemical properties of nanocrystalline mose2 as anode materials for the high performance

lithium-ion battery. *The Journal of Physical Chemistry C*, 119(19):10197–10205, 2015. ISSN 1932-7447. doi: 10.1021/acs.jpcc.5b00353. URL https://doi.org/10.1021/acs.jpcc.5b00353.

[320] Hui Wang, Xiaoyan Wang, Li Wang, Jin Wang, Danlu Jiang, Guopen Li, Yan Zhang, Honghai Zhong, and Yang Jiang. Phase transition mechanism and electrochemical properties of nanocrystalline mose2 as anode materials for the high performance lithium-ion battery. *The Journal of Physical Chemistry C*, 119(19):10197–10205, 2015. doi: https://doi.org/10.1021/acs.jpcc.5b00353. URL https://doi.org/10.1021/acs.jpcc.5b00353.

[321] Jianbiao Wang, Ling Yu, Ziwang Zhou, Lingxing Zeng, and Mingdeng Wei. Template-free synthesis of metallic ws2 hollow microspheres as an anode for the sodium-ion battery. *Journal of Colloid and Interface Science*, 557:722–728, 2019. ISSN 0021-9797. doi: https://doi.org/10.1016/j.jcis.2019.09.078. URL https://www.sciencedirect.com/science/article/pii/S0021979719311221.

[322] John Wang, Julien Polleux, James Lim, and Bruce Dunn. Pseudocapacitive contributions to electrochemical energy storage in tio2 (anatase) nanoparticles. *The Journal of Physical Chemistry C*, 111(40):14925–14931, 2007. ISSN 1932-7447. doi: 10.1021/jp074464w. URL https://doi.org/10.1021/jp074464w.

[323] Jue Wang, Ling Fan, Zhaomeng Liu, Suhua Chen, Qingfeng Zhang, Longlu Wang, Hongguan Yang, Xinzhi Yu, and Bingan Lu. In situ alloying strategy for exceptional potassium ion batteries. *ACS Nano*, 13(3):3703–3713, 2019. ISSN 1936-0851. doi: 10.1021/acsnano.9b00634. URL https://doi.org/10.1021/acsnano.9b00634.

[324] Ke Wang, Shu Luo, Yang Wu, Xingfeng He, Fei Zhao, Jiaping Wang, Kaili Jiang, and Shoushan Fan. Super-aligned carbon nanotube films as current collectors for lightweight and flexible lithium ion batteries. *Advanced Functional Materials*, 23(7):846–853, 2013. ISSN 1616-301X.

[325] Meice Wang, Dawei Fang, Nannan Wang, Shan Jiang, Jun Nie, Qiang Yu, and Guiping Ma. Preparation of pvdf/pvp core–shell nanofibers mats via homogeneous electrospinning. *Polymer*, 55(9):2188–2196, 2014. ISSN 0032-3861. doi: https://doi.org/10.1016/j.polymer.2014.02.035. URL https://www.sciencedirect.com/science/article/pii/S0032386114001372.

[326] Mengqi Wang, Xinlong Liu, Binyang Qin, Zhiyong Li, Yufei Zhang, Wei Yang, and Haosen Fan. In-situ etching and ion exchange induced 2d-2d mxene@co9s8/como2s4 heterostructure for superior na+ storage. *Chemical Engineering Journal*, 451:138508, 2023. ISSN 1385-8947. doi: https://doi.org/10.1016/j.cej.2022.138508. URL https://www.sciencedirect.com/science/article/pii/S1385894722039894.

[327] Nan Wang, Bingzhang Lu, Ligui Li, Wenhan Niu, Zhenghua Tang, Xiongwu Kang, and Shaowei Chen. Graphitic nitrogen is responsible for oxygen electroreduction on nitrogen-doped carbons in alkaline electrolytes: Insights from activity attenuation studies and theoretical calculations. *ACS Catalysis*, 8(8):6827–6836, 2018. doi: 10.1021/acscatal.8b00338. URL https://doi.org/10.1021/acscatal.8b00338.

[328] Xiao Hu Wang, Chang Cheng Zheng, and Ji Qiang Ning. Influence of curvature strain and van der waals force on the inter-layer vibration mode of ws2 nanotubes: A confocal micro-raman spectroscopic study. *Scientific Reports*, 6(1):33091, 2016. ISSN 2045-2322. doi: 10.1038/srep33091. URL https://doi.org/10.1038/srep33091.

[329] Xinsheng Wang, Hongbin Feng, Yongmin Wu, and Liying Jiao. Controlled synthesis of highly crystalline mos2 flakes by chemical vapor deposition. *Journal of the American Chemical Society*, 135(14):5304–5307, 2013. ISSN 0002-7863. doi: 10.1021/ja4013485. URL https://doi.org/10.1021/ja4013485.

[330] Ye Wang, Dezhi Kong, Wenhui Shi, Bo Liu, Glenn Joey Sim, Qi Ge, and Hui Ying Yang. Ice templated free-standing hierarchically ws2/cnt-rgo aerogel for high-performance rechargeable lithium and sodium ion batteries. *Advanced Energy Ma-*

terials, 6(21):1601057, 2016. ISSN 1614-6832. doi: https://doi.org/10.1002/aenm.201601057. URL https://doi.org/10.1002/aenm.201601057.

[331] Ye Wang, Dezhi Kong, Shaozhuan Huang, Yumeng Shi, Meng Ding, Yew Von Lim, Tingting Xu, Fuming Chen, Xinjian Li, and Hui Ying Yang. 3d carbon foam-supported ws2 nanosheets for cable-shaped flexible sodium ion batteries. *Journal of Materials Chemistry A*, 6(23):10813–10824, 2018. ISSN 2050-7488. doi: 10.1039/C8TA02773K. URL http://dx.doi.org/10.1039/C8TA02773K.

[332] Yunsong Wang, Zhimin Ma, Yijun Chen, Mingchu Zou, Muhammad Yousaf, Yanbing Yang, Liusi Yang, Anyuan Cao, and Ray P. S. Han. Controlled synthesis of core–shell carbon@mos2 nanotube sponges as high-performance battery electrodes. *Advanced Materials*, 28(46):10175–10181, 2016. ISSN 0935-9648. doi: https://doi.org/10.1002/adma.201603812. URL https://doi.org/10.1002/adma.201603812.

[333] Zhiyu Wang, Weike Zhang, Xuelian Li, and Lizhen Gao. Recent progress in flexible energy storage materials for lithium-ion batteries and electrochemical capacitors: A review. *Journal of Materials Research*, 31(12):1648–1664, 2016. ISSN 0884-2914.

[334] Shuangying Wei, Marco Serra, Stefanos Mourdikoudis, Huaijuan Zhou, Bing Wu, Lukáš Děkanovský, Jiří Šturala, Jan Luxa, Reshef Tenne, Alla Zak, and Zdeněk Sofer. Improved electrochemical performance of nts-ws2@c nanocomposites for lithium-ion and sodium-ion batteries. *ACS Applied Materials & Interfaces*, 14(41):46386–46400, 2022. ISSN 1944-8244. doi: 10.1021/acsami.2c06295. URL https://doi.org/10.1021/acsami.2c06295.

[335] Qingbo Wen, Zhaoju Yu, and Ralf Riedel. The fate and role of in situ formed carbon in polymer-derived ceramics. *Progress in Materials Science*, 109:100623, 2020. ISSN 0079-6425. doi: https://doi.org/10.1016/j.pmatsci.2019.100623. URL https://www.sciencedirect.com/science/article/pii/S0079642519301057.

[336] M. S. Whittingham. History, evolution, and future status of energy storage. *Proceedings*

of the IEEE, 100(Special Centennial Issue):1518–1534, 2012. ISSN 1558-2256. doi: 10.1109/JPROC.2012.2190170.

[337] M. Stanley Whittingham. Electrointercalation in transition-metal disulphides. *Journal of the Chemical Society, Chemical Communications*, (9):328–329, 1974.

[338] M. Stanley Whittingham. Electrical energy storage and intercalation chemistry. *Science*, 192(4244):1126–1127, 1976. ISSN 0036-8075.

[339] M. Stanley Whittingham. Lithium batteries and cathode materials. *Chemical reviews*, 104(10):4271–4302, 2004. ISSN 0009-2665.

[340] Bret C. Windom, W. G. Sawyer, and David W. Hahn. A raman spectroscopic study of mos2 and moo3: Applications to tribological systems. *Tribology Letters*, 42(3):301–310, 2011. ISSN 1573-2711. doi: 10.1007/s11249-011-9774-x. URL https://doi.org/10.1007/s11249-011-9774-x.

[341] Martin Winter, Jürgen O. Besenhard, Michael E. Spahr, and Petr Novak. Insertion electrode materials for rechargeable lithium batteries. *Advanced materials*, 10(10):725–763, 1998. ISSN 0935-9648.

[342] Seung Hee Woo, Lena Yadgarov, Rita Rosentsveig, Yuwon Park, Daesun Song, Reshef Tenne, and Sung You Hong. Fullerene-like re-doped mos2 nanoparticles as an intercalation host with fast kinetics for sodium ion batteries. *Israel Journal of Chemistry*, 55(5):599–603, 2015. ISSN 0021-2148. doi: https://doi.org/10.1002/ijch.201400124. URL https://doi.org/10.1002/ijch.201400124.

[343] Hsien-Ming Wu and Show-An Chen. Dopant-polymer interaction: Mocl5-doped polyacetylene. *Synthetic Metals*, 26(3):225–236, 1988. ISSN 0379-6779. doi: https://doi.org/10.1016/0379-6779(88)90239-1. URL https://www.sciencedirect.com/science/article/pii/0379677988902391.

[344] Yuhan Wu, Yang Xu, Yueliang Li, Pengbo Lyu, Jin Wen, Chenglin Zhang, Min Zhou, Yaoguo Fang, Huaping Zhao, Ute Kaiser, and Yong Lei. Unexpected intercalation-

dominated potassium storage in ws2 as a potassium-ion battery anode. *Nano Research*, 12(12):2997–3002, 2019. ISSN 1998-0000. doi: 10.1007/s12274-019-2543-0. URL https://doi.org/10.1007/s12274-019-2543-0.

[345] Xiaoxiang Xi, Zefang Wang, Weiwei Zhao, Ju-Hyun Park, Kam Tuen Law, Helmuth Berger, László Forró, Jie Shan, and Kin Fai Mak. Ising pairing in superconducting nbse2 atomic layers. *Nature Physics*, 12(2):139–143, 2016. ISSN 1745-2481. doi: 10.1038/nphys3538. URL https://doi.org/10.1038/nphys3538.

[346] Ji-Li Xia, Dong Yan, Li-Ping Guo, Xiao-Ling Dong, Wen-Cui Li, and An-Hui Lu. Hard carbon nanosheets with uniform ultramicropores and accessible functional groups showing high realistic capacity and superior rate performance for sodium-ion storage. *Advanced Materials*, 32(21):2000447, 2020. ISSN 0935-9648. doi: https://doi.org/10.1002/adma.202000447. URL https://doi.org/10.1002/adma.202000447.

[347] Ting Xiang, Shi Tao, Weiyu Xu, Qi Fang, Chuanqiang Wu, Daobin Liu, Yu Zhou, Adnan Khalil, Zahir Muhammad, Wangsheng Chu, Zhonghui Wang, Hongfa Xiang, Qin Liu, and Li Song. Stable 1t-mose2 and carbon nanotube hybridized flexible film: Binder-free and high-performance li-ion anode. *ACS Nano*, 11(6):6483–6491, 2017. ISSN 1936-0851. doi: 10.1021/acsnano.7b03329. URL https://doi.org/10.1021/acsnano.7b03329.

[348] L. M. Xie. Two-dimensional transition metal dichalcogenide alloys: preparation, characterization and applications. *Nanoscale*, 7(44):18392–18401, 2015. ISSN 2040-3364. doi: 10.1039/C5NR05712D. URL http://dx.doi.org/10.1039/C5NR05712D.

[349] Xiaobing Xie and Robert E. McCarley. Synthesis, structure, and characterization of n-ligated tungsten selenide cluster complexes w6se8l6. *Inorganic Chemistry*, 34(24):6124–6129, 1995. ISSN 0020-1669. doi: 10.1021/ic00128a025. URL https://doi.org/10.1021/ic00128a025.

[350] Huizhong Xu, Lei Sun, Wei Li, Mengyou Gao, Qiannan Zhou, Ping Li, Shikuan Yang,

and Jianjian Lin. Facile synthesis of hierarchical g-c3n4@ws2 composite as lithium-ion battery anode. *Chemical Engineering Journal*, 435:135129, 2022. ISSN 1385-8947. doi: https://doi.org/10.1016/j.cej.2022.135129. URL https://www.sciencedirect.com/science/article/pii/S1385894722006349.

[351] Jing Xu, Qing Liu, Zhong Dong, Lina Wang, Xingchen Xie, Yong Jiang, Zhengnan Wei, Yongping Gao, Yu Zhang, and Kejing Huang. Interconnected mos2 on 2d graphdiyne for reversible sodium storage. *ACS Applied Materials & Interfaces*, 13(46):54974–54980, 2021. ISSN 1944-8244. doi: 10.1021/acsami.1c15484. URL https://doi.org/10.1021/acsami.1c15484.

[352] Jun Xu, Junjun Zhang, Wenjun Zhang, and Chun-Sing Lee. Interlayer nanoarchitectonics of two-dimensional transition-metal dichalcogenides nanosheets for energy storage and conversion applications. *Advanced Energy Materials*, 7(23):1700571, 2017. ISSN 1614-6832. doi: https://doi.org/10.1002/aenm.201700571. URL https://doi.org/10.1002/aenm.201700571.

[353] Xiangdong Xu, Xuejin Li, Jingqi Zhang, Ke Qiao, Dezhi Han, Shaoting Wei, Wei Xing, and Zifeng Yan. Surfactant assisted electrospinning of ws2 nanofibers and its promising performance as anode material of sodium-ion batteries. *Electrochimica Acta*, 302:259–269, 2019. ISSN 0013-4686. doi: https://doi.org/10.1016/j.electacta.2019.02.042. URL https://www.sciencedirect.com/science/article/pii/S0013468619302853.

[354] Yang Xu, Farzaneh Bahmani, Min Zhou, Yueliang Li, Chenglin Zhang, Feng Liang, Sayed Habib Kazemi, Ute Kaiser, Guowen Meng, and Yong Lei. Enhancing potassium-ion battery performance by defect and interlayer engineering. *Nanoscale Horizons*, 4(1):202–207, 2019. ISSN 2055-6756. doi: 10.1039/C8NH00305J. URL http://dx.doi.org/10.1039/C8NH00305J.

[355] Yaobin Xu, Ke Wang, Zhenpeng Yao, Joohoon Kang, David Lam, Dan Yang, Wei Ai, Chris Wolverton, Mark C. Hersam, Ying Huang, Wei Huang, Vinayak P. Dravid, and Jinsong Wu. In situ, atomic-resolution observation of lithiation and sodiation of

ws2 nanoflakes: Implications for lithium-ion and sodium-ion batteries. *Small*, 17(24): 2100637, 2021. ISSN 1613-6810. doi: https://doi.org/10.1002/smll.202100637. URL https://doi.org/10.1002/smll.202100637.

[356] Hao Yan, Lihua Chu, Ze Li, Changxu Sun, Yuxin Shi, and Jing Ma. 2h-mos2/ti3c2tx mxene composites for enhanced no2 gas sensing properties at room temperature, 2022. URL https://www.sciencedirect.com/science/article/pii/S2666053922000303.

[357] Xiaojie Yan, Muhammad Sahimi, and Theodore T. Tsotsis. Fabrication of high-surface area nanoporous sioc ceramics using pre-ceramic polymer precursors and a sacrificial template: Precursor effects. *Microporous and Mesoporous Materials*, 241:338–345, 2017. ISSN 1387-1811. doi: https://doi.org/10.1016/j.micromeso.2016.12.027. URL https://www.sciencedirect.com/science/article/pii/S1387181116305868.

[358] Wanfeng Yang, Jiawei Wang, Conghui Si, Zhangquan Peng, Jan Frenzel, Gunther Eggeler, and Zhonghua Zhang. [001] preferentially-oriented 2d tungsten disulfide nanosheets as anode materials for superior lithium storage. *Journal of Materials Chemistry A*, 3(34):17811–17819, 2015. ISSN 2050-7488. doi: 10.1039/C5TA04176G. URL http://dx.doi.org/10.1039/C5TA04176G.

[359] Hyun Deog Yoo, Elena Markevich, Gregory Salitra, Daniel Sharon, and Doron Aurbach. On the challenge of developing advanced technologies for electrochemical energy storage and conversion. *Materials today*, 17(3):110–121, 2014. ISSN 1369-7021.

[360] Xueqiu You, Na Liu, Cheol Jin Lee, and James Jungho Pak. An electrochemical route to mos2 nanosheets for device applications. *Materials Letters*, 121:31–35, 2014. ISSN 0167-577X. doi: https://doi.org/10.1016/j.matlet.2014.01.052. URL https://www.sciencedirect.com/science/article/pii/S0167577X14000688.

[361] Bo Yu, Yuanfu Chen, Zegao Wang, Dongjiang Chen, Xinqiang Wang, Wanli Zhang, Jiarui He, and Weidong He. 1t-mos2 nanotubes wrapped with n-doped graphene

as highly-efficient absorbent and electrocatalyst for li–s batteries. *Journal of Power Sources*, 447:227364, 2020. ISSN 0378-7753. doi: https://doi.org/10.1016/j.jpowsour.2019.227364. URL https://www.sciencedirect.com/science/article/pii/S0378775319313576.

[362] Sunmoon Yu, Ji-Won Jung, and Il-Doo Kim. Single layers of ws2 nanoplates embedded in nitrogen-doped carbon nanofibers as anode materials for lithium-ion batteries. *Nanoscale*, 7(28):11945–11950, 2015. ISSN 2040-3364. doi: 10.1039/C5NR02425K. URL http://dx.doi.org/10.1039/C5NR02425K.

[363] Q. Yun, L. Li, Z. Hu, Q. Lu, B. Chen, and H. Zhang. Layered transition metal dichalcogenide-based nanomaterials for electrochemical energy storage. *Adv. Mater.*, 32, 2020. doi: 10.1002/adma.201903826. URL https://dx.doi.org/10.1002/adma.201903826.

[364] Qinbai Yun, Qipeng Lu, Xiao Zhang, Chaoliang Tan, and Hua Zhang. Three-dimensional architectures constructed from transition-metal dichalcogenide nanomaterials for electrochemical energy storage and conversion. *Angewandte Chemie International Edition*, 57(3):626–646, 2018. ISSN 1433-7851. doi: https://doi.org/10.1002/anie.201706426. URL https://doi.org/10.1002/anie.201706426.

[365] A. Zak, L. Sallacan-Ecker, A. Margolin, M. Genut, and R. Tenne. Insight into the growth mechanism of ws2 nanotubes in the scaled-up fluidized-bed reactor. *Nano*, 04 (02):91–98, 2009. ISSN 1793-2920. doi: 10.1142/S1793292009001551. URL https://doi.org/10.1142/S1793292009001551.

[366] A. Zak, L. Sallacan-Ecker, A. Margolin, Y. Feldman, R. Popovitz-Biro, A. Albu-Yaron, M. Genut, and R. Tenne. Scaling up of the ws2 nanotubes synthesis. *Fullerenes, Nanotubes and Carbon Nanostructures*, 19(1-2):18–26, 2010. ISSN 1536-383X. doi: 10.1080/1536383X.2010.488594. URL https://doi.org/10.1080/1536383X.2010.488594.

[367] Alla Zak, Yishay Feldman, Vera Lyakhovitskaya, Gregory Leitus, Ronit Popovitz-Biro, Ellen Wachtel, Hagai Cohen, Shimon Reich, and Reshef Tenne. Alkali metal intercalated fullerene-like ms2 (m = w, mo) nanoparticles and their properties. *Journal of the American Chemical Society*, 124(17):4747–4758, 2002. ISSN 0002-7863. doi: 10.1021/ja012060q. URL https://doi.org/10.1021/ja012060q.

[368] Hualing Zeng, Gui-Bin Liu, Junfeng Dai, Yajun Yan, Bairen Zhu, Ruicong He, Lu Xie, Shijie Xu, Xianhui Chen, Wang Yao, and Xiaodong Cui. Optical signature of symmetry variations and spin-valley coupling in atomically thin tungsten dichalcogenides. *Scientific Reports*, 3(1):1608, 2013. ISSN 2045-2322. doi: 10.1038/srep01608. URL https://doi.org/10.1038/srep01608.

[369] Lingxing Zeng, Yixing Fang, Lihong Xu, Cheng Zheng, Min-Quan Yang, Jiafang He, Hun Xue, Qingrong Qian, Mingdeng Wei, and Qinghua Chen. Rational design of few-layer mose2 confined within znse–c hollow porous spheres for high-performance lithium-ion and sodium-ion batteries. *Nanoscale*, 11(14):6766–6775, 2019. ISSN 2040-3364. doi: 10.1039/C9NR00146H. URL http://dx.doi.org/10.1039/C9NR00146H.

[370] Sifan Zeng, Wanlin Feng, Shuyuan Peng, Zhen Teng, Chen Chen, Haibin Zhang, and Shuming Peng. Dual-functional sioc ceramics coating modified carbon fibers with enhanced microwave absorption performance. *RSC Advances*, 9(53):30685–30692, 2019. doi: 10.1039/C9RA06166E. URL http://dx.doi.org/10.1039/C9RA06166E.

[371] Zhiyuan Zeng, Zongyou Yin, Xiao Huang, Hai Li, Qiyuan He, Gang Lu, Freddy Boey, and Hua Zhang. Single-layer semiconducting nanosheets: high-yield preparation and device fabrication. *Angewandte Chemie*, 123(47):11289–11293, 2011. ISSN 0044-8249.

[372] Wenwei Zhan, Ming Zhu, Jinle Lan, Haocheng Yuan, Haijun Wang, Xiaoping Yang, and Gang Sui. All-in-one mos2 nanosheets tailored by porous nitrogen-doped graphene for fast and highly reversible sodium storage. *ACS Applied Materials & Interfaces*, 12 (46):51488–51498, 2020. ISSN 1944-8244. doi: 10.1021/acsami.0c15169. URL https://doi.org/10.1021/acsami.0c15169.

[373] Yongjie Zhan, Zheng Liu, Sina Najmaei, Pulickel M. Ajayan, and Jun Lou. Large-area vapor-phase growth and characterization of mos2 atomic layers on a sio2 substrate. *Small*, 8(7):966–971, 2012. ISSN 1613-6810. doi: https://doi.org/10.1002/smll.201102654. URL https://doi.org/10.1002/smll.201102654.

[374] Bin Zhang, Chong Luo, Yaqian Deng, Zhijia Huang, Guangmin Zhou, Wei Lv, Yan-Bing He, Ying Wan, Feiyu Kang, and Quan-Hong Yang. Optimized catalytic ws2–wo3 heterostructure design for accelerated polysulfide conversion in lithium–sulfur batteries. *Advanced Energy Materials*, 10(15):2000091, 2020. ISSN 1614-6832. doi: https://doi.org/10.1002/aenm.202000091. URL https://doi.org/10.1002/aenm.202000091.

[375] Chenglin Zhang, Huaping Zhao, and Yong Lei. Recent research progress of anode materials for potassium-ion batteries. *ENERGY & ENVIRONMENTAL MATERIALS*, 3(2):105–120, 2020. doi: https://doi.org/10.1002/eem2.12059. URL https://doi.org/10.1002/eem2.12059.

[376] Jiyu Zhang, Keming Song, Liwei Mi, Chuntai Liu, Xiangming Feng, Jianmin Zhang, Weihua Chen, and Changyu Shen. Bimetal synergistic effect induced high reversibility of conversion-type ni@nico2s4 as a free-standing anode for sodium ion batteries. *The Journal of Physical Chemistry Letters*, 11(4):1435–1442, 2020. doi: 10.1021/acs.jpclett.9b03336. URL https://doi.org/10.1021/acs.jpclett.9b03336.

[377] Liang Zhang, Dan Sun, Jun Kang, Jun Feng, Hans A. Bechtel, Lin-Wang Wang, Elton J. Cairns, and Jinghua Guo. Electrochemical reaction mechanism of the mos2 electrode in a lithium-ion cell revealed by in situ and operando x-ray absorption spectroscopy. *Nano Letters*, 18(2):1466–1475, 2018. ISSN 1530-6984. doi: 10.1021/acs.nanolett.7b05246. URL https://doi.org/10.1021/acs.nanolett.7b05246.

[378] Ling Zhang, Ling-yu Tu, Yan Liang, Qi Chen, Ze-sheng Li, Chun-hai Li, Zhi-hui Wang, and Wen Li. Coconut-based activated carbon fibers for efficient adsorption of various

organic dyes. *RSC Advances*, 8(74):42280–42291, 2018. doi: 10.1039/C8RA08990F. URL http://dx.doi.org/10.1039/C8RA08990F.

[379] Mei Zhang, Juanxia Wu, Yiming Zhu, Dumitru O. Dumcenco, Jinhua Hong, Nannan Mao, Shibin Deng, Yanfeng Chen, Yanlian Yang, Chuanhong Jin, Sunil H. Chaki, Ying-Sheng Huang, Jin Zhang, and Liming Xie. Two-dimensional molybdenum tungsten diselenide alloys: Photoluminescence, raman scattering, and electrical transport. *ACS Nano*, 8(7):7130–7137, 2014. ISSN 1936-0851. doi: 10.1021/nn5020566. URL https://doi.org/10.1021/nn5020566.

[380] Mengzhi Zhang, Chunmei Tang, Wang Cheng, and Ling Fu. The first-principles study on the performance of the graphene/ws2 heterostructure as an anode material of li-ion battery. *Journal of Alloys and Compounds*, 855:157432, 2021. ISSN 0925-8388. doi: https://doi.org/10.1016/j.jallcom.2020.157432. URL https://www.sciencedirect.com/science/article/pii/S0925838820337968.

[381] Qingyong Zhang, Liang Mei, Xiehong Cao, Yuxin Tang, and Zhiyuan Zeng. Intercalation and exfoliation chemistries of transition metal dichalcogenides. *Journal of Materials Chemistry A*, 8(31):15417–15444, 2020. ISSN 2050-7488. doi: 10.1039/D0TA03727C. URL http://dx.doi.org/10.1039/D0TA03727C.

[382] Ruding Zhang, Jingze Bao, Yilong Pan, and Chuan-Fu Sun. Highly reversible potassium-ion intercalation in tungsten disulfide. *Chemical Science*, 10(9):2604–2612, 2019. ISSN 2041-6520. doi: 10.1039/C8SC04350G. URL http://dx.doi.org/10.1039/C8SC04350G.

[383] Sanpei Zhang, Gan Wang, Jun Jin, Linlin Zhang, Zhaoyin Wen, and Jianhua Yang. Robust and conductive red mose2 for stable and fast lithium storage. *ACS Nano*, 12 (4):4010–4018, 2018. ISSN 1936-0851. doi: 10.1021/acsnano.8b01703. URL https://doi.org/10.1021/acsnano.8b01703.

[384] Wenchao Zhang, Yajie Liu, and Zaiping Guo. Approaching high-performance

potassium-ion batteries via advanced design strategies and engineering. *Science Advances*, 5(5):eaav7412. doi: 10.1126/sciadv.aav7412. URL https://doi.org/10.1126/sciadv.aav7412.

[385] Wenchao Zhang, Jianfeng Mao, Sean Li, Zhixin Chen, and Zaiping Guo. Phosphorus-based alloy materials for advanced potassium-ion battery anode. *Journal of the American Chemical Society*, 139(9):3316–3319, 2017. ISSN 0002-7863. doi: 10.1021/jacs.6b12185. URL https://doi.org/10.1021/jacs.6b12185.

[386] Wenchao Zhang, Yajie Liu, and Zaiping Guo. Approaching high-performance potassium-ion batteries via advanced design strategies and engineering. *Science advances*, 5(5):eaav7412, 2019. ISSN 2375-2548.

[387] Xiangdan Zhang, Kangli Liu, Shijie Zhang, Fujun Miao, Weidong Xiao, Yonglong Shen, Peng Zhang, Zhuo Wang, and Guosheng Shao. Enabling remarkable cycling performance of high-loading mos2@graphene anode for sodium ion batteries with tunable cut-off voltage. *Journal of Power Sources*, 458:228040, 2020. ISSN 0378-7753. doi: https://doi.org/10.1016/j.jpowsour.2020.228040. URL https://www.sciencedirect.com/science/article/pii/S0378775320303438.

[388] Yingxi Zhang, Liao Zhang, Tu'an Lv, Paul K. Chu, and Kaifu Huo. Two-dimensional transition metal chalcogenides for alkali metal ions storage. *ChemSusChem*, 13(6):1114–1154, 2020. ISSN 1864-5631.

[389] Zhengwei Zhang, Peng Chen, Xidong Duan, Ketao Zang, Jun Luo, and Xiangfeng Duan. Robust epitaxial growth of two-dimensional heterostructures, multiheterostructures, and superlattices. *Science*, 357(6353):788–792, 2017. doi: 10.1126/science.aan6814. URL https://doi.org/10.1126/science.aan6814.

[390] Zhian Zhang, Xing Yang, and Yun Fu. Nanostructured wse2/c composites as anode materials for sodium-ion batteries. *RSC Advances*, 6(16):12726–12729, 2016. doi: 10.1039/C5RA25645C. URL http://dx.doi.org/10.1039/C5RA25645C.

[391] Lina Zhao, Teng Zhang, Wei Li, Tao Li, Long Zhang, Xiaoguang Zhang, and Zhiyi Wang. Engineering of sodium-ion batteries: Opportunities and challenges. *Engineering*, 2022. ISSN 2095-8099. doi: https://doi.org/10.1016/j.eng.2021.08.032. URL https://www.sciencedirect.com/science/article/pii/S2095809922003630.

[392] Tianfeng Zhao, Haibo Shu, Zihong Shen, Huimin Hu, Jun Wang, and Xiaoshuang Chen. Electrochemical lithiation mechanism of two-dimensional transition-metal dichalcogenide anode materials: Intercalation versus conversion reactions. *The Journal of Physical Chemistry C*, 123(4):2139–2146, 2019. ISSN 1932-7447. doi: 10.1021/acs.jpcc.8b11503. URL https://doi.org/10.1021/acs.jpcc.8b11503.

[393] Wenxi Zhao and Xiaoqing Ma. Hierarchical scalelike yolk–shell construction assembled via ultrathin mose2 nanoplates incorporated into metal–organic frameworks derived porous carbon spheres as highly durable anode for enhanced sodium storage. *ACS Sustainable Chemistry & Engineering*, 8(51):19040–19050, 2020. doi: 10.1021/acssuschemeng.0c07220. URL https://doi.org/10.1021/acssuschemeng.0c07220.

[394] Yu Zhao, Hyunjea Lee, Woong Choi, Weidong Fei, and Cheol Jin Lee. Large-area synthesis of monolayer mose2 films on sio2/si substrates by atmospheric pressure chemical vapor deposition. *RSC Advances*, 7(45):27969–27973, 2017. doi: 10.1039/C7RA03642F. URL http://dx.doi.org/10.1039/C7RA03642F.

[395] Mingbo Zheng, Hao Tang, Qin Hu, Shasha Zheng, Lulu Li, Jing Xu, and Huan Pang. Tungsten-based materials for lithium-ion batteries. *Advanced Functional Materials*, 28 (20):1707500, 2018. ISSN 1616-301X. doi: https://doi.org/10.1002/adfm.201707500. URL https://doi.org/10.1002/adfm.201707500.

[396] Jingwen Zhou, Jian Qin, Lichao Guo, Naiqin Zhao, Chunsheng Shi, En-zuo Liu, Fang He, Liying Ma, Jiajun Li, and Chunnian He. Scalable synthesis of high-quality transition metal dichalcogenide nanosheets and their application as sodium-ion battery anodes. *Journal of Materials Chemistry A*, 4(44):17370–17380, 2016. ISSN 2050-7488. doi: 10.1039/C6TA07425A. URL http://dx.doi.org/10.1039/C6TA07425A.

[397] Changbao Zhu, Peter Kopold, Weihan Li, Peter A. van Aken, Joachim Maier, and Yan Yu. Engineering nanostructured electrode materials for high performance sodium ion batteries: a case study of a 3d porous interconnected ws2/c nanocomposite. *Journal of Materials Chemistry A*, 3(41):20487–20493, 2015. ISSN 2050-7488. doi: 10.1039/C5TA05758B. URL http://dx.doi.org/10.1039/C5TA05758B.

[398] Qing Zhu, Wenhao Li, Jinxin Wu, Ningchen Tian, Yanwei Li, Jianwen Yang, Botian Liu, and Jiqiong Jiang. Vacancy engineering in ws2 nanosheets for enhanced potassium-ion storage. *Journal of Power Sources*, 542:231791, 2022. ISSN 0378-7753. doi: https://doi.org/10.1016/j.jpowsour.2022.231791. URL https://www.sciencedirect.com/science/article/pii/S0378775322007819.

[399] Y. Q. Zhu, W. K. Hsu, H. Terrones, N. Grobert, B. H. Chang, M. Terrones, B. Q. Wei, H. W. Kroto, D. R. M. Walton, C. B. Boothroyd, I. Kinloch, G. Z. Chen, A. H. Windle, and D. J. Fray. Morphology, structure and growth of ws nanotubes. *Journal of Materials Chemistry*, 10(11):2570–2577, 2000. ISSN 0959-9428. doi: 10.1039/B004433O. URL http://dx.doi.org/10.1039/B004433O.

[400] Cordt Zollfrank, Ralf Kladny, Heino Sieber, and Peter Greil. Biomorphous sioc/c-ceramic composites from chemically modified wood templates. *Journal of the European Ceramic Society*, 24(2):479–487, 2004. ISSN 0955-2219. doi: https://doi.org/10.1016/S0955-2219(03)00202-4. URL https://www.sciencedirect.com/science/article/pii/S0955221903002024.